A submesoscale modelling approach to understanding the past, present, and future carbonate chemistry balance of the Salish Sea

by

Tereza Jarníková

M. Sc., The University of British Columbia, 2016

B. Sc., McGill University, 2012

A THESIS SUBMITTED IN PARTIAL FULFILLMENT
OF THE REQUIREMENTS FOR THE DEGREE OF

Doctor of Philosophy

in

THE FACULTY OF GRADUATE AND POSTDOCTORAL STUDIES

(Oceanography)

The University of British Columbia

(Vancouver)

May 2022

The following individuals certify that they have read, and recommend to the Faculty of Graduate and Postdoctoral Studies for acceptance, the dissertation entitled:

A submesoscale modelling approach to understanding the past, present, and future carbonate chemistry balance of the Salish Sea

submitted by **Tereza Jarníková** in partial fulfillment of the requirements for the degree of **Doctor of Philosophy** in **Oceanography**.

Examining Committee:

Susan E. Allen, Department of Earth, Ocean and Atmospheric Sciences
Supervisor

Debby Ianson, Department of Earth and Ocean Sciences, University of Victoria
Co-Supervisor

Roger Francois, Department of Earth, Ocean and Atmospheric Sciences
University Examiner

William Cheung, Institute for the Oceans and Fisheries
University Examiner

Additional Supervisory Committee Members:

Christopher Harley, Department of Zoology
Supervisory Committee Member

Simon Donner, Department of Geography
Supervisory Committee Member

Abstract

Over the past 250 years, atmospheric levels of carbon dioxide (CO_2) have increased at an unprecedented rate. The ocean has absorbed a significant proportion of this anthropogenic carbon, resulting in changes to marine chemistry that negatively impact a wide variety of ocean organisms. Disproportionately productive coastal systems may be particularly vulnerable to these changes; however, the detection and impact of secular carbon trends in these systems is complicated by heightened natural variability as compared to open-ocean regimes and is comparatively poorly understood. This dissertation investigates the changing carbonate chemistry of the Salish Sea, a representative Northeast Pacific coastal system.

Both physical-oceanographic factors and primary productivity exert a control on the inorganic carbon balance. I first investigate their interaction in the Salish Sea by applying a clustering method to four factors relating to stratification and to depth-integrated phytoplankton biomass extracted from an existing biophysical model, finding coherent biophysical provinces. I then develop and evaluate a carbonate chemistry model for the Salish Sea and use it to evaluate biogeochemical changes between the pre-industrial and modern periods. I find that to date, the increase in inorganic carbon in the Salish Sea has been 29-39 mmol m^{-3}, a modest amount relative to other parts of the global ocean. However, because of the naturally high inorganic carbon content of Pacific waters, this increased carbon drives the estuary towards domain-wide undersaturation of aragonite year-round, negatively impacting shell-forming organisms. I then use a global database of coastal carbonate chemistry observations to show that estuaries throughout the Pacific Rim have likely already undergone a similar saturation state regime shift. I then quantify the relative components of the Salish Sea carbonate chemistry budget in the context of the identified biophysical provinces. I note the dominant role and large variability of lateral boundary fluxes in setting the inorganic carbonate chemistry of the system. Finally, I estimate that future anthropogenic carbon increase in the system by year 2050, under a conservative emissions scenario, will be approximately 80% of the increase from pre-industrial to present, and that this increase will have further significant effects on aragonite saturation states.

Lay Summary

The coastal ocean hosts rich ecosystems which are sensitive to human-caused climate change. I develop a detailed computer simulation to understand the carbon cycle in a complex, productive North Pacific coastal system. I determine which factors are most important in setting the local carbon balance. I also determine how much extra carbon has entered the system since the beginning of the industrial revolution and how much may enter in the near future. This increase is important because extra carbon in the ocean makes it harder for animals to build shells and structures. I find that large chemical changes have occurred, and am surprised to find that an important threshold under which shells dissolve has already been crossed in most of the region. I consider observations from other global coastal oceans and find that this same threshold may have been crossed throughout coastal oceans in much of the Pacific.

Preface

Chapters 2, 3, and 4 are self-contained after reading the introduction. This results in minor redundancies from chapter to chapter, but the background information in each chapter provides context for each specific study. Chapter 2 has been submitted for publication in a scientific journal as: Jarníková, T., Olson, E.M., Allen S.E., Ianson, D., and Suchy, K. D, 2021: A clustering approach to determine biophysical provinces and physical drivers of productivity dynamics in a complex coastal sea. A version of Chapter 3 has been submitted for publication in a scientific journal as: Jarníková, T., Ianson, D., Allen, S.E., Shao, A.E., and Olson, E.M: Anthropogenic carbon increase has caused critical shifts in aragonite saturation across a sensitive coastal system. Chapter 4 is currently in preparation for submission to a scientific journal.

I developed the application of the clustering method used in Chapter 2 based on guidance from a course taught by Prof. Valentina Radic (Data Analysis in Earth, Ocean and Atmospheric Sciences). The physical model used in this work, SalishSeaCast, is based on the NEMO (Nucleus for European Modelling of the Ocean) framework, and was tuned for use in the Salish Sea by Susan E. Allen, with input from multiple members of the past and present Mesoscale Ocean and Atmospheric Dynamics Group at the University of British Columbia. The nutrient-phytoplankton-zooplankton-detritus ecosystem model SMELT (Salish Sea Model Ecosystem - Lower Trophic) was developed by Elise M. Olson. I wrote the manuscript and produced the figures with significant scientific and editorial input from Elise M. Olson, Susan E. Allen, and Debby Ianson. Elise M. Olson developed some of the model evaluation framework that I customized. I consulted Karyn D. Suchy for her perspective on the ecosystem implications and contexts of primary productivity dynamics discussed in the paper.

I developed the SKOG (Smelt-Carbon-Oxygen-Gas Flux) carbonate chemistry model presented in Chapter 3, based on previous work by Ben Moore-Maley, Debby Ianson, and Susan Allen. I implemented the mocsy FORTRAN package (Orr & Epitalon, 2015) to resolve gas-flux and surface carbonate chemistry in SKOG. I also use the python version of mocsy extensively in results analysis. Debby Ianson taught me much of conceptual framework behind the C* method (Gruber, Sarmiento, & Stocker, 1996) that was used

to determine the initial conditions in the preindustrial case. Andrew E. Shao suggested the method for calculating watermass age data that is used in the chapter. I designed the experimental scenarios that form the basis of the chapter with significant input from Debby Ianson and Susan E. Allen. I wrote the chapter with significant scientific and editorial input from Debby Ianson and Susan E. Allen. I also consulted Elise M. Olson for her scientific and editorial input.

I designed the budget analysis presented in Chapter 4 with significant input from Susan E. Allen and helpful technical advice from Elise M. Olson. I developed the sensitivity scenarios presented with input from Susan E. Allen and Debby Ianson.

Table of Contents

List of Tables

List of Figures

List of Abbreviations

CSOG Central Strait of Georgia

DIC Dissolved Inorganic Carbon

DFO Department of Fisheries and Oceans Canada

GLODAP Global Ocean Data Analysis Project

HRDPS High Resolution Deterministic Prediction System

JDF Juan de Fuca Strait

NEMO Nucleus for European Modelling of the Ocean

NSOG Northern Strait of Georgia

PI Pre-Industrial

SOG Strait of Georgia

SSP Shared Socioeconomic Pathway

RMSE Root Mean Square Error

TA Total Alkalinity

VED vertical eddy diffusivity

WSS Willmott Skill Score

Acknowledgments

First, I thank Susan Allen and Debby Ianson for giving me their time, depth of expertise, and considerable patience over the course of this endeavour. I have significant admiration and respect for both of you on both a personal and a professional level, and I cannot quite express how much your guidance and support over the last years has impacted my life. I especially thank you for working with me through personal and work-related difficulties and showing me that they can be constructively surmounted. I likewise thank my committee members Chris Harley and Simon Donner for their expertise, time, and kindness. I thank Elise Olson, Karyn Suchy, and Andrew Shao, my recent co-authors, for the valuable mentorship in several disciplines and personal friendship. I thank Doug Latornell for the broadening of software-related horizons (and patience).

One of the best things about the Mesoscale Ocean and Atmospheric Dynamics group at UBC is its tendency to attract truly amazing people from around the world, many of whom have become close friends. Appreciation is best expressed in person – here I simply thank them all for the camaraderie and inspiration, scientific and otherwise. You made the hours of debugging Fortran, wrestling with Navier-Stokes formulations, and trying to get python packages to install fun. Thanks to Michael Lipsen for teaching mentorship (by example).

I forever look to my grandparents Zdeňka and Jiří Jarník, who, for me, truly set the bar in most respects. Thank you to my parents and brother Jakub for always working through both good and strange times. I thank the various folks I've met throughout my years in the Pacific Northwest for a depth of friendship that makes the world make sense. I thank many Czech(oslovak) friends for friendship, humour, and grounding and perspective-shifting from a distance. I thank Zuzana Harmáčková for what I'm now realizing is almost a decade of friendship and mentorship in science (and life). Finally, thanks forever to Ilya for kindness, patience, very good animal impressions, doing most (>50%) of the dishes, and love.

I gratefully acknowledge funding from The University of British Columbia through a Four Year Fellowship.

Chapter 1

Introduction

We observe a fraction of the process, like hearing the vibration of a single string in an orchestra of supergiants. We know, but cannot grasp, that above and below, beyond the limits of perception or imagination, thousands and millions of simultaneous transformations are at work, interlinked like a musical score by mathematical counterpoint. It has been described as a symphony in geometry, but we lack the ears to hear it — Stanislaw Lem, Solaris (1961)

Over the past 250 years, atmospheric levels of carbon dioxide (CO_2) have increased at an unprecedented, and accelerating, rate. Current levels of atmospheric CO_2 are approximately 40% higher than in pre-industrial times (Keeling et al., 2005). This upward shift in the atmospheric CO_2 balance is mirrored by a corresponding increase in the concentration of dissolved aqueous CO_2 in the ocean, resulting in a shift in the balance of oceanic carbonate species and a corresponding decrease in ocean pH (J. C. Orr et al., 2005). This process, commonly termed ocean acidification (OA; Caldeira and Wickett (2003); Raven et al. (2005)), results in far-reaching effects on ocean biogeochemistry and ecosystems and is detrimental to the health of many marine organisms, especially oysters and other organisms with aragonite shells (Haigh, Ianson, Holt, Neate, & Edwards, 2015). This decline has raised concerns about the health of marine and estuarine ecosystems.

Though oceanic carbonate chemistry and ocean acidification have been widely studied by the global oceanographic and climatological community, most research to date has been performed in open ocean environments, and impacts in coastal and estuarine systems have only recently begun to be studied (Waldbusser & Salisbury, 2014). Simultaneously, these regions are disproportionately productive (Longhurst, Sathyendranath, Platt, & Caverhill, 1995), sustain diverse natural ecosystems and human societies, and support highly valuable ecosystem services (e.g. Costanza et al. (1997)). This ecological and social value motivates the understanding of carbonate chemistry dynamics and

anthropogenic changes to them in these regions (Longhurst et al., 1995).

This thesis uses a numerical modelling approach to investigate the carbonate chemistry balance and anthropogenic carbon change to one representative coastal region of ecological importance, the Salish Sea. In this introduction, I first summarize the problem of ocean carbonate chemistry and ocean acidification and its implications in ecological and climate contexts. I then describe the context of ocean acidification in coastal and estuarine regions and discuss key challenges in the practice of regional ocean inorganic carbon modelling. Finally, I summarize the state of knowledge of carbonate chemistry in the Salish Sea, using previous studies. I identify major gaps in the current understanding of the Salish Sea carbonate chemistry balance. I finish the introduction by outlining the thesis objectives and the individual chapters.

1.1 The ocean inorganic carbon cycle

The dynamic balance of the oceanic inorganic carbon cycle is a problem of both climatic and ecological importance. Here, I give a general overview of the ocean inorganic carbon system and then briefly discuss global ocean inorganic carbon cycling in the context of climate and effects on marine organisms. I first introduce the governing equation of carbonate chemistry and the aragonite saturation state. I then discuss the changing balance of this equation in the context of both changing climate and ecosystems.

Carbonate Chemistry Equations and Quantities

As a trace gas, CO_2 acts as a link between ocean and atmospheric carbon reservoirs. The fundamental equation governing seawater carbonate chemistry is as follows:

$$CO_{2(atmos)} \rightleftharpoons CO_{2(aq)} + H_2O \rightleftharpoons H_2CO_3 \rightleftharpoons H^+ + HCO_3^- \rightleftharpoons 2H^+ + CO_3^{2-} \tag{1.1}$$

Of all carbonate species available in seawater, only aqueous CO_2 is an actor in the air-sea interface, and a resolution of the partial pressure of aqueous CO_2 (pCO_2) relative to atmospheric CO_2 is important in quantifying the magnitude of the air-sea exchange. As of 2021, atmospheric CO_2 is measured at roughly 415 μatm (at Mauna Loa) with an approximate interseasonal variability of $\pm$ 6 μatm (Keeling et al., (2005); https://scrippsco2.ucsd.edu/data/atmospheric_co2/primary_mlo_co2_record.html). When the surface ocean pCO_2 is lower than atmospheric pCO_2, the intrusion of CO_2 into ocean waters is thermodynamically favoured, and vice versa. Therefore, the anthropogenic increase in atmospheric CO_2 drives a corresponding increase in oceanic CO_2; its further dissolution into various species is described below. Seawater CO_2 concentrations equilibrate to atmospheric CO_2 concentrations on a time scale of approxi-

mately six months in the open ocean (Sarmiento & Gruber, 2006). Once dissolved in seawater, gaseous CO_2 reacts with water to form carbonic acid (H_2CO_3), which then disassociates and loses hydrogen ions to form bicarbonate (HCO_3^-) and carbonate (CO_3^{2-}). In seawater, these species are near equilibrium (Doney, Fabry, Feely, & Kleypas, 2009).

It is now useful to introduce simplified formulations of two commonly used metrics for measuring the ocean carbonate system: total dissolved inorganic carbon (DIC) and total alkalinity (TA) (Sarmiento & Gruber, 2006). DIC is equal to the sum total of all inorganic species in seawater (I use $CO_{2(aq)}$ here to express both $CO_{2(aq)}$ and H_2CO_3):

$$DIC = [CO_{2(aq)}] + [HCO_3^-] + [CO_3^{2-}] \tag{1.2}$$

TA may be thought of as the charge balance of the ocean (or equivalently as a measure of the excess of bases over acids) and is defined as (Sarmiento & Gruber, 2006):

$$TA = [HCO_3^-] + 2[CO_3^{2-}] + [B(OH)_4^-] + [OH^-] + [H^+] + \textit{minor acids and bases} \tag{1.3}$$

These two quantities are convenient for expressing the carbonate system in a modelling context, because they are conservative in seawater, which is to say that their quantity does not change with changes in temperature and pressure - unlike pH and aragonite saturation state. If both DIC and TA are known, the concentration of all individual carbonate species ($CO_{2(aq)}$, bicarbonate, and carbonate) may be calculated. The relative concentration of these species depends primarily on the relative concentration of DIC and TA. Temperature, salinity, and pressure are needed to estimate the solubility and dissociation constants of the individual carbonate system species in seawater (Sarmiento & Gruber, 2006).

For surface seawater with a pH of 8.1, bicarbonate ions account for approximately 90% of dissolved inorganic carbon, while carbonate ions account for 9% and aqueous CO_2 accounts for 1%. Adding CO_2 to the system increases the total DIC and simultaneously increases the concentration of aqueous CO_2, bicarbonate, and hydrogen ion concentration, while carbonate concentration declines and pH decreases. A full discussion of the speciation of inorganic carbon in seawater is available in Wolf-Gladrow et al. (2007).

Aragonite Saturation State

When considering the effect of the ocean carbonate chemistry conditions on marine organisms, another quantity is useful - the saturation state of calcium carbonate ($CaCO_3$), a mineral that makes up the shells and skeletons of marine organisms, including calcifying algae and corals (Doney et al., 2009; Weiner & Dove, 2003). The carbonate ion in

seawater interacts with the calcium ion to form calcium carbonate (Doney et al., 2009):

$$CO_3^{2-} + Ca^{2+} \rightleftharpoons CaCO_3 \tag{1.4}$$

However, as the concentration of carbonate in the water column decreases due to the increase in CO_2, the left side of the equation becomes favoured until a new equilibrium is reached, leading to calcium carbonate dissolution (Doney et al., 2009). The degree of saturation of calcium carbonate (Ω) is defined as the ratio of the product of the $[CO_3^{2-}]$ and $[Ca^{2+}]$ ions, divided by their solubility product K'_{sp} (Sarmiento & Gruber, 2006):

$$\Omega = \frac{[Ca^{2+}][CO_3^{2-}]}{K'_{sp}} \tag{1.5}$$

Because the concentration of the calcium ion in seawater is assumed proportional to seawater salinity, away from strong freshwater influence, Ω is mainly determined by variations in carbonate ion concentration (Riley & Tongudai, 1967). Calcium carbonate formation is kinetically favoured when $\Omega > 1$, and dissolution occurs when $\Omega < 1$. As shall be discussed later, the dissolution of calcium carbonate has far-reaching effects on many marine organisms. The solubility product K'_{sp} is defined as the product of the solutes at saturation:

$$K'_{sp} = [Ca^{2+}]_{sat}[CO_3^{2-}]_{sat} \tag{1.6}$$

K'_{sp} depends on environmental temperature, pressure and salinity, as well as on the mineral phase. $CaCO_3$ exists in several mineral phases, of which calcite and aragonite are most commonly discussed in oceanic settings (Weiner & Dove, 2003). Aragonite, a commonly used biogenic form, is significantly more soluble than calcite due to a less regular crystal lattice; therefore, calcium carbonate saturation state is specified as either aragonite saturation state (Ω_{arag}) or calcite saturation state (Ω_{calc}) (Mucci et al., 1983). In this work, I focus on Ω_{arag}. Both forms of calcium carbonate are more soluble with increasing pressure and decreasing temperature; as a result deep, cold waters are typically undersaturated with respect to calcite and aragonite, and shallower, warmer waters where inorganic carbon drawdown occurs have higher saturation states. The saturation horizon for both forms (i.e. the depth where Ω_{arag} or Ω_{calc} = 1) is used as a metric for carbonate cycling dynamics (e.g. Feely et al. (2004)).

Controls on global inorganic carbon cycling

Understanding oceanic inorganic carbon (DIC) cycling is a fascinating problem in natural science because it exists at the intersection of several fields - physical, biological, and chemical-oceanographic processes must all be considered to thoroughly appreciate the problem. Here I give a brief overview of key controls on ocean carbon cycling: ocean

circulation and the solubility pump, the biological pump, and the carbonate pump.

Ocean circulation, coupled with thermally-dependent inorganic carbon solubility, plays a dominant role in setting the ocean's capacity for absorbing carbon. At high latitudes, the solubility of CO_2 in seawater increases due to cold temperatures. CO_2 is taken up from the atmosphere at high latitudes, and cold, dense water parcels enriched in atmospheric CO_2 subsequently sink, transporting carbon to the deeper ocean. This carbon is eventually released back into the atmosphere by the upwelling of water in warm lower latitudes, where carbon solubility is lower, a process termed the solubility pump (Sarmiento & Gruber, 2006).

The global circulation more broadly plays a dominant role in setting the global inorganic carbon distributions; the Indian and Pacific Oceans are enriched in DIC due to the cumulative effect of respiration processes as ocean water circulates via the deep "conveyor belt" from the Atlantic to Indian and Pacific (Broecker, 1982; Feely et al., 2004). This DIC enrichment in Pacific waters is clearly visible in the calcite and aragonite saturation horizons, which tend to be shallower than in the Atlantic (Feely et al., 2004). Simultaneously, these waters have a lower anthropogenic DIC content, both because deep water formation does not occur in this region and because their naturally high DIC levels and resultant low buffering capacity make them less efficient at taking up inorganic carbon from the atmosphere, in contrast to the higher anthropogenic DIC uptake found in deep water formation zones such as the North Atlantic (Peng & Wanninkhof, 2010).

Marine primary producers take up inorganic carbon in the near-surface ocean at a near-constant ratio to macronutrients such as nitrogen. This uptake transforms the inorganic carbon to organic carbon and exports part of it to depth. This organic carbon is eventually remineralized back into inorganic carbon, thus increasing inorganic carbon concentrations away from the surface. This net vertical transport of organic carbon away from the surface of the ocean is commonly termed the biological pump. Disproportionately productive coastal regions contribute significantly to the biological pump (Sarmiento & Gruber, 2006; Gattuso, Frankignoulle, & Wollast, 1998).

Over long timescales, the capacity of the ocean to absorb atmospheric CO_2 is dependent on the formation and dissolution rates of calcium carbonate, which is dependent on the relative saturation state of calcium carbonate described above. The process of calcium carbonate production (calcification) by organisms and its subsequent export to depth from the surface is commonly termed the carbonate pump. Calcification leads to a decrease in the carbonate ion concentration and an increase in pCO_2. The overall net effect of this pump is the export of inorganic carbon from the surface ocean to depth and the redistribution of ocean total alkalinity. Together, these processes control the large-scale distribution of inorganic carbon in the global ocean (Sarmiento & Gruber, 2006).

The ocean as a carbon reservoir and the CO_2 increase

As the largest active global reservoir of carbon, the ocean determines the atmospheric concentration of carbon dioxide on long timescales. As atmospheric carbon dioxide increases, the ocean absorbs more carbon; therefore, knowledge of atmospheric carbon dioxide state and trends is useful for predicting the future state of the ocean.

The current anthropogenic increase in atmospheric CO_2 is most cohesively demonstrated by the timeseries of atmospheric CO_2 measurements at the Mauna Loa observatory, which began in 1958 (Keeling et al., 2005). The ocean has absorbed approximately a third of the anthropogenic CO_2 emitted since pre-industrial times, and in the process acts to slow the atmosphere-related effects of anthropogenic climate change (Sabine & Feely, 2007). This absorption has lead to an approximate average 0.1 unit decrease of seawater pH from pre-industrial times (Raven et al., 2005). A further decrease by 0.3-0.4 pH units is expected by the end of the century if atmospheric CO_2 concentrations reach 800 μatm, as projected by the Intergovernmental Panel on Climate Change (IPCC) business-as-usual emission scenario, and would correspond to a 150% increase in H+ and a 50% decrease in carbonate concentrations (Doney et al., 2009). The effect of the anthropogenic carbon increase on the calcium carbonate chemistry of the ocean is often expressed in terms of the shallowing (shoaling) of aragonite and calcite saturation horizons; estimations suggest that these horizons have, in various parts of the ocean, shoaled between 30-200m since pre-industrial times (Feely et al., 2004, 2016).

1.2 Effects of ocean acidification on marine biology

It is well-established that decreasing aragonite saturation state has negative impacts on the survival and growth of calcifying organisms, such as many species of shellfish (Haigh et al., 2015), but the effects of changing carbonate chemistry on ocean biology as a whole are more complex. The earliest studies of impacts of increased DIC on marine organisms were conducted almost a century ago (Redfield & Goodkind, 1929), and a wide array of literature is available, showing that biological responses to increases in DIC vary in magnitude and direction depending on organism type and environmental conditions. Most papers are written in the form of case studies, making general predictions about biological responses difficult. However, a meta-analysis of experimental studies that reported biological responses to carbonate chemistry manipulation across many organismal classes shows clearly negative effects for the survival of all calcifying species studied (Kroeker, Kordas, Crim, & Singh, 2010). Many of the calcifying species studied precipitate aragonite during larval stages. Predominantly negative effects are also seen on calcifier growth rates, while effects on photosynthesis and growth for non-calcifying species are mixed (Kroeker et al., 2010). In contrast, some species of non-calcifying

phytoplankton that appear carbon-limited under present conditions, in part due to lack of carbon concentrating mechanisms, may experience a competitive advantage under increased inorganic carbon levels (Haigh et al., 2015). Shifts in the relative competitive advantage of different phytoplankton functional groups under varying carbon conditions have been observed in experimental settings (Tortell, DiTullio, Sigman, & Morel, 2002), foreshadowing the possibility of assemblage shifts in nature.

Available studies and meta-analyses illustrate the complexity of biological responses to changing carbonate chemistry. However, the underlying trend is clear: large shifts in biogeochemical conditions, operating on very short time scales from the perspective of evolutionary biology, have the potential to fundamentally alter ecosystem structure and function, with potentially cascading effects that are likely to have deleterious consequences (e.g. Harley et al. (2006); Guinotte and Fabry (2008)). The ecosystem implications of shifts in Ω_{arag} and Ω_{calc} motivate the study of the changing global biogeochemical conditions.

1.3 Inorganic carbon cycling in a coastal context

Coastal systems are diverse, disproportionately productive regimes that host between 15% and 30% of oceanic primary production (Gattuso et al., 1998). However, resolving both the coastal carbonate balance and the anthropogenic carbon increase is challenging, because these systems are often orders of magnitude more spatiotemporally variable than open-ocean ones (e.g. Fassbender et al. (2018); Lowe, Bos, and Ruesink (2019)); e.g. on a sub-kilometer, diel scale, pH may change by up to 0.5 units per day, while ocean acidification decreases global ocean surface pH on scales of 0.001 pH units a year (Duarte et al., 2013). The dramatic coastal variability and plurality of contributing factors has led some researchers to argue that the concept of ocean acidification due to anthropogenic CO_2 emissions cannot be transposed to coastal ecosystems directly (Duarte et al., 2013).

Both physical and biological processes play a controlling role in setting the coastal carbonate chemistry balance. Because the physical circulation of water typically plays a large, perhaps dominant, role in determining biological processes (e.g. Giddings and MacCready (2017); Crawford and Dewey (1989); Davis et al. (2014)), adequate resolution of local physical dynamics is a preliminary step to any study of carbon cycling. However, biological processes, stemming from the physical environment, have been shown to strongly modulate both the inorganic carbon cycling and ocean acidification in coastal systems and thus require adequate consideration (Lowe et al., 2019). Different coastal regions globally have different controlling physical regimes, so here, I focus on two key features that are present in my study regions – estuarine circulation and coastal upwelling – and outline their effects on biological and biogeochemical processes.

Many coastal regions, including the Salish Sea, are dominated by a density-driven estuarine circulation in which outflowing stratified surface fresher water is replaced by incoming open-ocean water at depth (Hansen & Rattray Jr, 1966). Estuarine circulation is often strongly modified by interaction with locally-specific bathymetry (e.g. Valle-Levinson, Reyes, and Sanay (2003); Farmer, Pawlowicz, and Jiang (2002)). The movement of water may also be affected by localized mixing hotspots (e.g. Crean (1978); Ebbesmeyer and Barnes (1980)), as well as by locally-specific wind patterns (e.g. Moore-Maley and Allen (2021)). The riverine end-member typically has a higher DIC/TA ratio than seawater and may act as an acidifying force (Salisbury, Green, Hunt, & Campbell, 2008). However, the DIC and TA signature of individual freshwater end-members varies widely globally (e.g. Moore-Maley, Ianson, and Allen (2018)) and is a common source of uncertainty in coastal studies (e.g. S. A. Siedlecki, Pilcher, Hermann, Coyle, and Mathis (2017)).

Besides affecting the carbonate chemistry balance directly via the mixing of freshwater end-members with open-ocean waters, this physical circulation determines primary productivity dynamics by controlling the balance of light availability and nutrient availability for growth through the interaction of mixing and stratification (Sverdrup, 1953; Behrenfeld, 2010). A surface stratified layer may trap phytoplankton near the surface, creating favourable growth conditions and thus stimulating inorganic carbon drawdown, or conversely inhibit nutrient delivery, limiting growth. Similarly mixing may act in two opposing ways: either to bring growth-stimulating nutrients to the surface or to mix phytoplankton into the deeper watercolumn, causing light limitation and inhibiting growth. Primary productivity then controls the drawdown of inorganic carbon from the surface and significantly modulates the carbonate chemistry cycle on local scales (Lowe et al., 2019). The balance of inorganic carbon uptake by primary productivity and its production by respiration varies between coastal regions, and especially in estuaries under eutrophication pressure due to human input of nutrients, respiration can be a significant acidifying force (Feely et al., 2010; Cai et al., 2011). Finally, in some coastal zones, benthic processes and submerged aquatic vegetation play a major local role in carbonate system dynamics on multiple timescales (Pacella, Brown, Waldbusser, Labiosa, & Hales, 2018; Waldbusser & Salisbury, 2014).

Coastal upwelling occurs at coasts where wind-driven Ekman transport deflects the surface water from the coast (R. E. Thomson, 1981). The presence of shelf-break canyons enhances coastal upwelling, a prominent feature in the Pacific Northwest coastal ocean (Hickey & Banas, 2008; S. E. Allen & Hickey, 2010; Connolly & Hickey, 2014). Upwelled water is nutrient rich and drives remarkable primary productivity in coastal regions (e.g. Hickey and Banas (2008); Davis et al. (2014)). Simultaneously, upwelling delivers deep, old, comparatively high-carbon waters to the surface, acidifying the wa-

tercolumn and potentially driving surface CO_2 outgassing regionally (Feely, Sabine, Hernandez-Ayon, Ianson, & Hales, 2008; Feely et al., 2016). Along the Pacific coast, this presence of old, carbon-rich waters at depth and the strong, canyon-enhanced upwelling signal combine to create naturally corrosive conditions that may then be at particular risk of anthropogenic acidification (Feely et al., 2008, 2016).

1.4 Considerations in coastal and regional carbonate chemistry modelling

Three-dimensional global circulation models (GCMs) provide an overarching view of global-scale oceanic inorganic carbon cycling but typically have insufficient spatial resolution to take into account smaller-scale features that play a critical role in determining the coastal and regional carbon balance (e.g. Bourgeois et al. (2016); Fiechter et al. (2014); Lachkar, Orr, Dutay, and Delecluse (2007)). As a result, the coastal carbon balance remains an under-resolved component of global carbon budgeting (Fennel et al., 2019). Regional models, which are typically local configurations of one of several large global community models, can close this insight gap by establishing the controls on the regional carbonate chemistry balance at the critical coastal scale where GCMs cannot operate.

Three commonly used community models are NEMO (Nucleus for European Modelling of the Ocean; Madec et al. (2017)), ROMS (Regional Ocean Modelling System; Haidvogel et al. (2000)), and MITgcm (Massachusetts Institute of Technology general circulation model; Marshall, Hill, Perelman, and Adcroft (1997)). Largely because coastal models operate at a higher spatial and temporal resolution than global models and thus require accurate estimation of local forcing factors, their development entails specific challenges that I take into account when developing my own model. Here I discuss some key factors in regional carbonate chemistry modelling.

In systems with significant freshwater input, both the adequate simulation of freshwater input and the interaction of local-scale physical and biological factors is necessary to resolve the regional-scale inorganic carbon balance. In the Gulf of Alaska, two ROMS-based eddy-resolving inorganic carbon models by Siedlecki et al. (2017) and Hauri et al. (2020) have been used to study these factors in the regional inorganic carbon system. Both models have submesoscale spatial resolution (3.5 km and 4.5 km respectively), reproduce the seasonal carbon cycle seen in sparse observations of the region, and identify the vulnerability of the local waters to ocean acidification due to the high natural carbon state of the local ocean. Siedlecki et al. show regional differences in controls on Ω_{arag}, with offshore waters dominated by local biological processes, while nearshore waters are dominated by freshwater forcing, which exacerbates the effects of ocean acidification in

summer and fall. Simultaneously their study identifies a key knowledge gap: the controlling freshwater input regime and freshwater carbonate chemistry remain largely unconstrained and are expected to change in the future. The Hauri et al. study addresses this gap by adding explicit temporally and spatially varying coastal freshwater discharge from a terrestrial hydrological model and demonstrates its controlling influence on nearshore carbonate chemistry conditions. The two studies also highlight the importance of both winds and biological processes and identify a relative paucity of observations in the region as a limit to model evaluation.

Multiple studies have shown the importance of adequate model spatial resolution to accurately estimating carbon transport and carbon budgets. For example, in the California Current system, Fiechter et al. (2014) compared the estimated net air-sea gas transfer of CO_2 using 1/3°, 1/10°, and 1/30° simulations. The results of the smallest-scale (1/30°) simulation show significant enhanced outgassing as a result of localized wind-driven upwelling around topographic features. In contrast, the 1/3° resolution model, which does not resolve these features, underestimates the outgassing magnitude by a factor of three, highlighting the need for adequate resolution in both the ocean model and the wind product. Similarly, also in the California Current System, Siedlecki et al studied future climate-associated stressors at several resolutions (1°, 12km, and 1.5 km) and showed that the magnitude and spatial variability of changes to key quantities such as Ω_{arag}, pH and pCO_2 are significantly altered in the highest-resolution case compared to the 1° model (S. A. Siedlecki et al., 2021). In the Arctic, Terhaar, Orr, Gehlen, Ethé, and Bopp (2019) showed that increasing model resolution dramatically changes carbon transport estimates and that resolving this transport adequately is crucial to accurately estimating the anthropogenic carbon inventory and related effects, such as Ω_{arag} horizon shoaling. However, Terhaar and others also point out that the associated computational cost of these high-resolution models can be prohibitive, so well-calibrated models of key regions can be instrumental in commenting on coastal dynamics more broadly.

Finally, constraining model lateral boundary conditions and carefully modifying them for sensitivity studies has been identified as a key challenge in regional carbon modelling studies. Regional modelling studies often use property-property relationships between carbonate chemistry variables and temperature and salinity to force the lateral boundary condition (e.g. S. A. Siedlecki et al. (2017); Cahill, Wilkin, Fennel, Vandemark, and Friedrichs (2016); Bianucci et al. (2018)), which limits crucial local variability, for example that stemming from biological fluxes or short-term mixing events. Similarly, when calculating modifications to the lateral boundary conditions under hypothetical scenarios, first-order estimates are often made (for example, the addition of a constant ΔpCO_2 at the boundary to simulate past or future carbon conditions; e.g. Bednaršek, Pelletier, Ahmed, and Feely (2020)). The lack of robust, regional future projections of ocean state has also

been noted as limiting in exploring the future evolution of regional-scale carbon system properties (e.g. Cahill et al. (2016)).

Taken together, these studies demonstrate both the remarkable power of regional models to provide insight regarding mesoscale processes and the many moving parts that must be resolved to model coastal systems correctly. In this thesis, I aim to address these 'moving parts' at the state of the art when developing a local three-dimensional inorganic carbon system model. First, I couple my model to an existing biophysical regional configuration of NEMO for the Salish Sea (Soontiens et al., 2016; Soontiens & Allen, 2017; Olson, Allen, Do, Dunphy, & Ianson, 2020a) that benefits from good representation of many of the factors identified above as critical to the carbon balance: high spatiotemporal resolution, a regional atmospheric forcing model with hourly winds, comparatively well-resolved freshwater discharge, and an accurate primary productivity model.

In developing the carbon model, I leverage a well-defined multi-year local dataset containing DIC and TA data for all seasons (Ianson et al., 2016) for initialization and use additional independent data for a rigorous model evaluation (P. Chandler et al., 2021a, 2021b). I use a regional model at daily resolution to set my main lateral boundary condition, allowing for the capturing of small-scale variability at the (remarkably dynamic) boundary of my study area (MacCready, Siedlecki, & McCabe, 2018). Finally and crucially, in designing past, present and future carbonate chemistry scenarios, I leverage local watermass age estimates (Sonnerup, Mecking, & Bullister, 2013) and combine several existing methods (Matsumoto & Gruber, 2005; Gruber et al., 1996) to most accurately estimate the anthropogenic carbon change in each water parcel at the boundary between the scenarios. This combination of a well-resolved and well-performing biogeochemical model and careful scenario consideration using the most accurate available method may make the Salish Sea a good test region for assessing the effect of ocean acidification on similar upwelling-dominated coastal regions.

1.5 The Salish Sea and recent developments in local carbonate chemistry research

The estuarine system on which this carbonate chemistry modelling focuses is the Salish Sea, and a brief general introduction to this specific fjordal sea is necessary to frame and motivate the research questions. I then describe the current state of knowledge about the Salish Sea carbonate chemistry balance, using the carbonate chemistry research done in the region to date.

The Salish Sea, which is the ancestral home of the Coast Salish First Nations, is a region of enormous ecological richness that provides habitat to many species of ecologically important megafauna, including the Southern Resident killer whales (*Orcinus orca*)

and the local salmon populations (Preikshot, Beamish, & Neville, 2013). Simultaneously this coastal sea supports over 6 million people and several major ports with significant ship traffic. Consequently the general tension that exists between the need for stewardship of the natural environment and economic activity to support human well-being is very apparent here.

Specifically in the ocean acidification sphere, characterizing the seasonal variability of the Ω_{arag} state of the Salish Sea and the effect of anthropogenic perturbations on it is a problem of particular ecological and socioeconomic significance because the Salish Sea supports significant shellfish aquaculture on both sides of the border (*Ocean Acidification: From Knowledge to Action. Washington State's Strategic Response*, 2012; Haigh et al., 2015). Significantly heightened mortality of juvenile oysters has been experimentally linked to low Ω_{arag} conditions (Barton, Hales, Waldbusser, Langdon, & Feely, 2012); as a result, in the general Pacific Northwest, ocean acidification is already noted as a considerable concern for industry and policymakers, especially in the coastal zone within this region (Mathis et al., 2015; Ekstrom et al., 2015). For example, net revenue losses of $100 million have been reported by the oyster industry in Washington State (*Ocean Acidification: From Knowledge to Action. Washington State's Strategic Response*, 2012). It is the ongoing hope and goal of this work to contribute to informed stewardship of this remarkable part of the world through thoughtful improvements in the understanding of one aspect of its biogeochemical state.

From a physical-geographic perspective, the Salish Sea is a temperate, fjordlike estuary on the west coast of North America, straddling the Washington and British Columbia coasts. The Salish Sea is composed of the Strait of Georgia (SoG), the Juan de Fuca Strait (JdF), and Puget Sound (Fig. 1.1). The system receives freshwater input from over 200 rivers, but the primary freshwater source is the predominantly nival Fraser River (Pike et al., 2010), which drives high salinity-induced stratification in the central SoG and a strong, variable exchange through the Juan de Fuca Strait (Giddings & MacCready, 2017). Salinity stratification is opposed by wind and tidal action, and strong winds in the fall and winter months mix the surface and intermediate water masses (LeBlond, 1983). The SoG contains two deep basins (north and central), with the Fraser River plume mainly sitting on top of the central basin. Deep SoG water is relatively unmixed, except during deep water renewal events (Masson, 2002).

The primary exchange of water between the inner Strait of Georgia and the open Pacific through the Juan de Fuca Strait is strongly influenced by offshore wind patterns and currents (Thomson, 1981; Fig. 1.1). Summer northwesterly winds that blow surface water offshore result in upwelling conditions, while the winter wind reversal initiates downwelling by pushing surface water towards the coast (Foreman, Pal, & Merryfield, 2011). As a result, the Juan de Fuca exchange varies seasonally between an estuarine

regime, which occurs 90% of the time in the summer and 55% of the time in the winter, and a transient regime that dominates in the remaining time (R. E. Thomson, Mihály, & Kulikov, 2007). In the estuarine regime, coherent surface outflowing water is replaced at depth by two layers of inflowing water, including deep upwelled water, while the transient regime is less cohesive and shows significant horizontal variability in flow structure (R. E. Thomson et al., 2007). A secondary inflow to the Salish Sea, which is further from the open ocean and characterized by vigorous tidal mixing in narrow channels, occurs via Johnstone Strait (Fig. 1.1).

Though the water entering the Salish Sea is affected by a combination of currents, the permanent, poleward-flowing California Undercurrent is likely of particular importance, as it is a major source of nutrient and carbon-rich water to the continental shelf during upwelling events (R. E. Thomson & Krassovski, 2010). In contrast, the buoyancy-driven Vancouver Island Coastal Current forms a surface barrier that acts to prevent high-carbon upwelled waters from penetrating the inner shelf (Bianucci, Denman, & Ianson, 2011). Though a full discussion of the varying outer-shelf flow regimes is not provided here, it is apparent that the complex interplay of wind and flow patterns on the outer coast plays a controlling role in setting the physical and biogeochemical conditions of the Salish Sea, and the observed variability in these conditions motivates further study.

Observed carbonate chemistry conditions in the Salish Sea show regionally distinct structure as a response to differing physical and biological conditions. Notably, the Strait of Georgia seasonal Ω_{arag} cycle is opposite to that of the adjoining Juan de Fuca and Haro water masses. Surface Ω_{arag} tends to be highest in the Strait of Georgia during the spring and summer due to concentrated drawdown of carbon by phytoplankton in a strongly salinity-stratified surface layer (Ianson et al., 2016), though corrosive freshwater lowers local Ω_{arag} in the central Strait of Georgia during the freshet period. Meanwhile, in the Juan de Fuca Strait, surface Ω_{arag} is lowest during the summer due to the aforementioned seasonal upwelling of deep, carbon-rich water into the system from the outer coast. Simultaneously, tidal mixing increases light limitation in the Juan de Fuca and mixes phytoplankton deeper into the watercolumn (Masson & Peña, 2009), meaning that the summer high-DIC upwelling signature is not erased by phytoplankton drawdown when it is mixed into the Juan de Fuca surface (Ianson et al., 2016). The outflowing Strait of Georgia surface water and the deeper Juan de Fuca water are then coupled by vigorous tidal mixing in the Haro Strait (Fig. 1.1).

The Strait of Georgia is carbon-enriched (which is to say that salinity-normalized DIC is higher and thus Ω_{arag} is lower) compared to the adjoining Pacific (Ianson et al., 2016). Because of this local carbon enrichment, the upwelling of "acidified" outer coast water and corresponding estuarine return flow actually increases Strait of Georgia Ω_{arag}, a striking difference from the acidification by the same water mass observed in the ad-

joining Puget Sound during a water-properties study conducted by Feely et al. (2010). (Furthermore, the Puget sound, notably Hood Canal, is likely subject to additional acidification pressure from anthropogenic nutrient loading (Khangaonkar, Nugraha, Xu, & Balaguru, 2019), though the majority of the Salish Sea is considered at low risk for eutrophication (Sutton, Johannessen, & Macdonald, 2013).)

Due to local carbon enrichment, surface undersaturation of Ω_{arag} is seen in the Strait of Georgia in the winter (Ianson et al., 2016; Evans et al., 2019), and summer Ω_{arag} horizons are shallower (approximately 20 m) in the Strait of Georgia than on the outer coast (Ianson et al., 2016). On a local scale, these generally corrosive conditions may be strongly modulated by biological drawdown or physical factors such as wind, cloud fraction, or freshwater input. For example, in the Northern Strait of Georgia, local wind events can temporarily decrease surface Ω_{arag} in the summer by breaking up surface stratification and bringing high-carbon waters nearer to the surface (Evans et al., 2019). A similar mechanism was identified in a one-dimensional modelling study in the central Strait of Georgia, which shows an Ω_{arag} decrease with increasing wind speed and cloud fraction (Moore-Maley, Allen, & Ianson, 2016). This modelling study also reproduces the decrease in Ω_{arag} as a response to freshwater flux from the Fraser River freshet observed by Ianson et al (2016). Together, these modelling and observational results from the same region highlight both the notable regional-scale variability in carbonate chemistry conditions and the multiplicity of biophysical drivers that determine them in this estuarine system.

1.6 Gaps in the present knowledge and thesis objectives

The overarching goal of this thesis is to characterize the anthropogenically changing coastal carbonate chemistry balance of the Salish Sea and the dominant controls on this balance, with the hope that the insights gained here may be of use in other coastal regions more broadly. In surveying the practice of coastal carbon modelling, I have identified the need to characterize the interaction of physical and biological controls on carbonate chemistry as a first step to tackling the carbonate chemistry balance. I have also noted the importance of submesoscale numerical models in resolving these controls in coastal systems that experience spatiotemporal variability at scales not resolvable by global circulation models. With these two knowledge gaps in mind, I approach the problem through the analysis of an existing biophysical model of the Salish Sea, as well as through the development and analysis of a three-dimensional carbonate chemistry model for the entire Salish Sea domain. I now summarize the aims of the following three research chapters.

In Chapter 2, I broadly investigate large-scale patterns in physical-oceanographic phenomena in the Salish Sea and their relationship with phytoplankton biomass. Gaining

this big-picture biophysical overview of the system is important to resolving carbonate chemistry because of the discussed controlling influence of both physical and biological processes on the coastal carbonate chemistry balance. To this end, I develop an adaptation of a simple data science technique to look for spatial clusterings of physical-oceanographic variables and phytoplankton biomass and investigate the relationship between them. I aim to answer the following research question:

- How do physical oceanographic dynamics drive phytoplankton community dynamics in the Salish Sea, and what are the dominant spatial patterns of both?

In Chapter 3, I begin investigating the changing Salish Sea carbonate chemistry balance itself. I first develop and evaluate a three-dimensional carbonate chemistry model for the Salish Sea. I then consider two scenarios: one where all inorganic carbon forcing is set to pre-industrial levels, and another where inorganic carbon forcing remains at present-day conditions. By contrasting these two scenarios I investigate the following research questions:

- How has anthropogenic carbon from the air-sea and open-ocean boundary changed the inorganic carbon mass-balance and cycling pathways in the Salish Sea?
- What are the implications of this mass-balance change on Ω_{arag}?
- How do the carbonate chemistry conditions of the Salish Sea compare with available measurements in the rest of the global coastal ocean, and what are the implications of these conditions on Ω_{arag} globally?

In Chapter 4, I extend my analysis of the Salish Sea carbon balance by establishing a budget for major sources and sinks to the system. I then consider the effects of a potential future increase in anthropogenic CO_2 and a changing hydrological cycle on the carbon balance as a whole. I consider the following research questions:

- What are the dominant fluxes in the Salish Sea carbonate chemistry balance, and what is their relative magnitude and spatial and temporal structure?
- How variable is the aragonite saturation state of the different regions of the Salish Sea from year to year?
- How may the Salish Sea carbonate chemistry balance respond to a) likely future increase in anthropogenic CO_2 or b) potential future change in the hydrological cycle of dominant rivers?

1.7 Figures

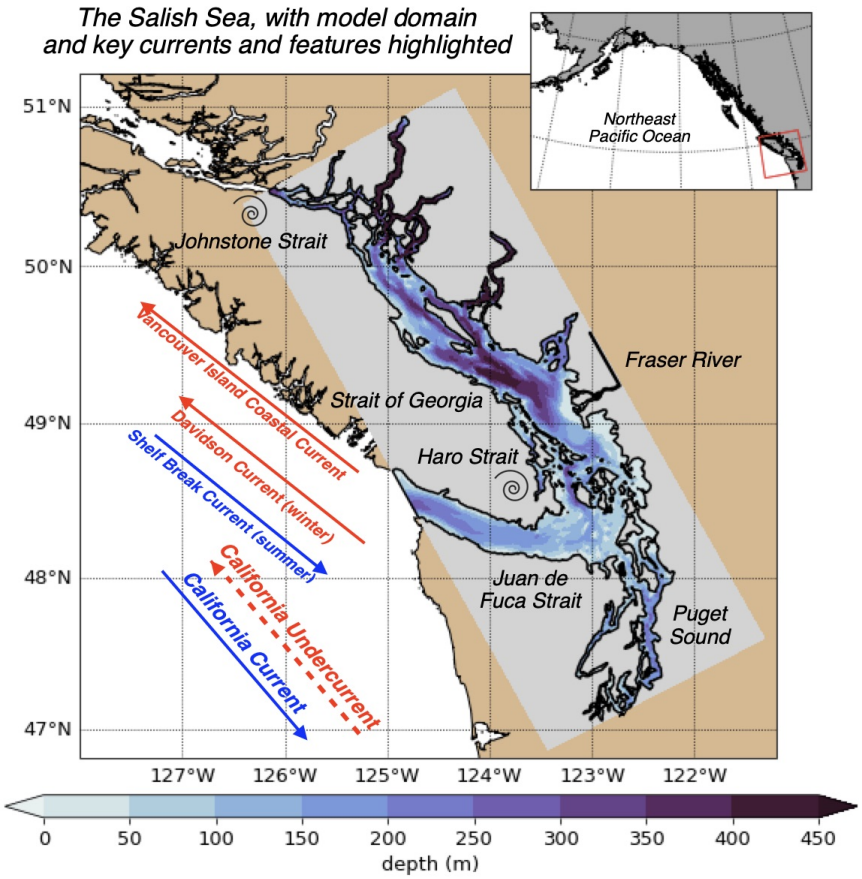

Figure 1.1: The SalishSeaCast model domain (grey), with model bathymetry shown and major geographic subregions and features highlighted. Regions of especially high tidal mixing are marked with adjacent spirals. The Salish Sea coastal system is composed of the Strait of Georgia, the Juan de Fuca Strait, and Puget Sound.

Chapter 2

A clustering approach to determine biophysical provinces and physical drivers of productivity dynamics in a complex coastal sea

2.1 Overview

The balance between ocean mixing and stratification influences primary productivity through light limitation and nutrient supply in the euphotic ocean. Here, I apply a hierarchical clustering algorithm (Ward's method) to four factors relating to stratification and depth-integrated phytoplankton biomass extracted from a biophysical regional ocean model of the Salish Sea to assess spatial co-occurrence. Running the clustering algorithm on four years of model output, I identify distinct regions of the model domain that exhibit contrasting wind and freshwater input dynamics, as well as regions of varying watercolumn-averaged vertical eddy diffusivity and halocline depth regimes. The spatial regionalizations in physical variables are similar in all four analyzed years. I also find distinct interannually consistent biological zones. In the Northern Strait of Georgia and Juan de Fuca Strait, a deeper winter halocline and episodic summer mixing coincide with higher summer diatom abundance, while in the Fraser River stratified Central Strait of Georgia, shallower haloclines and stronger summer stratification coincide with summer flagellate abundance. Cluster based model results and evaluation suggest that the Juan de Fuca Strait supports more biomass than previously thought. My approach elucidates probable physical mechanisms controlling phytoplankton abundance and composition. It also demonstrates a simple, powerful technique for finding structure in large datasets and

determining boundaries of biophysical provinces.

2.2 Introduction

Marine phytoplankton form the basis of the oceanographic food web and are responsible for approximately half of global carbon fixation (Field, Behrenfeld, Randerson, & Falkowski, 1998). To predict changes in global climate it is necessary to understand the complexities in the underlying controls of marine productivity. The rate of primary productivity in the near-surface ocean is controlled by the availability of macro- and micronutrients and light, as well as temperature, which are in turn controlled by the interplay of stratifying processes and sources of mixing. The breakdown of the surface ocean stratified layer may permit mixing to reduce the availability of light for phytoplankton, inhibiting growth (e.g. Sverdrup (1953)), or contrastingly bring nutrients from deeper waters to nutrient-depleted surface waters, thus stimulating growth. The breakdown of stratification may also inhibit the predatory action of zooplankton on phytoplankton by dilution, with net positive effects on phytoplankton growth (Behrenfeld, 2010).

The interplay of different stratification regimes exerts control on the structure of ocean ecosystems (e.g. Legendre (1981)), and changes in regime have been linked to shifts in phytoplankton community composition (e.g. Huisman et al. (2004)). The importance of phytoplankton in biogeochemical cycling, along with the position of phytoplankton at the base of the food web and impact on higher trophic levels, globally motivates the study of phytoplankton distribution and dynamics. Coastal regions are disproportionately more productive compared to the open ocean (Longhurst et al., 1995) and typically have more complex mixing, circulation, and stratification dynamics than the open ocean, making resolution of phytoplankton biomass patterns difficult. Simultaneously, because both ocean stratification patterns and phytoplankton biomass dynamics may be expected to shift under anthropogenic climate change, there exists a need to characterize their dynamic structure and identify key drivers.

2.2.1 Oceanographic setting

The Salish Sea is a semi-enclosed fjord-like estuary on the British Columbia coast, composed of the Strait of Georgia (SoG), Juan de Fuca Strait (JdF), and Puget Sound (Fig. 2.1). The SoG is connected to the open ocean by Juan de Fuca Strait to the south and Johnstone Strait to the north, with Juan de Fuca Strait serving as the site of primary seawater exchange with the open ocean (Khangaonkar, Long, & Xu, 2017). The Salish Sea receives freshwater input from over 200 rivers, but the primary freshwater source is the nival-glacial Fraser River (Pike et al., 2010), which drives high salinity-induced stratification in the CSoG and a strong estuarine exchange (Giddings & MacCready, 2017).

Salinity stratification is opposed by wind and tidal action. Strong winds in the fall and winter months lead to mixing of surface and intermediate water masses. The SoG contains two deep basins (North and Central), with the Fraser River plume sitting on top of the Central basin. Deep SoG water is relatively unmixed, except during deep water renewal events (Masson, 2002).

This coastal ocean is a region of significant ecological and cultural importance and provides habitat to many species of ecologically important megafauna, including the Southern Resident killer whales (*Orcinus orca*) and the local salmon populations. The ongoing significant decline of the local Coho and Chinook salmon (Preikshot et al., 2013) has been implicated as a factor in the low reproductive success of the killer whale populations (Wasser et al., 2017), which depend on these salmon as a food source. These population declines in upper trophic levels further motivate the understanding of factors controlling the base of the food web.

The physical environment of the Salish Sea is well known, with functionally-distinct physical-oceanographic regions (R. E. Thomson, 1981; LeBlond, 1983; Pawlowicz, Suzuki, Chappell, Ta, & Esenkulova, 2020). An ongoing subject of interest in this coastal sea is the relationship between known physical, and presumed ecological, regions. Three prominent parts of the Salish Sea - Juan de Fuca Strait (JdF), the Northern Strait of Georgia (NSoG), and the Central SoG (CSoG) can be defined by distinct stratification regimes and watermass characteristics, and available biological observations and model results (e.g. Masson and Peña (2009); Suchy, Le Baron, Hilborn, Perry, and Costa (2019); Peña, Masson, and Callendar (2016)) are typically discussed in the context of these differing physical environments. However, in situ sampling of phytoplankton biomass remains relatively sparse and episodic, and may not capture inherently dynamic phytoplankton biomass fluctuations, while remote sensing approaches can provide only surface chlorophyll concentrations. Here, I aim to use an unsupervised cluster analysis of a well-resolved submesoscale mechanistic biophysical model to consider the linkages between the regional physical oceanography of the system and its phytoplankton biomass dynamics.

2.3 Methods

2.3.1 The SalishSeaCast biophysical model

I use SalishSeaCast (v201905), a regional oceanographic model developed for the Salish Sea (Soontiens et al., 2016; Soontiens & Allen, 2017) using version 3.6 of the NEMO regional ocean modeling engine (Madec et al., 2017). The physical model solves the Reynolds-averaged Navier-Stokes equations on an Arakawa-C grid, with a 2 second

barotropic timestep, a 2 second vertical advection timestep, and a 40 second baroclinic timestep. Major physical model modifications since first implementation are summarized in Olson et al. (2020a).

The model domain (Fig. 2.1) is 898 (v) by 398 (u) horizontal cells with approximately 500 m horizontal resolution and 40 vertical z -layers ranging from 1 m resolution at the surface to 27 m resolution at the bottom. SalishSeaCast has two open boundaries, at JdF and Johnstone Strait, which are forced with eight tidal constituents and sea surface height predictions from NOAA's storm surge forecast at Neah Bay, in JdF near the seaward entrance. The model is forced with over 150 rivers; the Fraser River runoff is taken from the Environment and Climate Change Canada flow gauge at Hope, BC, and the remaining rivers, as well as the Fraser River downstream of Hope, are forced by a monthly climatology (Morrison, Foreman, & Masson, 2012). Atmospheric forcing, including winds and solar radiation, is derived from the High Resolution Deterministic Prediction System (HRDPS), a nested 2.5 km resolution operational atmospheric model (Milbrandt et al., 2016). Coupled to the physical model is a NPZD-type biological model (SMELT - Salish Sea Lower Trophic Ecosystem Model, Olson et al. (2020a)), which is described in summary below.

The SMELT biological model represents the transfer of matter, using nitrogen as currency, between three classes of primary producers (diatoms, flagellates, and the ciliate mixotroph *M. rubrum*), three classes of nutrients (nitrate, ammonia, and silicic acid), three classes of detritus (particulate and dissolved organic nitrogen and biogenic silica, called PON, DON, and bSi respectively) and one class of microzooplankton, with mesozooplankton grazing as a closure term. The growth rate of all three primary producer classes depends on the availability of nutrients, light, and on temperature. The diatom class is assigned the highest maximum growth rate and the highest optimal light level and is the only class to take up dissolved silica – in the gleaner-opportunist framework, I consider it an opportunist class (Grover, 1990; Grover, Hudziak, & Grover, 1997). Small flagellates have the lowest maximum growth rate while competing better at low nitrogen levels, low light, and higher temperature. Small flagellates have the lowest minimum nutrient requirement, and I consider them the gleaner class in the gleaner-opportunist framework. The mixotroph *M. rubrum* has intermediate growth parameters while grazing on the flagellate class in addition to photosynthesizing.

The detrital classes are handled as follows: The concentrations of detrital PON and DON are increased through inefficient grazing, mortality and excretion/egestion, while they decrease due to remineralization to ammonium. PON is also decreased by direct grazing by zooplankton. bSi is increased due to grazing on, mortality of, and excretion from silicon-containing diatom class only, while it is decreased by dissolution. PON and bSi are affected by sinking at class-specific rates. Details of phytoplankton growth rate

and nutrient and light level preference, as well as all other rates, are available in (Olson et al., 2020a).

SalishSeaCast has been operational since 2014 and is run daily with forecasts and nowcasts available at https://salishsea.eos.ubc.ca/nemo/results/. The entire model system, including run environment, is documented at https://salishsea-meopar-docs.readthedocs.io. In Appendix A I provide an evaluation of the model salinity, temperature, nitrate, dissolved silica, and chlorophyll against available observations for the years and model version analyzed, separated according to the major clusters found (Fig. A.1-A.2). In summary, the model shows consistently high skill across all clusters (Tables A.1-A.2), with Willmott skill scores for temperature and salinity ranging from 0.957-0.971 and 0.959-0.971 respectively across the clusters. Comparisons with log-transformed total chlorophyll data yield scores of 0.60-0.71, comparisons for nitrate yield scores of 0.9-0.97, and comparisons with dissolved silica yield scores of 0.79 - 0.91. Significant interannual variability is seen in the seasonal cycle of nitrogen and chlorophyll in the Salish Sea; the biophysical model captured this variability with high fidelity when comparing with a continuous time series of in-situ observations in the Central Strait of Georgia (Olson et al. (2020), Fig. 4). A summary of minor updates to the model tuning since publication in Olson et al. (2020) is provided in Appendix A.2.

2.3.2 Stations and clustering signals

I analyzed four years of daily output from SalishSeaCast (2013-2016), using an unsupervised clustering algorithm (Ward's Euclidean Distance Method, see section 2.3.3). I developed model-available year-long timeseries proxies ("signals") for four different factors relating to stratification and mixing activity (wind strength, freshwater influx, vertical eddy diffusivity, and halocline depth) and one for an indicator of biological productivity (total depth-integrated biomass of three phytoplankton functional groups from the model's NPZD module). These signals were extracted for each year at each of 571 model "stations" spaced 10 model grid points apart ($\sim$5 kilometers, Fig. 2.2). This spacing was chosen as a compromise between resolution and computing time, and I believe it well represents the different regions of the Salish Sea while being computationally manageable.

Several possible clusterings resulting from my analysis were visualized and compared for major differences. The most characteristic clusters are presented in the Results section, while an example visualization of all possible clusterings of one year of one of the variables is available in Fig. A.3. Here, I describe the signals.

Wind strength

The wind forcing used (HRDPS, see model description) has 2.5 km spatial resolution and hourly temporal resolution, and is used operationally by Environment Canada in the Canadian Pacific region. The skill of the HRDPS wind product in this region when compared to local meteorological stations has been evaluated by a previous study and accurately reproduces the climatology of observed wind magnitudes and directions (Moore-Maley & Allen, 2021). I first interpolate this product onto the model grid and then extract hourly windspeed. As wind energy available for mixing scales with the cube of wind speed, I cluster on the daily average of cubed hourly windspeed (Fig. 2.2a).

Vertical eddy diffusivity

The vertical eddy diffusivity represents the strength of mixing in the system (Soontiens & Allen, 2017) and depends on the choice of vertical turbulence closure scheme. SalishSeaCast uses a k-ε configuration of a generic length scale turbulence model to estimate sub-gridscale turbulent processes (Umlauf & Burchard, 2003), with background vertical eddy viscosity and diffusivity both set to 10^{-6} m^2 s^{-1}. I report a daily depth-averaged value here (Fig. 2.2b). Though average vertical eddy diffusivity reflects all sources of mixing and stratification present in the system, it is dominated by barotropic tidal activity, and I expect it to be highest at tidal mixing hotspots (Crean, 1978).

Freshwater index

The freshwater index (Fig. 2.2c) is intended as a proxy for freshwater influence on the watercolumn at a given station, and is expressed as the salinity difference between the mean of the surface 4 meters of the watercolumn and the salinity at depth 50 m, in units of g kg^{-1}. This metric may be thought of as a salinity stratification metric. Where the watercolumn is shallower than 50 meters, the salinity at 50 m at the nearest model point that is 50 m deep is used. Similar metrics have been used as indicators of stratification in the region (Suchy et al., 2019; Masson & Peña, 2009), but were typically based on the difference in water density between the surface and the deep waters; here I isolate the impact of salinity alone by using a salinity-based metric. As salinity dominates stratification in this region (LeBlond, 1983), I expect clusters derived from a salinity-based clustering to be broadly similar to those derived from a density-based clustering. The value of 50 m was chosen because the majority of the Salish Sea is more than 50 meters deep; however, I do not expect the results to change dramatically if a different depth were to be chosen.

Halocline depth

The halocline depth (Fig. 2.2d) is defined here as the depth of the maximum salinity gradient in the water column, which is estimated by finding the salinity difference of two adjacent cells in the vertical dimension and reporting the depth at the midpoint of the two cells that have maximum salinity gradient in the watercolumn at a given station.

Phytoplankton biomass

I extract daily-average depth-integrated phytoplankton biomass (mmol N m^{-2}) for each of the three phytoplankton functional groups to form three yearly signals (Fig. 2.2e). These signals are then connected in series to form an overall phytoplankton biomass signal that differentiates by functional group - thus, functional group identity, not just total phytoplankton biomass, is a factor in my clustering. Furthermore, my chosen metric of functional-group-differentiated phytoplankton biomass will capture functional-group specific responses to different habitat characteristics. While factors other than primary productivity that influence the standing stock biomass (e.g. mortality, grazing, and sinking rate) are reflected in this clustering, bottom-up effects dominate the response seen here.

2.3.3 Clustering method

I use Ward's method (Ward Jr, 1963), a type of hierarchical clustering method, to cluster my data. Broadly, clustering methods are a subset of unsupervised machine learning methods used to reveal the underlying structure of a dataset by grouping similar data points. In hierarchical clustering methods, every datapoint is initially a single-point data cluster. At each step of the clustering, the two 'closest' clusters are merged into a new cluster; this process is repeated until all points have been merged into a single cluster. Metrics of closeness vary between hierarchical clustering methods - while some methods use variations of the definition of the physical distance between clusters as a clustering criterion, Ward's method analyzes changing intracluster variance, or the "loss of information" (Wishart, 1969) if they were to merge into a single cluster. In Ward's method, at each step, the clusters whose merging results in the lowest increase in intracluster variance are combined.

Many hierarchical clustering methods exist; of these I chose Ward's method because the algorithm is straightforward to implement and compares favourably to other hierarchical clustering methods with regards to performance in identifying structure in known clusterings (e.g. Mangiameli, Chen, and West (1996)). I perform hierarchical clustering using Ward's method a total of twenty times - separately on four years of each of the five signals described above.

Cluster number selection

A common challenge in the application of clustering methods is the selection of cluster number. In hierarchical clustering, typical approaches include choosing a cutoff where the change in dendrogram distance between two cluster numbers is maximized. In my case, attempts to use objective metrics to determine cluster number, such as the Davies-Bouldin, Silhouette, or Calinski-Harabasz criteria, typically identified only two clusters in the a given dataset (not shown); though these may be the most prominent clusters, meaningful structure in the data persists at larger cluster numbers. Ultimately, my approach was to visualize several possible clustering outputs, with cluster number N varying from 2 to 15, and to visually compare emergent structure in multiple years of the clustering of a single variable (e.g. Fig. A.3). In all variables, the same typical structure emerged at a relatively low cluster number (eg, N = 3-5) and persisted with increasing cluster number in all years. For easy intercomparability of clusters between years, I thus chose an N=5 for all years for all clusters, but am confident that the structures described are robust to a selection of a variety of cluster numbers.

Interannual cluster persistence

Visually, it is immediately apparent that similar spatial structure in the clusterings of a single variable persists interannually. To formalize the interannual persistence of a single cluster between years, as well as spatial commonality of different variables, I establish a simple nondimensional cluster commonality metric (CC). For two clusters A and B, the cluster commonality CC_{AB} is defined as:

$$CC_{AB} = \frac{|A \cap B|}{0.5(|A| + |B|)}$$

For any two clusters, CC varies from 0 (clusters of any size with no stations in common) to 1 (two clusters of equal size with all stations in common) and may be used to compare clusters of unequal sizes. I use this metric to compare the persistence of clusters of individual variables between years, as well as the cluster persistence between different variables in a given year (Fig. A.4). Boundaries between clusters are not expected to be rigid, nor is the transition in biological or physical conditions expected to be abrupt - the signal shown for each cluster represents the mean of all stations' signals for that cluster, and variability within each cluster is non-zero.

2.4 Results

I describe the main physical-oceanographic subregions in the domain (CSog, NSoG, and JdF) determined by clustering the physical factors and interpret my results in the context

of previous work. I also consider some tidal mixing hotspots highlighted in the derived map of vertical eddy diffusivity. My results here typically extract the main known general physical-oceanographic features of this coastal sea. I then describe the observed spatial regions in biomass, which are remarkably cohesive, in the context of these physical factors. In the discussion, I propose some mechanisms through which the physical factors likely shape the biological structures seen here.

2.4.1 Central Strait of Georgia

The physical-oceanographic dynamics of the CSoG are dominated by stratification due to Fraser river runoff, which is easily visible in the derived clustering of the freshwater index (Fig. 2.3). Spatially, in all four years of my analysis, the highest freshwater index is seen near the mouth of the Fraser River and in Howe Sound (cluster 1/gold), and then radially decreases in bands (cluster 2/grey, cluster 3/sky blue) outward from this maximum. The tendency of the surface Fraser River plume to move north from the mouth of the Fraser due to the Coriolis force (Liu, 2014) is also easily observable in this visualisation. The stratifying tendency of the Fraser river (and of other major rivers) is then reflected in the clustering of the halocline signals (Fig. 2.4). The CSoG (cluster 3/sky blue) has consistently shallow haloclines with only limited seasonal variability ($\sim$5m in summer to $\sim$7m in winter). These shallow, stable haloclines also persist in most of the Puget Sound, owing to the influence of the Skagit River, and in the northern fjords with large rivers at their head (Toba Inlet, Bute Inlet, and Howe Sound), and the influence of these rivers is reflected in the clustering of the freshwater index. Because rivers other than the Fraser are forced by climatology in the model, the potential effects of the interannual variability of their hydrographs are not seen here.

In the wind clustering, the boundary between the CSoG and NSoG is farther south than that seen in the clusterings of freshwater index and halocline depth (Fig 2.5). Though winds in all clusters are highly episodic, all wind clusters show a marked decrease in wind energy during the summer months (Fig. 2.6) - this change in mean signal magnitude and variability is most pronounced in the NSoG (cluster 4/red), which consistently shows $\sim$2 times higher wind energies in the winter months than in the summer months. In contrast, the CSoG (cluster 3/sky blue) shows lowest variability between summer and winter energy magnitudes. Summer wind energies are actually higher in the CSoG than in the NSoG, likely due to the long wind fetch length in the CSoG, as summer winds in the Salish Sea are predominantly northerly (R. E. Thomson, 1981; Moore-Maley & Allen, 2021). Average vertical eddy diffusivity is lowest in the CSoG (Fig. 2.7), owing likely both to high stratification and to comparatively low tidal currents (R. E. Thomson, 1981), consistent with the historical idea of the Salish Sea as a system of relatively quiet basins interconnected by dynamic sills (Ebbesmeyer & Barnes, 1980).

2.4.2 Northern Strait of Georgia

As expected, the influence of the Fraser river is lower in the NSoG as the region is farther away from the rivermouth (Fig. 2.3). The resulting lower stratification is reflected in deeper and more variable haloclines in all seasons (on average, $\sim$ 10m in summer to $\sim$20m in winter) (Fig. 2.4). A striking feature in the clustering of the freshwater index signal and halocline signals in the NSoG and the CSoG is the dissimilarity of year 2016 to other years, reflected in a lower cluster persistence metric in this year (Fig. A.4). Maximum Fraser River discharge (freshet) during 2016 was remarkably low, in the lowest quartile of discharge on record, reaching only $\sim$8,000 m^3s^{-1}, or roughly 2/3 of the magnitude of the 2013-2014 freshets, which were both in the highest quartile (Fig. A.5). Interestingly, the mean freshwater index signal for each cluster in 2016 remains similar to the means for other years, as does the spatial extent of the most river-influenced cluster (cluster 1/gold), but the medium freshwater-influenced clusters (cluster 2/grey, cluster 3/sky blue) extend less far from the river mouth. As a result, the NSoG clusters with JdF in this year.

2.4.3 Juan de Fuca Strait

Dynamics in Juan de Fuca Strait are broadly characterized by limited local freshwater influence, though a small increase in freshwater index is visible in the summer months (Fig. 2.3, 2.6), in part because of the surface advection of freshet-driven water from the CSoG due to the estuarine circulation (R. Thomson, Miha‘ly, & Kulikov, 2007). The limited freshwater stratification, accompanied by a large tidal range, results in deep and variable haloclines (Fig. 2.4). The larger tidal velocities here are also reflected in slightly higher watercolumn-averaged VED (Fig. 2.7). In 2015, the VED in most of the Juan de Fuca is lower than in the remaining three years, and the region clusters with the Strait of Georgia. This interesting pattern is likely caused by the inhibition of water column mixing by higher thermal stratification of the system due to the significant marine heatwave in the North Pacific in the years 2013-2015 (Gentemann, Fewings, & García-Reyes, 2017), whose effects were most pronounced in the Salish Sea in 2015 (P. C. Chandler, King, & Perry, 2016). The dissimilarity of year 2015 to other years is reflected in the cluster persistence metric (Fig. A.4). However, all four years of these results may in part reflect the effects of the heat wave.

2.4.4 Tidal mixing hotspots

Watercolumn-averaged vertical eddy diffusivity in the Salish Sea is dominated by tidal mixing activity (Crean, 1978), allowing clustering VED to uncover dominant tidal hotspots. VED varies by three orders of magnitude in the model domain (Fig. 2.7). As expected,

this metric reaches its maximum in the Haro Strait region, as well as in parts of Puget Sound, for example in Admiralty Inlet, near known tidal mixing hotspots (Ebbesmeyer & Barnes, 1980; LeBlond, 1983; Moore et al., 2008; Deppe, Thomson, Polagye, & Krembs, 2018). Two stations in northern Johnstone Strait and the Discovery Passage region also exhibit heightened VED in all four years, consistent with the very high observed tidal velocities near Seymour Narrows in this region (R. E. Thomson, 1981). Fourier analysis of the annual vertical eddy diffusivity signals also shows local maxima in energy at weekly and fortnightly frequency (not shown) in all four years in all five clusters, consistent with the role of tides as the dominant source of mixing energy in the system (Crean, 1978).

The by-cluster seasonally-averaged means and standard deviations of average VED are consistent interannually (Fig. 2.6, 2.7). The same three stations in the San Juan islands (cluster 4/red) report highest VED in all four analyzed years, exhibiting maxima that are almost a factor of two larger than the next largest signal (cluster 2/grey). In the highly-variable Haro Strait and Johnstone Strait regions, the spatial frequency of my sampling likely plays a role in my derived map of tidal mixing hotspots - as I sample only approximately every 100th horizontal model coordinate, I likely miss other high-VED model points in this subregion. Analysis of tidal mixing hotspots is not the focus of this work, but a full characterization of this tidally-mixed zone using a more refined clustering approach may be an interesting focus of future work.

2.4.5 Biomass of primary producers

A similar biological clustering arises in all four years (Fig. 2.8, Fig. A.4). The boundaries of this clustering coincide broadly with the three major oceanographic subregions discussed above. The largest cluster (the CSoG - cluster 3/sky blue) is characterized by an early diatom bloom, followed by a transition to flagellate abundance in the summer months. In all four years, a functionally distinct NSoG region (cluster 4/red) arises, with sharp, episodic spikes in summer diatom biomass and diminished flagellate biomass. JdF (cluster 5/dark blue) reaches maximum biomass later in the year and, like the NSoG, shows a persistence of summer diatoms and diminished summer flagellate biomass. In contrast to the NSoG, where diatom biomass diminishes between episodic spikes, diatom biomass in JdF typically remains above 20 mmol N m^{-2} throughout the spring and summer seasons, with occasional spikes to higher biomass.

These three main regions have roughly similar mean seasonal biomass, with interannual variability larger than variability between clusters; the main differences between them are in the relative abundances of different functional groups and in the temporal characteristics of the phytoplankton biomass. Nearshore areas cluster together (cluster 2/grey) and have low depth-integrated biomass because they are limited by shallow depth. The largest depth-integrated biomass in the model in both the diatom and flagellate

groups is found in the tidal mixing region of Haro Strait (cluster 1/gold).

2.5 Discussion

I now consider the regional phytoplankton structure in the context of previous observational and modelling studies and discuss some mechanisms underlying the observed patterns. I focus on the three main regions found by the biological clustering (the CSoG, the NSoG, and JdF).

2.5.1 The North vs. the Central Strait of Georgia

In the model, the NSoG shows only slightly higher depth-averaged phytoplankton biomass in all seasons than the CSoG (Fig. 2.9). This biomass is consistent with the in-situ study of Masson and Peña conducted between 2001-2007 in this region, which shows lower surface chlorophyll but a deeper phytoplankton growing zone in the NSoG leading to slightly higher depth-integrated chlorophyll concentrations in the northern region in all four seasons of sampling (Masson and Peña 2009, henceforth MP09, Table 2). Remote sensing observations also show significantly lower surface chlorophyll in the NSoG throughout the year (Suchy et al., 2019). The majority of the modelled biomass difference between the NSoG and CSoG occurs in the subsurface maximum around 6-8 meters in depth (Fig. A.6) and may not be captured by surface observations. Previous modelling (of years 2007-2009) found somewhat higher depth-integrated phytoplankton biomass in the CSoG throughout the year, but with significant spatiotemporal variability (Peña et al., 2016). However, a recent year-round in-situ campaign in several parts the Strait of Georgia found no meaningful difference in depth-integrated chlorophyll between the NSoG and CSoG (Pawlowicz et al., 2020).

Together, these studies suggest that the difference between the two regions with respect to total depth-integrated biomass is subtle. However, I find a substantial difference in the modelled phytoplankton functional group composition and the temporal scale of variability of the phytoplankton signal between regions. In both regions of the Strait, the opportunist-class diatoms, which have the highest growth rate and highest nutrient requirements, peak first (typically in late March, though with considerable variability (S. Allen & Wolfe, 2013)) and form the majority of the phytoplankton biomass in the spring (fig. 2.8, 2.9). In the CSoG, the model then transitions to higher biomass of gleaner-type flagellates around day 150, near the beginning of June, and flagellates continue to exhibit high summer biomass in this region (Fig. 2.8, 2.9). In contrast, the NSoG continues to exhibit episodic short-lived peaks of high opportunist-type phytoplankton biomass, represented by diatoms, throughout the summer so that in all years except 2016, diatoms make up the bulk of summer phytoplankton biomass in this region.

In the Strait of Georgia, significant evidence of high summer biomass near strong mixing zones or in response to mixing driven nutrient delivery exists. For example, early surveys of the system find high chlorophyll associated with dynamic frontal regions in the northern and southern ends of the SoG (Parsons, Stronach, Borstad, Louttit, & Perry, 1981), and consequently warn against drawing firm conclusions about the nature of phytoplankton abundance and variability from episodic sampling in shifting frontal zones. Nutrient delivery via episodic tidal mixing events near Discovery Passage has been linked to increased biomass (e.g. (Parsons et al., 1981; Haigh & Taylor, 1991)) and modelled primary productivity (Olson et al., 2020a). Though this phenomenon has been recorded in the CSoG as well (Yin et al., 1997; St. John et al., 1993), higher stratification may dampen the magnitude of the nutrient pulses. Sudden introduction of abundant nutrients is expected to favour the opportunist functional group represented by diatoms over the slower-growing gleaner functional group represented by flagellates, as is seen in my clustering (Cloern & Dufford, 2005; Dutkiewicz, Follows, & Bragg, 2009). A recent four-year timeseries of phytoplankton composition data at a station near Quadra Island in the NSoG supports this idea by showing episodic blooms of summer diatoms after wind events (Belluz, Peña, Jackson, & Nemcek, 2021). Indirect evidence of episodic high biomass, sometimes following wind events, has been observed elsewhere in the NSoG (Evans et al., 2019; Mahara, Pakhomov, Dosser, & Hunt, 2021).

I suggest that my results reflect a controlling influence of stratification on phytoplankton biomass and community structure. Strong stratification concentrates phytoplankton biomass in a thin well-lit surface layer while limiting supply of nutrients after the initial biological drawdown. In the model, these conditions favour high abundance of the gleaner-flagellate group. In the NSoG, nutrient drawdown also occurs, but episodic wind events lead to stronger upwelling and mixing due to the comparatively weaker stratification and inject sharp pulses of nutrients into the near-surface, leading to sharp, short-lived diatom bloom (Moore-Maley & Allen, 2021). Faster-growing opportunist-diatoms tend to outcompete gleaner-flagellates when sufficient nutrients and light are available, but inherent variability in the physical environment promotes coexistence (Anderies & Beisner, 2000). The result is only a modest, if any, change in biomass but a significant change in functional group composition and temporal variability between the NSoG and CSoG.

Peña et al. find higher biomass in the CSoG due to the deeper nutricline in the NSoG (Peña et al., 2016). I find instead that the increased mixing in the NSoG provides increased nutrients and that biomass in both regions is about the same. These two views are not directly reconcilable and which view is more representative of actual conditions depends on accurately capturing the balance of between the action of mixing as a source of nutrients and mixing as a source of light reduction and phytoplankton dilution. Part of the noted dissimilarity between these results and those of Peña et al. may be due to the

different years studied (2007-2009 in the Peña et al. study, vs. 2013-2016 here).

My modelling study is necessarily subject to limitations. For example, very high biomass shown in the tidal mixing region (Fig. 2.8, cluster 1/ gold) could be an artifact of slower phytoplankton mortality rates, at least at times, than occur in nature, with phytoplankton mixed deep into the watercolumn and persisting too long before dieoff occurs. Such a rate imbalance would affect the response to mixing described above. Available observations support model phytoplankton levels in this region but are limited to the upper water column. The divide of the phytoplankton functional groups in the model may also not precisely correspond to a split between diatoms and flagellates and should instead be taken as a divide between opportunist-type primary producers with high nutrient needs and high light needs and gleaner-type primary producers with capacity to persist at lower nutrient and light levels. Because model-data agreement in biomass and nitrate is strong in these regions, I believe the mechanism of nutrient delivery by wind events in the less stratified north leading to dominance of faster-growing phytoplankton is robust.

2.5.2 Juan de Fuca Strait

My results suggest that the mean annual average depth-integrated biomass is about the same in all three physical regions, including the well-mixed, weakly-stratified JdF. In contrast, previous studies suggested a lower biomass in JdF (Masson & Peña, 2009; Peña et al., 2016) due to a deeper nutricline. However, recent in-situ chlorophyll and nutrient data (2013-2016) support my result. In fact, the evaluation suggests that, at dates and locations where observations are available, the model slightly underestimates observed biomass in Juan de Fuca Strait (Fig. A2, Table A2). Furthermore, the biological and physical components of the model perform similarly well across all three main clusters (Fig. A.1-A.2, Tables A.1-A.2), increasing confidence that the modelled features are robust.

One factor explaining the difference between these conclusions may be the vertical structure in the biomass observed by both MP09 and the model. In MP09, the spring phytoplankton biomass is much more prominent in the CSoG and NSoG than in JdF. The spring biomass exhibits a strong subsurface maximum ($\sim$10 meters in the chlorophyll observations) and persists relatively deep into the watercolumn (up to 40 meters). However, though overall concentrations reported in MP09 are lower in all seasons in JdF, observed chlorophyll concentrations $>= 1$ mg m^{-3} persist at deeper depths in most seasons in Juan de Fuca than in both regions of the Strait of Georgia (up to 50 meters in the spring, summer, and fall), and in summer and fall, the NSoG exhibits slightly deeper phytoplankton persistence compared to the CSoG. I replicate these trends in general vertical structure (Fig. A.6), with a prominent subsurface maximum at $\sim$6-8 meters and

phytoplankton biomass mixed deeper in Juan de Fuca Strait than in either region of the Strait of Georgia.

This vertical structure likely leads to a dilution effect - even when phytoplankton concentration at a given depth may be lower in Juan de Fuca Strait than in the Strait of Georgia, overall depth-integrated biomass may be simultaneously higher. This deep biomass is less likely to be captured by sampling campaigns, potentially leading to an underestimation of the phytoplankton biomass of the region as a whole. Furthermore, because of the interannual variability in spring bloom timing and differences in spring bloom timing between the Strait of Georgia and Juan de Fuca Strait (discussed further below), the spring in-situ survey that captures high biomass in Strait of Georgia may be too early to observe the full extent of the spring bloom in Juan de Fuca Strait.

In the NSoG and CSoG, the derived biological signals suggest a regime where stable growing conditions in the spring transition to varying degrees of summer nutrient limitation which are interrupted by episodic nutrient delivery, more frequently in the NSoG. In contrast, the diatom growth curve in JdF suggests a light-limited environment year round, consistent with the established understanding (Mackas & Harrison, 1997). Nutrients are rarely limiting in JdF, owing to the plentiful supply of oceanic nitrate (Sutton et al., 2013) and stronger watercolumn mixing in this region demonstrated in the VED clustering (Fig. 2.7). One factor that may potentially enhance growing conditions in the summer season here is the advection of a freshwater lens from the Strait of Georgia via the surface estuarine circulation (Pawlowicz, Riche, & Halverson, 2007; MacCready et al., 2021). This advection is visible as a slight increase in the summer freshwater index in JdF (Fig. 2.6) and may contribute to increased watercolumn stability, and hence light availability and favourable growing conditions, in this period.

Spring Bloom Timing

The timing of the first substantial increase in phytoplankton biomass (the spring bloom), in the Salish Sea varies considerably inter-annually and is driven by different factors, primarily wind speed and cloud cover, and secondarily temperature and freshwater discharge (S. Allen & Wolfe, 2013). While I do not evaluate spring bloom timing here, considering the spatial variability of the onset of the spring bloom throughout the domain may deliver insights regarding the functioning of the different regions. For the purposes of this informal exploration, at each station I define the spring bloom as the first peak in depth-integrated diatom biomass that is at least 30% of the maximum annual diatom biomass at that station. In all years, the spring bloom started in the CSoG and radiated outward toward to NSoG before eventually reaching JdF. This earlier bloom initiation in the CSoG than in the NSoG was also seen in multiple years of satellite observations of the region (Suchy et al., 2019). The late bloom timing in JdF was likely driven by stronger

mixing limiting light availability later into the year in JdF region (Fig. 2.10), consistent with the functional differences between JdF and the NSoG and CSoG discussed above.

This preliminary examination of modelled bloom timing shows the large interannual variability in the onset of the spring bloom, consistent with one-dimensional models of the region (Collins, Allen, & Pawlowicz, 2009; S. Allen & Wolfe, 2013) and in the in-situ and satellite based observations (Suchy et al., 2019; Gower, King, Statham, Fox, & Young, 2013; Boldt, Chandler, & Javorski, 2020). This variability is expected based on known interannual variability in the physical environment; for example, the Strait of Georgia experiences interannual variability in temperature in response to variability in large-scale atmospheric forcing over the northeast Pacific, typically visible as positive temperature anomalies following tropical El Niño events (Masson & Cummins, 2007). This work, which spans only four years, does not consider the temporal variability of the biological and physical conditions in the Salish Sea on long timescales. However, the significant spatial and temporal variability seen here underscores both the dynamical differences in environmental growing conditions in different regions of the Salish Sea and the interannual variability, and provides an interesting direction for future research.

2.5.3 Utility of clustering methods in the context of high-resolution models

My clustering approach identifies unambiguous regions of a complex coastal sea that exhibit distinct biological responses to disparate physical environments. These responses are not immediately obvious in time-averaged snapshots of the studied system. The simple machine learning technique used here enhances my way of looking at the problem - in this application, I am not using machine learning to predict unknown quantities, as is becoming common (e.g. (Keppler, Landschützer, Gruber, Lauvset, & Stemmler, 2020)), but instead I am asking it to show us what is already there. Using this simple technique, I am able to draw objective boundaries between regions based on emergent structures in my data and significantly advance my intuition about the system.

The simplicity of the approach may have utility in numerous contexts. For instance, many characterizations of environmental regions rely on sparse data with large spatial biases. Objective clusters determined from regional models, with mechanistic underpinnings, may be used to group sparse data. This approach allows clear characterization of complex systems. Furthermore, it may provide the necessary first step for machine learning studies that rely on well-organized training datasets to accurately predict target variables (Landschützer et al., 2013). Resource and environmental management situations and optimal monitoring strategies may also benefit from a data-driven approach to regional definitions. Finally, cluster-based model evaluation can inform model development by providing information about how well models simulate different biophysical features.

2.6 Conclusion

My work applies a hierarchical clustering algorithm to four years of SalishSeaCast model output. I extract four factors relating to stratification and one relating to depth-integrated phytoplankton biomass, differentiated by functional group. I identify distinct regions of the model domain that exhibit contrasting wind and freshwater input dynamics, as well as regions of varying watercolumn-averaged vertical eddy diffusivity and halocline depth regimes. Similar spatial regionalizations in physical variables persist in all four analyzed years.

Similarly, I find distinct, interannually persisting, biological regions with phytoplankton biomass patterns that may be explained by patterns in the physical factors. In the NSoG, a deeper winter halocline and episodic summer mixing coincide with higher summer opportunist-type phytoplankton abundance, represented in the model by diatoms, and episodic fluctuations in phytoplankton biomass. In contrast, in the Fraser River stratified CSoG, shallower haloclines and stronger summer stratification coincide with more consistent biomass and high summer abundance of gleaner-type phytoplankton with slower growth rates, represented in the model as the flagellate functional group. While the biomass signals in the CSoG and NSoG suggest varying degrees of nutrient limitation, the JdF biomass signal suggests a light-limited physical regime. Furthermore, the cluster-based model evaluation suggests that JdF supports more biomass here than previously thought, due likely to a deeper growing layer. My approach shows that stratification controls nutrient delivery and causes subtle structure in regional biological patterns, and demonstrates the utility of simple machine learning tools in extracting insight from large datasets in the context of oceanographic models.

2.7 Figures

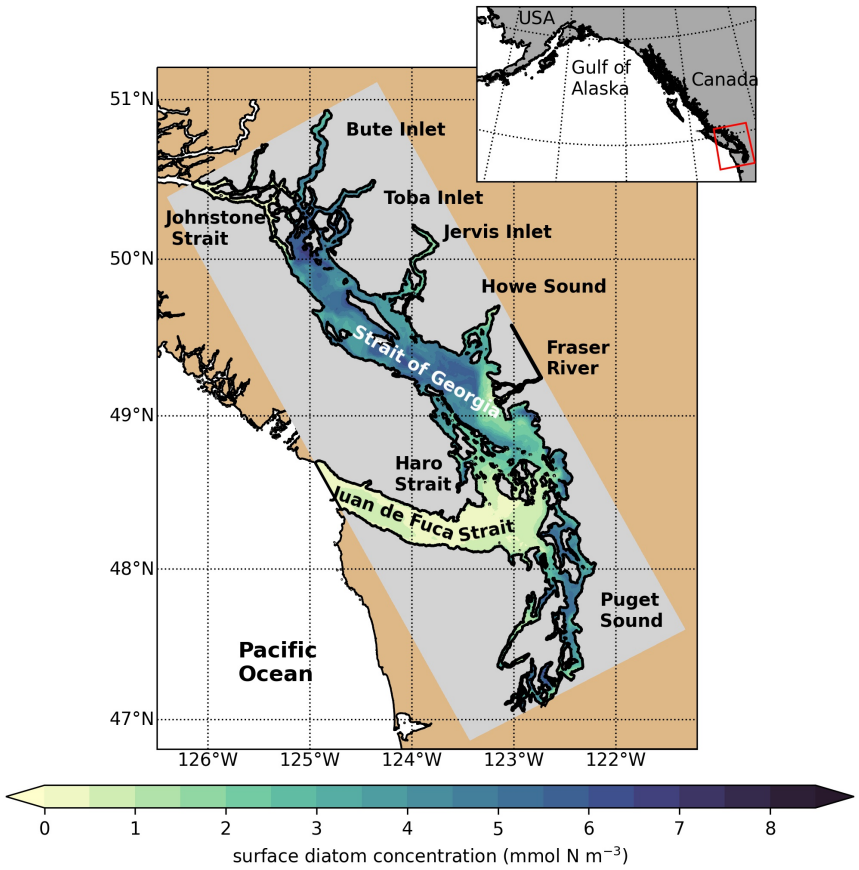

Figure 2.1: SalishSeaCast model domain coloured by one day of surface diatom concentration (April 1, 2016), highlighting major geographic subregions and features. The Strait of Georgia is often subdivided into the Central Strait of Georgia (CSoG) and Northern Strait of Georgia (NSoG).

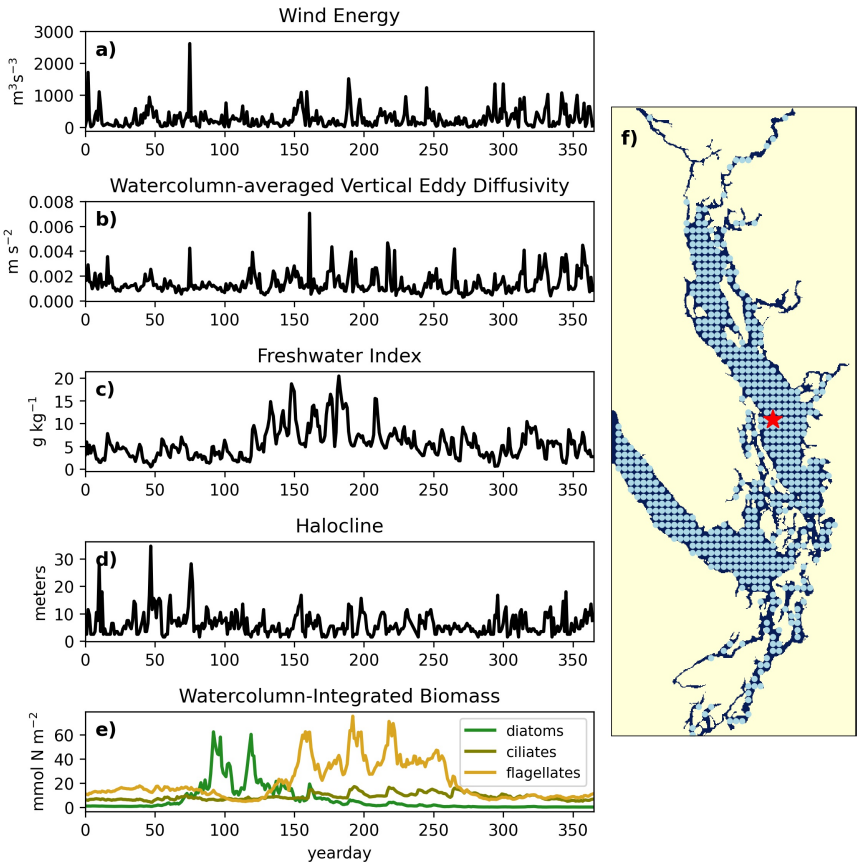

Figure 2.2: Example yearly signals of clustered physical (a-d) and biological (e) factors from one station in the CSoG (red star). The remaining 570 stations used in the clustering are shown as blue points. Depth-integrated phytoplankton biomass signals are combined in series for clustering (see Figure 2.8).

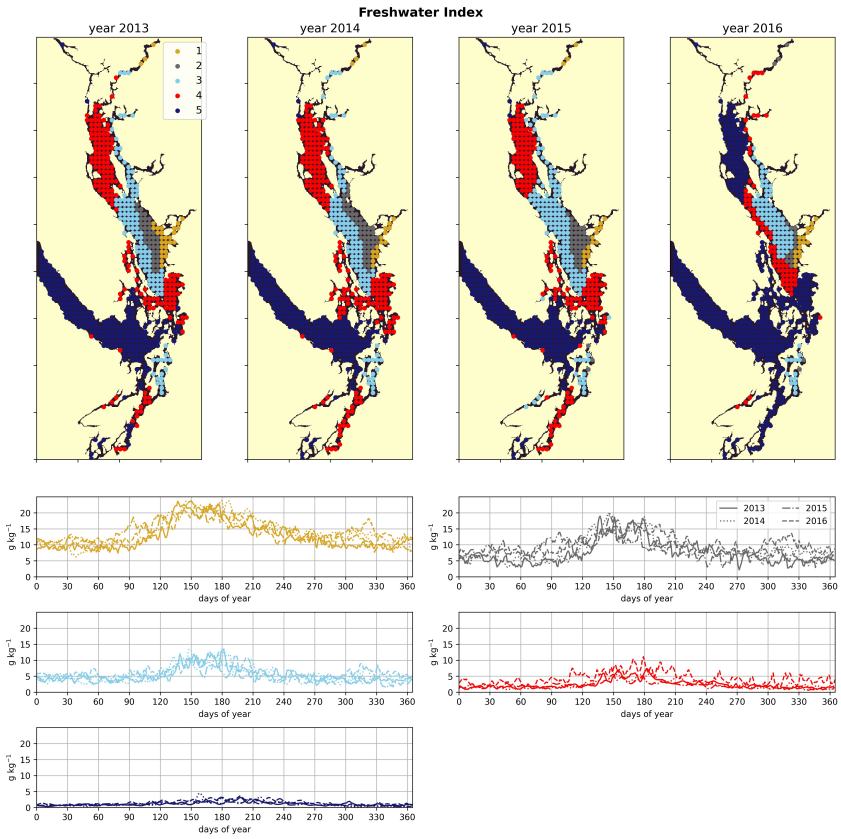

Figure 2.3: Clustering of the freshwater index signal (Section 2.2.2). As expected, areas near the mouth of the Fraser river have the highest freshwater index, with the freshwater plume turning north due to the Coriolis force, and the index decreases in bands from this maximum. Elevated freshwater index can also be seen in the vicinity of the Skagit river in Puget Sound and at the head of Toba Inlet, Bute Inlet, and Howe Sound, which contain glacial rivers. The magnitude of the freshwater index in the different clusters does not vary significantly interannually, but the spatial extent is diminished in year 2016, which had lowest freshet magnitude of the four years. In all clusters, the freshwater index peaks at the same time as the Fraser freshet does for a given year.

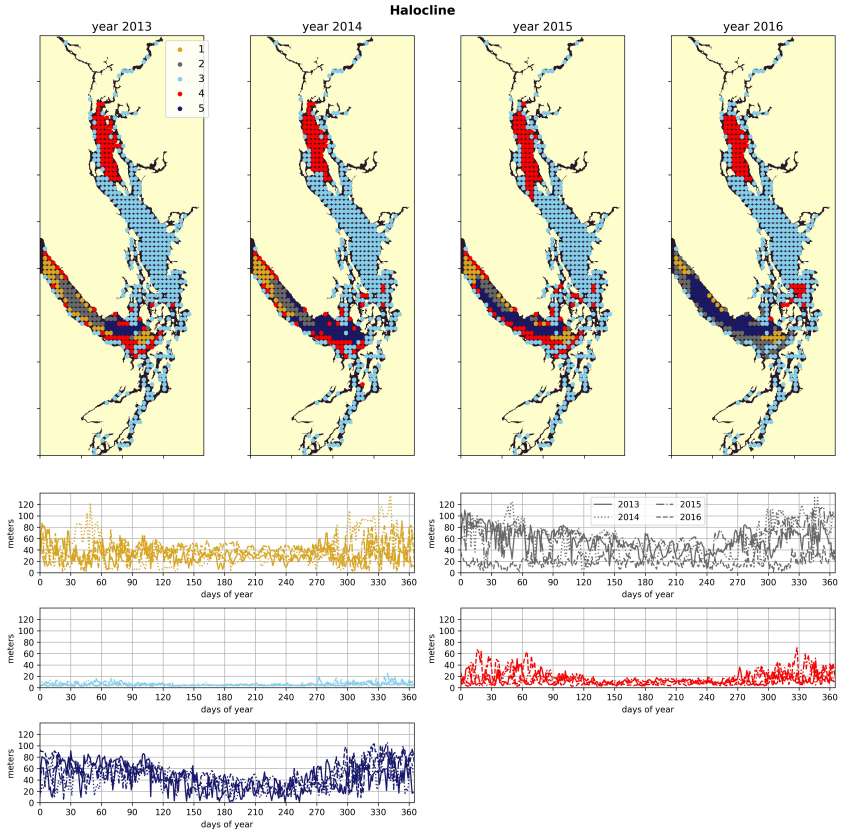

Figure 2.4: Clustering of the halocline signal, defined as the depth of the maximum salinity gradient. The largest region (cluster 3, light blue) is the freshwater influenced CSoG, with shallow (<10 m) haloclines and limited variability between seasons. Similar halocline dynamics are seen in Puget Sound and at the head of Toba Inlet, Bute Inlet, and Howe Sound, which contain glacial rivers. Significantly deeper and more variable haloclines are found in the NSoG (cluster 4, red), commonly deeper than 40 m in winter. The deepest and most spatially variable haloclines occur in the center of the JdF (clusters 1, 2, and 5), with nearshore regions of the JdF clustering with the NSoG in most years (cluster 4).

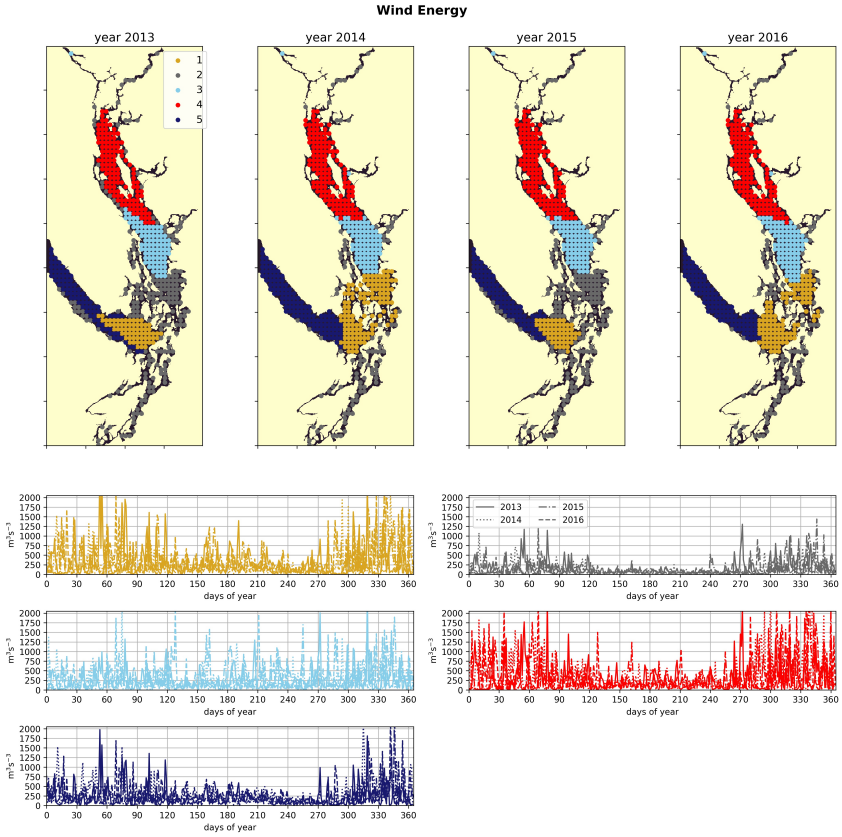

Figure 2.5: Clustering of the daily-average wind energy signal. Though spatial cluster boundaries are consistent, wind energy in all clusters is highly episodic, and all wind clusters show a marked decrease in wind energy during the summer months. Nearshore areas have lowest wind energy, owing to low fetch. Summer wind energies are higher in the CSoG than in the NSoG.

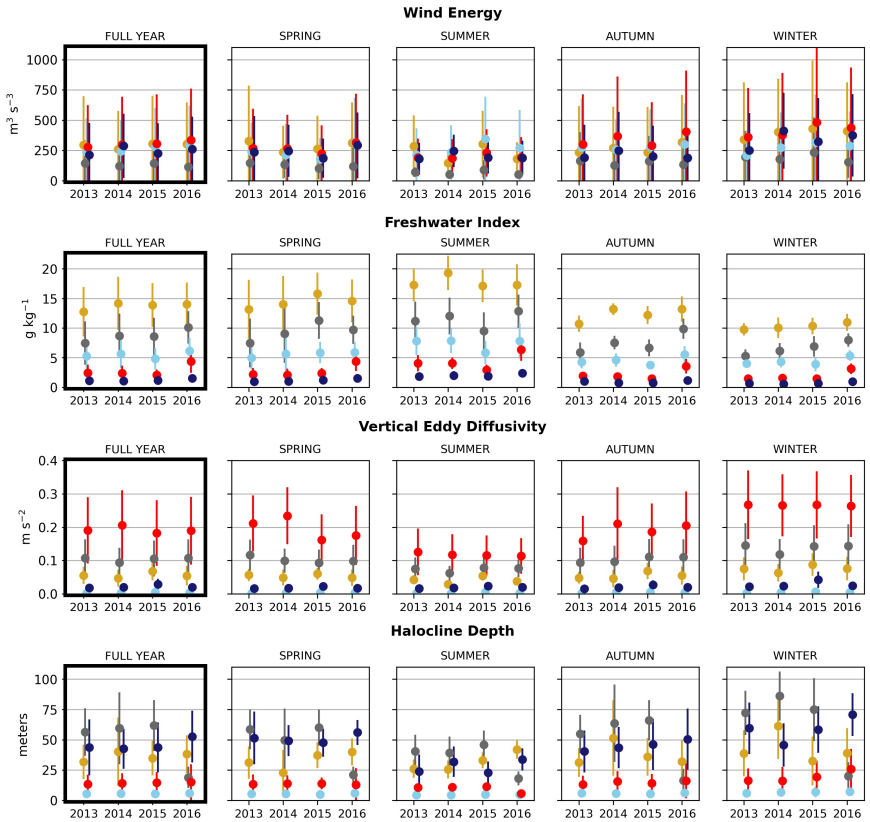

Figure 2.6: Seasonal means of the physical signals. Seasons are defined as follows: Winter is Dec-Feb, Spring is Mar-May, Summer is Jun-Aug, Fall is Sep-Nov. The temporal standard deviation of the seasonal mean signal for each cluster is shown.

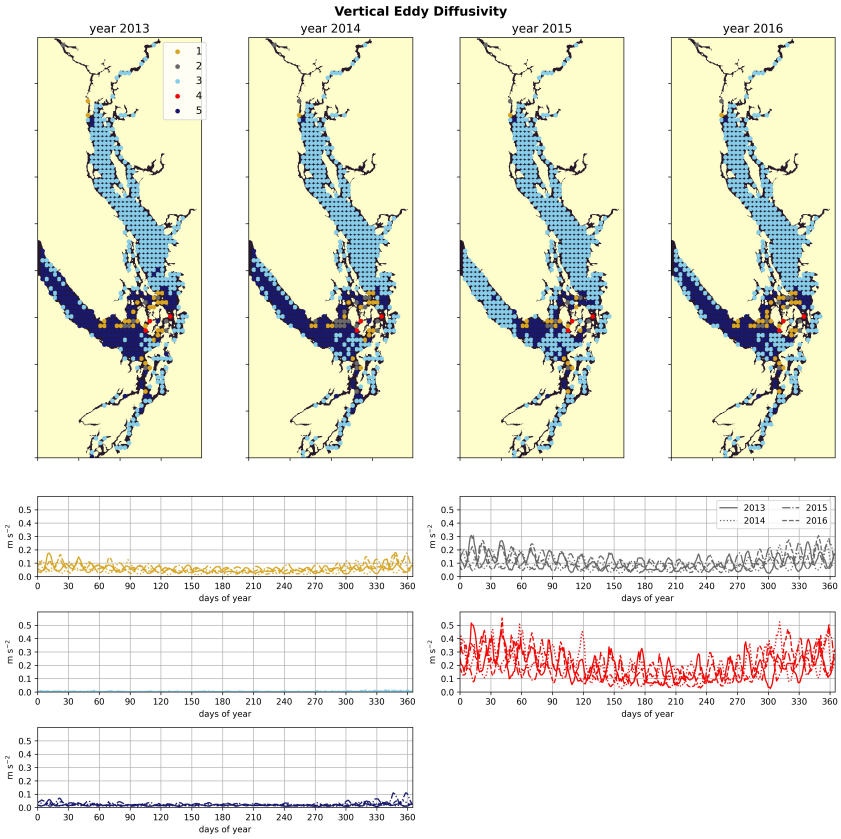

Figure 2.7: Clustering of the daily depth-averaged vertical eddy diffusivity signal. The domain is split into two major regions: the Strait of Georgia, which has universally low vertical eddy diffusivity, and Juan de Fuca Strait, with comparatively slightly higher VED due to stronger tidal currents. VED hotspots of various magnitudes are consistently found at tidal mixing hotspots, including Discovery Passage near Seymour Narrows and Haro Strait near the San Juan islands.

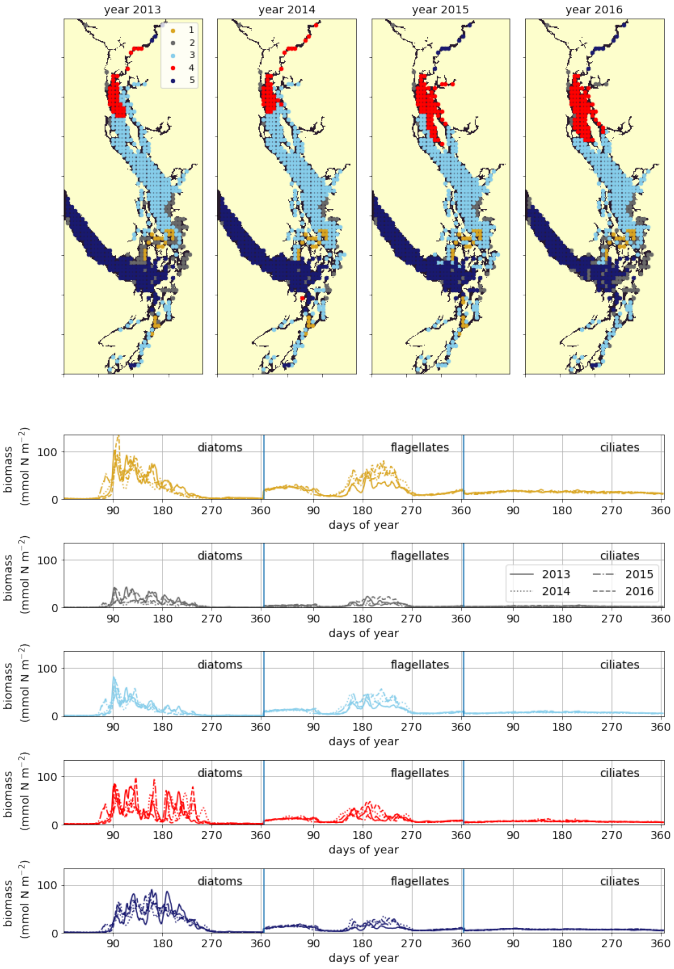

Figure 2.8: Clustering of vertically integrated phytoplankton biomass separated by model-defined functional group (diatoms, followed by flagellates, then ciliates). The domain is split into the CSoG, NSoG, and JdF, each of which exhibit distinct phytoplankton dynamics (see Section 2.3.5 and Discussion).

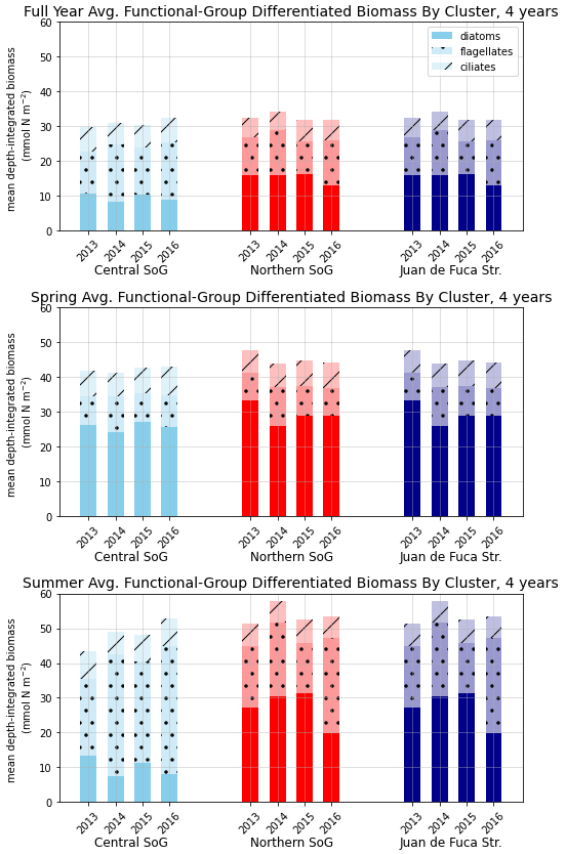

Figure 2.9: Depth-integrated phytoplankton biomass for the three main biological clusters (CSoG, NSoG, and JdF), differentiated by functional group. The annual, spring, and summer means of the derived clusters are shown for all four modelled years. All three clustered regions have similar total biomass, which stays relatively consistent interannually, but functional group composition varies by cluster, with higher summer diatom abundance in the NSoG and JdF than in the CSoG. Spring is defined as March-May, and Summer is June-August.

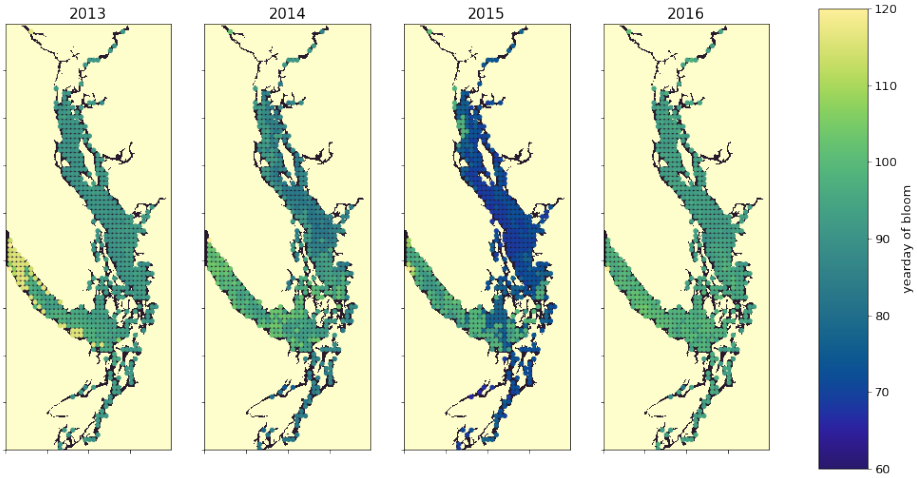

Figure 2.10: A spatial view of the onset of the spring bloom in the domain. Here the spring bloom is defined as the first peak in depth-integrated diatom biomass that is at least 30% of the maximum annual diatom biomass at that station. In all years, the spring bloom occurred earliest in the CSog and subsequently in the NSoG before reaching JdF with a variable delay.

Chapter 3

Anthropogenic carbon increase has caused critical shifts in aragonite saturation across a sensitive coastal system

Overview

Estuarine systems host a rich diversity of marine life, crucial both ecologically and economically, that is vulnerable to changes in ocean chemistry due to addition of anthropogenic carbon. However, the detection and impact of secular carbon trends in these systems is complicated by heightened natural variability as compared to open-ocean regimes. I investigate biogeochemical changes between the pre-industrial and modern periods using a high-resolution, three-dimensional, biophysical model of the Salish Sea, a representative Northeast Pacific coastal system. While the seasonal amplitude of the air-sea difference in pCO_2 has increased on average since pre-industrial times, the net CO_2 source has changed little. My simulations show that inorganic carbon has increased throughout the model domain by 29-39 mmol m^{-3} (28-38 μmol kg^{-1}) from the pre-industrial to present. While this increase is modest relative to other parts of the global ocean, the naturally high inorganic carbon content of Pacific waters and the low buffering capacity of the local carbonate system amplify the resultant effects. Notably, this increased carbon drives the estuary towards undersaturation of aragonite, negatively impacting shell-forming organisms. Undersaturation events were rare during the pre-industrial experiment, but under present-day conditions, the majority of the system experiences corrosive, undersaturated conditions year-round. These results are extended using

recent global coastal observations to show that estuaries throughout the Pacific Rim have already undergone a similar saturation state regime shift.

Plain Language Summary

The coastal ocean hosts rich ecosystems which are critical to marine organisms and people and sensitive to human-caused climate change. I used a detailed computer simulation to understand the carbon cycle in a complex, productive North Pacific coastal system, that is fed by a large un-dammed river, has connecting fjords, and narrows that have strong tides. I determine how much extra carbon has entered the system since the beginning of the industrial revolution. This increase is important because extra carbon in the ocean makes it harder for animals to build shells and structures. I find that large chemical changes have occurred. In fact, I am surprised to find that an important threshold under which shells dissolve has already been crossed in most of the region. I consider observations from other global coastal oceans and find that this same threshold may have been crossed throughout coastal oceans in much of the Pacific.

3.1 Introduction

The ocean has taken up a significant fraction of anthropogenic CO_2 emissions (McKinley, Fay, Lovenduski, & Pilcher, 2017; Gruber et al., 2019), slowing the rise of atmospheric carbon concentrations and causing changes to ocean carbon chemistry. These changes include decreases in pH and carbonate (CO_3^{2-}) ion concentration, a process commonly termed ocean acidification (Raven et al., 2005; IPCC, 2011; Caldeira & Wickett, 2003). The decrease in the CO_3^{2-} ion lowers the saturation state (Ω) of $CaCO_3$ minerals, including aragonite, a common biogenic form that is relatively soluble (Mucci et al., 1983). These minerals chemically dissolve once Ω decreases below the thermodynamic threshold of $\Omega = 1$. Many organisms require saturation states greater than unity for optimal growth, especially in the larval stage (Waldbusser et al., 2015), because less energy is required to calcify when Ω is higher (Kroeker et al., 2010; Spalding, Finnegan, & Fischer, 2017). Thus, ocean acidification may have far-reaching impacts on the structure of oceanic ecosystems (Fabry, Seibel, Feely, & Orr, 2008), many of which remain unknown (Haigh et al., 2015).

The waters of the Northeast Pacific Ocean are naturally carbon-enriched as compared to other ocean basins due to the accumulation of respired CO_2 (Feely et al., 2004). This high carbon content has several interrelated effects. First, metrics relating to ocean acidification, such as pH and Ω_{arag}, are lower in this region compared to the rest of the global ocean, implying more risk of corrosive conditions (Jiang et al., 2015). For example, aragonite saturation horizons (i.e. the water depth below which Ω_{arag} is < 1.0)

in the Northeast Pacific Ocean (Feely et al., 2008; Ross, Du Preez, & Ianson, 2020) are shallow. Second, the waters of this region are poorly buffered with respect to inorganic carbon, i.e. comparatively large changes in pH, Ω_{arag}, and pCO_2 occur for a given change in inorganic carbon, thus indicating that the system is highly sensitive to the addition of inorganic carbon. This poor buffering capacity means that waters of the Northeast Pacific Ocean are inefficient at taking up inorganic carbon from the atmosphere (Jiang, Carter, Feely, Lauvset, & Olsen, 2019). As a result of this carbon-enriched base state, even though the anthropogenic carbon increase in the North Pacific to date is small when compared to other regions in the global ocean (Carter et al., 2019; Franco et al., 2021), ocean acidification is a considerable concern for industry and policymakers, especially in the coastal zone within this region (Mathis et al., 2015; Ekstrom et al., 2015).

Understanding the impacts of ocean acidification on highly productive coastal regions is especially critical due to their ecological role and implications for human well-being. The large inherent natural variability of these systems, often several orders of magnitude larger than that of the open ocean, combined with a relatively short observational record, complicates the detection of secular trends due to anthropogenic carbon increase (Duarte et al., 2013; Fassbender et al., 2018). Similarly, because coastal oceans are dynamic and heterogeneous and remain sparsely sampled, the role of coastal oceans as an atmospheric carbon sink is difficult to determine (Bauer et al., 2013; Laruelle et al., 2018; Fennel et al., 2019; ?, ?).

The Salish Sea is a large, complex, productive, semi-enclosed temperate coastal system containing distinct regions that are dominated by different physical controls (LeBlond, 1983), yielding in turn unique biogeochemical zones. It is connected to the Northeast Pacific Ocean primarily via its western entrance - the Juan de Fuca Strait (here I call this the Ocean Exchange region, Fig. 3.1, highest salinity, teal). The ocean, and thus Juan de Fuca Strait, have strong seasonal variations in salinity driven by coastal upwelling and downwelling. Intense tidally-driven mixing in the Haro and Rosario Straits (here the Tidal Mixing Region, Fig. 3.1, red) leads to a coupling of the Ocean Exchange region and the inner estuarine waters of the Strait of Georgia. The Fraser River is the most significant freshwater source to the system, driving a strong estuarine circulation and elevated stratification in the central Strait of Georgia (here the Freshwater Influenced Region, Fig. 3.1, lowest salinity, blue). This influence decreases in the Northern Strait of Georgia (called the Northern Fjord Region, Fig. 3.1, green), which is characterized by stronger mixing and a relatively shallow, well-mixed secondary open-ocean exchange via Johnstone Strait (Jarnikova, Olson, Allen, Ianson, & Suchy, 2021; Olson et al., 2020a; Masson & Peña, 2009).

Strong winds in the fall and winter months lead to mixing of intermediate water into the surface layers over most of the domain. The estuary is a carbon-enriched system,

meaning that waters of comparable salinities have higher inorganic carbon concentration in Salish Sea waters than in the open Pacific Ocean due to local carbon sources (Ianson et al., 2016) leading to even lower aragonite saturation states than offshore and often surface undersaturation in winter (e.g. Feely et al. (2010); Ianson et al. (2016); Pelletier, Roberts, Keyzers, and Alin (2018); Evans et al. (2019); Cai et al. (2021)). Local rivers have low to moderately low alkalinity in a global context (Moore-Maley et al, (2018); Appendix B.1.4). Due to local biophysical factors, large seasonal cycles of pH have been reported inshore of the Tidal Mixing region compared with the adjoining open ocean (Fassbender et al., 2018; Lowe et al., 2019).

Here I investigate the impact of ocean acidification, driven primarily by the lateral influx of anthropogenic CO_2, on the Salish Sea system, using a submesoscale-resolving biogeochemical model. Specifically I estimate differences in the carbon system under 1) a present-day scenario, using present-day atmospheric CO_2 levels and open-ocean (lateral) dissolved inorganic carbon (DIC) boundary conditions and 2) a pre-industrial (PI) scenario, in which both atmospheric and lateral boundary carbon conditions are set to estimated pre-industrial values. All physical forcing is kept at present-day levels for both scenarios (see Methods 3.2.3 and Appendix B.1.1), and so any changes arise solely from the addition of anthropogenic carbon. I focus on biologically relevant Ω_{arag} thresholds as well as changes in overall sink strength with respect to atmospheric CO_2. I then use a global dataset of coastal inorganic carbon observations to contextualize my results with reference to present-day geographic trends in coastal carbonate chemistry conditions. Finally, I use projected future atmospheric CO_2, along with an available proxy for aragonite undersaturation, to estimate when different global coastal ocean regions may become undersaturated with respect to aragonite.

3.2 Methods

3.2.1 Biogeochemical model

SalishSeaCast (v201812) (Soontiens et al., 2016; Soontiens & Allen, 2017) is a high-resolution ($\sim$500m horizontal, 1-27m vertical resolution) biophysical model developed for the Salish Sea (Fig. 3.1), based on the NEMO modelling framework (Madec, 2015). The model includes a regionally-tuned biological nutrient–phytoplankton–zooplankton–detritus (NPZD) model with three classes of primary producers that accurately represents the local primary productivity dynamics in the Salish Sea (Olson et al., 2020a) (Fig. B.1). To this biophysical model, I have coupled the Moore-Maley et al. (2016) carbonate chemistry model that explicitly resolves dissolved inorganic carbon (DIC) and total alkalinity (TA) . The model equations are as follows:

$$\frac{\partial DIC}{\partial t} = -(U_N – Rm_N)R_{C:N} - U_{PC} + \text{transport} + \text{air-sea flux}$$

$$\frac{\partial TA}{\partial t} = (R_{P:N}+1)U_{NO_3^-} + (R_{P:N}-1)(U_{NH_4} - Rm_{NH_4}) – 2Rm_{NO_3^-} + \text{transport}$$

where U represents uptake, Rm represents remineralization, and $R_{X:Y}$ is the Redfield ratio of element X to element Y (Redfield, 1963). Essentially, the DIC equation states that the change in DIC in the system is equal to the difference between its uptake as substrate by phytoplankton and its remineralization from particulate and dissolved organic matter. Here uptake coupled with nitrogen is represented as U_N, and uptake that is not coupled with nitrogen is shown as U_{PC}. Uncoupled DIC uptake occurs when phytoplankton are nitrogen limited but not light limited and take up extra inorganic carbon, resulting in nutrient uptake ratios of C:N that are higher than the Redfield ratio Ianson and Allen (2002). We assume that this taken up inorganic carbon immediately enters the refractory DOM pool and no longer interacts with the other pools. In the model, the C:N ratio is Redfieldian in phytoplankton, detritus, and semi-labile dissolved organic matter. The DIC pool is then affected by physical transport, including advection and mixing. The TA equation states that the change in the system's total alkalinity is proportional to the change in cellular chemistry as a reaction to the uptake and remineralization of several groups of ions. As phytoplankton cells take up or expel charged ions associated with inorganic and organic N and P, they also release [H+] or [OH-] to maintain electrochemical equilibrium, and this exchange results in a change in the system total alkalinity (Brewer & Goldman, 1976). The TA pool is then affected by physical transport. In this study I assume that biocalcification has a negligible effect on DIC and TA mass balance in this region (Moore-Maley et al., 2016).

Air-sea gas exchange and pCO_2 are calculated at every timestep (40 s) using mocsy 2.0 (Orr & Epitalon, 2015). I derived an observationally-based seasonal cycle of atmospheric pCO_2 (Appendix B.1.3, Fig. B.2, B.3). The western open ocean boundary is forced with real-time output from the LiveOcean model (Brasseale, Grason, McDonald, Adams, & MacCready, 2019; MacCready et al., 2020), and the northern open ocean boundary is forced with a climatology based on local observations (Dosser et al. (2021); Appendix B.1.6). River nutrient and carbonate chemistry forcing is estimated from available regional observations (Appendix B.1.4).

The model was initialized using linear relationships (DIC vs. salinity and TA vs. salinity) which were calculated from a subset of available measurements, subdivided by the model's main dynamical regions (Fig. 3.1; Ianson et al. (2016)). The residence time of the system is quite short, ranging from weeks in the surface to 1-3 years in the deepest waters of the system (Pawlowicz, Hannah, & Rosenberger, 2019). The model

was allowed to spin up for 4 years after initialization (model year 2013 three times, then 2014). The modelled year, 2015, was then spun up for an additional two years in the present-day scenario and three years in the pre-industrial scenario. After these spin-up periods, differences of total and layer inventories of DIC, TA, nitrogen, and salinity in the domain between the last spinup year and the analyzed year were considered negligible ($< 0.1\%$ of layer-averaged concentration, Appendix B.1.5, Fig. B.4).

3.2.2 Model evaluation

I evaluate modelled DIC, TA and calculated Ω_{arag} against available observations in the Salish Sea from 2002-2016 (Figs. 3.2, S11, and S12; Table ST1). As few observations are available, I match by year day but not by year. To reflect interannual variability influencing my mismatched year evaluation, I use a 5 year (2013-2017) run of the contemporary model. Model evaluation shows high skill. Root mean squared error (RMSE) of a salinity-matched evaluation is 29–37 mmol m^{-3} for DIC (range given over the 5-year run, compared to a range of modelled values of $\sim$1600-2400), 21–24 mmol m^{-3} for TA, and 0.33-0.43 for Ω_{arag} (compared to a range of modelled values of $\sim$0.5-4). DIC is biased low by 11-19 mmol m^{-3}, TA is biased high by 10-13 mmol m^{-3} for TA, and Ω_{arag} is biased high by 0.17-0.23. The bias in the calculated Ω_{arag} is typically less than the error in Ω_{arag} (0.05-0.24) associated with measurement uncertainty (of observed DIC and TA) calculated using the error propagation routine of Orr et al. (2018).

3.2.3 Experimental scenarios

I ran two full-year carbon scenarios: 1) the present-day scenario, in which I used the current local seasonal cycle in atmospheric CO_2 and open-ocean (lateral) DIC and TA boundary conditions, and 2) the pre-industrial (PI) scenario, which used PI atmospheric CO_2 levels and estimated PI DIC levels at the lateral boundary. Pre-industrial atmospheric CO_2 was assumed to have a mean of 280 μatm (corresponding to approximately year 1800) with the same seasonal cycle as in 1). Lateral boundary condition DIC levels were calculated by estimating the anthropogenic increase in DIC experienced by a watermass based on its estimated age, which was derived from chlorofluorocarbon-11 observations (Sonnerup et al., 2013), then subtracting this increase from present-day DIC levels using the C* method (Appendix B.1.6, Fig. B.5-B10). In both the pre-industrial and present-day scenarios, one full year of model run was analyzed (model year 2015).

Except for differences in surface and lateral boundary conditions for inorganic carbon, all other forcings (e.g. ocean physics, temperature conditions, atmospheric model, river climatology and riverine carbon and nutrient inputs) were kept at existing present-day levels. I thus neglect the effect of increased temperature in the system, which has

been estimated to be $\sim$1°C per century (Riche, Johannessen, & Macdonald, 2014), which would have $\sim$1% impact on Ω_{arag} calculated here (Evans et al., 2019). I also do not model historical changes in nutrient loading, which have acidifying effects due to eutrophication in parts of the domain, notably some regions of Puget Sound (Khangaonkar et al., 2019), though the majority of the Salish Sea is considered at low risk for eutrophication (Sutton et al., 2013). Atmospheric forcing, including winds and solar radiation, was derived from the High Resolution Deterministic Prediction System (HRDPS), a nested 2.5 km resolution atmospheric model (Milbrandt et al., 2016).

3.2.4 Analysis of global coastal observations

To assess the similarity between my highly resolved model output and global observations, I analyze the global carbonate chemistry observational dataset, GLODAPv2.2020 (Olsen et al., 2016; Key et al., 2015), applying the following filters: near-surface water ($<$ 200 m), valid DIC, TA, temperature and salinity measurements, a bottom depth of $<$ 500 m, and a salinity $>$ 20 psu. Of the 1,275,558 available DIC measurements in the GLODAPv2.2020 dataset, 14,098 measurements remain when these filters are applied. A measurement constitutes an individual bottle sample which is representative of waters at a specific time, location and depth.

Determining future global coastal conditions

I roughly estimate future conditions; i.e., when the criterion of [TA-DIC]$<$ 50 mmol m^{-3}, a proxy for poorly buffered, low Ω_{arag} conditions ($\sim \Omega_{arag} \leq 1$) developed by Xu and Cai (2020), will be met in the coastal GLODAP.v2.2020 observations, assuming 1) that atmospheric concentrations of CO_2 (as estimated by Meinshausen et al. (2020)) increase following the shared socioeconomic pathway (SSP) 5-8.5, a 21st century scenario characterized by continued, high fossil fuel-based economic development (O'Neill et al., 2016) 2) oceanic circulation, mixing, temperature, total alkalinity, and salinity do not change and 3) the difference between surface ocean pCO_2 and atmospheric pCO_2 and all carbon variables other than DIC are fixed at present day.

Under these assumptions, calculating future [TA-DIC] requires only an estimate of anthropogenic CO_2 increase over the 21st century, which in turn requires an estimate of water parcel ventilation age (Γ) from chlorofluorocarbon-11, chlorofluorocarbon-12, or sulfur hexafluouride wherever available. Water parcel ventilation age is inferred using the 1-dimensional transit time distribution method (Hall & Plumb, 1994) assuming $\Delta/\Gamma = 1$ (i.e. advective and diffusive processes contribute equally to tracer transport). Of the original dataset, 2556 measurements meet the coastal filter described above and also have available chlorofluorocarbon or sulfur hexafluouride measurements. I calculate the

DIC value at a future date t_f using the C* method by assuming that the water parcel was last at the surface at $t = t_f - \Gamma$. The majority of the coastal waters (83%) are less than 10 years old.

These assumptions introduce systematic errors in the estimates of anthropogenic carbon. Using a related technique, He et al. (2018) estimated that ignoring changes in circulation, air-sea disequilibrium, and ocean mixing yields a difference in global DIC inventories of 13.6%. I do not attempt to quantify the uncertainty associated with holding other quantities fixed; however, because atmospheric concentrations in 2100 differ by roughly a factor of 3 amongst the SSPs, the uncertainty in my estimates for when the critical threshold is reached are likely dominated by the choice of scenario. I emphasize that these estimates should be interpreted broadly as a metric of susceptibility to future climate change rather than a robust metric of emergence time.

3.3 Results and Discussion

3.3.1 The Salish Sea carbon cycle

The seasonal features of the inorganic carbon balance are controlled by physics and biology. The mean summer (Jun. 1 - Aug. 31) and winter (Dec. 1 - Feb. 28) surface concentration of DIC is low in the Freshwater Influenced Region, driven by dilution in the vicinity of the Fraser River plume (Fig. 3.1, 3.3a, 3.3b). This dilution effect decreases in the Northern Fjord region but is also seen in the brackish northern inlets. Throughout the year, salty Pacific water enters through the Ocean Exchange Region, with a stronger DIC signal in the summer upwelling season (Figs. 3.3a, 3.3b, kilometers 0 - 180). During summer, phytoplankton draw down DIC in the top 20 m of the watercolumn throughout the domain (Fig. 3.3a), while in winter, high DIC from respired organic matter is mixed back into the surface (Fig. 3.3b, e.g. km 0-200). DIC in the Tidal Mixing region is more homogenous during the winter months (Fig. 3.3a, 3.3b, km 200-300), while a stronger along-thalweg gradient between high-DIC Ocean Exchange waters and Freshwater Influenced waters (km 300-490) persists in the summer, due to stratification driven by the freshwater from the Fraser River (Fig. 3.3a, 3.3b).

Layer-averaged DIC concentrations have a strong seasonal cycle (Fig. B.13a) with a characteristic decrease in surface DIC due to drawdown from the spring phytoplankton bloom (day 70 / March 11, Fig. B.13a). Dilution of the surface layer by increased river runoff further amplifies this decrease—the lowest domain-wide mean surface DIC concentration ($\sim$1600 mmol m^{-3}) coincides with the peak of the Fraser River freshet (day 152 / June 1), Fig. B.13b). The deeper sections of the domain (i.e. below 50 meters depth) are dominated by the seasonal upwelling signal advected into the Ocean

Exchange region, visible as an increase in mean domain DIC (around day 180 and later, Fig. B.13a). The Salish Sea has a relatively short residence time that varies by layer and subregion (Pawlowicz et al., 2007; MacCready et al., 2021). The upper and intermediate layers of the two inner zones are well-flushed, as are the outer and connecting zones. The deepest waters (>300 m) have the longest residence time, estimated at 1-3 yrs in winter by Pawlowicz et al. (2007), and experience inorganic carbon fluctuations as a response to seasonally varying deep water renewal events (Masson, 2002). Using an independent method, MacCready et al. (2021) found a mean residence time for the Salish Sea of 327 days, supporting the idea that the system is relatively well flushed overall.

3.3.2 Atmospheric CO_2 Flux

The carbon flux into and out of the estuarine system is dominated by lateral fluxes between the estuary and the open Pacific ($\sim$14000 Gmol year^{-1} into the system). In contrast, air-sea flux is much smaller (net outgassing in the present-day system is $\sim$10 Gmol year^{-1}). Integrated over the full domain, the Salish Sea appears to be a relatively weak net source of carbon to the atmosphere in the present-day scenario. The system experiences strong net outgassing (negative fluxes) in the winter (Dec-Feb) that is nearly balanced by net ingassing (positive fluxes) in the summer (Jun-Aug) (Fig. 3.4c). This seasonality is expected in Northeast Pacific coastal temperate zones where light limits winter productivity (Ianson & Allen, 2002; Evans, Hales, Strutton, & Ianson, 2012).

The majority of my study area functions as a weak net source of atmospheric CO_2, with the exception of the highly stratified Freshwater Influenced region, which acts as a net sink, agreeing broadly with limited observations (i.e. Evans et al. (2012); Fig. 3.4e, B12) and echoing global patterns in plume-affected near-shore areas (Bauer et al., 2013). The Fraser River and other very low salinity (< 2 g/kg) regions act as a strong source of carbon to the atmosphere (Fig. 3.4a), with continuous outgassing (mean flux -62.3 g C m^{-2} yr^{-1}, as compared to the whole domain mean -8.3 g C m^{-2} yr^{-1}). In my domain, the majority of rivers, including the dominant Fraser river, reach maximum runoff in the late spring (Fig. B.13b).

The high outgassing in many parts of the domain, notably the Tidal Mixing Region and Ocean Exchange Region (Fig. 3.4a) is explained by local estuarine circulation. In the Tidal Mixing region of the domain, the carbon-rich water coming into the system through canyon-enhanced upwelling through Juan de Fuca Strait is mixed to the surface (S. E. Allen, 2000) and acts as a ready source of high-carbon surface water especially in the summer months, where it counteracts the effects of the biological drawdown of carbon. Contemporaneously, in the Tidal Mixing region and parts of the Ocean Exchange region, light is always limiting (Mackas & Harrison, 1997), reducing biological drawdown; accordingly, summertime underway surface observations in the Tidal Mixing and

Ocean Exchange region show supersaturated pCO_2 (e.g. Nemcek, Ianson, and Tortell (2008)). In the Freshwater Influence region, stronger salinity stratification prevents high-carbon waters from reaching the surface while simultaneously creating favourable conditions for the drawdown of carbon by phytoplankton and the subsequent undersaturated pCO_2 conditions (Fig. 3.4a).

Gas-flux in this marginal sea is highly episodic: 25% of ingassing days account for over 50% of annual carbon uptake, and only 13% of outgassing days account for over 50% of the carbon outgassing in the model year, a pattern repeated in five years of a continuous hindcast of this model (years 2013-2017, Fig. B.14). Similarly, gas flux is spatially heterogeneous, with the present-day simulation showing that much of the domain exhibits a weak net flux in either direction (Fig. 3.4e, B14); the overall spatial distribution of gas fluxes exhibits long tails in both directions. These long-tail spatial distributions of air-sea flux, along with the observed temporal episodicity, underscore the difficulty of capturing the air-sea flux mass balance of estuarine systems and marginal seas through observational methods. Neither time-series measurements at a single station nor episodic sampling campaigns are likely to accurately capture variability or net fluxes. Current observational estimates of air-sea CO_2 fluxes in the region vary considerably (Fennel et al., 2019) and the global air-sea CO_2 flux balance remains poorly constrained in coastal regions (Bauer et al., 2013; Laruelle et al., 2018). Both observations and high-resolution modelling show dramatic variability in both sign and magnitude at scales much smaller than those captured by even mesoscale-eddy resolving models. My work shows that submesoscale-resolving simulations are an essential tool to estimate both the mean and variability of CO_2 air-sea fluxes within the coastal margin.

Comparison of air-sea CO_2 fluxes with available observations

I compare spatiotemporal air-sea CO_2 flux characteristics between the model and a survey conducted in the same region (years 2008-2010) (Evans et al., 2012). Due to the episodic nature of air-sea CO_2 fluxes, I do not match to model location and yearday but instead compare seasonal means, standard deviations, and maxima/minima of air-sea CO_2 fluxes from the model for three subregions and the three seasons with available observations from Evans et al. 2021 (Table 1 of that work). Seasonal definitions from Evans et al. (2012) are as follows: winter is January 1 to March 31, spring is April 1 to June 30, summer is July 1 to September 30, and autumn is October 1 to December 31. Region definitions for the Johnstone Strait, Strait of Georgia, and Strait of Juan de Fuca may be seen in Fig. 1 in that work. I note that part of the Johnstone Strait region in Evans et al. (2012) lies outside the SalishSeaCast model domain.

I do not necessarily expect the statistical summary of CO_2 fluxes for a full season of a subsection of the model domain to correspond exactly to that of an observational

campaign. However, considerable similarity can be seen between the distributions of the modelled air-sea fluxes and the observational air-sea fluxes (Fig. 3.5). In all subregions and seasons, the observations fall within the range of modelled values, and in most cases, the mean $\pm$ standard deviation of the two datasets is similar. I can also see some of the seasonal trends reported in Evans et al. (2012) in this visualisation, namely highest outgassing in autumn in all three subregions due to the coincidence of high pCO_2 disequilibrium with high wind speeds. The model reports higher maximum outgassing (negative values here represent flux out of the ocean) in all seasons in the Evans-defined Strait of Georgia and Johnstone Strait regions, likely due to the inclusion of fresh nearshore parts of the model domain that typically report high outgassing year-round and may have been undersampled by the observational campaign.

3.3.3 The anthropogenic signal

Anthropogenic DIC in the system was calculated from the difference in DIC between the present-day and pre-industrial simulations. The domain-averaged DIC increases by approximately 29-39 mmol m^{-3} from the pre-industrial run to the present-day run, with regionally-varying patterns in this increase (Fig. 3.3c). The areas near the Ocean Exchange Region experience a slightly lower DIC increase at depth than the domain average (Fig. 3.3c, teal) due to the comparatively old age of the waters coming in at this boundary (Appendix B.1.6), while the Tidal Mixing Region shows the most uniform concentrations in the system. In the Freshwater Influenced regions, the anthropogenic signal is significantly diluted at the surface due to freshwater input (Fig. 3.3c, blue), which is unchanged between the two runs. The opposite pattern emerges in the Northern Fjord region, which is adjacent to a relatively shallow open-ocean boundary delivering relatively young waters which are comparatively high in anthropogenic carbon (Appendix B.1.6), and simultaneously experiences less freshwater input. Due to the strong estuarine exchange in the system, the anthropogenic inorganic carbon increase in the Salish Sea is strongly influenced by the anthropogenic inorganic carbon intrusion at the open-ocean boundaries.

Net system outgassing has decreased only slightly ($< 2\%$) since pre-industrial conditions. Although domain-wide mean surface pCO_2 disequilibria in the present-day system are of similar magnitude in summer (May-Jun; $\sim$-95 μatm) and winter (Dec-Feb; $\sim$+95 μatm), stronger winter winds drive the net system outgassing (Fig. 3.4d, B14). Wintertime pCO_2 disequilibrium has increased only slightly between the pre-industrial and present-day system due to the anthropogenic carbon increase. However, the summertime disequilibrium was significantly lower in the pre-industrial case ($\sim$-35 μatm), and this lower disequilibrium is responsible for the lower ingassing during summer which leads to stronger net outgassing in the pre-industrial (-12.6 g C m^{-2} yr^{-1}). The increase in the

seasonal amplitude of the pCO_2 mirrors increases in seasonal amplitude of the pCO_2 cycle seen globally (Landschützer, Gruber, Bakker, Stemmler, & Six, 2018). In a five-year hindcast of the modern model (years 2013-2017), no obvious change in source strength is seen in the region (Fig. B14). Strong decreases in the winter storm climatology, either going back to pre-industrial or forward to 2100, could switch the system to net ingassing.

Furthermore, this comparison between the pre-industrial and present-day air-sea CO_2 flux disregards the effect of increasing temperature. The estimated $\sim$1°C increase in temperature may have acted to increase outgassing by decreasing the solubility of CO_2 in the surface. A secondary, opposing, effect of a temperature increase could be an increase in stratification, which may trap high-DIC water below the surface and contrastingly decrease outgassing. Untangling these non-linear relationships between temperature and carbon cycling at this local, submesoscale resolution may be an interesting area of future work.

My estimate of the anthropogenic carbon intrusion is commensurate with those made by other studies, which range from 13-49 μmol kg^{-1} in the Salish Sea and increase with increasing salinity (Table 3.1). The surface intrusion calculated in my domain is smaller than that observed at the surface on the outer shelf (Feely et al., 2016), due in part to the lowered buffering capacity and lower salinity of the Salish Sea surface waters as compared to outer shelf waters due to local carbon enrichment, as noted by previous studies of this region (Fassbender et al., 2018; Evans et al., 2019; Feely et al., 2010). In addition, the majority of the water from the outer shelf comes into the Salish Sea at depth through Juan de Fuca Strait (Giddings & MacCready, 2017), and the anthropogenic DIC content of these waters is lower than that of the outer shelf surface water (Feely et al., 2016). My estimate of the anthropogenic intrusion at the boundary of the system is slightly higher than that found by Feely et al. (2016) for waters of the outer shelf at 200m depth (Table 1). This difference is expected because the incoming water at the boundary of the Salish Sea contains a mix of younger subarctic waters and older California Undercurrent waters (Giddings & MacCready, 2017; R. E. Thomson & Krassovski, 2010), especially during winter downwelling when incoming water has been recently ventilated (Ianson et al., 2016). Further mixing of high-anthropogenic-DIC surface waters with older incoming waters occurs in the strongly tidally mixed parts of the Salish Sea (Ianson et al., 2016), further increasing the anthropogenic carbon signal at 200m.

3.3.4 Past and present Salish Sea aragonite conditions

In the pre-industrial system, the majority of waters by volume are supersaturated with respect to aragonite ($\Omega_{arag} > 1$, Fig. 3.6a,3.6c,3.6e). Undersaturated waters make up 9-25% of the volume of the total domain throughout the year, with a noticeable increase

in the volume of undersaturated water during the summer at depth, due to the seasonal upwelling of comparatively deep, carbon-rich water from the open Pacific (Fig. 3.6a (kms 0-180), 3.6e). The anthropogenic carbon increase has caused a mean decrease in Ω_{arag} of 0.3 units throughout the system. The fractional $<2\%$ increase in DIC domain-wide from the pre-industrial scenario to present-day is sufficient to tip the majority of the domain to an undersaturated state, with undersaturated water making up 54-74% of domain volume throughout the year (Fig. 3.6f).

Regional and seasonal variability in Ω_{arag} conditions is strong throughout the Salish Sea in both the pre-industrial and present-day scenario (example profiles in Fig. 3.7). Temporal variability is represented as shading between the 10th and 90th percentile of values seen throughout the season, and the spread in values reported here represents the typical conditions experienced in each region the majority of the time but excludes extremes (Fig. 3.7). These stations are representative of conditions in their respective regions (Fig. B.15). Clear dynamical differences between the regions exist in both summer and winter. In the summer months, phytoplankton drawdown of DIC leads to higher Ω_{arag} values at the surface in all regions. In the Ocean Exchange region, this comparatively high Ω_{arag} water is visible further down in the watercolumn than in the Freshwater Influenced and Northern Fjord regions, leading to deeper Ω_{arag} saturation horizons (approx. 50 m in the Ocean Exchange region, as compared to 25 m and 40 m in the Freshwater Influenced and Northern Fjord regions, respectively). These deeper Ω_{arag} saturation horizons are a result of the comparatively weak salinity-induced stratification in the Ocean Exchange Region as compared to the Freshwater Influenced and Northern Fjord regions, leading to deeper haloclines (e.g. Masson and Peña (2009)) and therefore drawdown of DIC and increase in Ω_{arag} by phytoplankton deeper in the watercolumn. Simultaneously, the Ocean Exchange region is characterized by the summertime canyon-enhanced upwelling of carbon-rich, corrosive waters (S. E. Allen, 2000), leading to low Ω_{arag} values at depth in the domain (<0.7 in the present-day case).

In contrast, the Freshwater Influenced region shows higher Ω_{arag} at the surface (>2.0 in the present-day case) due to phytoplankton drawdown of DIC, but strong freshwater stratification due to proximity to the Fraser River leads to the isolation of this high Ω_{arag} water near the surface, leading to shallow aragonite saturation horizons. A similar pattern may be seen in the Northern Fjord region, however weaker salinity stratification as copmpared to the Freshwater Influenced region leads to a deeper surface layer (Masson & Peña, 2009; Jarnikova et al., 2021), resulting in the lower Ω_{arag} at the surface and simultaneously deeper Ω_{arag} horizons than in the Freshwater Influenced region (approximately 40 m in the Northern Fjord Region, as compared to 25 m in the Freshwater Influenced region). The Tidal Mixing region acts as an intermediary between the Freshwater Influenced region and the Ocean Exchange regions (Fig. 3.3). The outgoing estuarine surface

water, which is high in Ω_{arag}, is mixed down with incoming open-ocean corrosive waters by high tidal mixing in this region (LeBlond, 1983). As a result of this dilution of supersaturated surface waters, summer aragonite saturation horizons in the Tidal Mixing region are the deepest of the domain.

In the winter, Ω_{arag} concentrations are more uniform with depth throughout the domain, due to lower salinity stratification and the reduction of biological activity in the surface. Modelled winter surface Ω_{arag} is lowest in the Freshwater Influenced region and increases slightly with depth from the surface to the immediate subsurface. This Ω_{arag} pattern is due to the dominant presence of the Fraser River, which has a moderately high DIC:TA ratio of 1.09 in the model. Temporal variability or flow dependence of this ratio could locally affect the modelled surface Ω_{arag} (Moore-Maley et al., 2018). In all other regions, which are less affected by fresh water, present-day Ω_{arag} decreases monotonically with depth, with this decrease more gradual in the Ocean Exchange region than in the Northern Fjord Region, due to the deeper mixing layers in the Ocean Exchange Region (Masson & Peña, 2009). Interestingly, in the Tidal Mixing region, the surface supersaturated water is mixed down to the bottom of the watercolumn, because the incoming water from the Ocean Exchange region has comparatively higher Ω_{arag} in the winter downwelling season and has less of a corrosive influence.

Seasonal distributions of the Ω_{arag} concentrations do not typically overlap between the present-day and pre-industrial scenarios, except near the surface in summer (Fig. 3.7). Summer variability in near-surface biological drawdown is the main driver of the large variability in Ω_{arag} that leads to an overlap in experienced Ω_{arag} conditions. In the Northern Fjord Region, the majority of the overlap in conditions is seen around 10m in depth due to the biological drawdown around the subsurface chlorophyll maximum, while conditions at the very surface are distinct. In contrast, in the Freshwater Influenced region, seasonally-variable freshwater input enhances the observed variability in Ω_{arag} at the surface. Because the variability shown here represents the majority (10th-90th percentile) of conditions experienced, I conclude that in the surface 15-25m, summer Ω_{arag} conditions are outside of normal pre-industrial variability over 50% of the time throughout the system, with some variability by region. Below 25m in the summer and at all depths in the winter, all normal Ω_{arag} conditions are outside those experienced in the pre-industrial scenario. This lack of overlap in Ω_{arag} conditions between the two scenarios has meaningful implications for the local ecosystem - present-day ecological studies cannot be taken as baseline evaluations of this coastal sea, as the system has already undergone fundamental geochemical change.

3.3.5 The Salish Sea in carbonate chemistry space

I next consider the variability of both Ω_{arag} (Fig. 3.8a) and the buffering capacity of seawater with respect to Ω_{arag}, expressed by the buffer factor $|\omega_{DIC}|$ (Fig. 3.8b; Egleston et al. (2010)), across the DIC and TA space occupied by my model experiment (Fig. 3.8c). The buffer factor $|\omega_{DIC}|$ is defined as:

$$|\omega_{DIC}| = \left| \left(\frac{\partial \ln \Omega}{\partial DIC} \right)^{-1} \right|$$

My calculations are made at approximately the mean annual temperature and salinity of the present-day Salish Sea (10 °C and 30 g kg^{-1} respectively); though the values of Ω_{arag} and $|\omega_{DIC}|$ change slightly with temperature and salinity, the general structure shown here persists at any temperature and salinity (Fig. B.16). The buffer factor $|\omega_{DIC}|$ reaches a minimum where the concentration of DIC is approximately equal to the concentration of TA (Fig. 3.8a). The Ω_{arag} = 1 threshold is crossed at values of TA typically close to, but slightly higher than, DIC (Fig. 3.8b). Isolines of ln(Ω_{arag}) are overlaid on panels Fig. 3.8b and 3.8c, with the highest density of ln(Ω_{arag}) corresponding to the highest fractional change in Ω_{arag} (i.e. $\Delta(\Omega_{arag})/\Omega_{arag}$). This heightened fractional change in Ω_{arag} by definition occurs where $|\omega_{DIC}|$ reaches a minimum. Heuristically, at a given temperature and salinity, the lower the value of [TA-DIC], the lower the $|\omega_{DIC}|$ and Ω_{arag}, and the critical Ω_{arag} = 1 threshold occurs near the minimum buffering capacity.

Both the pre-industrial and the present-day distribution occupy the poorly-buffered, low Ω_{arag} portion of the TA vs. DIC space, and the center of the distribution shifts to below the Ω_{arag} = 1 line from the pre-industrial to the present-day case (Fig. 3.8c); Two-dimensional histograms of model output corresponding to the summary ellipses are available in Fig. B.17). The subtle variability in Ω_{arag} shifts, as a response to the DIC increase, must be considered in the context of the carbonate chemistry space. Typically, absolute changes in Ω_{arag} from pre-industrial to present-day are slightly larger in the summer than in the winter (Fig. 3.7). Simultaneously, because absolute Ω_{arag} values are higher in the summer, when TA is high compared to DIC due to biological drawdown of DIC by phytoplankton, the corresponding fractional change in Ω_{arag} is lower (corresponding to a higher $|\omega_{DIC}|$).

This subtle difference between changes in Ω_{arag} and changes in fractional Ω_{arag} is also visible in the vertical structure of the Ω_{arag} profiles. For example, in the deep, low-Ω_{arag} Ocean Exchange Region, the absolute change Ω_{arag} is small during the summer upwelling period that introduces carbon-enriched waters here, but the fractional change is large. Further increases in DIC in the future, which will shift the present-day distribution

further to the right (Fig. 3.8c), will occur in the highly sensitive region of carbonate chemistry space, and will correspond to comparatively large fractional Ω_{arag} changes at low absolute Ω_{arag} values, as shown by the isolines.

This high sensitivity of the Salish Sea waters is also reflected in the Revelle factor, a measure of the sensitivity of a system's pCO_2 to changes in DIC (higher values of the Revelle factor correspond to higher changes in pCO_2 for a given change in DIC, Broecker, Takahashi, Simpson, and Peng (1979)). North Pacific waters are typically less well buffered than lower latitude waters (Feely et al., 2010). The mean surface Revelle factor of the Salish Sea is 12.1 in summer and 17.2 in winter but exhibits a considerable range (Fig. B.18). These values represent an increase of $\sim$1.2-1.7 units from pre-industrial values (which are on average 10.9 in summer and 15.5 in winter), similar to the Revelle factor increases (0.5-1.6) reported by Feely et al. (2010) in an observational campaign in the Ocean Exchange Region and Puget Sound (Fig. 3.1) and showing further evidence of the weaker buffering in the present-day system. Another modelling study (Cai et al., 2021), focused on the Puget Sound region of the Salish Sea, estimates present-day surface Revelle factors of 16-17 (annual average). This estimate is commensurate with both of the above estimates and suggests a slight increase in Revelle factor ($\sim$0.5-0.6) by 2050 if atmospheric CO_2 levels increase according a high-emissions scenario.

3.3.6 Global coastal aragonite saturation state conditions

I next visualize the available GLODAP coastal measurements on a map (Fig. 3.9a) and plot them in the TA vs. DIC space explored in Fig. 3.8 (Fig. 3.9b). I use the criterion of [TA-DIC]$<$ 50 mmol m^{-3}, a simple proxy for low Ω_{arag} conditions (Xue & Cai, 2020), to highlight low-Ω_{arag}, poorly buffered waters on the map. Selected data are from the upper 200 m at locations shallower than 500 m, with salinity $>$ 20 psu and thus do not include waters strongly affected by freshwater input. A striking geographical pattern emerges. The points satisfying the threshold criterion are abundant, but located almost exclusively in the North Pacific and Pacific Arctic sectors of the ocean (Fig. 3.9a), while Atlantic waters typically have the highest [TA-DIC] (Fig. 3.9b, Fig B19). The area of TA vs. DIC space occupied by my model (black and grey ellipses) overlaps considerably with the available Siberian Arctic and Coastal Pacific measurements (which include measurements from the Salish Sea), which also lie in the low $|\omega_{DIC}|$ region, near Ω_{arag} = 1. The waters of the Canadian Arctic, Russian/Alaskan interface and Kamchatka Region also exhibit a significant number of points in the poorly-buffered, low Ω_{arag} region of the carbonate chemistry space plot (Fig. 3.9b, Fig B19). I thus argue that the insights regarding carbonate chemistry, specifically the rapid shift in aragonite saturation state shown in all representative zones of my modelling experiment, are likely broadly applicable to

many coastal regions in the Pacific Rim sector. Most of this coast does not benefit from the availability of realistic high-resolution models or, in many cases, even minimal observations. In contrast, the comparatively well-sampled North Atlantic shows a tendency to high [TA-DIC] and almost no undersaturated observations at present, consistent with in-situ observations (S. Siedlecki et al., 2021). However, conditions under $\Omega_{arag} = 1.5$ may be widespread in parts of the North Atlantic by 2050 under RCP 8.5 (S. Siedlecki et al., 2021).

Future emergence of poorly buffered conditions in global coastal systems

While future Ω_{arag} conditions are hard to estimate directly, it is possible to estimate future DIC uptake based on existing observations and then use the [TA-DIC]$<$ 50 mmol m^{-3} threshold as a general proxy for poorly buffered, low Ω_{arag} conditions (Section 2.4.1). I use this proxy to provide a rough estimate in near-coast regions that are data-poor and not resolved by global climate models.

Using the historical atmospheric CO_2 record and projections of future CO_2 concentrations, I approximate the timing of the shift to [TA-DIC]$<$ 50 mmol m^{-3} conditions in available coastal observations by tracking the DIC increase in time (Fig. B.20). A portion of the Pacific Sector (Siberian Arctic, Coastal Pacific, and Russian/Alaskan) observations likely had the [TA-DIC]$<$ 50 mmol m^{-3} signal present in pre-industrial conditions, and the signal became more prominent in these waters throughout the 20th century. Looking to the future, in the latter half of the century this signal will likely emerge in the majority of waters in all coastal regions, including the regions with younger waters and less remineralized DIC (Fig. B.20). For coastal waters, I estimate that 97% of Southern Ocean observations, 50% of North Atlantic observations, and 60% of the global dataset cross the [TA-DIC]$<$ 50 mmol m^{-3} threshold by 2080 (Fig. B.20).

3.4 Conclusions

My work uses a submesoscale-resolving biogeochemical model to determine the impact of anthropogenic carbon on a heterogeneous North Pacific coastal system. The structure of Ω_{arag} conditions varies significantly throughout the Salish Sea and between seasons, emphasising the need for accurate models in variable coastal regions. I find that, since pre-industrial times, the DIC concentration of the Salish Sea coastal system has increased by approximately 34 mmol m^{-3}, with regional variations. I find that the increase was sufficient to tip the system from a regime where it rarely experienced undersaturation even in the deepest zones of the domain to one where the majority of the waters are undersaturated with respect to aragonite throughout all seasons. Furthermore, at most locations in the Salish Sea, excepting the variable and high-Ω_{arag} surface regions, the observed

shift in saturation state is larger than the variability in Ω_{arag} conditions experienced over the course of a season. This threshold-crossing suggests that the system has already undergone fundamental geochemical change, which may have major implications for ecosystem structure and function.

In contrast, net air-sea CO_2 flux in this complex coastal system has experienced little change through time. Summer uptake of atmospheric CO_2 is large, but balanced by winter outgassing, making the region a weak CO_2 source. In the pre-industrial system, summer uptake of atmospheric CO_2 was somewhat lower, slightly increasing the net CO_2 source strength in comparison to present day.

Spatiotemporal variability in these air-sea flux dynamics is exceptionally strong, highlighting the need for high-resolution modelling to evaluate the role of coastal zones in the global carbon balance. Present-day distributions of aragonite saturation state conditions and buffering capacity appear to be similar, and generally low, in this complex Pacific study region and in the rest of the Pacific Rim. I suggest that, like the Salish Sea, the majority of the Pacific Rim has already undergone significant shifts in carbonate chemistry.

3.5 Figures

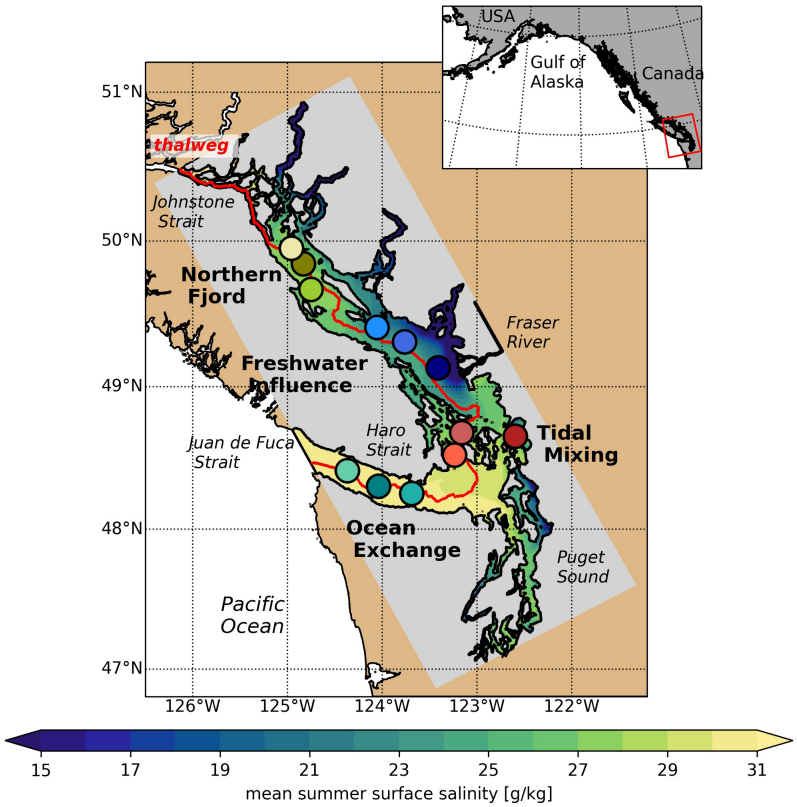

Figure 3.1: The model domain showing present-day mean summer surface salinity with the thalweg (contour of lowest elevation) indicated in red. Three colour-coded representative stations are indicated in each dynamical region: Teals - Ocean Exchange Region, Reds - Tidal Mixing Region, Blues: Freshwater Influenced Region, Greens - Northern Fjord Region.

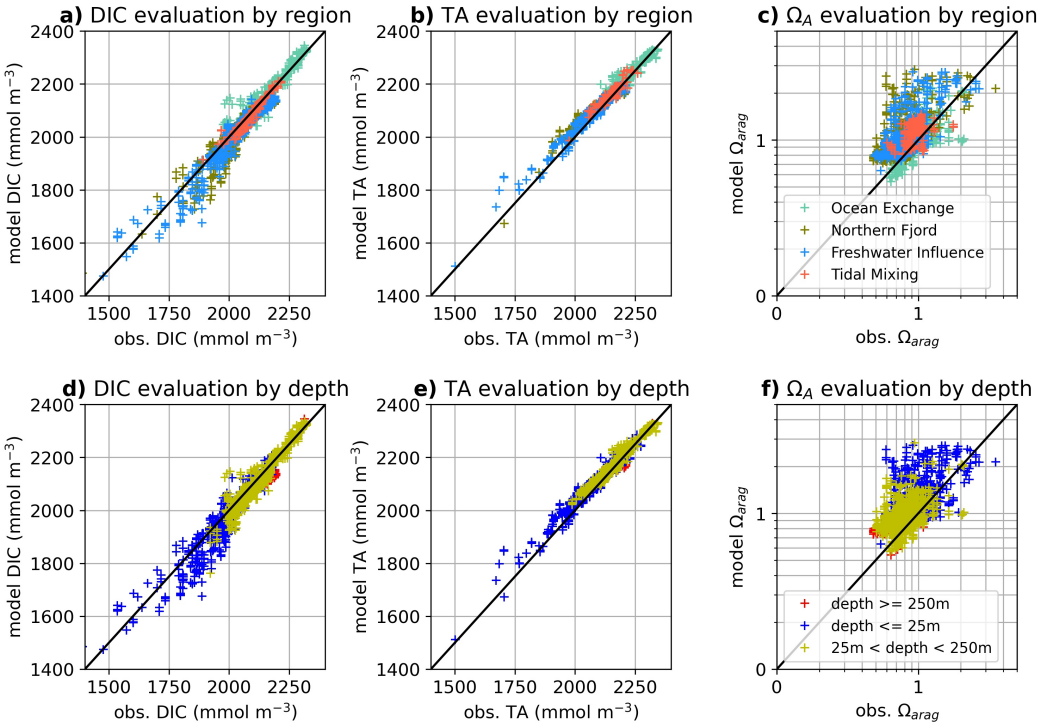

Figure 3.2: Scatterplots of modelled vs. observed DIC, TA, and Ω_{arag}. Model output for years 2013-2017 is shown vs. the observational dataset described in Appendix B. The top row of plots shows observations colour-coded by model region (Fig. 3.1), and the bottom row shows observations colour-coded by observational depth. The majority of the scatter is in the shallowest observations (depth <25m) and can be attributed in part to the year mismatch. Observations are matched to corresponding model salinity at a given location and yearday. A range of corresponding model evaluation metrics is given in Table B.1.

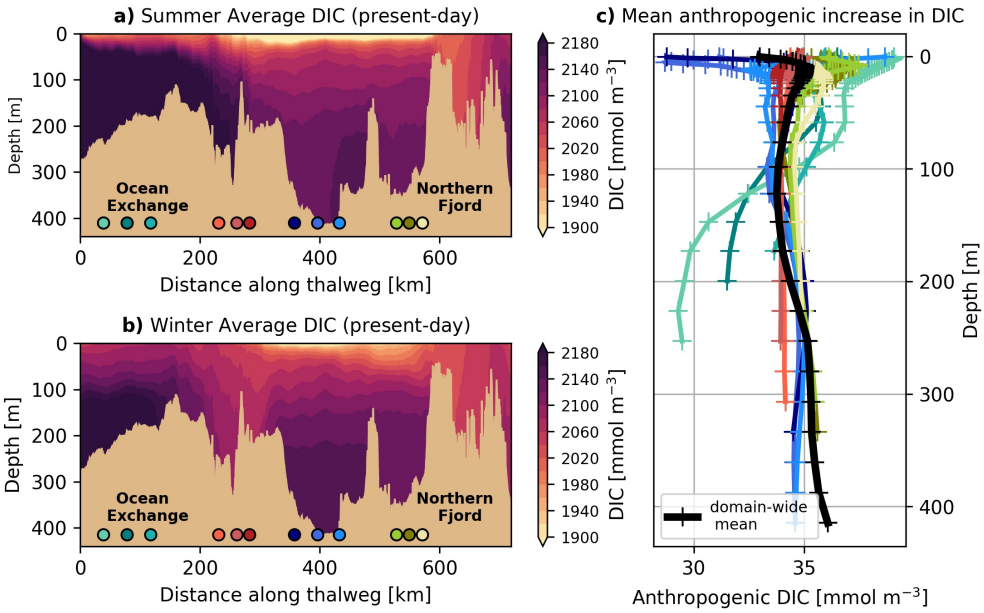

Figure 3.3: Along-thalweg transects of average summer (a) and winter (b) average DIC for the present-day run. Panel (c) shows depth profiles of anthropogenic DIC (calculated by subtracting the PI run from the present-day run and averaging by layer) with the domain mean shown in black with colored lines corresponding to locations in Fig. 3.1. Profiles are colour-coded by region: Teals - Ocean Exchange Region, Reds - Tidal Mixing Region, Blues: Freshwater Influenced Region, Greens: Northern Fjord Region.

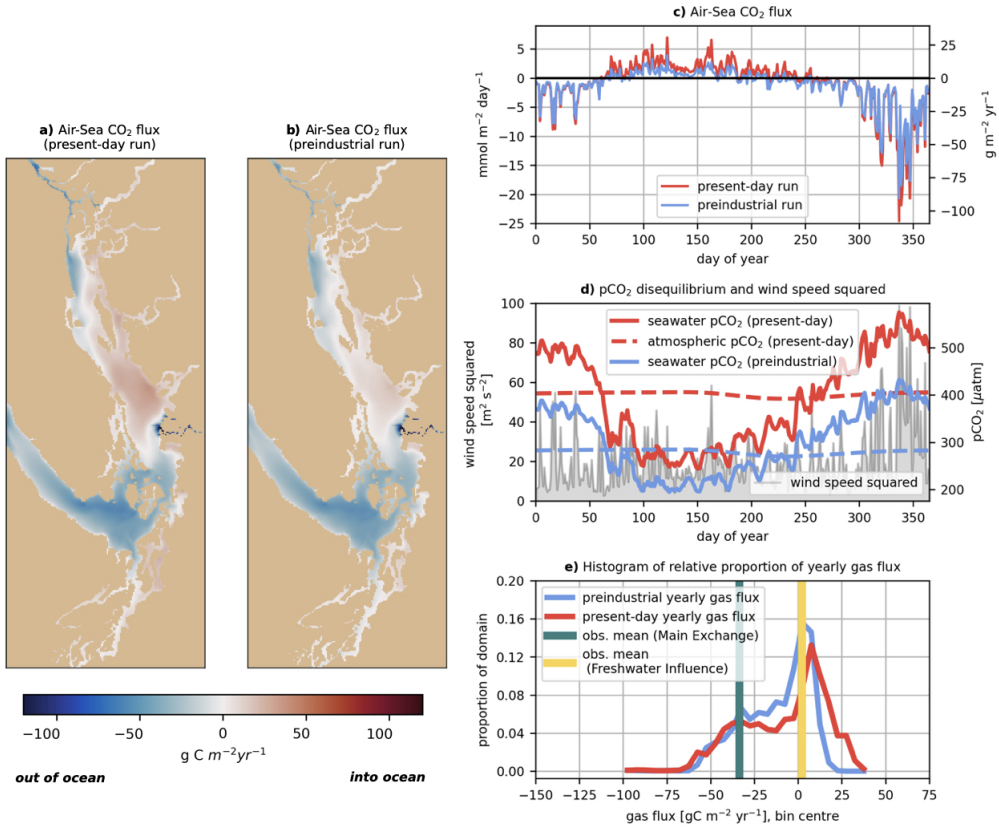

Figure 3.4: Net annual air-sea flux for the present-day (a) and PI (b) runs. (c) Domain-averaged air-sea flux, showing that the system is a net atmospheric CO_2 sink in summer and source in winter. (d) Domain-averaged seawater pCO_2 and square of domain-averaged, over-water windspeed. Present-day summer and winter disequilibria are of approximately equal magnitudes ($\sim$-95μatm and $\sim$+95μatm respectively), but stronger winter winds drive a net outgassing signal. In the pre-industrial system, the summer air-sea disequilibrium is weaker ($\sim$-35μatm), leading to stronger net annual outgassing. (e) Histograms of yearly air-sea flux seen in panels (a) and (b), with local observation-based annual mean fluxes indicated by vertical lines (Evans et al., 2012). Longer and thicker tails (present-day) indicate greater magnitude and frequency of extreme ingassing and outgassing events. See Fig. B14 for analysis of 5 years of contemporary hindcast.

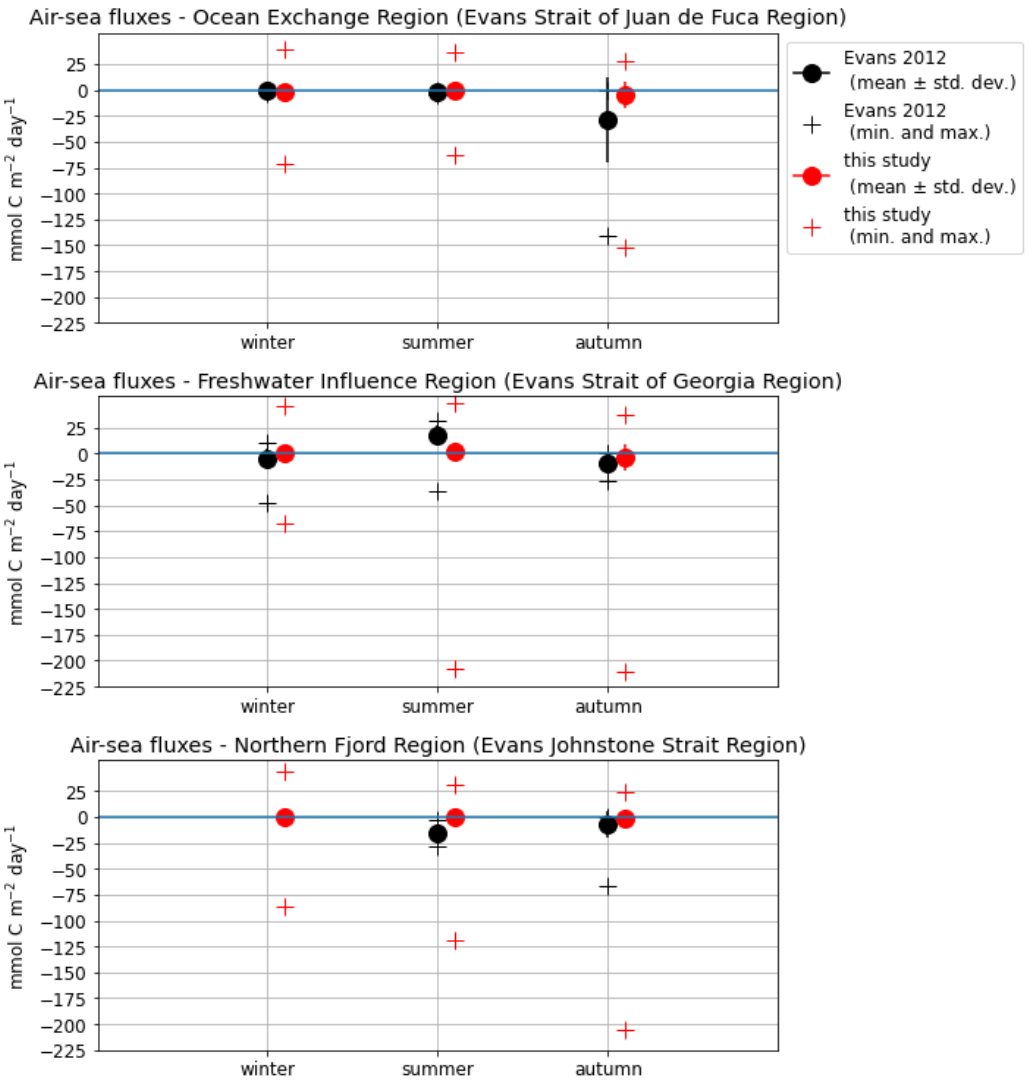

Figure 3.5: A comparison of some statistics of air-sea CO_2 between the present-day model output (year 2015) and a three-season observational campaign (Evans et al. (2012)) (years 2008-2010). The range of reported in-situ values always falls within the range of modelled values, and means of the two datasets are typically comparable. Seasonal definitions from Evans et al. (2012) are as follows: winter is January 1 to March 31, spring is April 1 to June 30, summer is July 1 to September 30, and autumn is October 1 to December 31.

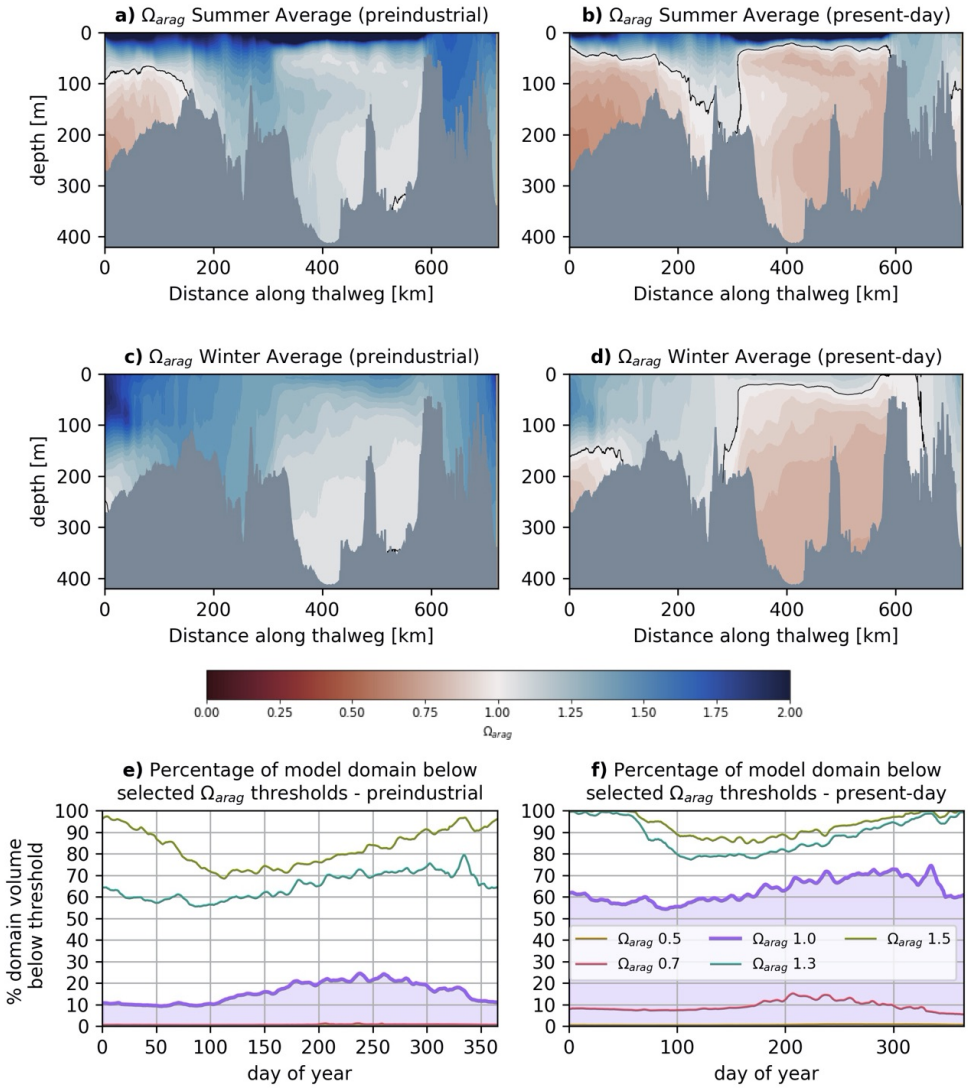

Figure 3.6: (a-d) Along-thalweg (Fig. 3.1) transects of summer and winter, PI and present-day aragonite saturation state (Ω_{arag}). Corrosive waters (red) enter the domain through the Ocean Exchange Region during the summer upwelling season (panels a and b, kms 0-100). Biological carbon drawdown drives high surface Ω_{arag} in summer (panels a and b), and winter mixing lowers near-surface Ω_{arag} (panels c and d). Increased DIC has shifted present-day subsurface Ω_{arag} to corrosive values. (e-f) Proportion of model domain that is below various pre-industrial (e) and present-day (f) aragonite saturation horizons. At the Ω_{arag} = 1.0 (purple colour) threshold, a modest seasonal cycle is associated with open-water summer upwelling of corrosive waters.

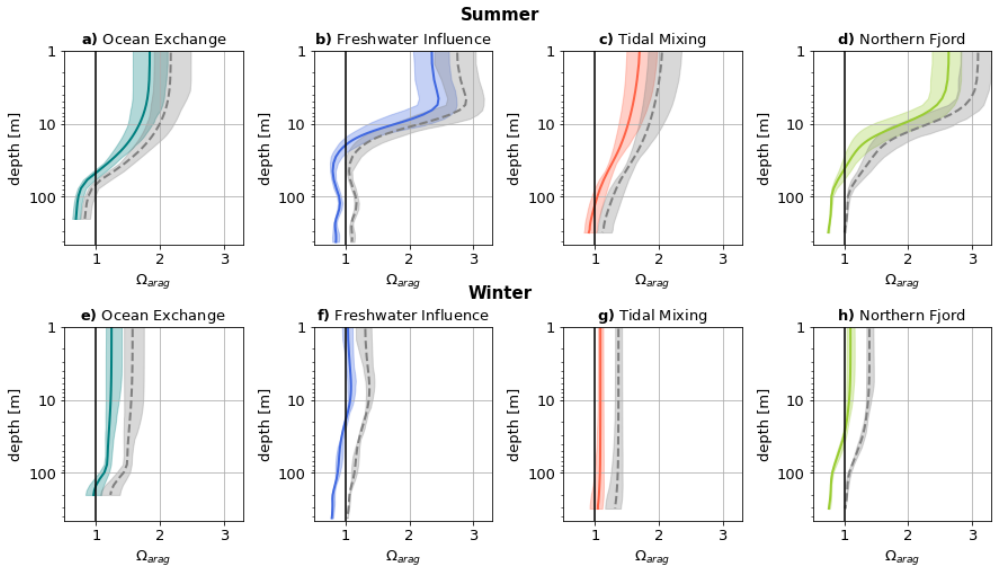

Figure 3.7: Depth profiles of Ω_{arag} for the present-day (coloured) and pre-industrial (gray) model runs for one station in each of the dynamical regions of the domain. To show seasonal temporal variability, the area between the 10th and 90th percentile of seasonal values, calculated from daily averages is shaded. A log-scale is used for depth, as most temporal variability occurs near the surface. Here the summer season is June 1 - Aug. 31, while the winter season is Dec. 1 - Feb. 28. Colours of the present-day depth profiles correspond to the stations in Fig. 3.1. (See Fig. B.15 for the mean depth profiles for all stations in Fig. 3.1, which are similar within each region.)

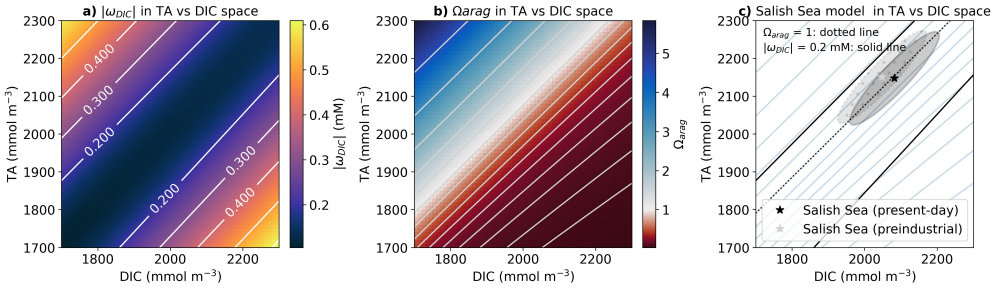

Figure 3.8: The buffer factor $|\omega_{DIC}|$ (panel a) and Ω_{arag} (panel b) as functions of DIC and TA, at a salinity of 30 psu and a temperature of 10 °C. Contours at Ω_{arag} = 1 and $|\omega_{DIC}|$ = 0.2 mM, are included to guide the viewer. $|\omega_{DIC}|$ reaches a minimum where the concentration of DIC is approximately equal to the concentration of TA (panel a). The Ω_{arag} = 1 threshold is crossed at values of TA typically close to, but slightly higher than, DIC (panel b). Ellipses summarising the pre-industrial (light grey stippled) and present-day (dark grey) model-derived Salish Sea distribution in TA vs. DIC space are shown in panel c. The ellipses are centered (stars) on the means of DIC and TA of each regional distribution and show the standard deviation of [TA+DIC] (major axis) and [TA-DIC] (minor axis). $|\omega_{DIC}|$ and Ω_{arag} vary only slightly with temperature and salinity, and the general structure shown here holds for all typically observed seawater temperatures and salinities (see Fig. B.16).

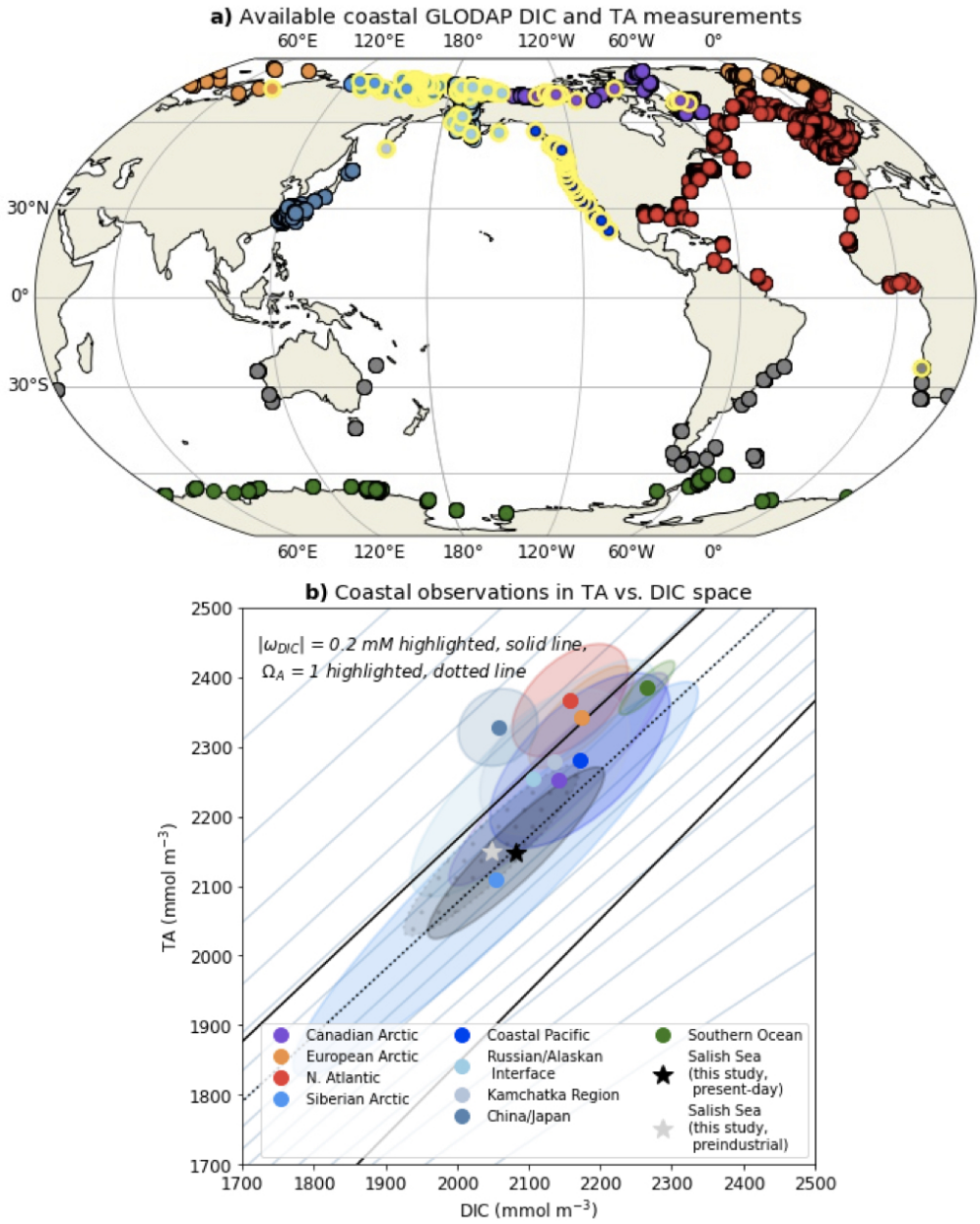

Figure 3.9: Locations of GLODAPv2.2020 carbonate chemistry observations, colored by region (panel a). Selected data are from the upper 200 m at locations shallower than 500 m, with salinity $>$ 20 psu. Yellow outlines indicate [TA-DIC] $<$50 mmol m^{-3}. (b) Ellipses approximating the location of available coastal observations, centered on the means of DIC and TA of each regional distribution and showing the standard deviation of [TA+DIC] (major axis) and [TA-DIC] (minor axis). The actual data cannot be easily visualized on a single plot and are presented, subdivided by region, in Fig. B.19. Ellipses summarizing the pre-industrial (centered on grey star) and present-day (centered on black star) model-derived Salish Sea distribution are overlaid.

Table 3.1: Anthropogenic DIC estimates from this modelling study compared to previous observational studies in the region. Estimates derived from this study are yearly averages, and except for 'domain-wide mean' are averages of approximately 10 km square subregions of the domain. Anthropogenic estimates for both Hare et al. (2020) and Evans et al. (2019) represent yearly averages at discrete locations; the Evans et al. (2019) estimate is from a continuous pCO_2-collection mooring while the Hare et al. (2020) estimate is from bottle samples.

Reference	Location	Estimate
this study	domain-wide mean, all depths	34 mmol m^{-3} ($\sim$33 μmol kg^{-1})
this study	Puget Sound Region (surface waters)	33-35 mmol m^{-3} ($\sim$32-34 μmol kg^{-1})
this study	Tidal Mixing Region (surface waters)	34-35 mmol m^{-3} ($\sim$33-34 μmol kg^{-1})
this study	Northern Fjord Region (surface waters)	35-38 mmol m^{-3} ($\sim$34-37 μmol kg^{-1})
Evans et al. 2019	Northern Salish Sea surface waters (Northern Fjord Region of this study)	49$\pm$5 μmol kg^{-1} (year 2018)
Evans et al. 2019	Northern Salish Sea surface waters (Northern Fjord Region of this study)	41$\pm$4 μmol kg^{-1} (year 2008)
Feely et al. 2010	Puget Sound (surface waters)	13-36 μmol kg^{-1}
Feely et al. 2016	Washington State outer shelf (surface waters)	47-55 μmol kg^{-1}
Feely et al. 2016	Washington State outer shelf (200m depth)	30-33 μmol kg^{-1}
Hare et al. 2020	Bute Inlet (surface waters)	44-50 μmol kg^{-1}
Hare et al. 2020	Bute Inlet (deep waters)	30-34 μmol kg^{-1}
Murray et al. 2015	Friday Harbor surface waters (Tidal Mixing Region of this study)	36 μmol kg^{-1}
Carter et al. 2019	Open Pacific 50°N (surface waters)	55 μmol kg^{-1}

Chapter 4

Controls on the present-day carbonate chemistry balance of the Salish Sea and sensitivity to changes in future drivers

4.1 Introduction

In Chapter 2, I used a simple machine learning approach to identify the typical biophysical clusters of the Salish Sea and describe their dominant physical-oceanographic and primary productivity features. In Chapter 3, I introduced and evaluated the carbonate chemistry model used to study the carbonate chemistry balance of the Salish Sea. I presented some snapshots of seasonally and spatially varying DIC, the surface air-sea flux balance, and Ω_{arag} conditions, and discussed some drivers of these distributions. I then considered the effect of the anthropogenic carbon increase from the pre-industrial to the present-day period on Ω_{arag}. In this chapter, I extend and build on the analysis of the carbonate chemistry balance of the Salish Sea from Chapter 3, utilizing the biophysical clustering of the system from Chapter 2. I focus this extended analysis on the following research questions:

- 1. What are the dominant fluxes in the Salish Sea carbonate chemistry balance, and what is their relative magnitude and spatial and temporal structure?
- 2. How variable is the aragonite saturation state of the different regions of the Salish Sea from year to year?
- 3. How may the Salish Sea carbonate chemistry balance respond to a) likely future

increase in anthropogenic CO_2 or b) potential future change in the hydrological cycle of dominant rivers?

To address the first question, I construct a quantitative budget and identify the relative contributions of all sources and sinks to the carbonate chemistry balance, as well as outlining the geographic and seasonal structure of selected fluxes: transport through the largest lateral boundary (Juan de Fuca Strait), uptake of DIC by phytoplankton, remineralization of marine organic matter, and air-sea gas exchange. This identification and characterization of the dominant fluxes in the system is critical both to understanding the variability of the present-day system and to predicting future changes to the system's carbonate chemistry budget (e.g. Hauri et al. (2020); S. A. Siedlecki et al. (2021)).

To address the second question, I report key statistics of aragonite saturation state (mean, standard deviation, and extremes) at several biologically-relevant depths in the three largest biophysical provinces found in Chapter 2, across five modelled years. I provide a comparison of interseasonal variability and variability between regions with interannual variability, as well as regional extreme values for each season and year. Understanding the typical variability over the course of a growing season in a region, as well as the range covered by the extremes, is key to local stakeholders, for example shellfish farmers (Waldbusser et al., 2015). My well-performing, submesoscale-resolution carbonate chemistry model is well-equipped to provide such estimates, and provides a detailed summary of regional conditions that are not captured by episodic sampling programs.

Finally, to address the third question, I take a first look at the response of the Salish Sea carbonate chemistry balance to two experimental scenarios of potential environmental change, including an anthropogenic carbon dioxide increase and a shifting hydrological cycle. Understanding the effects of future climate change to this already-sensitive region is critical to predicting the viability of natural ecosystems that exist in it, and hence to evaluating risk and planning adaptation scenarios (e.g. Mathis et al. (2015); Ekstrom et al. (2015)). Using the detailed methodology developed in Chapter 3, I consider the anthropogenic increase in the Salish Sea in response to a middle-of-the-road atmospheric carbon increase in the near future – year 2050 (Meinshausen et al., 2020). I intentionally choose a carbon scenario that represents a lower bound of the carbon increase in the near future to establish a conservative lower bound on its likely ecosystem effects. My choice of hydrological scenario is more experimental and follows the example of another study in the same region that shifts local rivers forward 60 days (S. A. Siedlecki et al., 2021). To date, a more subtle forward shift in the Fraser hydrograph has been observed: the mean date by which one-third of the total yearly discharge has occurred has moved forward at a rate of 11 days per century (Foreman et al., 2001). However, because I expect the effect of the changing river hydrographs on the carbon balance to be comparatively minor, I shift the hydrographs of nival and nival-glacial rivers forward 45 days to

examine potential extreme effects, focusing on selected nearshore regions. I also do not consider here the expected flattening of the hydrograph, i.e., the reduction in maximum flow in nival-glacial watersheds as winter snowfall decreases, or the expected increase in winter discharge as more precipitation falls as rain (e.g. (Shrestha, Schnorbus, Werner, & Berland, 2012)).

4.2 Methods

4.2.1 Model run description and evaluation

I analyse 5 years of the SalishSeaCast hindcast (years 2013-2017, version 201905) to ensure that both seasonal signals in the carbon balance and their interannual variability are captured. For the computationally-intensive budget-quantification run and sensitivity scenarios, I analyze year 2017, which I rerun with a real-time quantification of all carbon fluxes. The SalishSeaCast model used in this analysis is introduced and described in the Methods section of Chapter 3, and the biological and carbonate chemistry modules remain unchanged. The biological module has changed since publication in Olson et al. (2020), with the most major changes to the biological model since implementation concerning the silicon cycle. These changes are summarized in Appendix A2.

The carbonate chemistry model evaluation for years 2013-2017 is presented in Chapter 3 (Fig. 3.2, Table B.1) and only very briefly summarized here. The model typically slightly underestimates DIC (bias -11 – -19 mmol m^{-3}, compared to a mean value of 2050 mmol m^{-3}) and overestimates TA (bias 10-13 mmol m^{-3}, compared to a mean value of 2120 mmol m^{-3}). This combination of opposing biases leads to a slight positive bias in Ω_{arag} (0.17-0.23). The bias in the calculated Ω_{arag} is typically less than the error in Ω_{arag} (0.05-0.24) associated with measurement uncertainty (of observed DIC and TA) calculated using the error propagation routine of Orr et al. (2018). Details of the model evaluation dataset and air-sea flux evaluation are given in Appendix B.

4.2.2 Two concepts for establishing a model budget

I determine the evolution of the inorganic carbon content of the Salish Sea over the course of one modelled year. I approach this problem by quantifying the main sources and sinks of inorganic carbon in the system: lateral boundary fluxes at two boundaries, riverine input, phytoplankton uptake, remineralization, and air-sea flux. This budget analysis is simultaneously considered through two perspectives, which I call the **Absolute DIC budget** and the **ΔDIC budget** respectively. These two budgets provide complementary views of the system. I describe both budgets briefly below.

In the Absolute DIC budget, fluxes are considered in terms of the absolute movement

of matter into and out of the system. For example, in this view the flux of 1 m^{-3} of seawater from the deep Juan de Fuca Strait, containing 2240 mmol m^{-3} is counted as a flux of 2240 mmol of DIC into the system; the flux of 1 m^{-3} of fresh water from the Fraser river, containing 820 mmol m^{-3}, is counted as a flux of 820 mmol of DIC into the system. In the ΔDIC budget, the fluxes of carbon into the system are considered in terms of how much they concentrate or dilute the DIC content of the system's waters with respect to the system's mean value (approximately 2050 mmol m^{-3}). In this view, in the above example, the influx of Juan de Fuca water contributes a net 190 mmol of DIC, while the riverine input actually dilutes the DIC concentration, contributing net -1230 mmol of DIC. The ΔDIC budget view was developed to avoid overemphasising the effect of the movement of water through the lateral boundaries on the overall budet, because this water sometimes has a DIC signature quite similar to that of the interior Salish Sea.

4.2.3 Biophysical provinces

To consider regional tendencies in biophysical controls on the coastal carbonate chemistry balance, I analyse these features in the context of the three main biophysical provinces determined in Chapter 2: the Central Strait of Georgia, the Northern Strait of Georgia, and Juan de Fuca Strait. These provinces were discussed in depth in Chapter 2 from a biophysical perspective, but I provide a short summary here.

The Central Strait of Georgia is subject to significant stratification from the Fraser River, which leads to the shallowest, most stable haloclines of the three regions. This environment results in strong initial diatom blooms during the spring bloom period and a transition to flagellate abundance in the second half of the productive season as nutrient limitation of phytoplankton growth becomes a controlling influence. The Northern Strait of Georgia, which is further away from the dominant river in the system (the Fraser) but receives significant freshwater input from the rivers at the head of the nearby Toba, Bute, and Jervis Inlets (Fig 2.1, Fig 4.3). Therefore this region still experiences freshwater stratification but has less shallow and less stable haloclines and is more likely to experience nutrient injection from the subsurface waters. As a result, episodic diatom blooms are observed in the Northern Strait of Georgia even in the latter part of the productive season (Fig 2.4, 2.8, section 2.5.1). Juan de Fuca Strait is the least influenced by freshwater and is more affected by tidal mixing than either the Northern Strait or the Central Strait. This low-freshwater, tidally-mixed regime results in deep, variable haloclines with little nutrient limitation (Fig. 2.4). Consequently phytoplankton blooms occur later in Juan de Fuca Strait than in either the Central or Northern Strait, with their biomass following a light-limitation curve (Fig 2.8, section 2.5.2). In the studied years (2013-2016) the three regions were found to have similar biomass overall, but the relative abundance of different functional groups (diatoms vs. flagellates) and vertical structure of phytoplankton

biomass differed from region to region, with the phytoplankton persisting deeper in Juan de Fuca Strait than in the Central and Northern Strait.

Together, these provinces cover approximately 65% of the model domain by volume, so while the main biophysical influences on the carbonate chemistry balance are captured by this view, several interesting localized microregions of the Salish Sea are not covered in this study. Notably missing are the fjordal inlets of the British Columbia mainland (Toba, Bute, and Jervis Inlets, and Howe Sound). I also do not include the Tidal Mixing region (Cluster 1 in Chapter 2), as the exact boundary of this region is difficult to establish and varies somewhat interannually. The near-shore regions and the Puget Sound are also not considered – in most years, the majority of the Puget Sound exhibits similar phytoplankton biomass dynamics as the Central Strait of Georgia. (Fig. 2.8).

4.2.4 Sensitivity scenarios

In the last section, I take a first look at the response of the system to two likely types of environmental change: increased anthropogenic carbon and a shifting hydrological cycle. In both scenarios, as in the study in Chapter 3, all other forcings in the system (e.g. ocean physics, temperature conditions, the atmospheric model, the biological model, and the riverine carbon and nutrient inputs) are kept at existing present-day levels, year 2017. Therefore, these runs represent sensitivity scenarios, as opposed to realistic projections of a future state. As in Chapter 3, both scenarios were spun up until the differences of total and layer inventories of DIC, TA, nitrogen, and salinity in the domain between the last spinup year and the analyzed year were considered negligible ($< 0.1\%$ of layer-averaged concentration). I next describe the scenarios.

The Carbon 2050 (CAR50) scenario

To consider the effect of the future anthropogenic carbon increase on the carbon balance of the Salish Sea, I run a sensitivity scenario with future atmospheric CO_2 and lateral boundary DIC conditions at year 2050, following a middle-of-the road carbon emissions scenario, SSP 2-4.5 (Meinshausen et al., 2020). Under this scenario, atmospheric CO_2 concentrations in the northern hemisphere are estimated to be approximately 509 μatm by year 2050 (Fig. 4.2). As societal decarbonization efforts are currently progressing only slowly, the middle-of-the road scenario was chosen as a potential lower bound on carbon emissions to year 2050. It is worth noting that the large divergence between scenarios doesn't occur until the latter half of the 21st century; in 2050, the difference between the most carbon-emission intensive scenario and the least intensive one is only about 130 μatm, while by 2100, this difference is about 750 μatm (Fig. 4.2).

According to this scenario, the atmospheric boundary condition was set at 509 μatm,

with the same seasonal cycle as derived in Chapter 3. Juan de Fuca lateral boundary conditions were also set using the same method as in Chapter 3. For waters heavier than σ_θ =25.0, the C* method was used to calculate a DIC increase (Gruber et al., 1996) for each watermass based on its assumed age from a cfc-11 relationship (Fig. B.8). For surface waters, which are exposed to current atmospheric CO_2 concentrations, the ΔTCO_2 method was used to calculate an increase (Matsumoto & Gruber, 2005; Simpson, Ianson, & Kohfeld, 2022). To avoid discontinuities in the carbon field, for every depth profile I then linearly interpolated from the ΔTCO_2 derived surface value to the C*-derived value at σ_θ =25.0. The increase derived this way ranges from 8.6 – 34.1 mmol m^{-3}, with the mean increase at 100 m depth approximately 26.0 mmol m^{-3} (Fig. C.1, C.2).

At the Johnstone Strait Boundary, all water is light relative to Juan de Fuca boundary (maximum σ_θ = 24.7) and is likely to have been ventilated recently (Appendix B.1.6). I thus use the ΔTCO_2 method to calculate the surface increase and then, as in Chapter 3, create a linear regression of DIC increase vs. salinity to account for the mixing in of older waters from the open ocean with lower increase values. The two end members are derived from the mean monthly surface salinities of Johnstone Strait and the open-ocean Juan de Fuca water at (σ_θ=26.0). The estimated additional anthropogenic increase between 2017 and 2050 obtained this way ranges from 29-31 mmol m^{-3} (Fig. C.3).

The shifted hydrograph (RIVSHIFT) scenario

The Salish Sea model is forced with over 150 rivers, split into eight major watersheds (Fig. 4.3). The Fraser River runoff is taken from the Environment and Climate Change Canada flow gauge at Hope, BC, and the remaining rivers, as well as the Fraser River downstream of Hope, are forced by a monthly climatology specific to each watershed (Morrison et al., 2012). The Fraser river discharge accounts for about 44% of the total freshwater input into the Salish Sea (measured at Hope and not accounting for additional inputs between Hope and the river mouth).

In the coming century, the freshets of nival rivers are expected to move earlier in the year due to the increase of rain and decrease in snowpack (Morrison, Quick, & Foreman, 2002; Riche et al., 2014). To explore the effects of this hydrograph shift on the Salish Sea inorganic carbon cycling, especially in the nearshore regions, I designed a sensitivity scenario that shifts the freshet of the major nival-glacial watersheds (Fraser, Howe, Toba, Bute, and Skagit) forward by 45 days (Fig. 4.3, dotted lines). Though most downscaled runoff projections for the Fraser river include a forward shift in the freshet, there is considerable uncertainty in how future hydrographs will be affected by climate change (Pacific Climate Impacts Consortium, 2020), and this sensitivity study is designed as a simple first exploration. A similar approach was taken in a regional modelling study of

the coastal North Pacific by Siedlecki et al. (2021), who moved the freshets forward by 2 months (60 days). In my analysis, I focus on the effects of this shift on the near-shore, freshwater-dominated regions near three rivers: the Fraser, the Squamish at the head of Howe Sound, and the Homathko at the head of Bute Inlet (Fig. 4.3, stars). For each river, I report sea surface carbonate chemistry properties in a radius of 5 km from the rivermouth for both the base scenario and the RIVSHIFT scenario, and discuss some implications of these changes.

4.3 Results and Discussion

4.3.1 The inorganic carbon content of the Salish Sea

As a first step to understanding the dynamic carbon budget of the Salish Sea, I quantify the yearly evolution of the system's inorganic carbon pool. Organic carbon forms, including particulate and dissolved organic carbon and organismal carbon, are not included in this view (Fig. B1). Strait of Georgia measured dissolved organic concentrations are much lower than dissolved inorganic carbon concentrations, ranging from $\sim 30-100 \mu$mol L^{-1} (Johannessen, Masson, & Macdonald, 2014).

The mean inorganic carbon content of the Salish Sea for the studied year (2017) was 4.80 Tmol, with daily-averaged inorganic carbon content ranging from 4.73 – 4.89 Tmol throughout one year (Fig. 4.4a); the range in DIC content represents approximately 3.3% of the mean. The most striking feature of the temporal evolution of the carbon content is its slight decline in the first part of the year, with a minimum reached around day 120 (approximately May 1st), followed by a steady increase throughout the late spring and summer season until around day 300 (approximately Nov. 1st), at which point the carbon content starts declining again (Fig. 4.4a).

In 2017, the total inorganic carbon content of the system at the beginning of the year is 4.80 Tmol, compared to 4.83 Tmol at the end of the year. This 0.6% difference is likely attributable to short term interannual differences in DIC fluxes and should not be taken as representative of the yearly increase in DIC content. In fact, over five years, the range in the system's end-of-year DIC content (December 31st in years 2013-2017) is 1.5% of the mean DIC content on December 31st in that same time period, likely due to interannual variability in lateral boundary fluxes (see section 4.3.3). On balance, the system is expected gain carbon over time as the global ocean absorbs the extra anthropogenic CO_2 from the atmosphere, but this increase is small compared to the carbon content of the ocean. Indeed, the total inorganic carbon content of the Salish Sea has only increased by 2% in total due to the anthropogenic carbon increase since the pre-industrial era, and as we have seen in Chapter 3, this increase has led to very large,

potentially paradigm-shifting decreases in biologically relevant metrics such as aragonite saturation state. However, because both the annual cycle in inorganic carbon content and the interannual variability are large compared to the climate change signal, quantifying the long term DIC change trends in the Salish Sea, the broader North Pacific or other systems globally is non-trivial and is the subject of active research (e.g. Franco et al. (2021); Carter et al. (2019, 2021)).

Simultaneously, the major effects of the small carbon increase to date on Ω_{arag} conditions emphasize the need to understand the controls on the Salish Sea carbon balance, because the large short-term variability of the system is anticipated to have major implications for biologically-relevant metrics and thus the entire ecosystem. In the next sections, I summarize the main contributors to the carbon balance from the absolute DIC budget and the ΔDIC budget perspectives. In the following sections I then discuss notable spatiotemporal features of several key components of the budgets.

4.3.2 The absolute DIC budget of the Salish Sea

The flux of DIC across the two lateral boundaries of the system accounts for approximately 97% of both the absolute source and absolute sink terms and is driven by the freshwater-induced exchange flow. In this model, the Juan de Fuca Strait exchange is approximately 5.6 times larger than the Johnstone Strait exchange. Total flux of carbon into and out of the system through the lateral boundaries is on the order of 14.0 Tmol year^{-1}, or almost three times larger than the total carbon content, implying a low mean DIC residence time for the system ($\sim$4 months) which is nevertheless expected to vary widely by region and depth (MacCready et al., 2021). Previous work has estimated the water residence time to range from weeks in the surface to 1-3 years at depth (Pawlowicz et al., 2007).

From the absolute budget perspective, biological fluxes play a secondary role in the system. Phytoplankton take up DIC and convert it to organic matter, which may be thought of as a biological sink, (or equivalently loss term) of the inorganic forms of carbon (DIC). In the Salish Sea, this process accounts for 3% of the total carbon sink. As modelled, the majority (94%) of phytoplankton uptake of DIC occurs between April 1st ($\sim$ day 90) and November 1st ($\sim$ day 300) in year 2017, with interannual variability due to differences in bloom timing expected (Fig. 4.4b, 4.4d). Remineralization, or the conversion of organic carbon back into DIC, is tightly coupled to primary production by phytoplankton but is a smaller term in this system, accounting for 1.9% of the DIC source (or increase). As with phytoplankton uptake, 94% occurs between April 1st ($\sim$ day 90) and November 1st ($\sim$ day 300) in the studied year. I consider drivers of regional variability in phytoplankton uptake and remineralization in section 4.3.4.

Riverine input contributes 1.2% of the absolute flux of DIC into the system. The ma-

jority (65.7%) of riverine input of DIC also occurs between April 1st and November 1st, coincident with the freshets of the major snow-driven rivers feeding into the Salish Sea, which typically occur around the beginning of June ($\sim$ day 150). The rain-driven rivers of Juan de Fuca, Puget, and Vancouver Island watersheds contribute the most inorganic carbon in the winter months, when they reach maximum discharge. There is some uncertainty in the actual contribution of riverine DIC to the overall budget as the DIC signature of the rivers in the system is an estimate based on available observations, which have a large range, and the actual DIC content of a given river likely varies seasonally or with flow volume (see Appendix B.1.4, Simone Alin, pers. comm., Simpson et al. (2022); Moore-Maley et al. (2018)). For the Fraser river, the DIC concentration in the model is set to a constant 820 mmol DIC m^{-3}, while the other rivers have a DIC signature of 660 mmol m^{-3} (see Appendix B.1.4). The relatively high DIC content of the Fraser river is due to the presence of carbonate minerals in its drainage basin (Moore-Maley et al., 2018). The total carbon sources from rivers and remineralization during the productive season defined above are nearly balanced by the carbon sink via primary productivity (0.37 Tmol vs. -0.41 Tmol respectively). Consequently the relatively large carbon increase in the domain between days 150 to 300 is attributable not to remineralization and riverine input but mainly to the increased lateral flux of carbon through the JdF boundary (Fig. 4.4a, 4.4b).

Finally, air-sea flux of CO_2 accounts for a negligible fraction of the total exchange: 0.05% of the source and 0.2% of the sink (Fig. 4.4b, 4.4c). Though the absolute contribution of the air-sea gas exchange to the system's DIC balance is small, its spatiotemporal patterns are of interest because they reflect the physical and biological controls on the inorganic carbon cycling. In section 4.3.5, I present a brief consideration of the air-sea flux analysis done in chapter 3, using the five year model run and considering the biophysical provinces.

4.3.3 The ΔDIC budget of the Salish Sea

An alternate visualization of the system's net fluxes via the ΔDIC budget highlights the larger role of inflowing Juan de Fuca water as a net carbon source to the system, in contrast to the smaller role of the outflow as a sink (section 4.2.2). This large source strength, accounting for 72% of net DIC fluxes into the system, is particularly apparent during the summer upwelling season between days 150 and 300, when the comparatively more dense and carbon-rich upwelled water has a consistently higher DIC signature than the interior Salish Sea, with only minor fluctuations that are likely tidally-driven (Fig. 4.5b); this dense upwelling signal is also easily visible in the monthly average influx of salt through the boundary (Fig. C.4). The water exiting through Juan de Fuca at the surface has a much less consistent DIC signature and in the summer is actually sometimes

a net source of DIC, because it has a concentration less than the average of 2050 mmol m^{-3} due to surface phytoplankton drawdown and dilution by freshwater; it accounts for 23% of net DIC fluxes out of the system.

Of note is the relatively small role that carbon flux through the Johnstone Strait in both directions plays in this view of the budget, accounting for approximately 1% of the sink and 3% of the source. This net exchange is small because the DIC concentration near the Johnstone Strait boundary in the model, which is estimated from limited observations (Appendix B.1.6), is similar to the system mean. Thus, when considering only the net effect of the lateral boundary carbon flux, the importance of biological processes in controlling the Salish Sea carbon balance becomes more apparent. Phytoplankton uptake accounts for 41% of the net carbon sink, while dilution of the DIC signature by freshwater accounts for 31% of the net sink. Remineralization accounts for 25% of the net DIC source. The air-sea flux continues to play a small role in this view, accounting for a negligible ($<$1%) fraction of the total source and only a slightly larger proportion of the sink (4%) (Fig. 4.5c, 4.5d).

The importance of episodic events to the modelled air-sea flux balance in this region that was noted in Chapter 3 (Fig. B.14) is again seen here. For example, a week-long high-wind event beginning on day 313 of the studied year (Nov. 9, 2017), accounts for 10% of the total yearly outgassing! During winter, high-wind events also appear to play an important role in slowing the lateral influx of DIC into the system through Juan de Fuca Strait. During these events, outer-shelf surface low-DIC waters may penetrate deeper into the water-column and be advected into the Salish Sea. In part due to the noted difficulty in quantifying air-sea gas exchange arising from episodic events by observational methods (e.g. Lueker et al. (2003) and references therein), I was not able to directly quantitatively compare the temporal air-sea flux distribution calculated from this model to any observationally-derived estimates. However, multiple observational studies note the controlling role of episodic wind events, sometimes associated with upwelling episodes, in setting the air-sea flux balance of coastal regions (e.g. Nakaoka et al. (2006); Norman, Parampil, Rutgersson, and Sahlée (2013); Morgan et al. (2019)).

The evident dominant control that the incoming Juan de Fuca lateral boundary water exerts on the DIC balance of the system motivates a brief consideration of the general structure and interannual variability of the transport there. The vertical structure of monthly mean ΔDIC fluxes complements the general picture discussed above, showing that the high influx of DIC at depth, occurring during the summer (May- September), is remarkably similar interannually in the five studied years (Fig. 4.6) . Summer surface outflow of low-DIC water is counted as a net influx in the surface 20 meters, below which point the DIC signature of the outflowing water becomes higher than the 2050 mmol m^{-3} mean value and is counted as a sink. In all 5 years, the switch from outflowing water to

inflowing water occurs at a depth of around 50 meters in this summer season, below which point a strong, interannually consistent inflow occurs, peaking near 100 meters. In contrast, in the winter months, a weaker surface outflow of waters (with DIC signature higher than the year-round domain average) is visible until ∼70 meters. A weaker surface inflow occurs below that depth, and greater interannual variability is seen in the winter flux structure, likely due to the episodicity of winter storm events such as the one on November 9 discussed above (Fig. 4.6).

A consideration of five years of Juan de Fuca flux structure reinforces the general seasonal picture seen in the budget view: in the summer we see a strong, interannually consistent inflow of upwelled high-carbon water and a strong surface outflow driven by the estuarine circulation enhanced by high freshwater input, while winter lateral fluxes are weaker and more variable between years, influenced by episodic storm events. The resulting variability is seen in the relatively large interannual range (1.5%) in end-of-year DIC content reported in Section 4.3.1. A parallel view of this structure is also visible in a consideration of salt fluxes (Fig. C.4), with interannually consistent deep summer inflow of salty water and more variability in the winter. Future changes in wind timing and strength, as well as the timing of freshwater input, would be the likely drivers of a changing lateral flux structure, but the key role of the summer upwelling water in setting the overall carbon balance is likely to remain in any future scenario.

4.3.4 Regional dynamics in phytoplankton uptake of carbon and remineralization

Phytoplankton biomass patterns determine the patterns of DIC uptake by phytoplankton throughout the productive season (Fig. 4.7a, 4.7e). In year 2017, the initial spring phytoplankton bloom occurs almost simultaneously in the more-stratified Central and Northern Strait, shortly after day 100, before appearing in Juan de Fuca Strait several days later (Fig. 4.7e). The phytoplankton biomass patterns differ between the provinces: In the Central and Northern Strait, biomass production throughout the productive season does not surpass the initial spring bloom peak, while in Juan de Fuca Strait, phytoplankton biomass is light limited and the initial bloom is smaller, while highest accumulation of biomass is seen around day 180 (the beginning of July).

Slightly higher peaks in summer biomass are seen in the Northern Strait as compared to the Central Strait, likely due to wind- or tidal-driven nutrient delivery to the less-stratified surface (Fig. 2.4, 4.7e); however, in the studied year, there is on the whole no meaningful difference in mean total depth-integrated biomass between the two provinces (in both provinces, ∼40 mmol N m^{-2} between days 90-300, as compared to ∼50 mmol N m^{-2} in Juan de Fuca Strait). The timing and patterns in phytoplankton biomass discussed here are consistent with the analysis from Chapter 2, but I am now able to quantify the

biological sink of DIC by phytoplankton drawdown (Table 4.1). As seen in Chapter 2, phytoplankton biomass, and consequently DIC drawdown, is expected to vary somewhat interannually (Masson & Peña, 2009), but the approximate 3% contribution to the total absolute DIC sink calculated in the studied year represents a useful order-of-magnitude estimate.

The net contribution of mean vertically integrated uncoupled DIC uptake to the total DIC uptake is small, ranging from a yearly average of 0.24%-0.75% between provinces. Uncoupled DIC uptake occurs when phytoplankton are nitrogen limited but not light limited and take up extra inorganic carbon as an alternate substrate for growth (Ianson and Allen (2002); Section 3.2.1). In all three provinces, uncoupled DIC uptake increases concurrently with, or immediately after, a strong phytoplankton bloom. The highest uncoupled DIC uptake occurs in the Central Strait, which may be expected, as in this region, the strong freshwater-driven stratification slows the replenishing of nitrate after it has been drawn down during the productive season, resulting in significant nutrient limitation (Fig. 4.7d). In contrast, the Northern Strait shows a more pronounced increase in nitrate after approximately day 140, with the structure of this nitrate delivery suggesting that it may be tidally modulated (Fig. 4.7d), consistent with the tidally-modulated nutrient delivery documented in Olson et al. (2020), leading to lower uncoupled DIC uptake overall. This tidally-modulated nitrate delivery is even more prominent in Juan de Fuca Strait region, where deeper, nutrient-rich water has better access to the surface layer through stronger tidal mixing. Consequently more nitrate is available in the top 30 m throughout the productive season than in either of the provinces of the Strait of Georgia (Fig. 4.7d), leading to lower uncoupled DIC uptake (Fig. 4.7b). The storm event beginning around Nov. 9 that was discussed in Section 4.3.3 is visible in a prominent decrease in nitrate in the JdF region but not in the Strait of Georgia, possibly due to the downwelling of surface low-nitrate water near the outer coast.

Finally, less DIC is remineralized in the water column than is drawn down by phytoplankton, with the source strength of DIC through remineralization varying from 48% of the drawdown in Juan de Fuca Strait to 74% in the Northern and Central Strait. Within a given area, remineralization may be decreased compared to uptake by two main mechanisms: export out of the system (in which organic matter leaves the area before it is remineralized) or burial (in which organic matter reaches the seafloor before it is remineralized). In this region, the lower remineralization ratio in Juan de Fuca Strait compared to the Strait of Georgia is likely primarily due to increased export caused by the expected lower residence time in this region. A secondary reason may be very simply the shorter water column in Juan de Fuca Strait as compared to the Northern and Central Strait, so more organic matter may sink to the bottom and be buried before it has a chance to remineralize.

Table 4.1: Mean and standard deviation of vertically-integrated phytoplankton uptake and remineralization by biophysical province (Fig. 4.1). Uncoupled DIC uptake is uptake not tied to inorganic nitrogen uptake and occurs when phytoplankton are nitrogen limited but not light limited and take up extra inorganic carbon as an alternate substrate for growth (Ianson and Allen (2002), section 3.2.1).

	Central Strait	Northern Strait	Juan de Fuca
mean DIC uptake $\pm$ std. dev. (mmol m^{-2} day^{-1})	$1.3 * 10^{-3}$ $\pm 6.1 * 10^{-4}$	$1.3 * 10^{-3}$ $\pm 6.9 * 10^{-4}$	$1.7 * 10^{-3}$ $\pm 1.0 * 10^{-3}$
mean uncoupled DIC uptake (mmol m^{-2} day^{-1}) (% mean DIC uptake)	$9.5 * 10^{-6}$ (0.75%)	$8.2 * 10^{-6}$ (0.62%)	$4.0 * 10^{-6}$ (0.24%)
mean DIC remineralization $\pm$ std. dev. (mmol m^{-2} day^{-1})	$9.6 * 10^{-4}$ $\pm 3.7 * 10^{-4}$	$9.6 * 10^{-4}$ $\pm 4.0 * 10^{-4}$	$8.2 * 10^{-4}$ $\pm 4.1 * 10^{-4}$

4.3.5 Regional dynamics in sea-surface pCO_2 and air-sea CO_2 flux

In all three provinces, sea-surface pCO_2 and air-sea flux is highest in the winter, when phytoplankton drawdown of DIC in the surface layer is low and higher wind mixing introduces DIC-rich waters to the surface (Fig. 4.8a, 4.8b, 4.9a, 4.9b). In the Northern and Central Strait, phytoplankton drawdown of DIC following the spring bloom leads to lower surface pCO_2 values than the atmospheric pCO_2, leading to both provinces taking up CO_2 from the atmosphere throughout most of the productive season (Fig. 4.8a, 4.8b, 4.9a, 4.9b). In the Northern Strait, larger episodic spikes of higher pCO_2 are visible than in the Central Strait (Fig. 4.8b), possibly due to the episodic wind driven mixing of higher-pCO_2 waters into the surface in the less-stratified watercolumn (Fig. 4.8b, section 2.4.2), leading to marginally lower summer in-gassing there (Fig. 4.9a, 4.9b). As a result, while both the Central and Northern Strait of Georgia have lower mean annual sea-surface pCO_2 than the atmosphere on average (Fig. 4.8c) and similar rates of DIC drawdown by phytoplankton (Table 4.1), only the Central Strait is on average a clear net-ingassing region over the course of a year. In contrast, the Northern Strait is almost perfectly balanced as a net-zero source (Fig. 4.9c) due to higher winter winds increasing outgassing in the winter as compared to summer ingassing.

In Juan de Fuca Strait, surface pCO_2 dips below atmospheric pCO_2 only in the beginning of the productive season. In the second half of the productive season (days ∼180-300), this region experiences an tidally-modulated increase in surface pCO_2 despite high phytoplankton biomass due to the mixing of deeper, high-carbon waters into the surface during the summer upwelling season (Fig. 4.8b), leading to strong net outgassing in all months except some Mays and Junes (Fig. 4.9a, 4.9b, section 3.3.2), a pattern also seen in observational studies (Nemcek et al., 2008; Evans et al., 2012). Overall, the 10th-90th percentile of the distribution of sea-surface pCO_2 and air-sea flux exhibits remarkable interannual consistency in all three provinces (Fig. 4.8c, 4.9c). As expected, stronger variability is seen in the winter in all three provinces (Fig. 4.8a, Fig. 4.9a) due to the higher net winds and episodic wind events. This variability may be attributable both to the increased variability in surface pCO_2 concentrations due to the mixing up of diverse watermasses and to the subsequent variability in wind stress that causes air-sea CO_2 transfer. Untangling these two mechanisms may be an interesting focus of future work, especially in the Juan de Fuca Strait, which is the only region that is a strong net source of CO_2.

4.4 Regional patterns in aragonite saturation state

In Chapter 3, I discussed the large spatial and seasonal variability in aragonite conditions in the system in the studied year; here I also consider the interannual variability, again in the context of the three major biophysical provinces (Fig. 4.1). I consider the seasonal structure of aragonite saturation state using the following seasonal definitions: the pre-bloom winter period (Jan. 1 - Feb. 28), the spring bloom (Mar. 1 - May 10), the productive season (May 11 - Aug 30), and the end of the year (Aug. 31 - Dec. 31). The spring bloom season is defined broadly in order to encompass the large observed interannual variability in spring bloom timing in the Salish Sea (S. Allen & Wolfe, 2013). The end of the productive season is defined as the interannual average of the time-period when the modelled surface nitrate depletion ceases in another study of the Salish Sea using the same model (Moore-Maley & Allen, 2021). I consider the distributions of aragonite saturation state in the five studied years at three biologically relevant depths (the surface, 50 meters, and 100 meters), taking a spatiotemporal average of aragonite saturation state over all days and all cells of each of the three biophysical provinces.

The majority of the variability in aragonite saturation state conditions occurs in the surface during the spring bloom and productive season, due to two opposing influences: spatially and temporally varying primary productivity (which raises Ω_{arag} via DIC drawdown) and freshwater input (which lowers Ω_{arag} via dilution by water with an Ω_{arag} of zero) (Ianson et al., 2016; Moore-Maley et al., 2016). During the spring bloom period,

surface aragonite conditions are typically lowest (5-year mean Ω_{arag} = 1.25) and least variable in Juan de Fuca Strait due to lower surface drawdown by phytoplankton, while both regions of the Strait of Georgia have comparable aragonite saturation state conditions that are approximately 0.3 units higher on average (5-year mean Ω_{arag} = 1.55, Fig. 4.10). The opposite pattern can be seen during bloom conditions at depth - Juan de Fuca Strait has higher and more variable Ω_{arag} conditions at 50 meters than the Strait of Georgia, due likely to a combination of deeper persistence of phytoplankton and stronger tidal mixing of the watercolumn.

During the productive season, when the freshwater input by nival rivers peaks, the Central Strait of Georgia has lower and more variable Ω_{arag} than the Northern Strait of Georgia (Fig. 4.10). While both regions have similar phytoplankton biomass that is concentrated in a shallow near-surface growing region, the Central Strait is more influenced by the Fraser River. In Juan de Fuca Strait, lower surface phytoplankton biomass than in the Strait of Georgia leads to the lowest summertime aragonite saturation state in the domain, a pattern also seen in observations of the system (Ianson et al., 2016). During the productive season, at both 50 m and 100 m, all three provinces have comparable aragonite saturation states that are interannually consistent. These stable conditions are expected because strong stratification in the Central and Northern Strait confines biologically-induced variability near the surface, and simultaneously the dominant influence of the summer inflow through Juan de Fuca, which is largest at a depth of 100m, is remarkably interannually consistent (Section 4.3.3, Fig. 4.6).

Because the Strait of Georgia is carbon-enriched compared to the Juan de Fuca Strait, winter pre-bloom aragonite saturation states in the surface are higher in Juan de Fuca Strait than in both regions of the Strait of Georgia (Fig. 4.10), a pattern also seen in observations (Ianson et al., 2016). End-of-year surface aragonite saturation shows the opposite pattern, likely due to the inclusion of autumn in the seasonal definition - surface carbon drawdown, which persists into autumn, is stronger in the Strait of Georgia. At depth, more interannual variability is seen in Ω_{arag} conditions in Juan de Fuca Strait than in the Strait of Georgia, likely due to stronger tidal mixing in this region and interannual variability in DIC and TA flux through the boundary in the winter downwelling season (see section 4.3.3 and Fig. 4.6).

4.5 Response of the Inorganic Carbon Balance to Future Scenarios

Finally, I take a first look at some aspects of the response of the system to the two scenarios of environmental change outlined above (section 4.2.4). Based on the significant system-wide anthropogenic DIC increase in the system from pre-industrial to present-day

seen in Chapter 3, driven primarily by the lateral boundary conditions, I expect a further system-wide increase in DIC under the CAR50 scenario. Here I focus on quantifying it and its direct effects on Ω_{arag} in the main biophysical provinces of the domain. Because the riverine input plays a smaller role in the absolute DIC budget of the Salish Sea as a whole, the effects of any change may be more subtle. Here I focus my study on changes in some sample near-shore regions, close to some of the major nival rivers, which are significant for both aquaculture and natural ecosystems. A shift in the timing of freshwater input may also have a subtle effect on the estuarine carbon circulation patterns, which may be the focus of future work.

4.5.1 The CAR50 scenario

Under the SSP 2-4.5 scenario (Meinshausen et al., 2020), by year 2050, the DIC concentration of the Salish Sea is projected to increase by a yearly domain-wide average of 27 mmol m^{-3} compared to year 2017 (Fig. 4.11). Remarkably, the projected increase over the next thirty years, under a conservative emissions scenario, represents approximately 80% of the total inorganic carbon increase from the pre-industrial period to year 2015. As expected, some variability is present in this increase. The Northern Strait, whose waters are influenced by the Johnstone Strait exchange containing comparatively young waters, shows a higher anthropogenic carbon increase than the Juan de Fuca Strait, which is dominated by the summer upwelling of comparatively old waters containing less anthropogenic carbon (Fig. 4.11, C.1,C.2, C.3).

Because the present-day Salish Sea occupies a poorly-buffered, sensitive region of carbonate chemistry space, the decrease in aragonite saturation state associated with the inorganic carbon increase may again be expected to be considerable (section 3.3.5). This expectation is confirmed: the projected inorganic carbon increase causes a further decrease of between 0.1-0.2 Ω_{arag} in the CAR50 scenario throughout the domain (Fig. 4.13). This decrease has variable effects in the domain which are most dramatic in Juan de Fuca Strait (Fig. 4.12). In the summer, surface saturation states are lower in Juan de Fuca Strait and saturation horizons are simultaneously deeper than those in the Strait of Georgia, because vertical gradients in Ω_{arag} are weak due to strong tidal mixing (see section 3.3.4). This barely-supersaturated water becomes undersaturated in the CAR50 scenario, leading to approximately 20 m of shoaling in the Juan de Fuca Strait (Fig. 4.12a, 4.12b, kms 0-200) and even stronger shoaling in the tidal mixing region (near km 300). In contrast, in the Strait of Georgia, strong stratification confines supersaturated water near the surface, leading to almost no shoaling of saturation horizons (kms 300-600). Near the Johnstone Strait exchange, strongly mixed waters that are barely supersaturated in the present day (with shallow Ω_{arag} horizons) become fully undersaturated in the future.

In the winter, the present-day Juan de Fuca Strait is mostly slightly supersaturated

with respect to aragonite in winter, with deep saturation horizons (below 100m; Fig. 4.12c, kms 0-200). The additional 0.1-0.2 Ω_{arag} decrease is then sufficient to push the entire watercolumn below aragonite saturation. In the winter, in the Strait of Georgia, waters that are presently hovering near saturation are similarly pushed to undersaturation in the future. Overall, the projected 0.1-0.2 Ω_{arag} decrease under the CAR50 scenario drives domain-wide undersaturation in winter and undersaturation below 25 m in summer. These future dramatically undersaturated conditions are in stark contrast to projections for the coastal North Atlantic, where surface undersaturation is not expected even at the end of the 21st century under the SSP 5-8.5 scenario (Ostle et al., 2016).

The SSP 2-4.5 scenario was chosen to establish a conservative lower bound on future Ω_{arag} decreases in the near future at a local scale. Debate exists as to which scenario society is currently on track for; however, the discussion is typically bounded by scenarios SSP 4-6.0 and SSP 5-8.5 ((Schwalm, Glendon, & Duffy, 2020; Hausfather & Peters, 2020)) and the scenario used here is likely too optimistic. However, as noted in the methods, the likely difference in atmospheric pCO_2 between all five emissions scenarios remains relatively small in 2050, so the projection shown here is likely reasonable, if slightly optimistic, regardless of scenario followed. Remarkably, these results show that even using optimistic assumptions and looking only into the near future, effects of the future anthropogenic carbon increase on ecologically critical parameters such as Ω_{arag} are likely to be both non-negligible and environmentally relevant. Future work may consider the differences in Ω_{arag} projections to 2100 under different scenarios. Here I briefly consider one future projection of the Salish Sea carbonate chemistry state to year 2095, which follows RCP 8.5 and includes downscaled projections for the future wind field, future temperature change, changes in river hydrograph patterns, and changes in nutrient loading (Khangaonkar et al. 2019, called K19 here). K19 found significantly higher increases in DIC at the Salish Sea open ocean boundary (approximately 98 mmol m^{-3}) (Khangaonkar et al., 2019). Though this result is not directly comparable to the changes that I see in this study because the years and scenarios projected are different, the overall pattern of changes to the carbon cycle projected by K19 is similar to what my study shows: the strongest driver of changes to the carbon levels is incoming water from the open ocean boundary between the Salish Sea and the adjoining open Pacific Ocean. The lowest values of ocean acidification-related metrics (pH in K19 and Ω_{arag} in my study) occur in the deepest, least-flushed basins, while mixing reduces the changes to the carbon levels in the main basins of the system. The results seen in K19 represent a first estimate of the upper bound of the DIC increase in the Salish Sea to 2100 under a high-emissions scenario.

4.5.2 The RIVSHIFT scenario

I finally take a first look at the effect of the forward-shifted hydrograph on the nearshore carbonate chemistry balance near the mouths of the Fraser, Homathko, and Squamish rivers (Fig. 4.14, C.5, C.6). Because nearshore regions provide habitat to both wild and and cultivated shellfish species, which require suitable Ω_{arag} conditions for growth (Haigh et al., 2015), both the interannual variability in the timing of freshwater delivery and any projected future change in this timing may have important ecosystem effects. Because many marine invertebrates spawn and release planktonic larvae at around the time of the spring bloom (e.g. Starr, Himmelman, and Therriault (1990)), a forward shift in comparatively undersaturated conditions could more directly co-occur with the most sensitive life stages for many species. In all three rivers, the first order effect of the forward hydrograph shift is a corresponding forward shift in the yearly salinity and DIC minima, as expected (Figs. 4.14b, 4.14d, C.5b,C.5d, C.6b,C.6d). A secondary, less obvious effect is a dampening of the spring diatom bloom, most visible in the Fraser nearshore (Fig. 4.14c) and to a lesser extent in the Homathko and Squamish nearshore (Fig. C.5c, C.6c), likely due to the disruption of stable growing conditions via a flushing effect (e.g. Ianson, Pond, and Parsons (2001)). Thus, the earlier freshet may drive surface acidification via two interacting pathways: reduction of surface inorganic carbon drawdown via the introduction of naturally aragonite-undersaturated freshwater (Moore-Maley et al., 2018) and spring bloom dampening. At all three nearshore areas, in the shifted scenario, surface Ω_{arag} levels are comparatively depressed during the spring bloom period (Fig. 4.14e, C.5e, C.6e, day 60-130), and in the Fraser nearshore, a new lowest-yearly Ω_{arag} value is reached due to this effect.

In the summer season, when freshwater input is lower in the shifted scenario, the opposite pattern is seen and nearshore Ω_{arag} levels are typically higher. No strong shift in the mean yearly DIC or Ω_{arag} is observed at any of the three near-shore areas. Nevertheless the main observed effect of the shifted hydrograph – lower Ω_{arag} earlier in the year due to increased freshwater delivery and a dampened spring bloom – has potential to adversely affect shell-forming organisms early in the growing season.

In the Fraser and Squamish nearshore, a switch to stronger outgassing earlier in the year is visible in the shifted scenario (Fig. 4.14f, C.6f). However, the magnitude of this change differs between the areas, likely due to differing local winds on the studied days. In the Fraser nearshore (and to a lesser extent in the Squamish nearshore), strong winds combine with the early-spring shift to high pCO_2 to create strong outgassing events (around day 100), while in the Homathko, almost no outgassing is observed during the same period.

Importantly, the wind forcing used for the model, which is an interpolated 2.5km resolution HRDPS product, may not accurately represent the near-shore fjord system winds,

again highlighting the importance of an accurate wind product of sufficient resolution in resolving the atmospheric carbon flux magnitude. Another limitation of these projections is that they do not consider the expected future changes in hydrograph shape, which include a reduction in maximum flow. As a result, the effects on Ω_{arag} seen here are likely an overestimation, and the realistic effect of a forward-shifted hydrograph on low-Ω_{arag} conditions early in the year would be more subtle.

4.6 Conclusion

This budget-focused analysis of the Salish Sea shows that the incoming Juan de Fuca boundary water exerts a major control on the system's carbonate balance. This inflow is strongest and most interannually consistent in the summer season, while inflow-outflow patterns in the winter are both weaker and more interannually variable. I also consider the system's biological sinks (phytoplankton uptake) and sources (remineralization) in the context of three distinct biophysical regions, finding subtle differences. In all three regions, uncoupled DIC uptake contributes only a small amount of total DIC uptake by phytoplankton when nitrogen is limiting. Sea-surface pCO_2 and air-sea CO_2 flux show clear regional differences but are remarkably interannually consistent in five studied years.

The system's Ω_{arag} state is set by a combination of physical and biological drivers, and regional variability in Ω_{arag} conditions is larger than interannual variability over the studied timeperiod. Considering the system's response to an anthropogenic carbon increase according to the SSP2-4.5 scenario, I find that the projected increase over the next thirty years is equal to approximately 80% of the total inorganic carbon increase from the pre-industrial period to year 2015. This inorganic carbon increase drives an additional Ω_{arag} decrease of 0.1-0.2 units, leading to system-wide undersaturation in winter and undersaturation below 25 meters in summer. The response of the system to an experimental forward shift in the hydrographs of major nival rivers is more subtle, but a combination of earlier freshwater input and dampening of the spring bloom may lead to lower Ω_{arag} earlier in the season, with potential effects on near-shore shell-forming organisms.

4.7 Figures

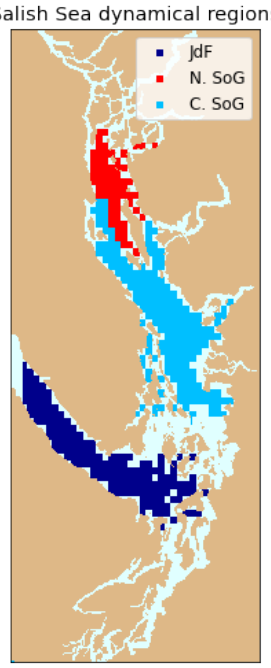

Figure 4.1: The three main biophysical provinces considered in this text: Juan de Fuca Strait (dark blue), the Northern Strait of Georgia (red), and the Central Strait of Georgia (sky blue). See section 4.2.3 for description of the main biophysical dynamics governing each region.

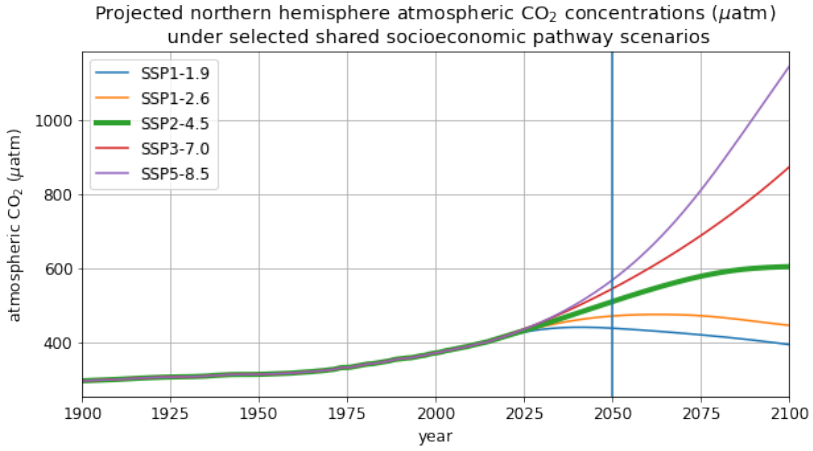

Figure 4.2: Atmospheric CO_2 concentrations for five shared socioeconomic pathways, years 1900-2100 (Meinshausen et al., 2020). The pathway used in the CAR50 sensitivity model run, SSP 2-4.5, is highlighted.

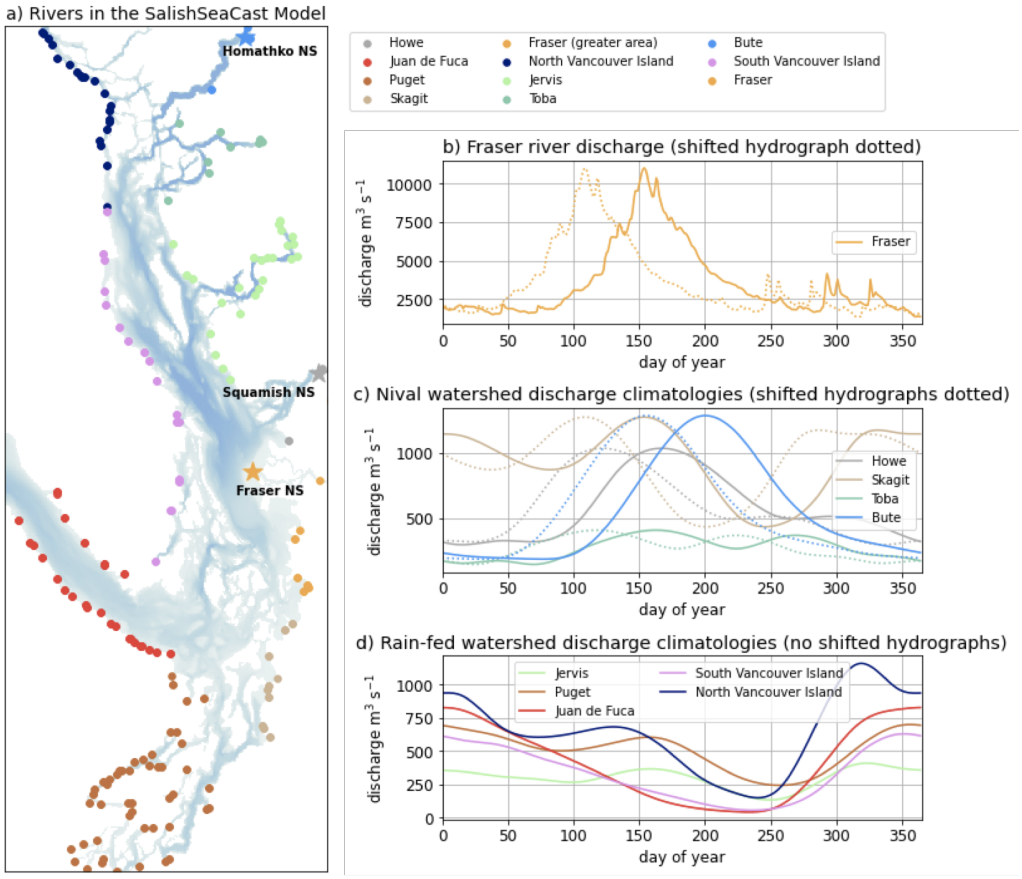

Figure 4.3: Rivers in the SalishSeaCast model, separated by watershed. Hydrographs showing total discharge per watershed shown in panels b)-d). The Fraser, Howe, Toba, Skagit, and Bute watershed hydrographs are rotated forward 45 days in the RIVSHIFT sensitivity scenario. Three stations near the mouths of major rivers (the Fraser (orange), Squamish (grey), and Homathko (sky blue)) are highlighted with stars (NS = nearshore station).

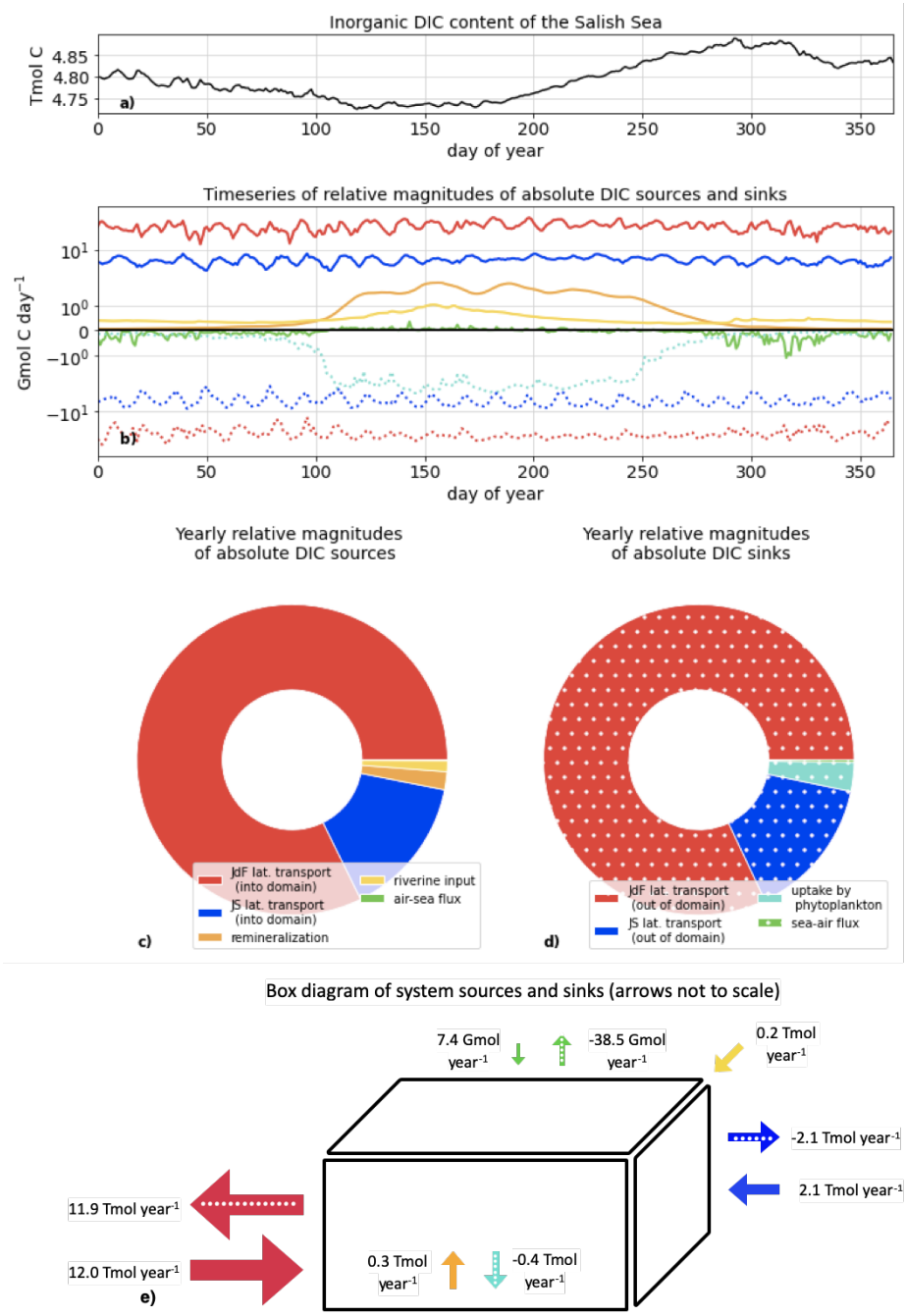

Figure 4.4: An overview of the absolute DIC budget of the Salish Sea. Panel a) shows the evolution of the total inorganic DIC content over the course of a year, with a characteristic increase from days 150-300 due to the summer upwelling. Panel b) shows timeseries of relative magnitudes of net DIC sources (solid lines) and sinks (dotted lines). Red = Juan de Fuca lateral transport, royal blue = Johnstone Strait lateral transport, orange = remineralization, yellow = riverine input, green = air-sea flux, cyan = DIC uptake by phytoplankton. Panel c) and d) show the total yearly relative magnitudes of net DIC sources and sinks, respectively. Panel e) shows a cartoon of the sources and sinks to the system (arrows not to scale).

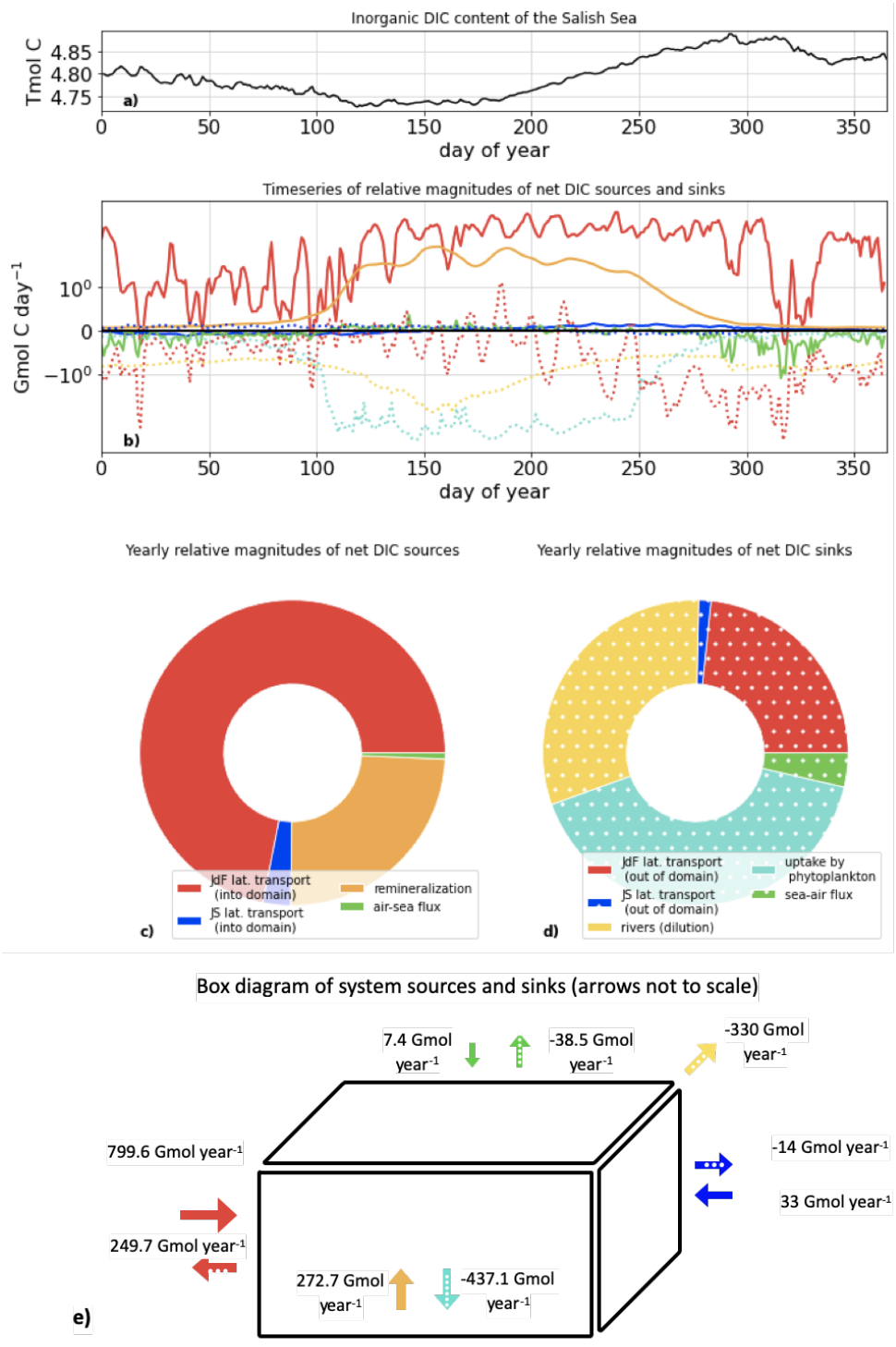

Figure 4.5: An overview of the ΔDIC budget of the Salish Sea. Panel a) as in Fig. 4.4. Panel b) shows timeseries of relative magnitudes of net DIC sources and sinks. Colours and line conventions are as in Fig. 4.4. Panel c) and d) show the total yearly relative magnitudes of net DIC sources and sinks, respectively. Panel e) shows the sources and sinks to the system as a box diagram.

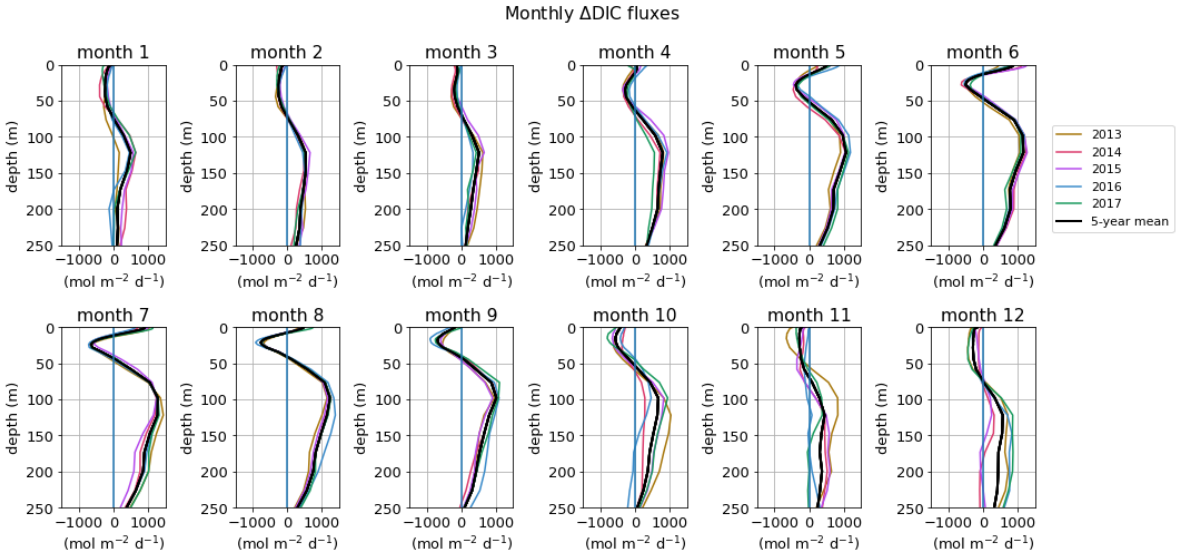

Figure 4.6: Mean monthly ΔDIC flux (mol m^{-2} d^{-1}) for years 2013-2017 at the Juan de Fuca boundary (∼5 km from the domain edge). Depth profiles show the mean for the full cross-section at the boundary at a given depth. Summers are marked by interannually consistent inflow (positive flux) of carbon-rich water at depth and a prominent outflow of low-DIC waters at the surface (seen here as a positive flux of ΔDIC). Winters have weaker, more variable inflow and outflow patterns, likely influenced by episodic events and a transient flow regime.

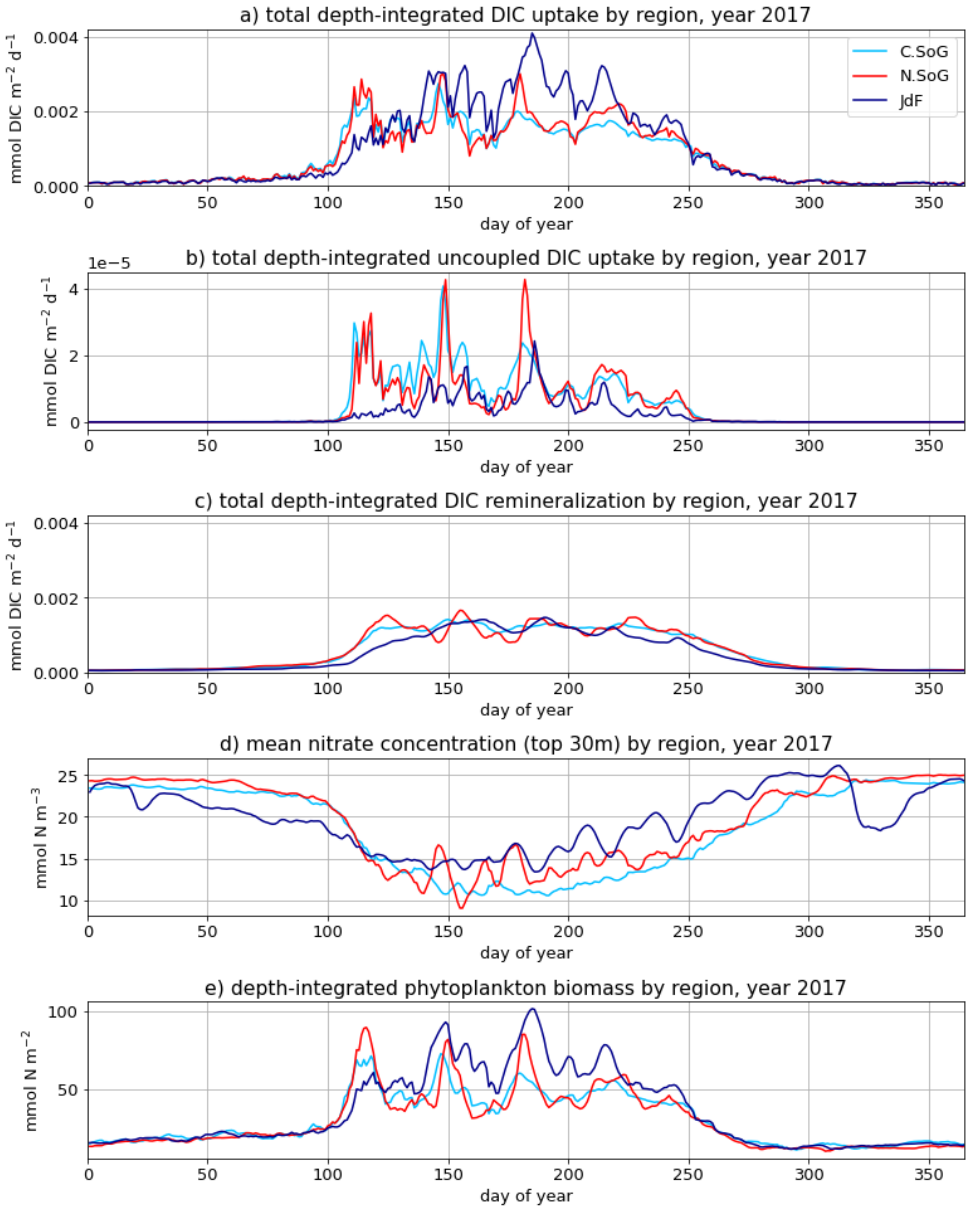

Figure 4.7: Mean timeseries of key biological DIC sources and sinks, separated by biophysical province (Fig. 4.1): total DIC uptake by phytoplankton (panel a), total uncoupled DIC uptake (panel b), total remineralization (panel c). For context, mean near-surface (top 30m) nitrate concentration (panel d) and total depth-integrated phytoplankton biomass (panel e) are also shown.

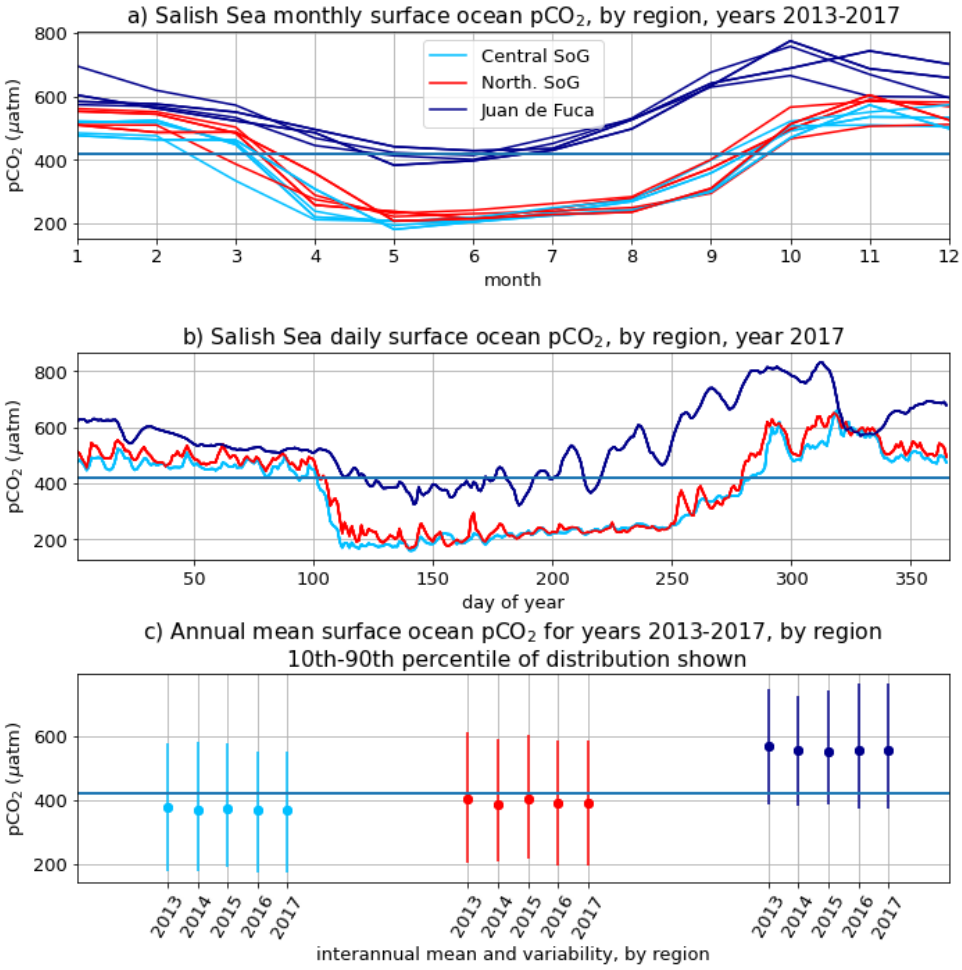

Figure 4.8: A summary view of Salish Sea surface pCO_2, separated by biophysical province (Fig. 4.1): monthly province-wide surface ocean pCO_2 for the five studied years (five lines per province, panel a), daily province-wide mean surface ocean pCO_2 (panel b), and the 10th-90th percentile of annual mean surface pCO_2 for the five studied years (panel c). In all three panels, mean annual atmospheric pCO_2 ($\sim$420) is shown as a horizontal blue line.

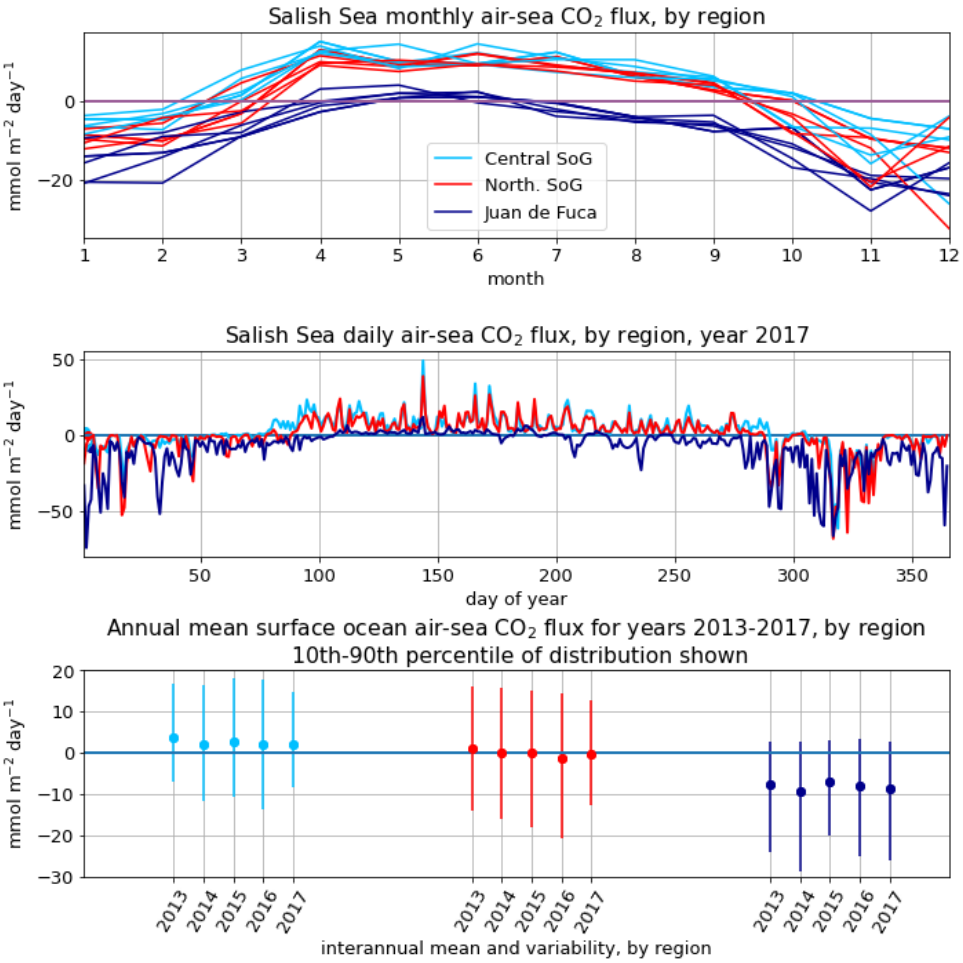

Figure 4.9: A summary view of Salish Sea air-sea CO_2 flux, separated by biophysical province (Fig. 4.1): monthly province-wide mean air-sea CO_2 flux for the five studied years (panel a), daily province-wide mean air-sea CO_2 flux (panel b), and the 10th-90th percentile of annual air-sea CO_2 flux for the five studied years (panel c).

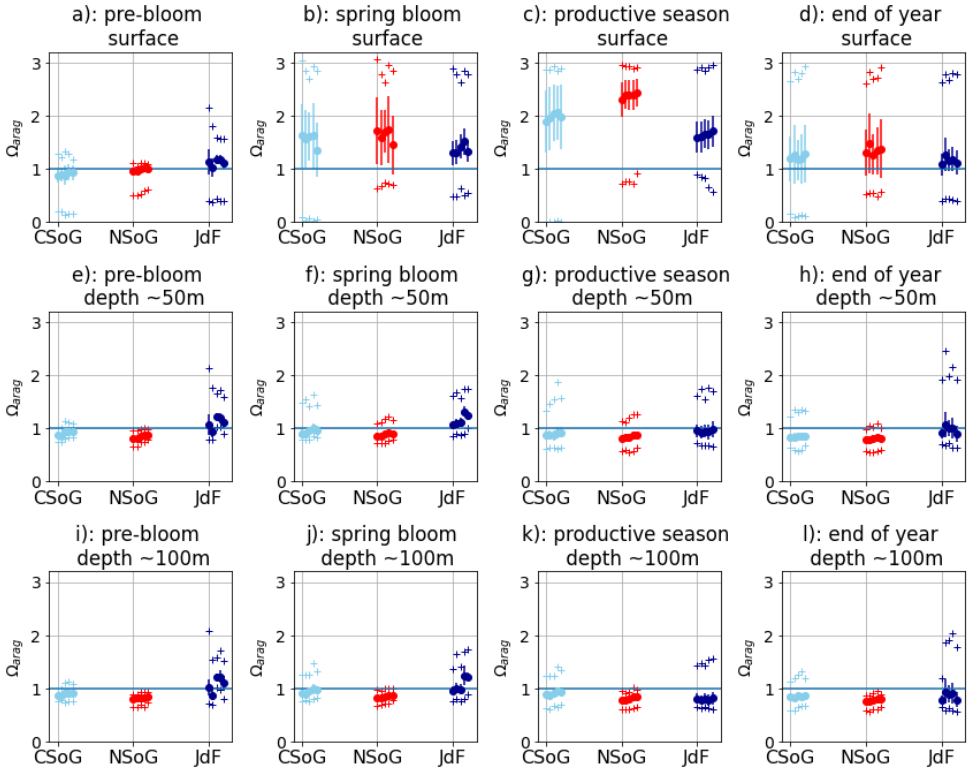

Figure 4.10: Seasonal characteristics of Ω_{arag} saturation state for the three biophysical provinces (Fig. 4.1) at the surface, 50 meters, and 100 meters. The mean, standard deviation, maximum and minimum are shown for each of five studied years (2013-2017, left to right). Means and standard deviations are calculated spatiotemporally (that is, a seasonal mean for a given biophysical province is calculated by averaging all days and all cells in the given province and season). Seasons are defined as follows: the pre-bloom winter period (Jan. 1 - Feb. 28), the spring bloom (Mar. 1 - May 10), the productive season (May 11 - Aug 30), and the end of the year (Aug. 31 - Dec. 31).

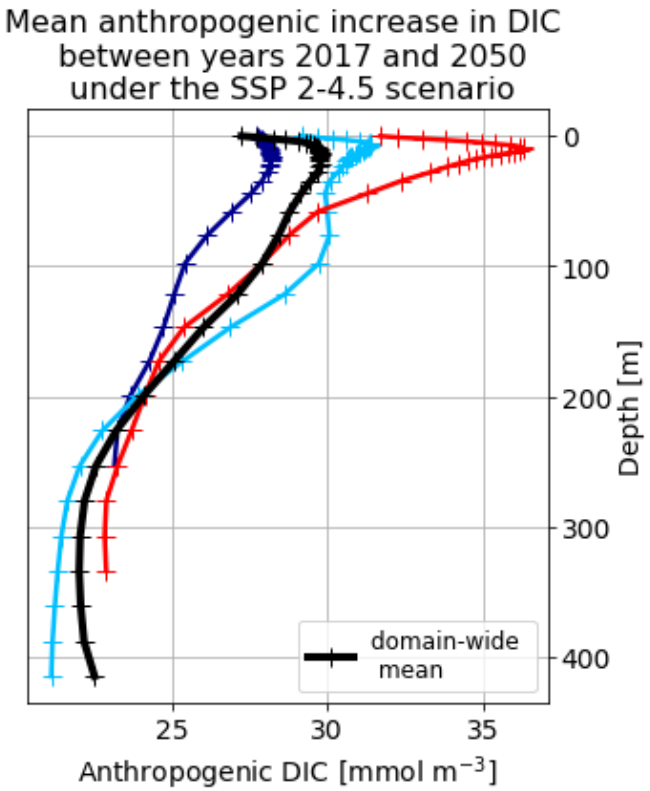

Figure 4.11: The mean anthropogenic increase in DIC between years 2017 and 2050 under the SSP 2-4.5 scenario (section 4.2.4), by biophysical province (Fig. 4.1)

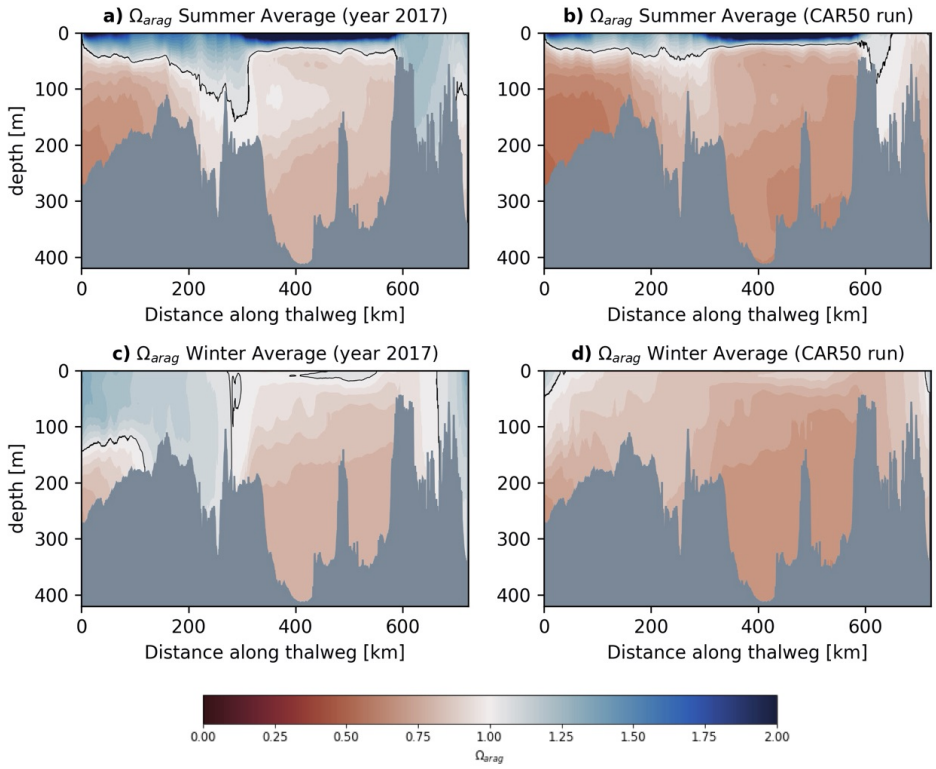

Figure 4.12: Along-thalweg (Fig. 3.1) transects of summer and winter, year 2017 and projected Ω_{arag} saturation state for the CAR50 scenario (year 2050, SSP2-4.5). The Ω_{arag} = 1 isoline is shown in black.

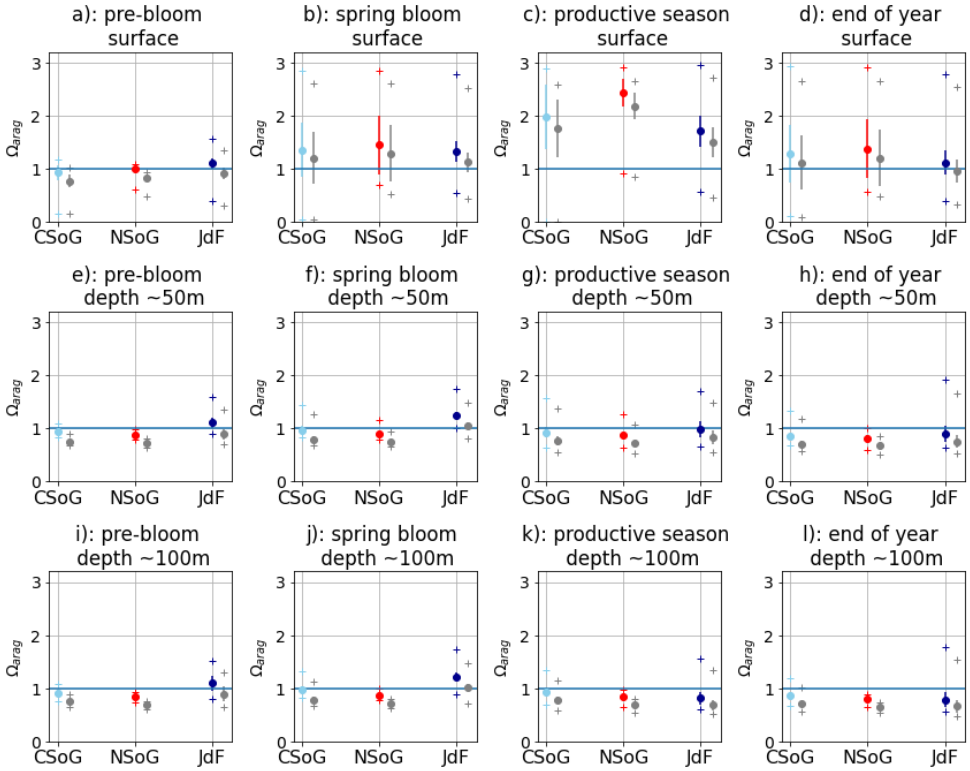

Figure 4.13: Seasonal characteristics of Ω_{arag} saturation state (mean, standard deviation, maximum and minimum) for the three biophysical provinces (Fig. 4.1) at the surface, 50 meters, and 100 meters for the present-day (coloured) and projected future CAR50 (grey) runs (adjacent). Metrics are calculated as in Fig. 4.10. Seasons are defined as follows: the pre-bloom winter period (Jan. 1 - Feb. 28), the spring bloom (Mar. 1 - May 10), the productive season (May 11 - Aug 30), and the end of the year (Aug. 31 - Dec. 31).

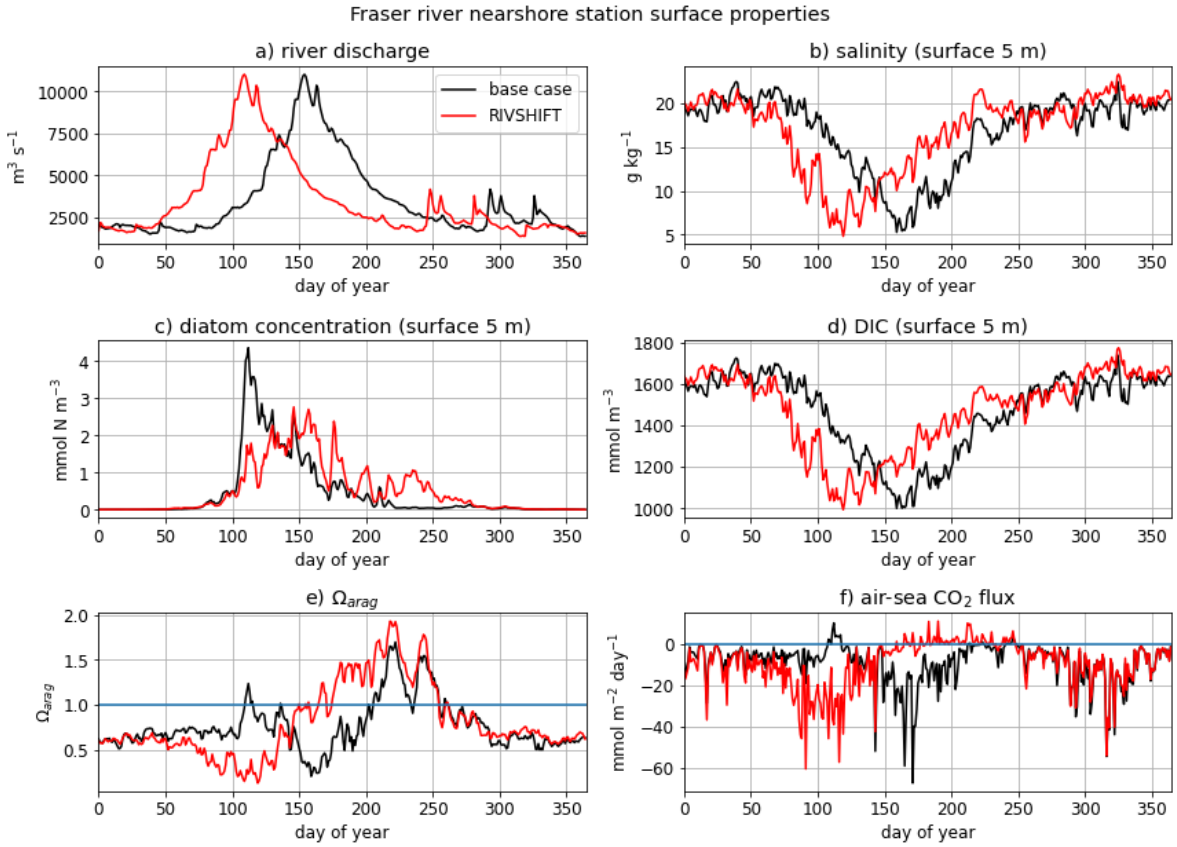

Figure 4.14: Nearshore water properties of the vicinity of the Fraser rivermouth (Fig. 4.3) in the base and RIVSHIFT scenarios. Panel a) shows the base case (black) and shifted (red) hydgrographs. Panels b)-e) show surface 5m mean salinity, diatom concentration, DIC, and Ω_{arag}, respectively, while panel f) shows air-sea CO_2 flux.

Chapter 5

Conclusion

Now this is not the end. It is not even the beginning of the end. But it is, perhaps, the end of the beginning. — Winston Churchill

This thesis investigated several aspects of the changing carbonate chemistry balance of the Salish Sea using a submesoscale numerical ocean modelling approach. Here, I first briefly summarize the key findings of my research by answering the stated research questions as laid out in the introduction. I then more broadly outline some of the contributions of the thesis to the relevant fields. These contributions include both the insights into aspects of the Salish Sea biogeochemistry gained from the research projects, their implications for coastal carbon and biophysical dynamics more broadly, and the tools that I developed in the process of this research. Finally, I ponder some future directions for this work.

5.1 Summary of answers to research questions

- *How do physical oceanographic dynamics drive phytoplankton community dynamics in the Salish Sea, and what are the dominant spatial patterns of both?*

I approached this problem by applying an unsupervised machine learning algorithm (hierarchical clustering by Ward's method) to yearly timeseries of four factors relating to stratification and to depth-integrated phytoplankton biomass, differentiated by functional group, that I extracted from the SalishSeaCast. I identified three main biophysical provinces in the Salish Sea which persist in all four analyzed years (2013-2016) – the Juan de Fuca Strait, the Northern Strait of Georgia, and the Central Strait of Georgia. These three regions experience distinct combinations of physical-oceanographic drivers (wind energy, freshwater influence, and tidal mixing) that cause three distinct halocline regimes which in turn spatially correlate with differing phytoplankton biomass and functional group dynamics.

The Central Strait of Georgia is strongly stratified by the dominant Fraser River, which leads to the shallowest, most stable haloclines of the three regions. These stable haloclines support strong initial diatom blooms during the spring bloom period and a transition to flagellate abundance in the second half of the productive season as nutrient limitation of phytoplankton growth becomes a controlling influence. The Northern Strait of Georgia, which is further away from the Fraser river but receives significant freshwater input from the rivers at the head of the nearby fjords, still experiences freshwater stratification but has less shallow and less stable haloclines and is more likely to experience nutrient injection from the subsurface waters and as a result supports episodic diatom blooms even in the latter part of the productive season.

Juan de Fuca Strait is the least influenced by freshwater and is more affected by tidal mixing than either the Northern Strait or the Central Strait. This low-freshwater, tidally-mixed regime results in deep, variable haloclines with little nutrient limitation. Consequently phytoplankton blooms occur later in Juan de Fuca Strait than in either the Central or Northern Strait, with their biomass following a light-limitation curve. Phytoplankton also persist deeper in the watercolumn in this region than in the Central or Northern Strait. In the studied years, the three regions were found to have similar total biomass overall, with the major differences between the region concerning functional group dynamics and vertical distribution.

- *How has anthropogenic carbon from the air-sea and open-ocean boundary changed the inorganic carbon mass-balance and cycling pathways in the Salish Sea?*

On average, the DIC content of the Salish Sea has increased by 29-39 mmol m^{-3} from pre-industrial to present day, a value that represents $<2\%$ of the system's mean inorganic carbon concentration. This increase is dominated by lateral fluxes between the Salish Sea and the open Pacific and is consequently higher near the Johnstone Strait, which has young waters that have experienced a higher intrusion of CO_2, than near the Juan de Fuca Strait, which experiences summer upwelling of comparatively old and less affected waters. This system-wide increase has had only a modest impact on net air-sea CO_2 flux. Because present-day summer uptake of atmospheric CO_2 is large, but balanced by winter outgassing, the region is only a weak CO_2 source. In the pre-industrial system, summer uptake of atmospheric CO_2 was somewhat lower, slightly increasing the net CO_2 source strength in comparison to present day.

- *What are the implications of this mass-balance change on Ω_{arag}?*

In the Salish Sea, the inorganic carbon increase to date has been sufficient to tip the system from a regime where undersaturation was rare even in the deepest zones of the domain to one where the majority of waters are undersaturated with respect to aragonite

throughout all seasons. Furthermore, in most places, outside of the variable and high-Ω_{arag} surface regions, the observed shift in saturation state is larger than the variability in Ω_{arag} conditions experienced over the course of a season. This threshold-crossing suggests that the Salish Sea has already undergone fundamental geochemical change, with likely implications for local ecosystems.

- *How do the carbonate chemistry conditions of the Salish Sea compare with available measurements in the rest of the global coastal ocean, and what are the implications of these conditions on Ω_{arag} globally?*

A comparison of model output with global coastal carbonate chemistry observations show that present-day distributions of aragonite saturation state conditions and buffering capacity appear to be similar, and generally low, in the Salish Sea and the rest of the coastal Pacific Rim. This similarity suggests that the majority of the Pacific Rim has already undergone significant shifts in carbonate chemistry, with potential implications for ecosystem functioning. In contrast, the comparatively well-sampled North Atlantic coastal waters are relatively safe from Ω_{arag}-undersaturated conditions at present.

- *What are the dominant fluxes in the Salish Sea carbonate chemistry balance, and what is their relative magnitude and spatial and temporal structure?*

The incoming Juan de Fuca boundary water exerts the largest control on the Salish Sea's inorganic carbon balance. This inflow is strongest and most interannually consistent in the summer season, while inflow-outflow patterns in the winter are both weaker and more interannually variable. In contrast, the Johnstone Strait changes Salish Sea inorganic carbon chemistry little, and the air-sea CO_2 exchange, which is remarkably interannually consistent in magnitude, represents the smallest flux in the system.

Biological and riverine fluxes play an important role in the system, especially from the ΔDIC perpective. The DIC sink represented by uptake by phytoplankton is nearly balanced by the DIC source from remineralization and riverine input. Notable spatial differences between air-sea CO_2 fluxes and biological fluxes can be observed between the different biophysical provinces established in Chapter 2. In all three regions, uncoupled DIC uptake contributes only a small proportion ($<$1%) of total DIC uptake by phytoplankton when nitrogen is limiting.

- *How variable is the aragonite saturation state of the different regions of the Salish Sea from year to year?*

I compared Ω_{arag} conditions at three depths in the three established biophysical provinces over the course of five years. I found that because the system's Ω_{arag} state

is set by a combination of physical and biological drivers that differ between the three established biophysical provinces, inter-regional variability in Ω_{arag} conditions is typically larger than interannual variability in a given region over the studied timeperiod, except in the surface.

- *How may the Salish Sea carbonate chemistry balance respond to a) likely future increase in anthropogenic CO_2 or b) potential future change in the hydrological cycle of dominant rivers?*

a): Under the relatively conservative SSP2-4.5 emissions scenario, the projected anthropogenic carbon increase in the Salish Sea over the next thirty years is equal to approximately 80% of the total inorganic carbon increase from the pre-industrial period to year 2015. This inorganic carbon increase drives an additional Ω_{arag} decrease of 0.1-0.2 units, leading to system-wide undersaturation in winter and widespread undersaturation below 25 meters in summer. b): The response of the system to an experimental forward shift in the hydrographs of major nival rivers is subtle. However, three near-shore test cases show that a combination of earlier freshwater input and dampening of the spring bloom may lead to more corrosive Ω_{arag} earlier in the season, with potential effects on near-shore shell-forming organisms.

5.2 Contributions to the field

5.2.1 Perspectives on biophysical regions in the Salish Sea

This work adds a new perspective to an existing local-scale discussion regarding regional patterns in phytoplankton dynamics in the Salish Sea (Peña et al., 2016; Masson & Peña, 2009; Pawlowicz et al., 2020). My approach builds on and responds to this previous work from a novel perspective: by applying an objective data science method to high-resolution model output, I'm able to formalize spatial boundaries between different biophysical regimes in the region that were previously estimated and suggest plausible mechanisms for these spatial patterns. This work also provides a new view of the system's biophysical dynamics by showing that one region, the Juan de Fuca Strait, may support more phytoplankton biomass than previously thought (Masson & Peña, 2009); this higher biomass is both observed in the model and supported by the model evaluation against available measurements. This work is relevant in designing both future observational studies of the lower trophic levels of the system and in delineating different functional areas of the Salish Sea in management applications.

5.2.2 Utility of Clustering Methods in Regional Modelling

From a methodological perspective, this work's strength in a way lies in its simplicity. Ocean and climate modelling is simultaneously fascinating and challenging because it produces enormous, complex datasets that offer more analysis opportunities than any one research team can practically complete - there is always another plot to make. Developing ways to identify structure in these large datasets is thus very relevant. While data science approaches to understanding large datasets are becoming increasingly common across many disciplines, these techniques are still underutilized in the context of regional ocean modelling. Furthermore, some data science and machine learning techniques, for example neural nets, have 'black box' workflows, in which several known parameters interact in unspecified ways to produce a target variable, which may be operationally very useful but may not explain underlying drivers.

In contrast, the machine learning application that I developed here, based on a known clustering technique, is both transparent and relatively simple to both understand and implement. I extracted well-known oceanographic parameters from the model, in effect reducing dataset size while keeping meaningful information. I then clustered these parameters and explore the reasons for the patterns found in them. In addition to identifying meaningful features in model-generated data, this approach is useful in model evaluation - comparing model performance across different physical or biogeochemical regimes identified by clustering has potential to illuminate and diagnose sources of model error. The relative ease of method implementation means that it can be easily adapted for use with other parameters or models. Accordingly, the method has already been used by colleagues in the Mesoscale Ocean and Atmospheric Dynamics (MOAD) Group to explore zooplankton ecology questions, and as part of the publication of this work, I am providing an open-source annotated example of my workflow, including Python code, as a GitHub repository.

5.2.3 Contributions to understanding the carbonate chemistry of the Salish Sea

As a first step to investigating the Salish Sea carbonate chemistry balance, I developed and carefully evaluated a remarkably well-performing three-dimensional carbonate chemistry module for the existing quasi-operational regional model, SalishSeaCast, that will be run operationally by the MOAD group. Model results are publicly available to all interested researchers and stakeholders, including shellfish farmers, environmental managers, and researchers interested in the effects of changing carbonate chemistry conditions on marine organisms and ecological communities. The model output has already been used in a research project whose aim was to identify the challenges faced by Pacific Northwest shellfish farmers (lead author Evie Morin, MSc thesis from Simon Fraser

University, in preparation for publication). A researcher who focuses on the biological responses of organisms to changing carbonate chemistry conditions also plans to use the carbonate chemistry model output (Matthew Miller, PhD Candidate at the University of Victoria).

5.2.4 Contributions to modelling regional anthropogenic carbon increase

From a scientific point of view, this work is the first to estimate the anthropogenic carbon increase in the entire Salish Sea from the pre-industrial to the present day using a modelling approach. The estimated increase is comparable to that calculated in observational studies (Table 3.1) while simultaneously exhibiting significant spatiotemporal variability that highlights the need for a modelling approach. With the benefit of the model, I was then able to investigate the large-scale effects of this increase on Ω_{arag}, finding a major domain-wide shift to majority undersaturated conditions year-round from the pre-industrial to present-day, due to the system's naturally poorly-buffered state. Using compiled carbonate chemistry observations from around the world, I was then able to demonstrate that carbonate chemistry conditions in the Salish Sea are comparable to those found around the Pacific Rim, suggesting that the insights gained in this system are relevant in similar systems that do not have the benefit of well-tuned, high-resolution coastal models. I then considered the system's inorganic carbon balance from a more quantitative, budget-focused view. I provided a first look at the likely anthropogenic carbon increase in the system from 2017 to 2050 under a conservative emissions scenario (SSP2-4.5) and considered the system's Ω_{arag} response.

This work also developed a careful approach to estimating past and future changes to inorganic carbon conditions at the lateral boundary of the model domain, utilizing local watermass age estimates (Sonnerup et al., 2013) and combining several existing methods (Matsumoto & Gruber, 2005; Gruber et al., 1996) to most accurately estimate the anthropogenic carbon change in each water parcel between scenarios. This approach should be considered for other regional carbon chemistry modelling studies, especially in regions that experience significant variability in present watermasses.

5.3 Future research directions

The work shown here has attempted to fill some of the research gaps surrounding the complex carbonate chemistry balance of the Salish Sea , focusing on broad views of the system as a whole and emphasising effects of the inorganic carbon balance on air-sea CO_2 flux and Ω_{arag}. Inevitably, this process of inquiry has engendered multiple new questions. Here, I outline three directions of further research that I find particularly interesting.

- *How does the inflow of inorganic carbon from the open ocean into the Juan de*

Fuca Strait vary in space and time, and what is the exact origin and fate of this inorganic carbon?

The physical fluxes of water through Juan de Fuca Strait under different flow regimes have been studied extensively previously, and their dynamic and variable nature is well characterized (e.g. LeBlond (1983); R. E. Thomson et al. (2007); MacCready et al. (2021)). Simultaneously, the watermasses existing both in the Juan de Fuca Strait and in the broader Northeast Pacific Ocean are relatively well characterized (e.g. Davenne, Masson, et al. (2001); R. E. Thomson and Krassovski (2010). However, there still exists a gap in understanding how the changing influx of the open-ocean water into the Salish Sea controls the carbon balance of the system.

In this work, I have shown clearly that the influx of this inorganic carbon through the Juan de Fuca boundary plays the dominant role in setting the balance of the carbonate chemistry of the Salish Sea as a whole. Simultaneously, my work showed that the known switches between the estuarine and transient flow regimes in the Juan de Fuca Strait described by Thomson et al (2007) have large effects on carbon transport here. Broadly, summers are characterized by an interannually consistent estuarine-type inflow of relatively old, high-DIC waters driven by canyon-enhanced upwelling into the Juan de Fuca Strait, while winter watermasses are young and lower-DIC, and their flow through the system is more transient in nature.

This sketch is however an oversimplification and merits further consideration. In Chapter 4, I took a first look at quantifying the seasonal and interannual variability of this inorganic carbon inflow, showing that the majority of the significant interannual variability in the transport of inorganic carbon into the system occurs in the winter. However, this first look may be significantly expanded by more fully characterizing the origin of this water, its flow pathways into the system, and residence times within it, with a focus on DIC as a tracer. These flow patterns can then be more directly tied to the fate of the inorganic carbon carried by the water within the Salish Sea and the subsequent effects of this carbon on the system.

- *How do wind and storm patterns contribute to variability in sea surface pCO_2 and CO_2 outgassing, especially in winter?*

This work shows that the Salish Sea is neither a strong source nor a strong sink of atmospheric CO_2 and air-sea CO_2 flux is only a minor component of the system's inorganic carbon balance as a whole. However, episodic events contribute disproportionately to the system's net air-sea CO_2 flux, and these events are heterogeneous in time and space, and futhermore their structure may change as the prevailing wind patterns change in the future. The outgassing of CO_2 requires the co-ocurrence of two factors: a high ΔpCO_2 between the ocean and the atmosphere, typically due to the presence of deeper-origin

water at the surface because of wind mixing or upwelling, and a high wind speed for the subsequent air-sea gas transfer. Untangling these two phenomena and understanding when they do and do not co-occur would be very interesting and have implications well beyond the Salish Sea, and they can easily be studied in this system because these events occur often here and simultaneously well-performing carbonate chemistry model and a high resolution wind model are both available.

- *What is the impact of the changing Ω_{arag} and pH conditions in the Salish Sea on the organisms that live in it?*

The Salish Sea is part of the broader Northeast Pacific coastal ocean, which is at heightened risk of ocean acidification compared to other coastal regions, for example the coastal Atlantic Ocean, due to the naturally carbon-enriched state of its waters (e.g. Stewart-Sinclair, Last, Payne, and Wilding (2020); Mathis et al. (2015)). In this region, the vulnerability of both natural ecosystems and multiple species of commercial interest has been the subject of significant study and policy focus in recent years (Adelsman & Whitely Binder, 2012; Mathis et al., 2015; Ekstrom et al., 2015). Consequently the development of adequate monitoring tools to assess ocean acidification risk in the Pacific Northwest is a noted priority in global ocean observation internationally (e.g. Newton, Feely, Jewett, Williamson, and Mathis (2015)).

This work developed a powerful tool for looking at small-scale coastal carbonate chemistry conditions that form an important part of the ambient environment for a wide variety of organisms. The model has begun to be used by researchers looking at the impact of the changing Salish Sea on the livelihoods of shellfish farmers. It would be a natural extension of this idea to use this model output in conjunction with some of the recently developed pH and Ω_{arag} sensitivity thresholds for different organisms in order to estimate expected effects of the carbonate chemistry shifts on marine ecology (e.g. Gimenez, Waldbusser, Hales, and Keister (2018); Bednaršek et al. (2020)). For example, during my doctorate, in dialogue with ecologists, I and several others performed two pilot studies, not included in this dissertation, concerning the changing viability of Salish Sea Ω_{arag} conditions from preindustrial to present day. It would be very interesting to expand on this work.

References

Adelsman, H., & Whitely Binder, L. (2012). Ocean acidification: From knowledge to action, washington state's strategic response. *Washington State Blue Ribbon Panel on Ocean Acidification. Olympia, Washington Washington Department of Ecology*. → page 111

Allen, S., & Wolfe, M. (2013). Hindcast of the timing of the spring phytoplankton bloom in the Strait of Georgia, 1968–2010. *Progress in Oceanography*, *115*, 6–13. → pages 28, 31, 32, 85

Allen, S. E. (2000). On subinertial flow in submarine canyons: Effect of geometry. *Journal of Geophysical Research: Oceans*, *105*(C1), 1285–1297. → pages 52, 56

Allen, S. E., & Hickey, B. M. (2010). Dynamics of advection-driven upwelling over a shelf break submarine canyon. *Journal of Geophysical Research: Oceans*, *115*(C8). → page 8

Anaconda software distribution. (2019). Retrieved from https://anaconda.com

Anderies, J. M., & Beisner, B. E. (2000). Fluctuating environments and phytoplankton community structure: a stochastic model. *The American Naturalist*, *155*(4), 556–569. → page 29

Barton, A., Hales, B., Waldbusser, G. G., Langdon, C., & Feely, R. A. (2012). The pacific oyster, crassostrea gigas, shows negative correlation to naturally elevated carbon dioxide levels: Implications for near-term ocean acidification effects. *Limnology and oceanography*, *57*(3), 698–710. → page 12

Bauer, J. E., Cai, W.-J., Raymond, P. A., Bianchi, T. S., Hopkinson, C. S., & Regnier, P. A. (2013). The changing carbon cycle of the coastal ocean. *Nature*, *504*(7478), 61–70. doi: doi:https://doi.org/10.1038/nature12857 → pages 46, 52, 53

Bednaršek, N., Pelletier, G., Ahmed, A., & Feely, R. A. (2020). Chemical exposure due to anthropogenic ocean acidification increases risks for estuarine calcifiers in the Salish Sea: biogeochemical model scenarios. *Frontiers in Marine Science*, *7*, 580. → pages 10, 111

Behrenfeld, M. J. (2010). Abandoning Sverdrup's critical depth hypothesis on phytoplankton blooms. *Ecology*, *91*(4), 977–989. → pages 8, 18

Belluz, J. D. B., Peña, M. A., Jackson, J. M., & Nemcek, N. (2021). Phytoplankton composition and environmental drivers in the northern Strait of Georgia (Salish Sea), British Columbia, Canada. *Estuaries and Coasts*, 1–21. → page 29

Bianucci, L., Denman, K., & Ianson, D. (2011). Low oxygen and high inorganic carbon on the Vancouver Island Shelf. *Journal of Geophysical Research: Oceans*, *116*(C7). → page 13

Bianucci, L., Long, W., Khangaonkar, T., Pelletier, G., Ahmed, A., Mohamedali, T., … Miller, L. A. (2018). Sensitivity of the regional ocean acidification and carbonate system in Puget Sound to ocean and freshwater inputs. *Elementa: Science of the Anthropocene*, *6*. → page 10

Boldt, J. L., Chandler, P. C., & Javorski, A. (2020). *State of the physical, biological and selected fishery resources of Pacific Canadian marine ecosystems in 2019*. Department of Fisheries and Oceans. → page 32

Bourgeois, T., Orr, J. C., Resplandy, L., Terhaar, J., Ethé, C., Gehlen, M., & Bopp, L.

(2016). Coastal-ocean uptake of anthropogenic carbon. *Biogeosciences*, *13*(14), 4167–4185. → page 9

Brasseale, E., Grason, E. W., McDonald, P. S., Adams, J., & MacCready, P. (2019). Larval transport modeling support for identifying population sources of European Green Crab in the Salish Sea. *Estuaries and Coasts*, *42*(6), 1586–1599. doi: doi:https://doi.org/10.1007/s12237-019-00586-2 → pages 48, 142, 143

Brewer, P. G., & Goldman, J. C. (1976). Alkalinity changes generated by phytoplankton growth. *Limnology and Oceanography*, *21*(1), 108–117. doi: doi:https://doi.org/10.4319/lo.1976.21.1.0108 → page 48

Broecker, W. S. (1982). Tracers in the a sea. *Lamont-Doherty Geological Observatory*. → page 5

Broecker, W. S., Takahashi, T., Simpson, H., & Peng, T.-H. (1979). Fate of fossil fuel carbon dioxide and the global carbon budget. *Science*, *206*(4417), 409–418. → page 59

Cahill, B., Wilkin, J., Fennel, K., Vandemark, D., & Friedrichs, M. A. (2016). Interannual and seasonal variabilities in air-sea co_2 fluxes along the us eastern continental shelf and their sensitivity to increasing air temperatures and variable winds. *Journal of Geophysical Research: Biogeosciences*, *121*(2), 295–311. → pages 10, 11

Cai, W.-J., Feely, R. A., Testa, J. M., Li, M., Evans, W., Alin, S. R., ... others (2021). Natural and anthropogenic drivers of acidification in large estuaries. *Annual Review of Marine Science*, *13*. doi: doi:https://doi.org/10.1146/annurev-marine-010419-011004 → pages 47, 59

Cai, W.-J., Hu, X., Huang, W.-J., Murrell, M. C., Lehrter, J. C., Lohrenz, S. E., ... others (2011). Acidification of subsurface coastal waters enhanced by eutrophication. *Nature geoscience*, *4*(11), 766–770. → page 8

Caldeira, K., & Wickett, M. E. (2003). Anthropogenic carbon and ocean pH. *Nature*, *425*(6956), 365–365. doi: doi:https://doi.org/10.1038/425365a → pages 1, 45

Carter, B. R., Bittig, H. C., Fassbender, A. J., Sharp, J. D., Takeshita, Y., Xu, Y.-Y., ... Barbero, L. (2021). New and updated global empirical seawater property estimation routines. *Limnology and Oceanography: Methods*, *19*(12), 785–809. → page 79

Carter, B. R., Feely, R. A., Wanninkhof, R., Kouketsu, S., Sonnerup, R. E., Pardo, P. C., ... others (2019). Pacific anthropogenic carbon between 1991 and 2017. *Global Biogeochemical Cycles*, *33*(5), 597–617. doi: doi:https://doi.org/10.1029/2018GB006154 → pages 46, 79, 143

Chandler, P., Davelaar, M., Caleb, D., Ianson, D., Gatien, G., Romaine, S., ... Fraser, T. (2021a). *Discrete profile measurements of dissolved inorganic carbon (DIC), total alkalinity (TA), water temperature, salinity, nutrients and dissolved oxygen during the CCGS Vector Water Properties Survey cruise 2014-50 (EXPOCODE 18VT20141027) in the Strait of Georgia, Juan de Fuca Strait of the North American Pacific coast from 2014-10-27 to 2014-10-30.* doi: doi:https://doi.org/10.25921/vr8n-x476 → pages 11, 150

Chandler, P., Davelaar, M., Caleb, D., Ianson, D., Gatien, G., Romaine, S., ... Fraser, T.

(2021b). *Discrete profile measurements of dissolved inorganic carbon (DIC), total alkalinity (TA), water temperature, salinity, nutrients and dissolved oxygen during the CCGS Vector Water Properties Survey cruise 2015-17 (EXPOCODE 18VT20150401) in the Strait of Georgia, Juan de Fuca Strait of the North American Pacific coast from 2015-04-01 to 2015-04-05.* doi: doi:https://doi.org/10.25921/0cnc-x944. → page 11

Chandler, P. C., King, S. A., & Perry, R. I. (2016). *State of the physical, biological and selected fishery resources of Pacific Canadian marine ecosystems in 2016*. Department of Fisheries and Oceans. → page 26

Cloern, J. E., & Dufford, R. (2005). Phytoplankton community ecology: principles applied in San Francisco Bay. *Marine Ecology Progress Series*, *285*, 11–28. → page 29

Collins, A. K., Allen, S. E., & Pawlowicz, R. (2009). The role of wind in determining the timing of the spring bloom in the Strait of Georgia. *Canadian Journal of Fisheries and Aquatic Sciences*, *66*(9), 1597–1616. → page 32

Connolly, T. P., & Hickey, B. M. (2014). Regional impact of submarine canyons during seasonal upwelling. *Journal of Geophysical Research: Oceans*, *119*(2), 953–975. → page 8

Costanza, R., d'Arge, R., De Groot, R., Farber, S., Grasso, M., Hannon, B., ... others (1997). The value of the world's ecosystem services and natural capital. *Nature*, *387*(6630), 253–260. → page 1

Crawford, W. R., & Dewey, R. K. (1989). Turbulence and mixing: Sources of nutrients on the Vancouver Island continental shelf. *Atmosphere-ocean*, *27*(2), 428–442. doi: doi:https://doi.org/10.1080/07055900.1989.9649345 → page 7

Crean, P. (1978). A numerical model of barotropic mixed tides between Vancouver Island and the mainland and its relation to studies of the estuarine circulation. *Elsevier Oceanography Series*, *23*, 283–313. → pages 8, 22, 26, 27

Davenne, E., Masson, D., et al. (2001). Water properties in the straits of georgia and juan de fuca. *Fisheries and Oceans Canada www-sci. pac. dfo-mpo. gc. ca/osap/projects/straitofgeorgia/JdFG_e. pdf*. → page 110

Davis, K. A., Banas, N. S., Giddings, S. N., Siedlecki, S. A., MacCready, P., Lessard, E. J., ... Hickey, B. M. (2014). Estuary-enhanced upwelling of marine nutrients fuels coastal productivity in the US Pacific Northwest. *Journal of Geophysical Research: Oceans*, *119*(12), 8778–8799. → pages 7, 8

Deppe, R. W., Thomson, J., Polagye, B., & Krembs, C. (2018). Predicting deep water intrusions to Puget Sound, WA (USA), and the seasonal modulation of dissolved oxygen. *Estuaries and coasts*, *41*(1), 114–127. → page 27

Dickson, A., & Riley, J. (1979). The estimation of acid dissociation constants in seawater media from potentionmetric titrations with strong base. I. the ionic product of water—Kw. *Marine Chemistry*, *7*(2), 89–99. doi: doi:https://doi.org/10.1016/0304-4203(79)90001-X

Dickson, A. G., Sabine, C. L., & Christian, J. R. (2007). *Guide to best practices for ocean CO_2 measurements.* North Pacific Marine Science Organization. → page 142

Doney, S. C., Fabry, V. J., Feely, R. A., & Kleypas, J. A. (2009). Ocean acidification:

the other co2 problem. *Annual review of marine science*, *1*, 169–192. → pages 3, 4, 6

Dosser, H., Waterman, S., Jackson, J., Hannah, C., Evans, W., & Hunt, B. (2021). Stark physical and biogeochemical differences and implications for ecosystem stressors in the Northeast Pacific coastal ocean. *Journal of Geophysical Research: Oceans*, *126*(11), e2020JC017033. → pages 48, 142

Duarte, C. M., Hendriks, I. E., Moore, T. S., Olsen, Y. S., Steckbauer, A., Ramajo, L., … McCulloch, M. (2013). Is ocean acidification an open-ocean syndrome? Understanding anthropogenic impacts on seawater pH. *Estuaries and Coasts*, *36*(2), 221–236. doi: doi:https://doi.org/10.1007/s12237-013-9594-3 → pages 7, 46

Dutkiewicz, S., Follows, M. J., & Bragg, J. G. (2009). Modeling the coupling of ocean ecology and biogeochemistry. *Global Biogeochemical Cycles*, *23*(4). → page 29

Ebbesmeyer, C. C., & Barnes, C. A. (1980). Control of a fjord basin's dynamics by tidal mixing in embracing sill zones. *Estuarine and Coastal Marine Science*, *11*(3), 311–330. → pages 8, 25, 27

Egleston, E. S., Sabine, C. L., & Morel, F. M. (2010). Revelle revisited: Buffer factors that quantify the response of ocean chemistry to changes in DIC and alkalinity. *Global Biogeochemical Cycles*, *24*(1). doi: doi:https://doi.org/10.1029/2008GB003407

Ekstrom, J. A., Suatoni, L., Cooley, S. R., Pendleton, L. H., Waldbusser, G. G., Cinner, J. E., … Edwards, R., Peter E. T. Portela (2015). Vulnerability and adaptation of US shellfisheries to ocean acidification. *Nature Clim. Change*, *5*(3). doi: doi:10.1038/nclimate2508 → pages 12, 46, 73, 111

Evans, W., Hales, B., Strutton, P. G., & Ianson, D. (2012). Sea-air CO_2 fluxes in the western Canadian coastal ocean. *Progress in Oceanography*, *101*(1), 78–91. doi: doi:Sea-air{CO$_2$}fluxesinthewestern{Canadian}coastalocean → pages 52, 53, 54, 85

Evans, W., Pocock, K., Hare, A., Weekes, C., Hales, B., Jackson, J., … Feely, R. A. (2019). Marine CO_2 patterns in the northern Salish Sea. *Frontiers in Marine Science*, *5*, 536. → pages 14, 29, 47, 50, 55

Fabry, V. J., Seibel, B. A., Feely, R. A., & Orr, J. C. (2008). Impacts of ocean acidification on marine fauna and ecosystem processes. *ICES Journal of Marine Science*, *65*(3), 414–432. doi: doi:https://doi.org/10.1093/icesjms/fsn048 → page 45

Farmer, D., Pawlowicz, R., & Jiang, R. (2002). Tilting separation flows: a mechanism for intense vertical mixing in the coastal ocean. *Dynamics of Atmospheres and Oceans*, *36*(1-3), 43–58. → page 8

Fassbender, A. J., Alin, S. R., Feely, R. A., Sutton, A. J., Newton, J. A., Krembs, C., … others (2018). Seasonal carbonate chemistry variability in marine surface waters of the US Pacific Northwest. *Earth System Science Data*, *10*(3). doi: doi:https://doi.org/10.5194/essd-10-1367-2018 → pages 7, 46, 47, 55

Feely, R. A., Alin, S. R., Carter, B., Bednaršek, N., Hales, B., Chan, F., … others

(2016). Chemical and biological impacts of ocean acidification along the west coast of North America. *Estuarine, Coastal and Shelf Science*, *183*, 260–270. doi: doi:https://doi.org/10.1016/j.ecss.2016.08.043 → pages 6, 9, 55, 143

Feely, R. A., Alin, S. R., Newton, J., Sabine, C. L., Warner, M., Devol, A., … Maloy, C. (2010). The combined effects of ocean acidification, mixing, and respiration on pH and carbonate saturation in an urbanized estuary. *Estuarine, Coastal and Shelf Science*, *88*(4), 442–449. doi: doi:https://doi.org/10.1016/j.ecss.2010.05.004 → pages 8, 14, 47, 55, 59

Feely, R. A., Sabine, C. L., Hernandez-Ayon, J. M., Ianson, D., & Hales, B. (2008). Evidence for upwelling of corrosive "acidified" water onto the continental shelf. *Science*, *320*(5882), 1490–1492. doi: doi:10.1126/science.1155676 → pages 9, 46

Feely, R. A., Sabine, C. L., Lee, K., Berelson, W., Kleypas, J., Fabry, V. J., & Millero, F. J. (2004). Impact of anthropogenic CO_2 on the $CaCO_3$ system in the oceans. *Science*, *305*, 362. doi: doi:10.1126/science.1097329 → pages 4, 5, 6, 45

Fennel, K., Alin, S., Barbero, L., Evans, W., Bourgeois, T., Cooley, S., … Aleck Wang, Z. (2019). Carbon cycling in the North American coastal ocean: a synthesis. *Biogeosciences*, *16*(6), 1281–1304. doi: doi:10.5194/bg-16-1281-2019 → pages 9, 46, 53

Fiechter, J., Curchitser, E. N., Edwards, C. A., Chai, F., Goebel, N. L., & Chavez, F. P. (2014). Air-sea co_2 fluxes in the California Current: Impacts of model resolution and coastal topography. *Global Biogeochemical Cycles*, *28*(4), 371–385. → pages 9, 10

Field, C. B., Behrenfeld, M. J., Randerson, J. T., & Falkowski, P. (1998). Primary production of the biosphere: integrating terrestrial and oceanic components. *science*, *281*(5374), 237–240. → page 18

Foreman, M., Lee, D., Morrison, J., Macdonald, S., Barnes, D., & Williams, I. (2001). Simulations and retrospective analyses of fraser watershed flows and temperatures. *Atmosphere-Ocean*, *39*(2), 89–105. → page 73

Foreman, M., Pal, B., & Merryfield, W. (2011). Trends in upwelling and downwelling winds along the British Columbia shelf. *Journal of Geophysical Research: Oceans*, *116*(C10). → page 12

Franco, A. C., Ianson, D., Ross, T., Hamme, R. C., Monahan, A. H., Christian, J. R., … others (2021). Anthropogenic and climatic contributions to observed carbon system trends in the Northeast Pacific. *Global Biogeochemical Cycles*, *35*(7), e2020GB006829. → pages 46, 79

Garcia, H. E., & Gordon, L. I. (1992). Oxygen solubility in seawater: Better fitting equations. *Limnol. Oceanog.*, *37*(6), 1307–1312. doi: doi:https://doi.org/10.4319/lo.1992.37.6.1307 → page 143

Garcia, H. E., & Gordon, L. I. (1993). Erratum: Oxygen solubility in seawater: Better fitting equations. *Limnol. Oceanog.*, *38*(3), 656. → page 143

Gattuso, J.-P., Frankignoulle, M., & Wollast, R. (1998). Carbon and carbonate metabolism in coastal aquatic ecosystems. *Annual Review of Ecology and*

Systematics, *29*(1), 405–434. → pages 5, 7

Gentemann, C. L., Fewings, M. R., & García-Reyes, M. (2017). Satellite sea surface temperatures along the West Coast of the United States during the 2014–2016 northeast Pacific marine heat wave. *Geophysical Research Letters*, *44*(1), 312–319. → page 26

Giddings, S. N., & MacCready, P. (2017). Reverse estuarine circulation due to local and remote wind forcing, enhanced by the presence of along-coast estuaries. *Journal of Geophysical Research: Oceans*, *122*(12), 10184–10205. doi: doi:https://doi.org/10.1002/2016JC012479 → pages 7, 12, 18, 55

Gimenez, I., Waldbusser, G. G., Hales, B., & Keister, J. E. (2018). Ocean acidification stress index for shellfish (oasis): Linking pacific oyster larval survival and exposure to variable carbonate chemistry regimes. *Elementa: Science of the Anthropocene*, *6*. → page 111

Gower, J., King, S., Statham, S., Fox, R., & Young, E. (2013). The Malaspina Dragon: a newly-discovered pattern of the early spring bloom in the Strait of Georgia, British Columbia, Canada. *Progress in Oceanography*, *115*, 181–188. → page 32

Grover, J. P. (1990). Resource competition in a variable environment: phytoplankton growing according to Monod's model. *The American Naturalist*, *136*(6), 771–789. → page 20

Grover, J. P., Hudziak, J., & Grover, J. D. (1997). *Resource competition* (Vol. 19). Springer Science & Business Media. → page 20

Gruber, N., Clement, D., Carter, B. R., Feely, R. A., Van Heuven, S., Hoppema, M., ... others (2019). The oceanic sink for anthropogenic CO_2 from 1994 to 2007. *Science*, *363*(6432), 1193–1199. doi: doi:DOI:10.1126/science.aau5153 → page 45

Gruber, N., Sarmiento, J. L., & Stocker, T. F. (1996). An improved method for detecting anthropogenic CO_2 in the oceans. *Global Biogeochemical Cycles*, *10*(4), 809–837. doi: doi:https://doi.org/10.1029/96GB01608 → pages v, 11, 77, 109, 143

Guinotte, J. M., & Fabry, V. J. (2008). Ocean acidification and its potential effects on marine ecosystems. *Annals of the New York Academy of Sciences*, *1134*(1), 320–342. → page 7

Haidvogel, D. B., Arango, H. G., Hedstrom, K., Beckmann, A., Malanotte-Rizzoli, P., & Shchepetkin, A. F. (2000). Model evaluation experiments in the north atlantic basin: simulations in nonlinear terrain-following coordinates. *Dynamics of atmospheres and oceans*, *32*(3-4), 239–281. → page 9

Haigh, R., Ianson, D., Holt, C. A., Neate, H. E., & Edwards, A. M. (2015). Effects of ocean acidification on temperate coastal marine ecosystems and fisheries in the Northeast Pacific. *PLoS One*, *10*(2). doi: doi:https://doi.org/10.1371/journal.pone.0117533 → pages 1, 6, 7, 12, 45, 89

Haigh, R., & Taylor, F. (1991). Mosaicism of microplankton communities in the northern Strait of Georgia, British Columbia. *Marine Biology*, *110*(2), 301–314. → page 29

Hall, T. M., & Plumb, R. A. (1994). Age as a diagnostic of stratospheric transport.

Journal of Geophysical Research: Atmospheres, *99*(D1), 1059-1070. doi: doi:10.1029/93JD03192 → page 50
Hansen, D. V., & Rattray Jr, M. (1966). Gravitational circulation in straits and estuaries. → page 8
Harley, C. D., Randall Hughes, A., Hultgren, K. M., Miner, B. G., Sorte, C. J., Thornber, C. S., ... Williams, S. L. (2006). The impacts of climate change in coastal marine systems. *Ecology letters*, *9*(2), 228–241. → page 7
Hauri, C., Schultz, C., Hedstrom, K., Danielson, S., Irving, B., Doney, S. C., ... Stock, C. A. (2020). A regional hindcast model simulating ecosystem dynamics, inorganic carbon chemistry, and ocean acidification in the Gulf of Alaska. *Biogeosciences*, *17*(14), 3837–3857. → page 73
Hausfather, Z., & Peters, G. P. (2020). *Emissions–the 'business as usual'story is misleading*. Nature Publishing Group. → page 88
He, Y.-C., Tjiputra, J., Langehaug, H. R., Jeansson, E., Gao, Y., Schwinger, J., & Olsen, A. (2018). A model-based evaluation of the inverse gaussian transit-time distribution method for inferring anthropogenic carbon storage in the ocean. *Journal of Geophysical Research: Oceans*, *123*(3), 1777-1800. doi: doi:10.1002/2017JC013504 → page 51
Hickey, B. M., & Banas, N. S. (2008). Why is the northern end of the California Current System so productive? *Oceanography*, *21*(4), 90–107. → page 8
Huisman, J., Sharples, J., Stroom, J. M., Visser, P. M., Kardinaal, W. E. A., Verspagen, J. M., & Sommeijer, B. (2004). Changes in turbulent mixing shift competition for light between phytoplankton species. *Ecology*, *85*(11), 2960–2970. → page 18
Hunter, J. D. (2007). Matplotlib: A 2d graphics environment. *Computing in Science & Engineering*, *9*(3), 90–95. doi: doi:10.1109/MCSE.2007.55
Ianson, D., & Allen, S. E. (2002). A two-dimensional nitrogen and carbon flux model in a coastal upwelling region. *Global Biogeochemical Cycles*, *16*(1), 11–1. doi: doi:https://doi.org/10.1029/2001GB001451 → pages 48, 52, 83
Ianson, D., Allen, S. E., Moore-Maley, B. L., Johannessen, S. C., Macdonald, & W, R. (2016). Vulnerability of a semienclosed estuarine sea to ocean acidification in contrast with hypoxia. *Geophysical Research Letters*, *43*(11), 5793–5801. → pages 11, 13, 14, 47, 48, 55, 85, 86, 142, 150
Ianson, D., Pond, S., & Parsons, T. (2001). The spring phytoplankton bloom in the coastal temperate ocean: growth criteria and seeding from shallow embayments. *Journal of oceanography*, *57*(6), 723–734. → page 89
IPCC. (2011). *Workshop Report of the Intergovernmental Panel on Climate Change Workshop on Impacts of Ocean Acidification on Marine Biology and Ecosystems* (C. B. Field et al., Eds.). Stanford, USA: Working Group II Technical Support Unit, Carnegie Institution. → page 45
Jarnikova, T., Olson, E. M., Allen, S. E., Ianson, D., & Suchy, K. D. (2021). A clustering approach to determine biophysical provinces and physical drivers of productivity dynamics in a complex coastal sea. *Ocean Science Discussions*, *2021*, 1–36. Retrieved from https://os.copernicus.org/preprints/os-2021-66/ doi: doi:10.5194/os-2021-66 → pages 46, 56
Jiang, L.-Q., Carter, B. R., Feely, R. A., Lauvset, S. K., & Olsen, A. (2019). Surface

ocean pH and buffer capacity: past, present and future. *Scientific reports*, *9*(1), 1–11. → page 46

Jiang, L.-Q., Feely, R. A., Carter, B. R., Greeley, D. J., Gledhill, D. K., & Arzayus, K. M. (2015). Climatological distribution of aragonite saturation state in the global oceans. *Global Biogeochemical Cycles*, *29*(10), 1656-1673. doi: doi:10.1002/2015GB005198 → page 45

Johannessen, S. C., Masson, D., & Macdonald, R. W. (2014). Oxygen in the deep strait of georgia, 1951–2009: The roles of mixing, deep-water renewal, and remineralization of organic carbon. *Limnology and Oceanography*, *59*(1), 211–222. → page 78

Keeling, C. D., Piper, S. C., Bacastow, R. B., Wahlen, M., Whorf, T. P., Heimann, M., & Meijer, H. A. (2005). Atmospheric CO_2 and $^{13}CO_2$ exchange with the terrestrial biosphere and oceans from 1978 to 2000: observations and carbon cycle implications. , 83-113. doi: doi:https://doi.org/10.1007/0-387-27048-5_5 → pages 1, 6, 140

Keppler, L., Landschützer, P., Gruber, N., Lauvset, S., & Stemmler, I. (2020). Seasonal carbon dynamics in the near-global ocean. *Global Biogeochemical Cycles*, e2020GB006571. → page 32

Key, R. M., Olsen, A., van Heuven, S., Lauvset, S. K., Velo, A., Lin, X., ... others (2015). *Global Ocean Data Analysis Project, version 2 (GLODAPv2), ORNL/CDIAC-162, ND-P093*. Carbon Dioxide Information Analysis Center, Oak Ridge National Laboratory. doi: doi:10.3334/CDIAC/OTG.NDP093_GLODAPv2 → page 50

Khangaonkar, T., Long, W., & Xu, W. (2017). Assessment of circulation and inter-basin transport in the Salish Sea including Johnstone Strait and Discovery Islands pathways. *Ocean Modelling*, *109*, 11–32. → page 18

Khangaonkar, T., Nugraha, A., Xu, W., & Balaguru, K. (2019). Salish sea response to global climate change, sea level rise, and future nutrient loads. *Journal of Geophysical Research: Oceans*, *124*(6), 3876–3904. → pages 14, 50, 88

Khangaonkar, T., Nugraha, A., Xu, W., Long, W., Bianucci, L., Ahmed, A., ... Pelletier, G. (2018). Analysis of hypoxia and sensitivity to nutrient pollution in Salish Sea. *Journal of Geophysical Research: Oceans*, *123*(7), 4735–4761. doi: doi:https://doi.org/10.1029/2017JC013650 → page 142

Kluyver, T., Ragan-Kelley, B., Pérez, F., Granger, B., Bussonnier, M., Frederic, J., ... Willing, C. (2016). Jupyter notebooks – a publishing format for reproducible computational workflows. In F. Loizides & B. Schmidt (Eds.), *Positioning and power in academic publishing: Players, agents and agendas* (p. 87 - 90).

Kroeker, K. J., Kordas, R. L., Crim, R. N., & Singh, G. G. (2010). Meta-analysis reveals negative yet variable effects of ocean acidification on marine organisms. *Ecology letters*, *13*(11), 1419–1434. doi: doi:https://doi.org/10.1111/j.1461-0248.2010.01518.x → pages 6, 45

Lachkar, Z., Orr, J., Dutay, J.-C., & Delecluse, P. (2007). Effects of mesoscale eddies on global ocean distributions of cfc-11, co_2, and δ14 c. *Ocean Science*, *3*(4), 461–482. → page 9

Landschützer, P., Gruber, N., Bakker, D. C., Schuster, U., Nakaoka, S.-i., Payne, M. R., … Zeng, J. (2013). A neural network-based estimate of the seasonal to inter-annual variability of the Atlantic Ocean carbon sink. *Biogeosciences*, *10*(11), 7793–7815. → page 32

Landschützer, P., Gruber, N., Bakker, D. C., Stemmler, I., & Six, K. D. (2018). Strengthening seasonal marine CO_2 variations due to increasing atmospheric CO_2. *Nature Climate Change*, *8*(2), 146–150. → page 55

Laruelle, G. G., Cai, W.-J., Hu, X., Gruber, N., Mackenzie, F. T., & Regnier, P. (2018). Continental shelves as a variable but increasing global sink for atmospheric carbon dioxide. *Nature communications*, *9*(1), 454. doi: doi:https://doi.org/10.1038/s41467-017-02738-z → pages 46, 53

LeBlond, P. H. (1983). The Strait of Georgia: functional anatomy of a coastal sea. *Canadian Journal of Fisheries and Aquatic Sciences*, *40*(7), 1033–1063. → pages 12, 19, 22, 27, 46, 57, 110

Lee, K., Kim, T.-W., Byrne, R. H., Millero, F. J., Feely, R. A., & Liu, Y.-M. (2010). The universal ratio of boron to chlorinity for the North Pacific and North Atlantic oceans. *Geochimica et Cosmochimica Acta*, *74*(6), 1801–1811. doi: doi:https://doi.org/10.1016/j.gca.2009.12.027

Legendre, L. (1981). Hydrodynamic control of marine phytoplankton production: the paradox of stability. In *Elsevier oceanography series* (Vol. 32, pp. 191–207). Elsevier. → page 18

Liu, J. (2014). *Evaluation of a NEMO model of the Strait of Georgia and insights into mixing and transport of the Fraser River plume* (Master's thesis, University of British Columbia, Vancouver, British Columbia). Retrieved from https://open.library.ubc.ca/cIRcle/collections/ubctheses/24/items/1.0343600 → page 25

Longhurst, A., Sathyendranath, S., Platt, T., & Caverhill, C. (1995). An estimate of global primary production in the ocean from satellite radiometer data. *Journal of plankton Research*, *17*(6), 1245–1271. → pages 1, 2, 18

Lowe, A. T., Bos, J., & Ruesink, J. (2019). Ecosystem metabolism drives pH variability and modulates long-term ocean acidification in the Northeast Pacific coastal ocean. *Scientific Reports*, *9*(1), 1–11. doi: doi:https://doi.org/10.1038/s41598-018-37764-4 → pages 7, 8, 47

Lueker, T. J., Walker, S. J., Vollmer, M. K., Keeling, R. F., Nevison, C. D., Weiss, R. F., & Garcia, H. E. (2003). Coastal upwelling air-sea fluxes revealed in atmospheric observations of o2/n2, co2 and n2o. *Geophysical Research Letters*, *30*(6). → page 81

MacCready, P., McCabe, R. M., Siedlecki, S. A., Lorenz, M., Giddings, S. N., Bos, J., … Garnier, S. (2020). Estuarine circulation, mixing, and residence times in the Salish Sea. *Journal of Geophysical Research: Oceans*, e2020JC016738. doi: doi:https://doi.org/10.1029/2020JC016738 → pages 48, 142, 143

MacCready, P., McCabe, R. M., Siedlecki, S. A., Lorenz, M., Giddings, S. N., Bos, J., … Garnier, S. (2021). Estuarine circulation, mixing, and residence times in the

Salish Sea. *Journal of Geophysical Research: Oceans*, *126*(2), e2020JC016738. → pages 31, 52, 79, 110

MacCready, P., Siedlecki, S. A., & McCabe, R. M. (2018). Liveocean: a daily forecast model of biogeochemistry in Washington marine waters. → page 11

Mackas, D. L., & Harrison, P. J. (1997). Nitrogenous nutrient sources and sinks in the Juan de Fuca Strait/Strait of Georgia/Puget Sound estuarine system: assessing the potential for eutrophication. *Estuarine, Coastal and Shelf Science*, *44*(1), 1–21. doi: doi:https://doi.org/10.1006/ecss.1996.0110 → pages 31, 52, 142

Madec, G. (2015). *NEMO ocean engine, Note du Pole de Modelisation 27, Institut Pierre-Simon Laplace, France.* ISSN. → pages 47, 137

Madec, G., Bourdallé-Badie, R., Bouttier, P.-A., Bricaud, C., Bruciaferri, D., Calvert, D., … others (2017). NEMO ocean engine. → pages 9, 19

Mahara, N., Pakhomov, E., Dosser, H., & Hunt, B. (2021). How zooplankton communities are shaped in a complex and dynamic coastal system with strong tidal influence. *Estuarine, Coastal and Shelf Science*, *249*, 107103. → page 29

Mangiameli, P., Chen, S. K., & West, D. (1996). A comparison of SOM neural network and hierarchical clustering methods. *European Journal of Operational Research*, *93*(2), 402–417. → page 23

Marshall, J., Hill, C., Perelman, L., & Adcroft, A. (1997). Hydrostatic, quasi-hydrostatic, and nonhydrostatic ocean modeling. *Journal of Geophysical Research: Oceans*, *102*(C3), 5733–5752. → page 9

Masson, D. (2002). Deep water renewal in the Strait of Georgia. *Estuarine, Coastal and Shelf Science*, *54*(1), 115–126. → pages 12, 19, 52

Masson, D., & Cummins, P. F. (2007). Temperature trends and interannual variability in the strait of georgia, british columbia. *Continental Shelf Research*, *27*(5), 634–649. → page 32

Masson, D., & Peña, A. (2009). Chlorophyll distribution in a temperate estuary: The Strait of Georgia and Juan de Fuca Strait. *Estuarine, Coastal and Shelf Science*, *82*(1), 19–28. → pages 13, 19, 22, 30, 46, 56, 57, 83, 107

Mathis, J., Cooley, S., Lucey, N., Colt, S., Ekstrom, J., Hurst, T., … Feely, R. (2015). Ocean acidification risk assessment for Alaska's fishery sector. *Progress in Oceanography*, *136*, 71–91. doi: doi:https://doi.org/10.1016/j.pocean.2014.07.001 → pages 12, 46, 73, 111

Matsumoto, K., & Gruber, N. (2005). How accurate is the estimation of anthropogenic carbon in the ocean? An evaluation of the δc* method. *Global Biogeochemical Cycles*, *19*(3). → pages 11, 77, 109

McKinley, G. A., Fay, A. R., Lovenduski, N. S., & Pilcher, D. J. (2017). Natural variability and anthropogenic trends in the ocean carbon sink. *Annual Review of Marine Science*, *9*(1), 125-150. (PMID: 27620831) doi: doi:10.1146/annurev-marine-010816-060529 → page 45

Meinshausen, M., Nicholls, Z. R., Lewis, J., Gidden, M. J., Vogel, E., Freund, M., … others (2020). The shared socio-economic pathway (SSP) greenhouse gas

concentrations and their extensions to 2500. *Geoscientific Model Development*, *13*(8), 3571–3605. → pages 50, 73, 76, 87, 91

Milbrandt, J. A., Bélair, S., Faucher, M., Vallée, M., Carrera, M. L., & Glazer, A. (2016). The pan-Canadian high resolution (2.5 km) deterministic prediction system. *Weather and Forecasting*, *31*(6), 1791–1816. doi: doi:https://doi.org/10.1175/WAF-D-16-0035.1 → pages 20, 50, 138

Millero, F. J. (2010). Carbonate constants for estuarine waters. *Marine and Freshwater Research*, *61*(2), 139–142. doi: doi:https://doi.org/10.1071/MF09254

Moore, S. K., Mantua, N. J., Newton, J. A., Kawase, M., Warner, M. J., & Kellogg, J. P. (2008). A descriptive analysis of temporal and spatial patterns of variability in Puget Sound oceanographic properties. *Estuarine, Coastal and Shelf Science*, *80*(4), 545–554. → page 27

Moore-Maley, B. L., & Allen, S. E. (2021). Wind driven upwelling and surface nutrient delivery in a semi-enclosed coastal sea. *Ocean Science Discussions*, 1–32. → pages 8, 22, 25, 29, 85

Moore-Maley, B. L., Allen, S. E., & Ianson, D. (2016). Locally driven interannual variability of near-surface pH and Ω_A in the Strait of Georgia. *Journal of Geophysical Research: Oceans*, *121*(3), 1600–1625. doi: doi:https://doi.org/10.1002/2015JC011118 → pages 14, 48, 85, 138

Moore-Maley, B. L., Ianson, D., & Allen, S. E. (2018). The sensitivity of estuarine aragonite saturation state and pH to the carbonate chemistry of a freshet-dominated river. *Biogeosciences*, *15*(12), 3743. doi: doi:https://doi.org/10.5194/bg-15-3743-2018 → pages 8, 57, 80, 89, 141

Morgan, E. J., Lavric, J. V., Arévalo-Martínez, D. L., Bange, H. W., Steinhoff, T., Seifert, T., & Heimann, M. (2019). Air–sea fluxes of greenhouse gases and oxygen in the northern benguela current region during upwelling events. *Biogeosciences*, *16*(20), 4065–4084. → page 81

Morrison, J., Foreman, M., & Masson, D. (2012). A method for estimating monthly freshwater discharge affecting British Columbia coastal waters. *Atmosphere-Ocean*, *50*(1), 1–8. → pages 20, 77, 138

Morrison, J., Quick, M. C., & Foreman, M. G. (2002). Climate change in the Fraser River watershed: flow and temperature projections. *Journal of Hydrology*, *263*(1-4), 230–244. → page 77

Mucci, A., et al. (1983). The solubility of calcite and aragonite in seawater at various salinities, temperatures, and one atmosphere total pressure. *Am. J. Sci*, *283*(7), 780–799. → pages 4, 45

Nakaoka, S.-I., Aoki, S., Nakazawa, T., Hashida, G., Morimoto, S., Yamanouchi, T., & Yoshikawa-Inoue, H. (2006). Temporal and spatial variations of oceanic pco2 and air–sea co2 flux in the greenland sea and the barents sea. *Tellus B: Chemical and Physical Meteorology*, *58*(2), 148–161. → page 81

Nemcek, N., Ianson, D., & Tortell, P. D. (2008). A high-resolution survey of DMS, CO_2, and O_2/Ar distributions in productive coastal waters. *Global*

Biogeochemical Cycles, *22*(2). doi: doi:https://doi.org/10.1029/2006GB002879 → pages 53, 85

Newton, J., Feely, R., Jewett, E., Williamson, P., & Mathis, J. (2015). Global ocean acidification observing network: requirements and governance plan. → page 111

Norman, M., Parampil, S. R., Rutgersson, A., & Sahlée, E. (2013). Influence of coastal upwelling on the air–sea gas exchange of co2 in a baltic sea basin. *Tellus B: Chemical and Physical Meteorology*, *65*(1), 21831. → page 81

Ocean Acidification: From Knowledge to Action. Washington State's Strategic Response. (2012). Washington State Blue Ribbon Panel on Ocean Acidification. Retrieved from https://fortress.wa.gov/ecy/publications/publications/1201015.pdf → page 12

Oliphant, T. E. (2006). *A guide to NumPy* (Vol. 1). Trelgol Publishing USA.

Olsen, A., Key, R. M., Van Heuven, S., Lauvset, S. K., Velo, A., Lin, X., ... others (2016). The Global Ocean Data Analysis Project version 2 (GLODAPv2))–an internally consistent data product for the world ocean. *Earth System Science Data (Online)*, *8*(2), 297–323. doi: doi:10.3334/CDIAC/OTG.NDP093_GLODAPv2 → page 50

Olson, E. M., Allen, S. E., Do, V., Dunphy, M., & Ianson, D. (2020a). Assessment of nutrient supply by a tidal jet in the Northern Strait of Georgia based on a biogeochemical model. *Journal of Geophysical Research: Oceans*, *125*(8), e2019JC015766. → pages 11, 20, 21, 29, 46, 47

Olson, E. M., Allen, S. E., Do, V., Dunphy, M., & Ianson, D. (2020b). Assessment of nutrient supply by a tidal jet in the northern Strait of Georgia based on a biogeochemical model. *Journal of Geophysical Research: Oceans*, *125*(8), e2019JC015766. Retrieved from https://agupubs.onlinelibrary.wiley.com/doi/abs/10.1029/2019JC015766 doi: doi:10.1029/2019JC015766 → page 138

O'Neill, B. C., Tebaldi, C., van Vuuren, D. P., Eyring, V., Friedlingstein, P., Hurtt, G., ... Sanderson, B. M. (2016). The scenario model intercomparison project (scenariomip) for CMIP6. *Geoscientific Model Development*, *9*(9), 3461–3482. Retrieved from https://gmd.copernicus.org/articles/9/3461/2016/ doi: doi:10.5194/gmd-9-3461-2016 → page 50

Orr, & Epitalon, J.-M. (2015). Improved routines to model the ocean carbonate system: mocsy 2.0. *Geoscientific Model Development*, *8*(3), 485–499. doi: doi:https://doi.org/10.5194/gmd-8-485-2015 → pages v, 139

Orr, J. C., Epitalon, J.-M., Dickson, A. G., & Gattuso, J.-P. (2018). Routine uncertainty propagation for the marine carbon dioxide system. *Marine Chemistry*, *207*, 84–107. doi: doi:https://doi.org/10.1016/j.marchem.2018.10.006

Orr, J. C., Fabry, V. J., Aumont, O., Bopp, L., Doney, S. C., Feely, R. A., ... others (2005). Anthropogenic ocean acidification over the twenty-first century and its impact on calcifying organisms. *Nature*, *437*(7059), 681. doi: doi:https://doi.org/10.1038/nature04095 → page 1

Ostle, C., Willliamson, P., Artioli, Y., Bakker, D. C., Birchenough, S., Davis, C. E., ... others (2016). Carbon dioxide and ocean acidification observations in uk waters. synthesis report with a focus on 2010–2015. → page 88

Pacella, S. R., Brown, C. A., Waldbusser, G. G., Labiosa, R. G., & Hales, B. (2018). Seagrass habitat metabolism increases short-term extremes and long-term offset of CO_2 under future ocean acidification. *Proceedings of the National Academy of Sciences*, *115*(15), 3870–3875. doi: doi:https://doi.org/10.1073/pnas.1703445115 → page 8

Pacific Climate Impacts Consortium, U. o. V. (2020). *VIC-GL BCCAQ CMIP5 RVIC: Station Hydrologic Model Output.* Retrieved 2022-01-01, from https://www.pacificclimate.org/data/station-hydrologic-model-output → page 77

Parsons, T., Stronach, J., Borstad, G., Louttit, G., & Perry, R. (1981). Biological fronts in the Strait of Georgia, British Columbia, and their relation to recent measurements of primary productivity. *Mar. Ecol. Prog. Ser*, *6*, 237–242. → page 29

Pawlowicz, R., Hannah, C., & Rosenberger, A. (2019). Lagrangian observations of estuarine residence times, dispersion, and trapping in the Salish Sea. *Estuarine, Coastal and Shelf Science*, *225*, 106246. doi: doi:https://doi.org/10.1016/j.ecss.2019.106246 → page 48

Pawlowicz, R., Riche, O., & Halverson, M. (2007). The circulation and residence time of the Strait of Georgia using a simple mixing-box approach. *Atmosphere-Ocean*, *45*(4), 173–193. doi: doi:https://doi.org/10.3137/ao.450401 → pages 31, 52, 79

Pawlowicz, R., Suzuki, T., Chappell, R., Ta, A., & Esenkulova, S. (2020). Atlas of oceanographic conditions in the Strait of Georgia (2015-2019) based on the Pacific Salmon Foundation's citizen science dataset. *Canadian Technical Report of Fisheries and Aquatic Sciences*, *3374*. → pages 19, 28, 107

Pelletier, G., Roberts, M., Keyzers, M., & Alin, S. R. (2018). Seasonal variation in aragonite saturation in surface waters of Puget Sound–a pilot study. *Elem Sci Anth*, *6*(1). doi: doi:https://doi.org/10.1525/elementa.270 → page 47

Peña, M. A., Masson, D., & Callendar, W. (2016). Annual plankton dynamics in a coupled physical–biological model of the Strait of Georgia, British Columbia. *Progress In Oceanography*, *146*, 58–74. → pages 19, 28, 29, 30, 107

Peng, T.-H., & Wanninkhof, R. (2010). Increase in anthropogenic co2 in the atlantic ocean in the last two decades. *Deep Sea Research Part I: Oceanographic Research Papers*, *57*(6), 755–770. → page 5

Pike, R. G., Redding, T., Moore, R., Winkler, R., Bladon, K., et al. (2010). Compendium of forest hydrology and geomorphology in British Columbia. *Land Management Handbook-Ministry of Forests and Range, British Columbia*(66). → pages 12, 18

Preikshot, D., Beamish, R. J., & Neville, C. M. (2013). A dynamic model describing ecosystem-level changes in the Strait of Georgia from 1960 to 2010. *Progress in Oceanography*, *115*, 28–40. → pages 12, 19

Raven, J., Caldeira, K., Elderfield, H., Hoegh-Guldberg, O., Liss, P., Riebesell, U., … Watson, A. (2005). *Ocean acidification due to increasing atmospheric carbon dioxide*. The Royal Society. → pages 1, 6, 45

Redfield, A. C. (1963). The influence of organisms on the composition of seawater. *The sea*, *2*, 26–77. → page 48

Redfield, A. C., & Goodkind, R. (1929). The significance of the Bohr effect in the respiration and asphyxiation of the squid, Loligo pealei. *Journal of Experimental Biology*, *6*(4), 340–349. → page 6

Riche, O., Johannessen, S. C., & Macdonald, R. W. (2014). Why timing matters in a coastal sea: Trends, variability and tipping points in the Strait of Georgia, canada. *Journal of Marine Systems*, *131*, 36–53. doi: doi:https://doi.org/10.1016/j.jmarsys.2013.11.003 → pages 50, 77

Riley, J., & Tongudai, M. (1967). The major cation/chlorinity ratios in sea water. *Chemical Geology*, *2*, 263–269. → page 4

Ross, T., Du Preez, C., & Ianson, D. (2020). Rapid deep ocean deoxygenation and acidification threaten life on Northeast Pacific seamounts. *Global change biology*, *26*(11), 6424–6444. → page 46

Sabine, C. L., & Feely, R. A. (2007). The oceanic sink for carbon dioxide. *Greenhouse gas sinks*, *31*. → page 6

Salisbury, J., Green, M., Hunt, C., & Campbell, J. (2008). Coastal acidification by rivers: a threat to shellfish? *Eos, Transactions American Geophysical Union*, *89*(50), 513–513. → page 8

Sarmiento, J. L., & Gruber, N. (2006). *Ocean biogeochemical dynamics*. Princeton University Press. → pages 3, 4, 5

Schwalm, C. R., Glendon, S., & Duffy, P. B. (2020). Rcp8. 5 tracks cumulative co2 emissions. *Proceedings of the National Academy of Sciences*, *117*(33), 19656–19657. → page 88

Shrestha, R. R., Schnorbus, M. A., Werner, A. T., & Berland, A. J. (2012). Modelling spatial and temporal variability of hydrologic impacts of climate change in the fraser river basin, british columbia, canada. *Hydrological Processes*, *26*(12), 1840–1860. → page 74

Siedlecki, S., Salisbury, J., Gledhill, D., Bastidas, C., Meseck, S., McGarry, K., … others (2021). Projecting ocean acidification impacts for the gulf of maine to 2050: New tools and expectations. *Elem Sci Anth*, *9*(1), 00062. → page 60

Siedlecki, S. A., Pilcher, D., Howard, E. M., Deutsch, C., MacCready, P., Norton, E. L., … others (2021). Coastal processes modify projections of some climate-driven stressors in the California Current System. *Biogeosciences*, *18*(9), 2871–2890. → pages 10, 73

Siedlecki, S. A., Pilcher, D. J., Hermann, A. J., Coyle, K., & Mathis, J. (2017). The importance of freshwater to spatial variability of aragonite saturation state in the Gulf of Alaska. *Journal of Geophysical Research: Oceans*, *122*(11), 8482–8502. → pages 8, 10

Simpson, E., Ianson, D., & Kohfeld, K. E. (2022). Using endmember models to estimate seasonal carbonate chemistry and acidification sensitivity in temperate estuaries. *Geophysical Research Letters*, e2021GL095579. → pages 77, 80

Sonnerup, R. E., Mecking, S., & Bullister, J. L. (2013). Transit time distributions and oxygen utilization rates in the Northeast Pacific Ocean from chlorofluorocarbons and sulfur hexafluoride. *Deep Sea Research Part I: Oceanographic Research Papers*, *72*, 61–71. doi: doi:https://doi.org/10.1016/j.dsr.2012.10.013 → pages 11, 49, 109, 143

Soontiens, N., & Allen, S. E. (2017). Modelling sensitivities to mixing and advection in a sill-basin estuarine system. *Ocean Modelling*, *112*, 17–32. → pages 11, 19, 22, 47, 137

Soontiens, N., Allen, S. E., Latornell, D., Le Souëf, K., Machuca, I., Paquin, J.-P., … Korabel, V. (2016). Storm surges in the Strait of Georgia simulated with a regional model. *Atmosphere-Ocean*, *54*(1), 1–21. → pages 11, 19, 47, 137, 138

Spalding, C., Finnegan, S., & Fischer, W. W. (2017). Energetic costs of calcification under ocean acidification. *Global Biogeochemical Cycles*, *31*(5), 866-877. doi: doi:10.1002/2016GB005597 → page 45

Starr, M., Himmelman, J. H., & Therriault, J.-C. (1990). Direct coupling of marine invertebrate spawning with phytoplankton blooms. *Science*, *247*(4946), 1071–1074. → page 89

Stewart-Sinclair, P. J., Last, K. S., Payne, B. L., & Wilding, T. A. (2020). A global assessment of the vulnerability of shellfish aquaculture to climate change and ocean acidification. *Ecology and evolution*, *10*(7), 3518–3534. → page 111

St. John, M., Marinone, S., Stronach, J., Harrison, P., Fyfe, J., & Beamish, R. (1993). A horizontally resolving physical–biological model of nitrate concentration and primary productivity in the Strait of Georgia. *Canadian Journal of Fisheries and Aquatic Sciences*, *50*(7), 1456–1466. → page 29

Suchy, K. D., Le Baron, N., Hilborn, A., Perry, R. I., & Costa, M. (2019). Influence of environmental drivers on spatio-temporal dynamics of satellite-derived chlorophyll a in the Strait of Georgia. *Progress in Oceanography*, *176*, 102134. → pages 19, 22, 28, 31, 32

Sutton, J., Johannessen, S., & Macdonald, R. (2013). A nitrogen budget for the Strait of Georgia, British Columbia, with emphasis on particulate nitrogen and dissolved inorganic nitrogen. *Biogeosciences*, *10*(11), 7179–7194. doi: doi:https://doi.org/10.5194/bg-10-7179-2013 → pages 14, 31, 50, 142

Sverdrup, H. (1953). On conditions for the vernal blooming of phytoplankton. *J. Cons. Int. Explor. Mer*, *18*(3), 287–295. → pages 8, 18

Terhaar, J., Orr, J. C., Gehlen, M., Ethé, C., & Bopp, L. (2019). Model constraints on the anthropogenic carbon budget of the Arctic Ocean. *Biogeosciences*, *16*(11), 2343–2367. → page 10

The pandas development team. (2020, February). *pandas-dev/pandas: Pandas.* Zenodo. Retrieved from https://doi.org/10.5281/zenodo.3509134 doi: doi:10.5281/zenodo.3509134

Thomson, R., Miha'ly, S., & Kulikov, E. (2007). Estuarine versus transient flow regimes in Juan de Fuca Strait. *Journal of Geophysical Research*, *112*. doi: doi:10.1029/2006JC003925 → page 26

Thomson, R. E. (1981). *Oceanography of the British Columbia coast*. Ottawa:

Department of Fisheries and Oceans. → pages 8, 19, 25, 27
Thomson, R. E., & Krassovski, M. V. (2010). Poleward reach of the California undercurrent extension. *Journal of Geophysical Research: Oceans*, *115*(C9). doi: doi:https://doi.org/10.1029/2010JC006280 → pages 13, 55, 110
Thomson, R. E., Mihály, S. F., & Kulikov, E. A. (2007). Estuarine versus transient flow regimes in Juan de Fuca Strait. *Journal of Geophysical Research: Oceans*, *112*(C9). → pages 13, 110
Thyng, K. M., Greene, C. A., Hetland, R. D., Zimmerle, H. M., & DiMarco, S. F. (2016). True colors of oceanography. *Oceanography*, *29*(3), 10.
Tortell, P. D., DiTullio, G. R., Sigman, D. M., & Morel, F. M. (2002). Co2 effects on taxonomic composition and nutrient utilization in an equatorial pacific phytoplankton assemblage. *Marine Ecology Progress Series*, *236*, 37–43. → page 7
Umlauf, L., & Burchard, H. (2003). A generic length-scale equation for geophysical turbulence models. *Journal of Marine Research*, *61*(2), 235–265. → pages 22, 137
Valle-Levinson, A., Reyes, C., & Sanay, R. (2003). Effects of bathymetry, friction, and rotation on estuary–ocean exchange. *Journal of Physical Oceanography*, *33*(11), 2375–2393. → page 8
Virtanen, P., Gommers, R., Oliphant, T. E., Haberland, M., Reddy, T., Cournapeau, D., … SciPy 1.0 Contributors (2020). SciPy 1.0: Fundamental Algorithms for Scientific Computing in Python. *Nature Methods*, *17*, 261–272. doi: doi:https://doi.org/10.1038/s41592-019-0686-2
Waldbusser, G. G., Hales, B., Langdon, C. J., Haley, B. A., Schrader, P., Brunner, E. L., … Gimenez, I. (2015). Saturation-state sensitivity of marine bivalve larvae to ocean acidification. *Nature Climate Change*, *5*(3), 273–280. → pages 45, 73
Waldbusser, G. G., & Salisbury, J. E. (2014). Ocean acidification in the coastal zone from an organism's perspective: multiple system parameters, frequency domains, and habitats. *Annual review of marine science*, *6*, 221–247. → pages 1, 8
Wanninkhof, R. (1992). Relationship between wind speed and gas exchange over the ocean. *Journal of Geophysical Research: Oceans*, *97*(C5), 7373–7382. doi: doi:https://doi.org/10.1029/92JC00188
Wanninkhof, R. (2014). Relationship between wind speed and gas exchange over the ocean revisited. *Limnology and Oceanography: Methods*, *12*(6), 351–362. doi: doi:https://doi.org/10.4319/lom.2014.12.351
Ward Jr, J. H. (1963). Hierarchical grouping to optimize an objective function. *Journal of the American Statistical Association*, *58*(301), 236–244. → page 23
Wasser, S. K., Lundin, J. I., Ayres, K., Seely, E., Giles, D., Balcomb, K., … Booth, R. (2017). Population growth is limited by nutritional impacts on pregnancy success in endangered Southern Resident killer whales (Orcinus orca). *PLoS One*, *12*(6), e0179824. → page 19
Weiner, S., & Dove, P. M. (2003). An overview of biomineralization processes and the problem of the vital effect. *Reviews in mineralogy and geochemistry*, *54*(1), 1–29. → pages 3, 4
Weiss, R. (1974). Carbon dioxide in water and seawater: the solubility of a non-ideal gas. *Marine chemistry*, *2*(3), 203–215. doi:

doi:https://doi.org/10.1016/0304-4203(74)90015-2
Willmott, C. J. (1981). On the validation of models. *Physical geography*, *2*(2), 184–194. doi: doi:https://doi.org/10.1080/02723646.1981.10642213
Wishart, D. (1969). 256. note: An algorithm for hierarchical classifications. *Biometrics*, 165–170. → page 23
Wolf-Gladrow, D. A., Zeebe, R. E., Klaas, C., Körtzinger, A., & Dickson, A. G. (2007). Total alkalinity: The explicit conservative expression and its application to biogeochemical processes. *Marine Chemistry*, *106*(1-2), 287–300.
Xue, L., & Cai, W.-J. (2020). Total alkalinity minus dissolved inorganic carbon as a proxy for deciphering ocean acidification mechanisms. *Marine Chemistry*, 103791. doi: doi:https://doi.org/10.1016/j.marchem.2020.103791 → page 59
Yin, K., Goldblatt, R. H., Harrison, P. J., John, M. A. S., Clifford, P. J., & Beamish, R. J. (1997). Importance of wind and river discharge in influencing nutrient dynamics and phytoplankton production in summer in the central Strait of Georgia. *Marine Ecology Progress Series*, *161*, 173–183. → page 29

Appendix A

Appendix to Chapter 2

A.1 Model Evaluation

I evaluate the version of the SalishSeaCast biophysical model used in this clustering analysis regionally against available data from the Department of Fisheries and Oceans Canada (dfo2020), specifically; nitrate, dissolved silica, log-transformed chlorophyll, absolute salinity, and conservative temperature, along with the spread of locations and times of collection (Figures A1, A2; Tables A1, A2).

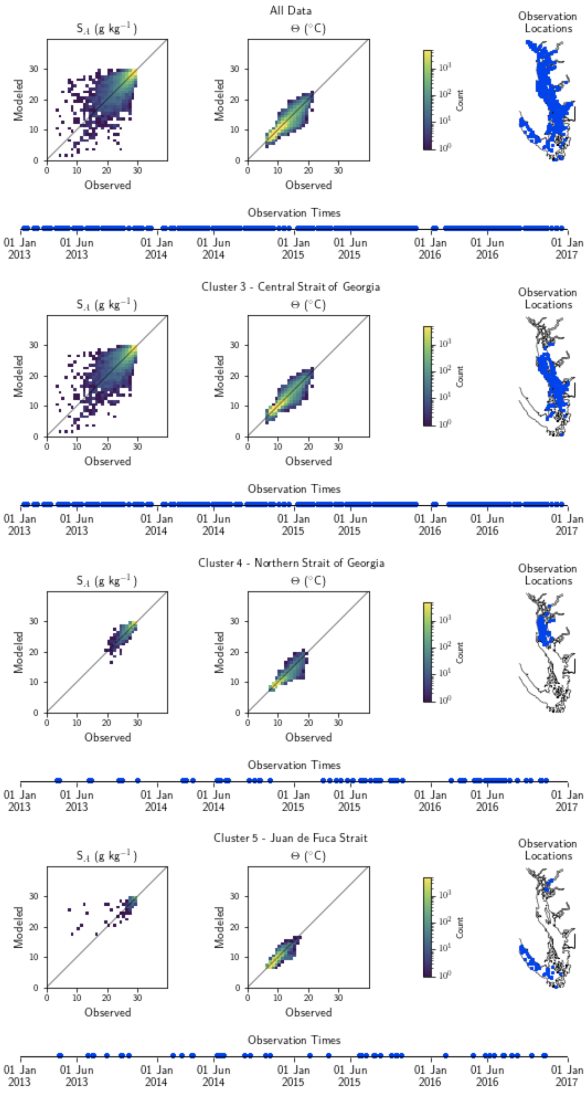

Figure A.1: Model comparison with DFO CTD temperature and salinity data. The plots show modeled vs observed values for salinity and temperature for the entire model domain, as well as points matched only to the three major biological clusters (cluster boundaries are specific to the year of observation). Because of the large amount of data available for comparison, a histogram view is presented. The timeline and rightmost panel display observation times and locations. Summary statistics corresponding to these plots are shown in Table A1.

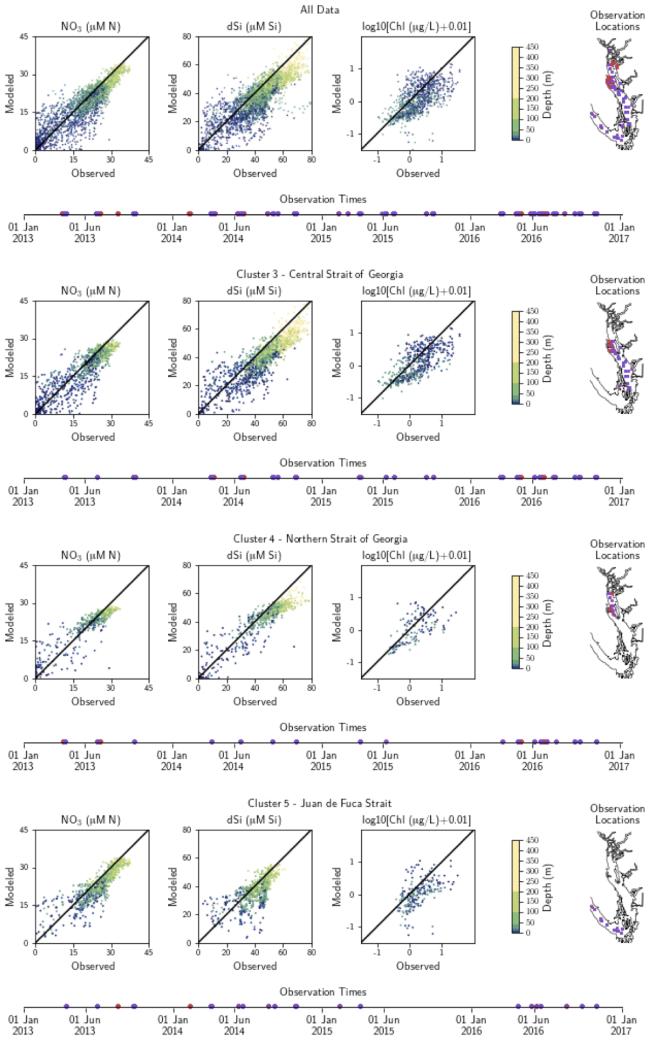

Figure A.2: Model comparison with DFO nitrate, salinity and log-transformed chlorophyll data. The plots show modeled vs observed values for nitrate, salinity and log-transformed chlorophyll for the entire model domain, as well as points matched only to the three major biological clusters (cluster boundaries are specific to the year of observation). The timeline and rightmost panel display observation times and locations. Stations with nutrients but no chlorophyll data are shown in red, while stations with observations of all three parameters are shown in purple. Summary statistics corresponding to these plots are shown in Table A2.

	metric	All data	Cluster 3 (CSoG)	Cluster 4 (NSoG)	Cluster 5 (JdF)
Temperature (°C)	N	502228	308314	56479	37858
	Model Mean	9.5	9.5	9.6	8.7
	Bias	0.01	0.044	-0.075	-0.068
	RMSE	0.47	0.44	0.45	0.51
	WSS	0.967	0.966	0.961	0.966
Salinity g/kg	N	502228	308314	56479	37858
	Model Mean	31	30	30	32
	Bias	0.046	0.067	0.15	-0.066
	RMSE	0.47	0.48	0.32	0.42
	WSS	0.967	0.960	0.970	0.971

Table A.1: Summary statistics corresponding to the model-data comparison of temperature and salinity shown in Fig. A.1. Model bias is low compared to model means, and model bias and skill score do not vary significantly between biological clusters.

	metric	All data	Cluster 3 (CSoG)	Cluster 4 (NSoG)	Cluster 5 (JdF)
Nitrate	N	4732	2212	682	933
	Model Mean	21	22	22	23
	Bias	-2.0	-2.1	-0.94	-2.4
	RMSE	3.9	3.7	3.7	4.3
	WSS	0.94	0.97	0.95	0.90
Dissolved silica	N	4732	2212	682	933
	Model Mean	39	41	42	37
	Bias	-6.2	-7.0	-5.9	-4.2
	RMSE	9.7	9.7	9.1	8.57
	WSS	0.865	0.866	0.913	0.786
Chlorophyll (l10)	N	950	475	133	222
	Model Mean	-0.58	-0.69	-0.71	-0.55
	Bias	-0.23	-0.19	-0.17	-0.28
	RMSE	0.48	0.42	0.43	0.53
	WSS	0.712	0.786	0.757	0.599

Table A.2: Summary statistics corresponding to the model-data comparison of biological variables shown in Fig. A.2. Chlorophyll data are log-10 transformed. Model bias is low compared to model means and RMSE, and model bias and skill score do not vary significantly between biological clusters.

A.2 Changes to biophysical model since first publication

Several adjustments to the biological model have been made from the simulation described in Olson et al. (2020) to the present run. The most significant concerns the silicon cycle. The rate of silica dissolution was adjusted from $3.089 \times 10^{-6} s^{-1}$ to 1.221×10^{-6} s^{-1}, and a bottom flux of silicon of 6.66×10^{-5} mmol $m^{-2} s^{-1}$ was added across the land-ocean interface below 250 m. The sinking rate of biogenic silicon was increased from 1.44×10^{-4} m s^{-1} to 3.108×10^{-4} m s^{-1}. The bottom reflection coefficient for biogenic silicon was increased from 0.8 to 0.92 and the reflection coefficient for diatoms was changed from 0.8 to 0. Additionally, the ratio of diatom silicon to nitrogen content was increased from 1.5 to 1.8 μmol Si:umol N.

Diatom growth parameters were adjusted slightly, with an increase of the optimal light level from 42 W m^{-2} to 45 W m^{-2}, an increase in silicate half saturation constant from 1.2 to 2.2 μM Si, and a 1% decrease in maximum growth rate. The flagellate half saturation constant for ammonium increased from 0.1 to 0.2 μM N.

Several small adjustments were made to grazing rates, prey preferences, and predation threshold, primarily to decrease the minimum standing stock of phytoplankton and increase grazing by microzooplankton relative to mesozooplankton. Additionally, the seasonally varying mesozooplankton maximum grazing level was adjusted slightly, decreasing winter and mid-summer grazing rates and bringing the cycle forward by approximately 5 days. The western boundary and riverine nutrient concentrations have been updated. The namelists specifying these small adjustments are available from the paper's associated GitHub repository.

A.3 Supplementary figures

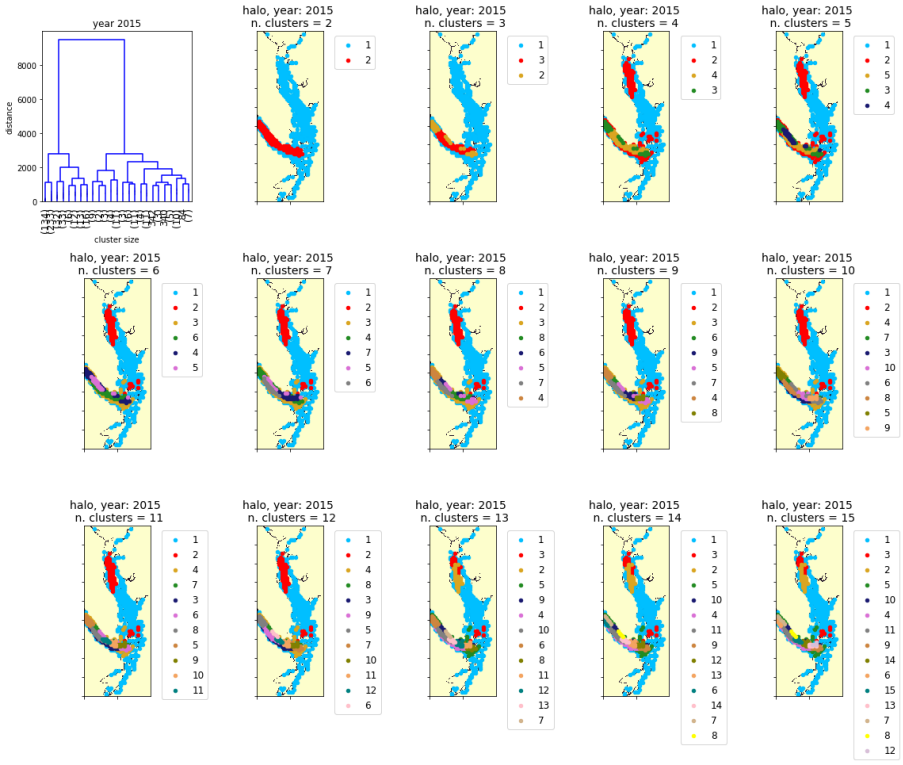

Figure A.3: One example clustering output by Ward's method, for the annual halocline depth signal, year 2015 (see Sections 2.2-2.3).

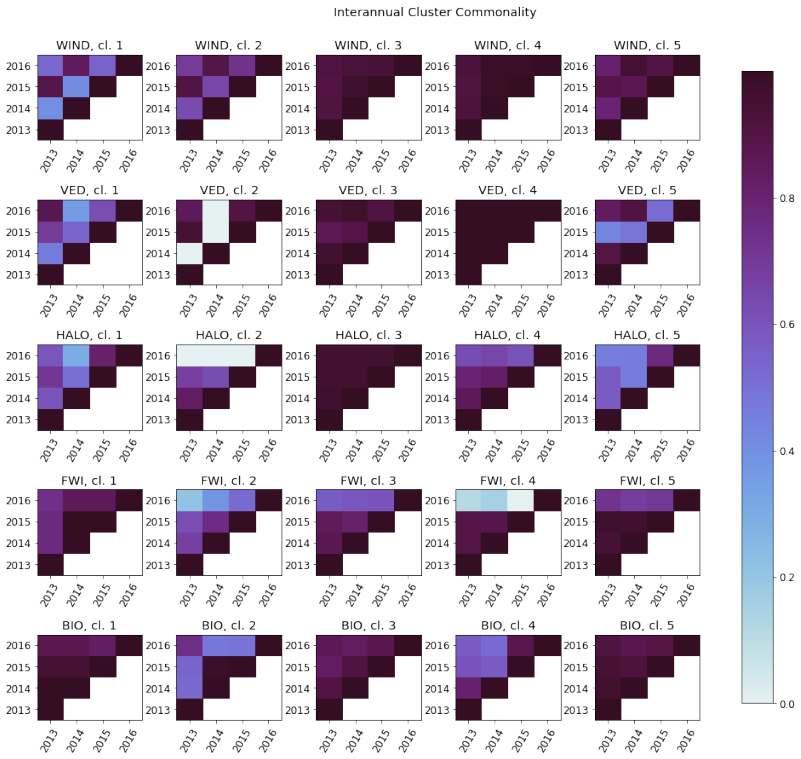

Figure A.4: The interannual cluster commonality metric, measuring interannual cluster persistence for each factor. For any two clusters, cluster commonality varies from 0 (clusters of any size with no stations in common) to 1 (two clusters of equal size with all stations in common) and may be used to compare clusters of unequal sizes.

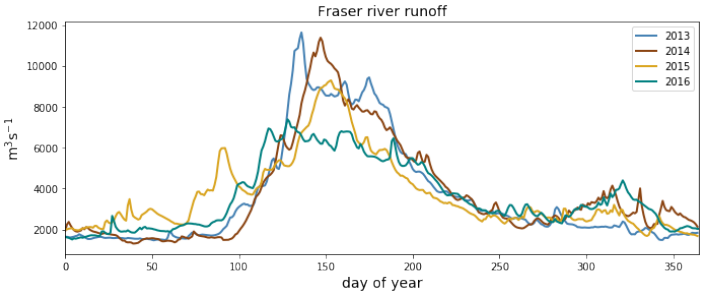

Figure A.5: Fraser river flow at Hope, British Columbia for the four modelled years - from Environment and Climate Change Canada (https://wateroffice.ec.gc.ca/report/real_time_e.html?stn=08MF005, accessed June 2021).

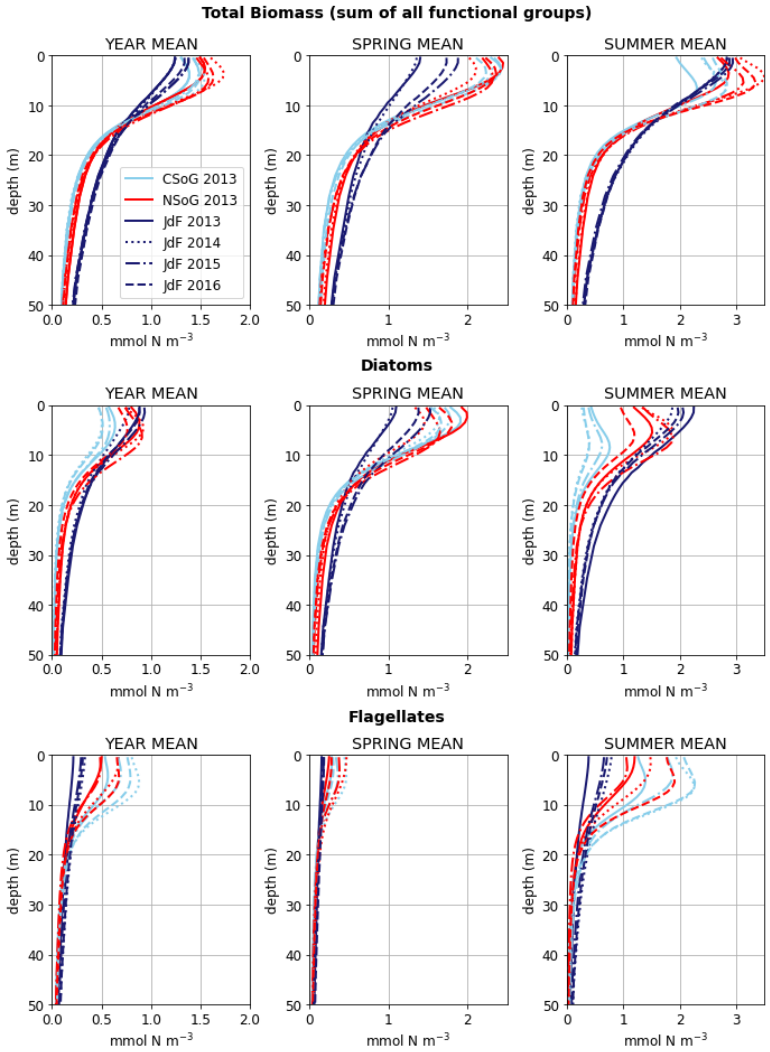

Figure A.6: Mean depth profiles of phytoplankton biomass for the three main biological clusters (CSoG, NSoG, and JdF), for all four modeled years. Spring is defined as March-May, Summer is June-August, Autumn is September-November, and Winter is December-February.

Appendix B

Appendix to Chapter 3

B.1 Expanded model description

B.1.1 Physical model

The biophysical model used in this work is SalishSeaCast, a regional oceanographic model developed for the Salish Sea, using version 3.6 of the NEMO (Nucleus for European Modelling of the Ocean) ocean modelling engine (Madec, 2015). The physical model solves the Reynolds averaged Navier-Stokes equations on an Arakawa-C grid, with a 2 second barotropic timestep, a 2 second vertical advection timestep, and a 40 second baroclinic timestep. The model uses a total variance diminishing (TVD) advection scheme. Vertical turbulence and mixing is calculated through the k-ε configuration of the generic length scale (GLS) turbulence closure (Umlauf & Burchard, 2003; Soontiens & Allen, 2017). The model domain is 898 (y) by 398 (x) horizontal cells, with 40 vertical z-layers, ranging from 1 m resolution at the surface to 27 m resolution at the bottom. Minimum model depth is 4 m. Horizontal resolution is approximately 500 meters, as compared to the 30 km width of the central Strait of Georgia (Freshwater Influenced Region, chapter 3, Fig. 1). The strongest mixing in the domain occurs in the Haro Strait Region, referred to as the Tidal Mixing region in Chapter 3 (Fig. 3.1). SalishSeaCast has two open boundaries, at Juan de Fuca Strait (JdF) and Johnstone Strait (JS), which are forced with eight tidal constituents and sea surface height observations from NOAA's station at Neah Bay (Soontiens et al., 2016). Sea surface height is forced to be 9.8 cm + NOAA observations at the JS boundary for the model run presented in the manuscript. For the continuous contemporary run used for model evaluation, sea surface height is forced to be 5 cm + NOAA observations.

The model is forced with approximately 150 rivers; the Fraser River runoff at Hope, British Columbia, Canada, is taken from the Environment and Climate Change Canada

flow gauge, and the remaining rivers are forced by a climatology (Morrison et al., 2012; Soontiens et al., 2016). Atmospheric forcing is taken from the High Resolution Deterministic Prediction System atmospheric model based on the Global Environmental Multiscale model (Milbrandt et al., 2016). Model results used here are written at daily resolution as netCDF files.

B.1.2 Biological model

I employ a custom biological Nitrate-Phytoplankton-Zooplankton-Detritus (NPZD) model, SMELT (Salish sea Model Ecosystem - Lower Trophic) (Olson, Allen, Do, Dunphy, & Ianson, 2020b), based on a one-dimensional model (Moore-Maley et al., 2016). This model replaces the standard PISCES (Pelagic Interactions Scheme for Carbon and Ecosystem Studies) biogeochemical model in NEMO 3.6. The model represents the transfer of matter between nutrient, primary producer, grazer, and detrital pools, using nitrogen as currency, and tracking a total of 10 tracers (Fig. B.1). The model contains three classes of primary producer (diatoms, flagellates, and the mixotrophic ciliate *Mesodinium rubrum*), two grazers (microzooplankton and mesozooplankton as a closure term), three nutrients (nitrate, ammonium, and dissolved silica), and three detrital pools (biogenic silica, particulate organic nitrogen, and dissolved organic nitrogen). A full discussion of the SMELT biophysical model, including initialization and evaluation, is available in Olson et al. (2020b).

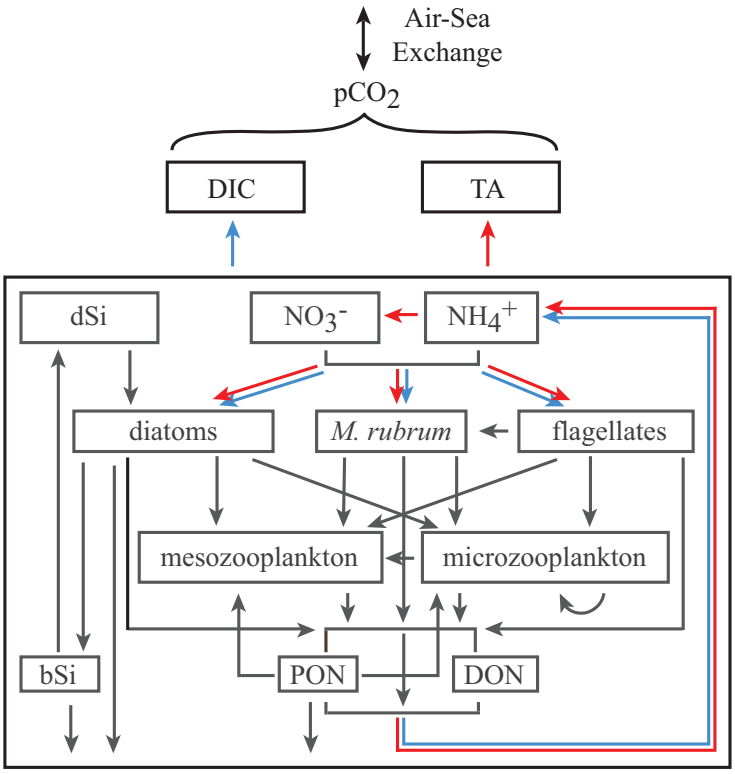

Figure B.1: Pathways represented in the NPZD model, with processes affecting DIC (dissolved inorganic carbon) shown in blue and processes affecting TA (total alkalinity) shown in red. Arrows show direction of flow between tracers; e.g. nitrate $[NO_3^-]$ is taken up by diatoms. *M. rubrum* is *Mesodinium rubrum*, a locally-important ciliate. PON: particulate organic nitrogen; DON: dissolved organic nitrogen; bSi: biogenic silica; dSi: dissolved silica.

B.1.3 Air-sea CO_2 flux

To calculate air-sea flux of CO_2, I replaced the standard PISCES air-sea flux routine with the mocsy (model the ocean carbonate system) series of routines (Orr & Epitalon, 2015) to determine the carbonate system, which explicitly solves for pCO_2 (partial pressure of CO_2) from DIC and TA at every timestep in the surface layer of the model. I used the Lee et al. (2010) formulation for total boron, the Millero (2010) formulation for K_1 and K_2, the first and second dissociation constants of carbonic acid (which allows for salinities less than 20 psu), and the Dickson and Riley (1979) formulation for K_f, the dissociation constant of hydrogen fluoride. CO_2 solubility follows Weiss (1974). Air-sea flux is then

calculated following Wanninkhof (2014), with gas transfer velocity k parameterized as follows:

$$k = \kappa < U^2 > (Sc/660)^{-0.5}$$

Here $< U^2 >$ is the average squared wind speed and Sc is the Schmidt number. The effective value of κ of 0.279 is between those of Wanninkhof (1992) and Wanninkhof (2014) (see Olson et al. (2020) for discussion of effective rates). Initialization of atmospheric CO_2 levels is discussed below.

Pre-industrial and Present-Day Atmospheric CO_2 Forcing

Atmospheric CO_2 forcing includes a seasonal cycle in both the pre-industrial and present-day experimental runs. Because there are no available long timeseries of atmospheric CO_2 observations in the Salish Sea, to estimate the magnitude of this cycle, I averaged the readings from the observational timeseries at La Jolla and Point Barrow (Keeling et al., 2005) (Fig. B.2). These stations are approximately equidistant from my study area, in opposite latitudinal directions. This averaged observational timeseries was then detrended and an average seasonal cycle was found. Because of the shape of the cycle, a composite Gaussian curve was then fit to this average seasonal cycle.

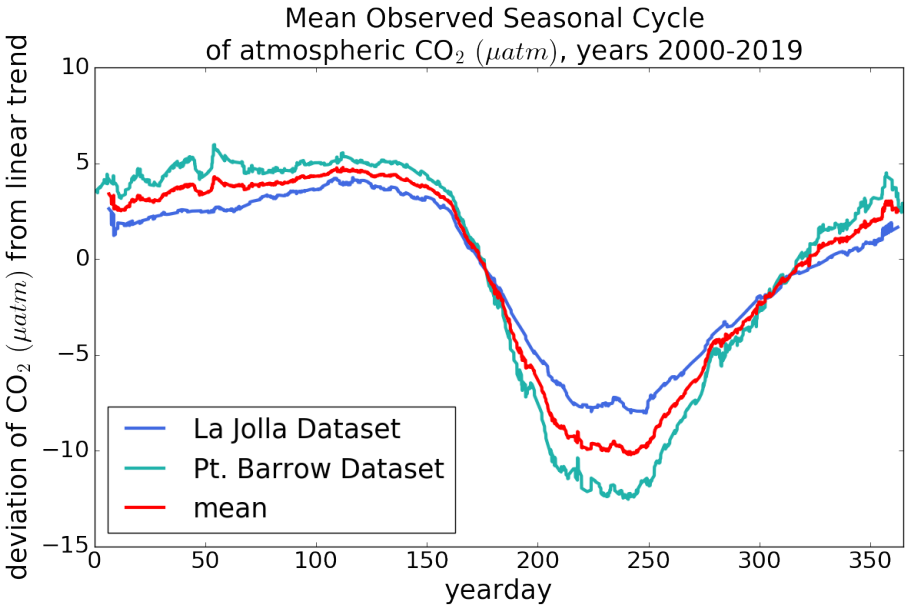

Figure B.2: The mean atmospheric CO_2 seasonal cycle, derived from an average of observations at the La Jolla and Point Barrow stations (years 2000-2019).

The model was then forced with the observed linear increase added to the derived

composite Gaussian curve (Fig. B.3). The amplitude of the seasonal cycle was assumed to be constant between the pre-industrial and present-day runs. The present-day CO_2 values were taken from the calculated Gaussian (409 μatm +/- Gaussian-defined seasonal-cycle), while the pre-industrial CO_2 was assumed to be 280 μatm +/- the Gaussian-defined seasonal cycle shown in Fig. B.2.

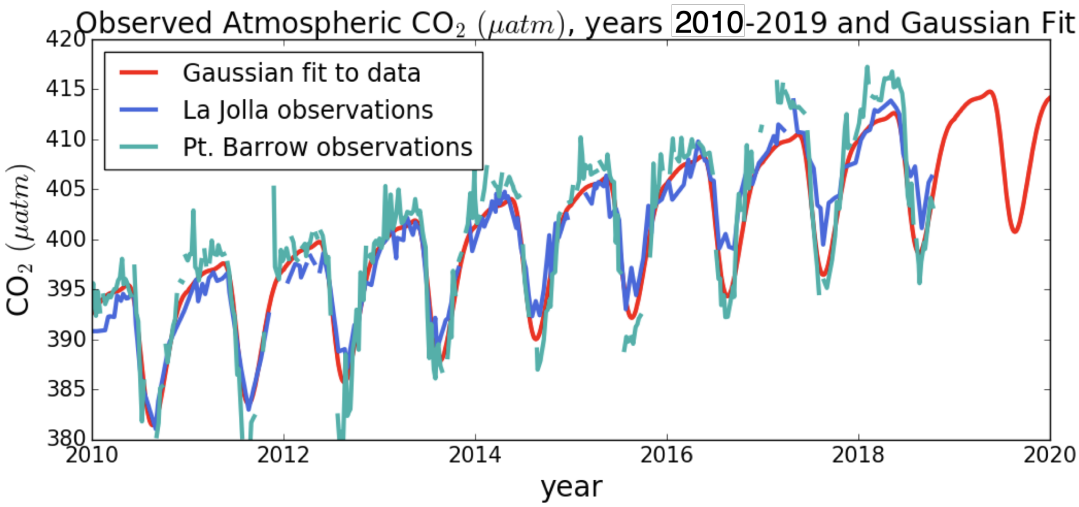

Figure B.3: The atmospheric CO_2 concentrations used in the model, derived from an average of observations at the La Jolla and Point Barrow stations.

B.1.4 River DIC, TA, and nutrient forcing

The Fraser River has constant values of 820 mmol DIC m^{-3} and 750 mmol TA m^{-3}, while the remaining model rivers have constant DIC and TA values of 660 mmol m^{-3} and 630 mmol m^{-3}, respectively. The Fraser River values were chosen to correspond to the mean alkalinity (750 mmol TA m^{-3}) and DIC:TA ratio of approximately 1.089 from the medium carbon scenario of a Fraser River inorganic carbon study; its relatively high carbonate alkalinity is caused by the presence of carbonate minerals in its drainage basin (Moore-Maley et al., 2018). The non-Fraser DIC and TA values were chosen to be close to the mean value of available observations (S. Alin, pers. comm.).

The present-day river nutrient forcing is described in Section 2.2.5 and Supporting Information Text S1 of Olson et al. (2020). Briefly, data available from Environment and Climate Change Canada were supplemented with additional data from MEOPAR sampling efforts to estimate river nutrient concentrations. Seasonal climatologies were calculated for Fraser River silicate and nitrate. Due to limited temporal resolution of observations in other rivers and for Fraser River ammonium, mean nutrient concentrations were applied throughout the year. The total nutrient input due to rivers is a product of the runoff and the concentration, and runoff for rivers other than the Fraser is set by a

climatology. Upper Fraser River runoff is based on measurements at Hope, BC. Riverine inputs of PON, DON, and biogenic silica were not included. I do not expect the omission of terrigenous organic matter to significantly impact my results because riverine nutrient inputs form a small component of the nutrient cycle in the Strait of Georgia (Khangaonkar et al., 2018; Mackas & Harrison, 1997; Sutton et al., 2013).

B.1.5 Model spinup

The model spinup procedure is discussed in Chapter 3 (Section 3.2.1). Here I show the by-layer mean difference of concentrations of DIC and TA in the analyzed year and the preceding year as a measure of model spinup. In both the present-day case and PI case this mean difference was less than 0.1% (Fig. B.4), or approximately 2 mmol m^{-3}, less than the typical analytical uncertainty associated with DIC measurements (A. G. Dickson, Sabine, & Christian, 2007).

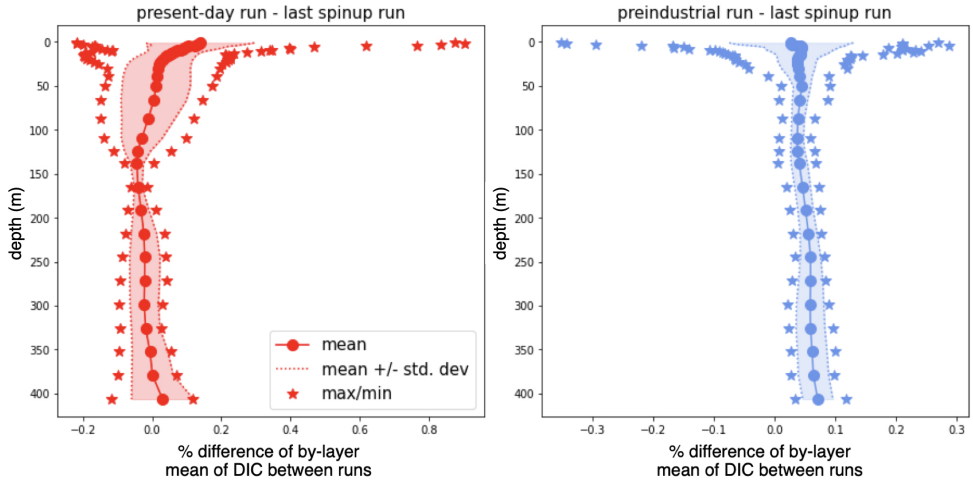

Figure B.4: By-layer percent differences of model DIC concentration between the model year and the previous spinup year, showing mean over the domain, standard deviation, and maximum and minimum.

B.1.6 Lateral boundary conditions

The model's two open boundaries are at Juan de Fuca Strait (JdF) in the west of the domain and at Johnstone Strait (JS) in the north. At the JdF boundary, I used the daily output from the University of Washington's LiveOcean model for all model fields except velocity, sea surface height and biomass (but including DIC and TA) (Brasseale et al., 2019; MacCready et al., 2020). At the JS boundary, I used a monthly climatology (Dosser et al., 2021) and derived DIC and TA from linear relationships with salinity as in the Initial Conditions (Ianson et al., 2016). Data used for the monthly climatology was

collected by the Department of Fisheries and Oceans, the University of British Columbia, and the Hakai Institute.

Estimating pre-industrial DIC levels at the lateral boundaries

Juan de Fuca Strait boundary

I initialized pre-industrial DIC boundary conditions at the Juan de Fuca Strait (western) open ocean boundary based on present-day boundary conditions from the LiveOcean model (Brasseale et al., 2019; MacCready et al., 2020) using a method based on Gruber et al. (1996). Similarly as in Feely et al. (2008), the anthropogenic CO_2 intrusion of these waters was determined in one of two ways. The anthropogenic CO_2 intrusion of the higher density waters (σ_θ >25.0) was calculated using the C* method, based on locally-available cfc-freon-11 watermass age (see section 3.2.3). The cfc tracer method is not appropriate for very young waters, so we do not use it for lower-density waters (σ_θ <25.0). These lower density waters are typically recently-ventilated waters found near the surface and are likely to be tracking the current atmospheric CO_2 concentrations. I used a surface intrusion value of 60 mmol m^{-3} for these waters (σ_θ <25.0); this estimate is within the range of the reported surface values for the shelf values in the region based on (Feely et al., 2016) and the broader open Pacific (Carter et al., 2019). To avoid discontinuities in the carbon field, for every depth profile I then linearly interpolated from a value of 60 mmol m^{-3} at surface to the value at σ_θ =25.0.

Fig. B.5 shows monthly mean present-day DIC, reconstructed pre-industrial DIC, and TA at the western boundary. Fig. B.6 shows the mean monthly anthropogenic DIC intrusion. The impact of the uncertainty in the surface water intrusion (set to 60 mmol m^{-3}) at the boundary on the system will be small, as due to local estuarine circulation, at the western boundary, only a small fraction of the positive water transport into the Salish Sea occurs at (σ_θ <25.0) - less than 15 % of the yearly total at the western boundary (Fig. B.7).

Summary of C* method

Here I summarize my application of the C* method described in Gruber et al. (1996). I first derive an exponential relationship between potential density and cfc-freon 11 estimated watermass age from available observations between 135°W and 125°W longitude (Sonnerup et al., 2013) (Fig. B.8). Second, I apply this relationship to the boundary condition potential density fields to obtain water age for each water parcel. Third, I determine the atmospheric CO_2 that each water parcel saw when it was last at surface. Fourth, I calculate each water parcel's apparent oxygen utilization (AOU) (Garcia & Gordon, 1992, 1993), multiply it by the stoichiometric C:O ratio of 117:170 (Gruber et al., 1996), and

subtract it from the parcel's present-day DIC concentration to remove the remineralized carbon and obtain DIC*, the preformed DIC concentration of the water parcel. Here, the AOU accounts for alterations to DIC due to biological activity that have happened since the watermass was at the surface. Fifth, I use DIC* and assume that salinity, temperature, and TA in the water parcel have not changed in time to calculate pCO_2* (the corresponding preformed pCO_2 to the preformed DIC*). Using the atmospheric CO_2 when the water parcel was last at surface, I next calculate the pCO_2 disequilibrium. Seventh, assuming that the degree of disequilibrium is not changing in time, I can add this disequilibrium value to the pre-industrial atmospheric CO_2 to obtain pre-industrial pCO_2*. From the pre-industrial pCO_2* and unchanged temperature, salinity, and TA fields, I can then calculate pre-industrial DIC*. The difference between pre-industrial DIC* and the present-day DIC* is then ΔDIC, the DIC intrusion. Last, I subtract this ΔDIC from the DIC to get the final pre-industrial DIC concentration for each water parcel.

Johnstone Strait boundary

At the Johnstone Strait boundary, which is relatively distant from the open ocean (see Fig. 3.1), all water is light relative to the Juan de Fuca boundary (maximum σ_θ = 24.7) and is therefore likely to been ventilated recently. In addition, high resolution oxygen data is unavailable there, and therefore I cannot implement the C* method. I therefore set the DIC value of my boundary conditions at the Johnstone Strait boundary using an estimate from Evans et al. (2019), who approximated a 49 μmol kg^{-1} anthropogenic DIC intrusion at the surface in the Northern Salish Sea. To account for the mixing in of older waters from the open ocean with lower intrusion values, I create a linear regression of DIC intrusion vs. salinity. My two end members are the mean monthly surface salinities of Johnstone Strait (assumed intrusion 50 mmol m^{-3}) and the open-ocean Juan de Fuca water at (σ_θ=26.0). The estimated anthropogenic intrusion obtained this way ranges from 46-52 mmol m^{-3}. Fig. B.9 shows monthly mean present-day DIC, reconstructed pre-industrial DIC, and TA at the northern boundary, and Fig. B.10 shows the mean monthly anthropogenic DIC intrusion. The Johnstone Strait open boundary is of secondary importance to the system (Fig B.7); total yearly positive transport of water into the system at the Johnstone Strait boundary is approximately 17% of the total yearly positive transport of water into the system at the Juan de Fuca Strait boundary.

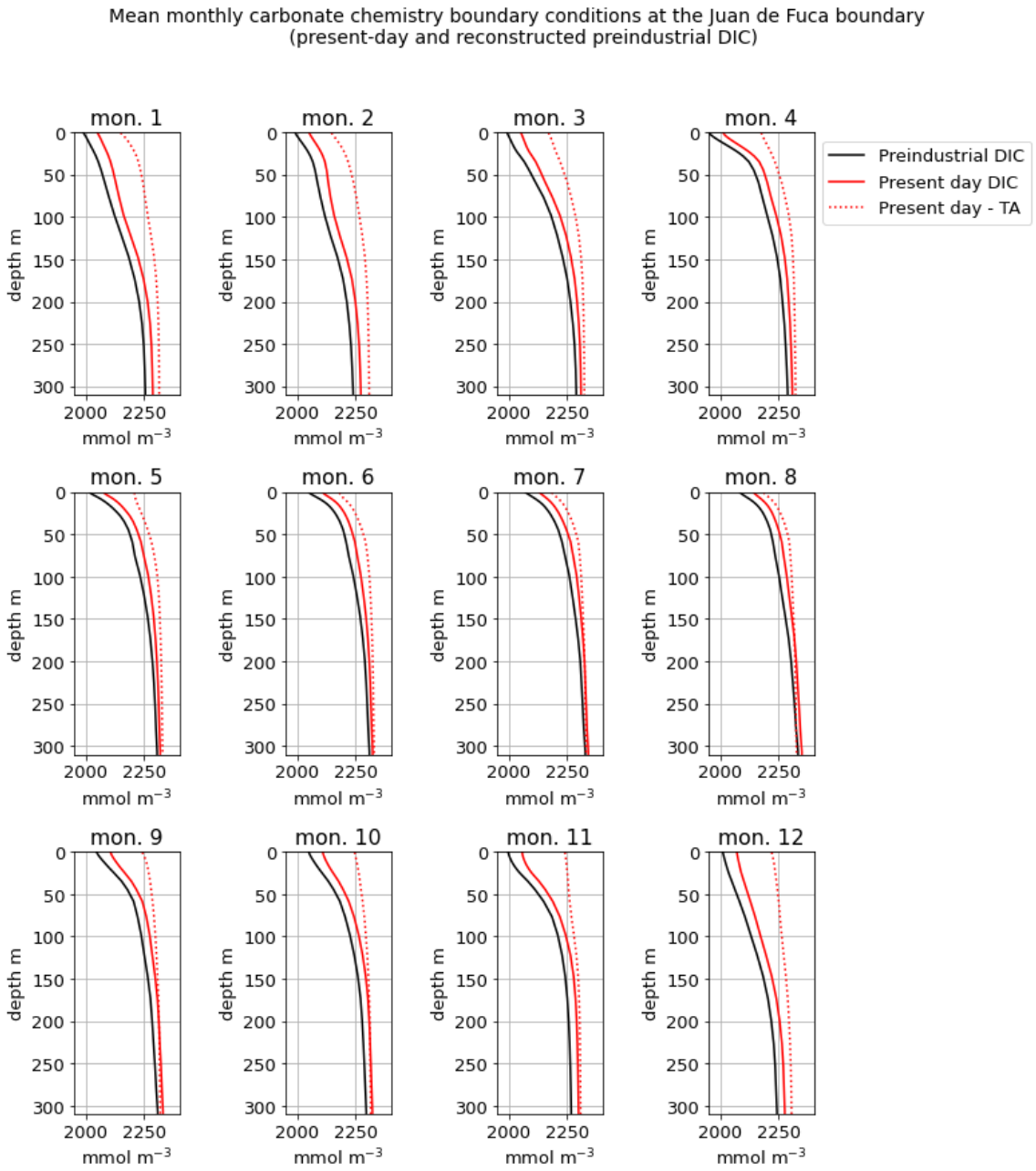

Figure B.5: Mean monthly carbonate chemistry boundary conditions at the Juan de Fuca boundary (present-day and reconstructed pre-industrial DIC, present-day TA). Note that the boundary conditions for Juan de Fuca Strait are calculated daily.

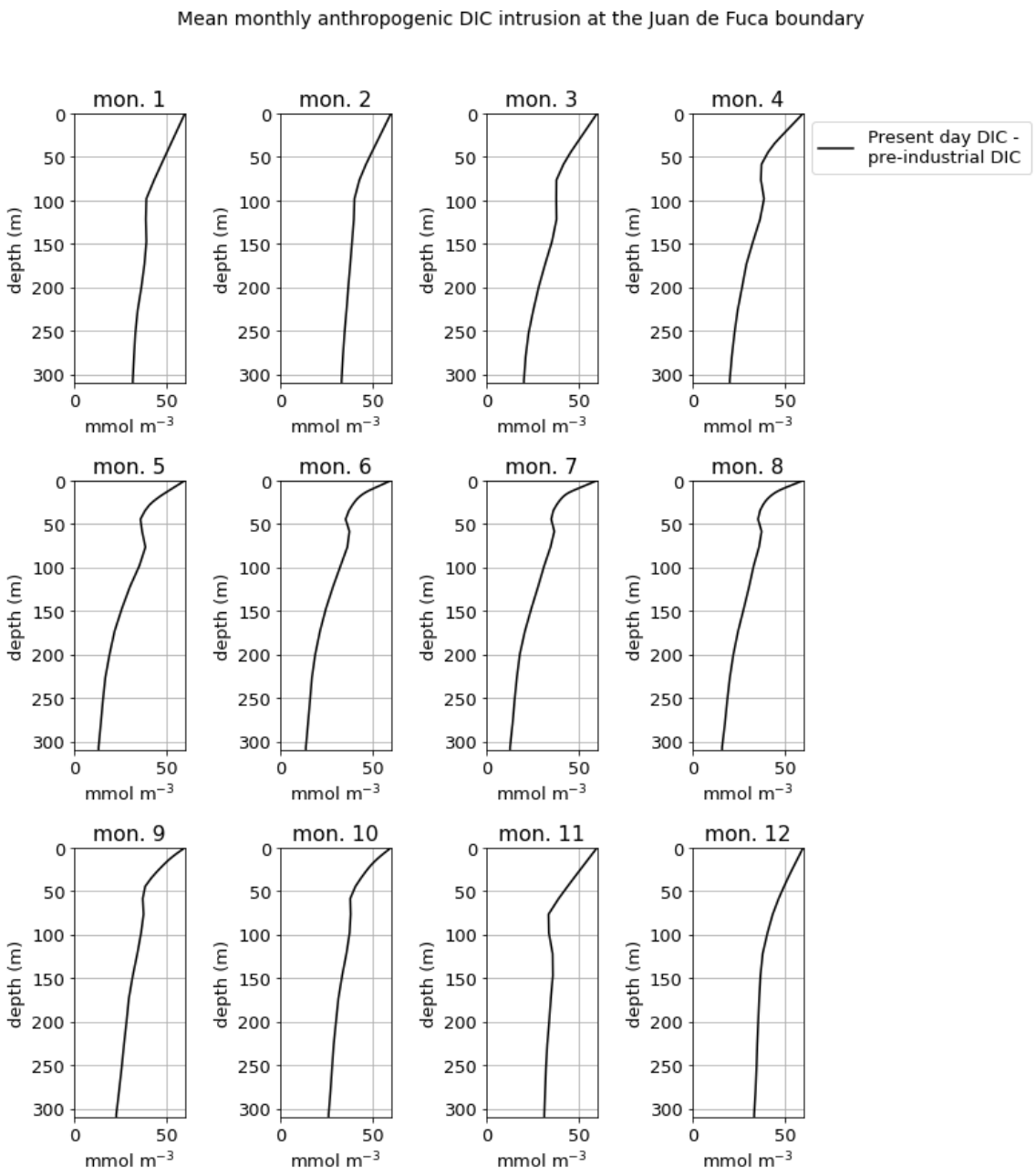

Figure B.6: Mean monthly anthropogenic DIC intrusion at the Juan de Fuca boundary.

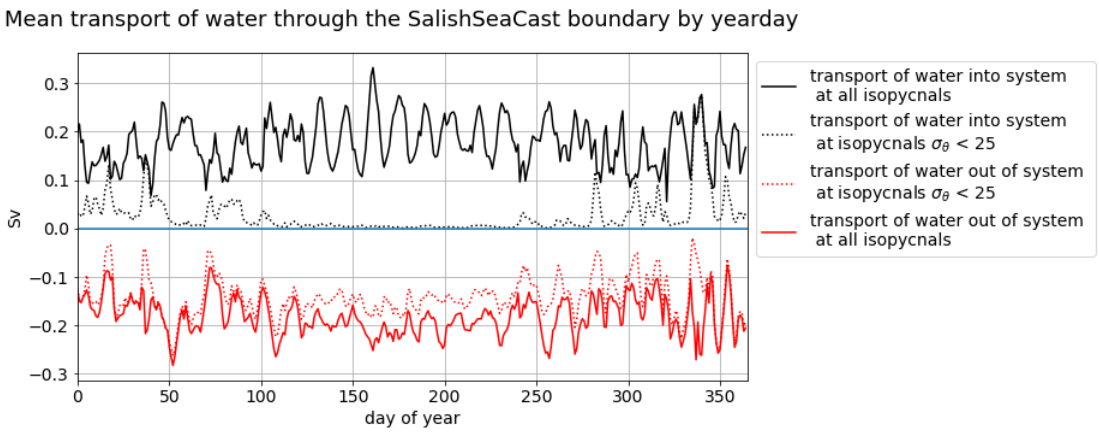

Figure B.7: Daily mean positive and negative water transport at the Juan de Fuca and Johnstone Strait boundaries (Sv), for model year 2015.

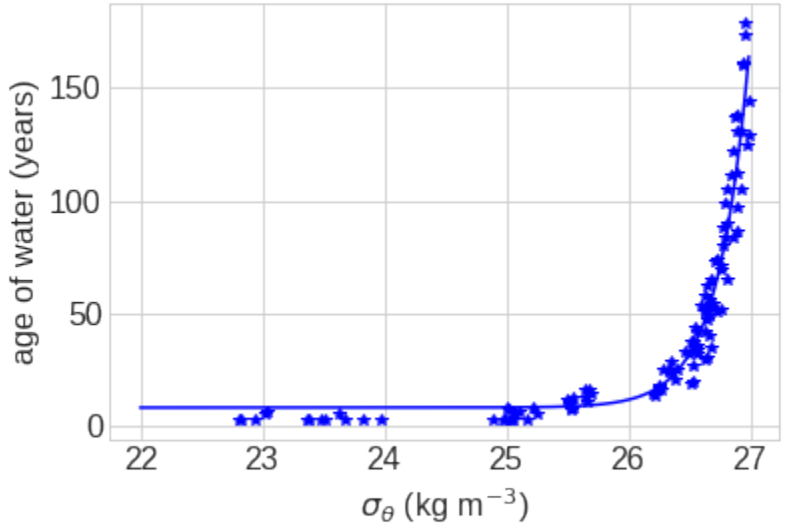

Figure B.8: The derived relationship between potential density and chlorofluorocarbon-11 estimated watermass age, using available observations between -135° and -125° longitude. Stars show the data and the line is the fit. The fit equation is age = 0.13 $e^{-3.85*(25.15-\sigma_\theta)}$ + 8.30.

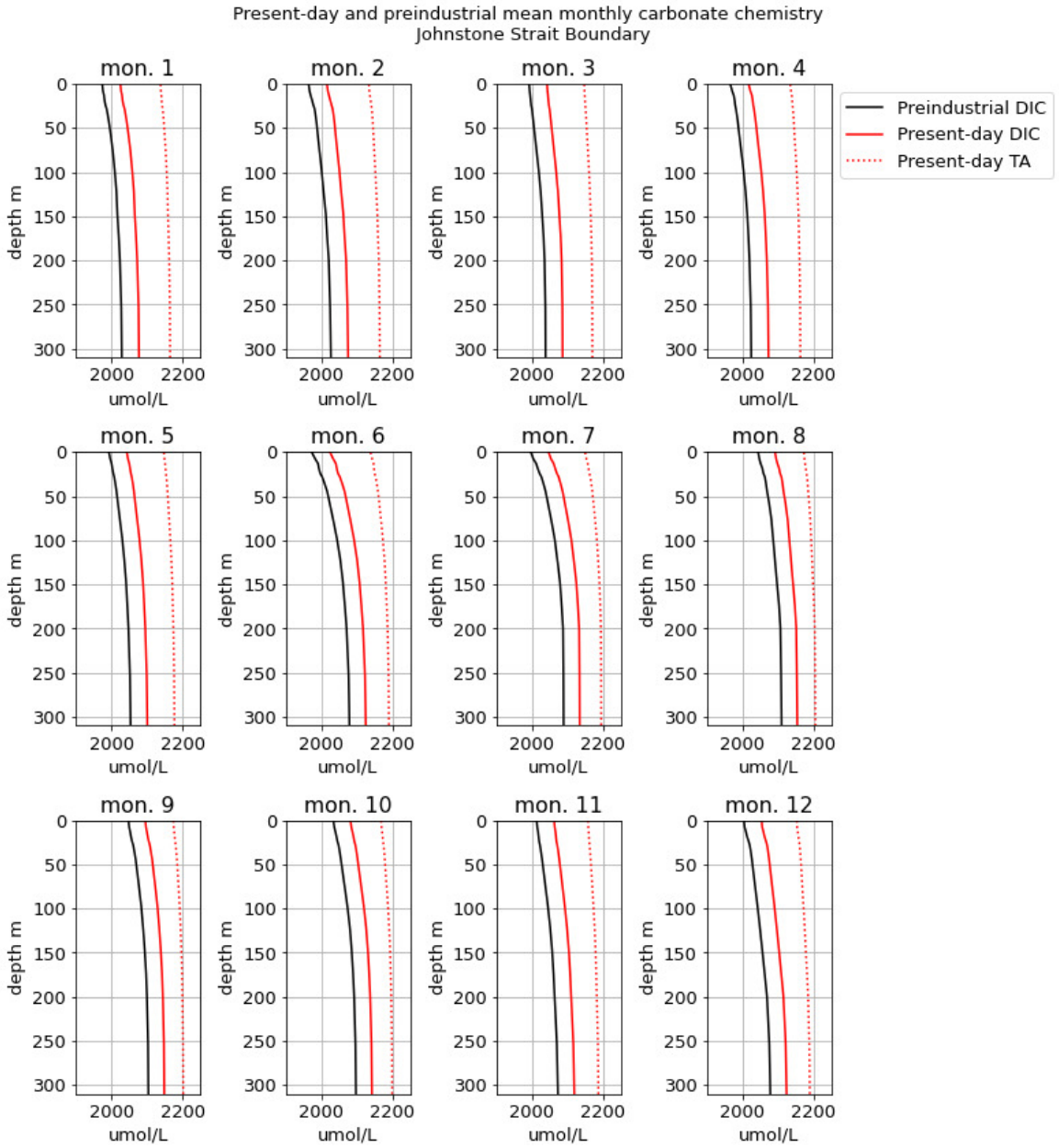

Figure B.9: Mean monthly carbonate chemistry boundary conditions at the Johnstone Strait boundary (present-day and reconstructed pre-industrial DIC, present-day TA). Note that the boundary conditions are calculated monthly at the Johnstone Strait boundary.

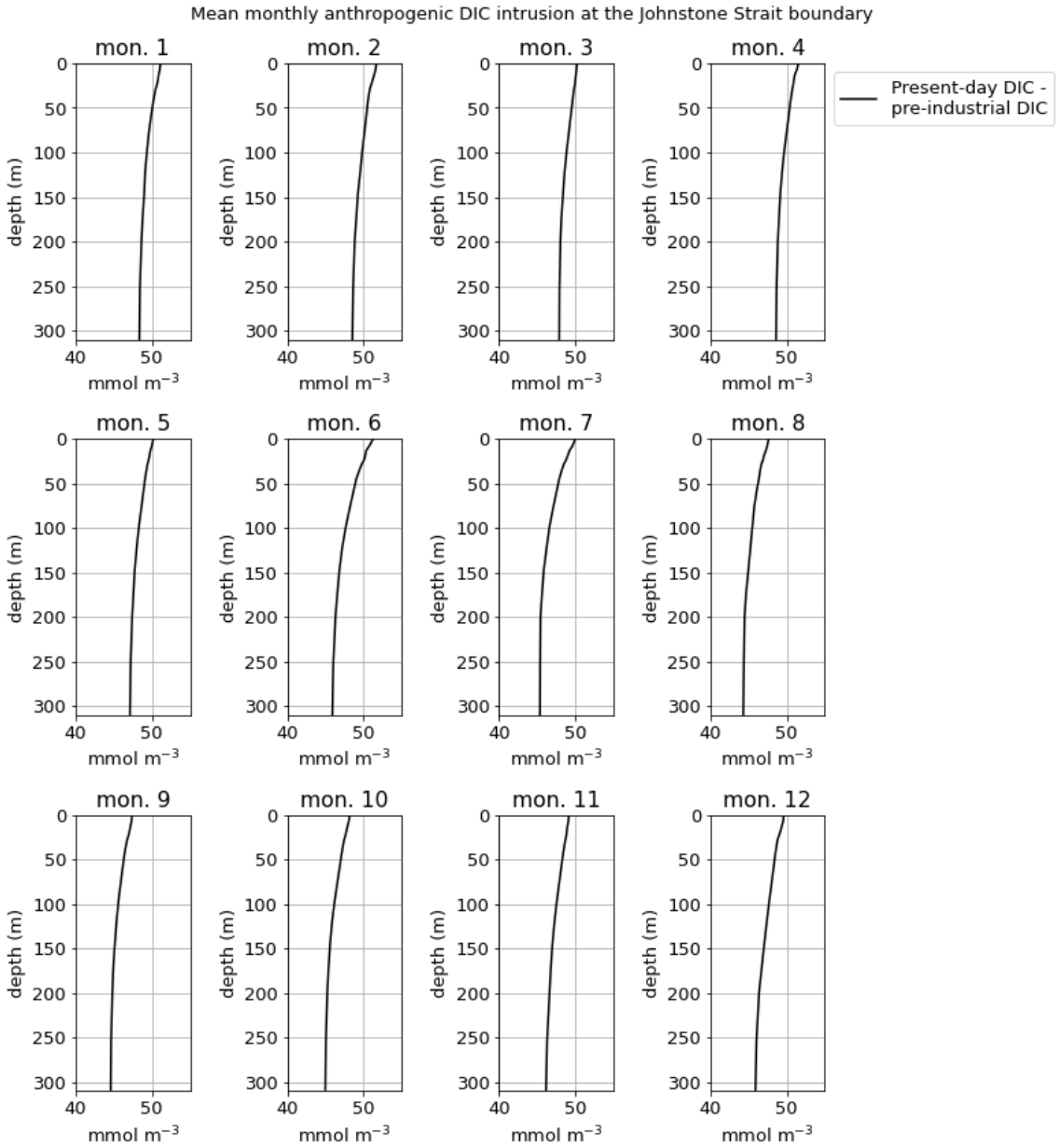

Figure B.10: Mean monthly anthropogenic DIC intrusion at the Johnstone Strait boundary.

B.2 Carbonate chemistry model evaluation

I evaluate model DIC, TA, and calculated Ω_{arag} against available DIC and TA observations. I report key metrics for the evaluation of model salinity and refer the reader to a full evaluation of the biophysical model presented in Olson et al. (2020). I compare air-sea CO_2 fluxes from the model with a year-round survey of observational CO_2 fluxes

in the same region.

B.2.1 DIC, TA, and Ω_{arag}

I evaluate five years of DIC and TA of a contemporary model run (2013-2017) against available observations (Ianson et al., 2016; P. Chandler et al., 2021a) (in μmol kg^{-1}), converted to model units (mmol m^{-3}). The dataset (n = 576) is well resolved in both space and time, though the surface layers are typically overrepresented (Fig. B.11). Because the majority of the evaluation dataset is not collected during the modelled year (2015), at a given yearday and location, I use a salinity-matched evaluation - that is, I evaluate DIC, TA, and Ω_{arag} at the model salinity interpolated to observational salinity. (For example, if the salinity of an observation is 30.2 g kg^{-1} (converted to reference salinity), and the model water column at the given location and yearday has salinities of 30.0 and 30.4 g kg^{-1} at two depths, I interpolate model DIC and TA to a salinity of 30.2 g kg^{-1} using the DIC and TA at 30.0 g kg^{-1} and 30.4 g kg^{-1} as bounds and use this value as the model output corresponding to the given observation. This approach allows us to account for the fact that at a given location, watermass salinity, which acts as a major control on DIC and TA, varies somewhat interannually.

In general, the carbonate chemistry model exhibits high skill: bias and RMSE for DIC and TA is low ($<$1% and $<$2% of modelled quantity, respectively), while the Willmott Skill Score (WSS) is consistently high ($>$0.97 for all 5 years for both quantities (Fig. 2, Table ST1). As Ω_{arag} is a derived quantity dependent on DIC, TA, salinity, and temperature, I may expect slightly lower agreement between model and observations here, and correspondingly WSS decreases to a range of 0.64 - 0.71. A small positive bias is present in the Ω_{arag} (typically < 0.2 units). This bias is typically less than the error in Ω_{arag} (0.05-0.24) associated with measurement uncertainty (4 μmol kg^{-1} for DIC and 10 μmol kg^{-1} for TA) calculated using the error propagation routine of Orr et al. (2018).

The biophysical model also exhibits high skill; a comprehensive evaluation is available in Olson et al. (2020). The Willmott Skill Score, RMSE, and bias for model salinity for the year 2015, calculated from observations collected in year 2015, are as follows: 0.98, 0.82 g kg^{-1}, and 0.02 g kg^{-1} respectively (N=560).

ST1

Table B.1: Range of model evaluation metrics (salinity-matched model evaluation) for DIC, TA, and Ω_{arag} for years 2013-2017, corresponding to the data shown in Fig. 3.2.

	bias	RMSE	WSS
DIC	-11 – -19 (mmol m^{-3})	29 – 40 (mmol m^{-3})	0.97 – 0.98
TA	13 – 18 (mmol m^{-3})	21 – 27 (mmol m^{-3})	0.98 – 0.98
Ω_{arag}	0.17 – 0.28	0.30 – 0.47	0.54 - 0.72

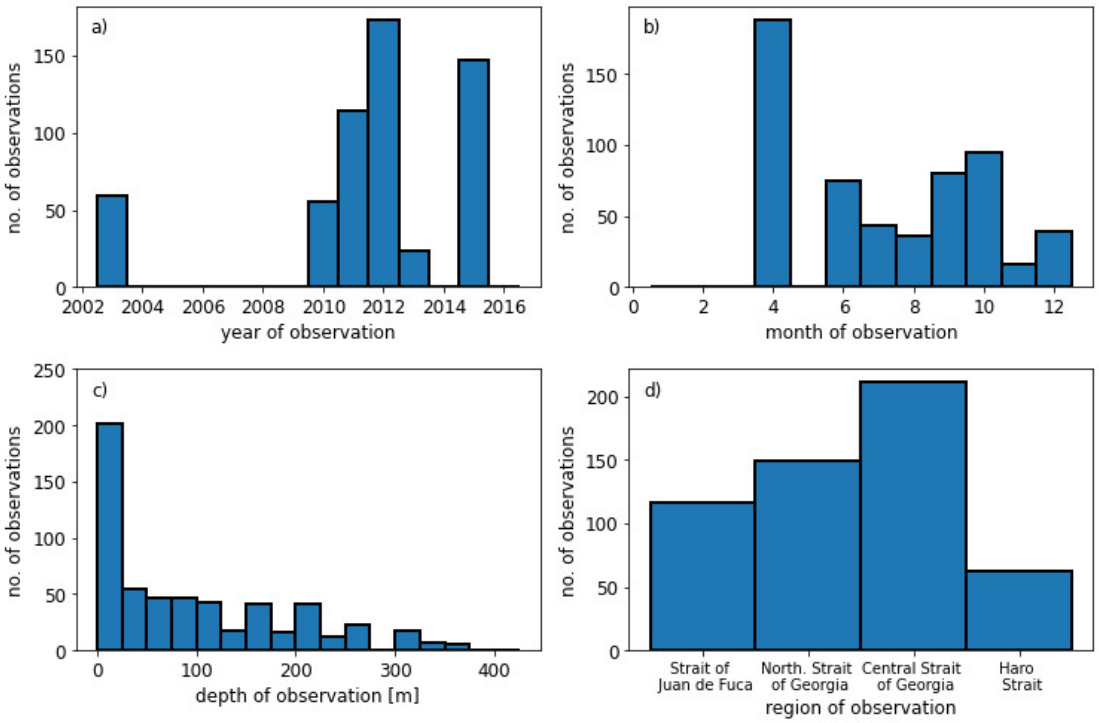

Figure B.11: Histograms of some parameters of the observational dataset used for model evaluation: a) observation year, b) observation month, c) observation depth, d) observation region.

B.3 Supplementary figures

- Fig. B.12: Companion to Fig. 3.3, showing layer-averaged DIC in the domain over the course of a year, as well as Fraser river discharge and mean phytoplankton biomass.
- Fig. B.13: Spatial and temporal air-sea flux distribution for five years (2013-2017) of a contemporary model run.
- Fig. B.14: Depth profiles of Ω_{arag} in for the present-day (solid lines) and pre-industrial (dotted lines) model runs for all three stations in each of the main dynamical regions of the domain.
- Fig. B.15: Contours of $\Omega_{arag} = 1$ and $|\omega_{DIC}| = 0.2$ mM at differing temperatures and salinities
- Fig. B.16: Histograms of Salish Sea model results corresponding to the summary ellipses shown in Fig. 3.7.
- Fig. B.17: The present-day and historical Revelle factor for the surface waters of the domain for the summer (Jun-Aug) and winter (Dec-Feb) seasons.
- Fig. B.18: Available coastal observations in each of the regions in the GLODAP dataset, coloured by Ω_{arag}.
- Fig. B.19: A cumulative distribution function showing the year of emergence of the [TA-DIC] $<$50 mmol m^{-3} signal as a proportion of observations, by ocean region.

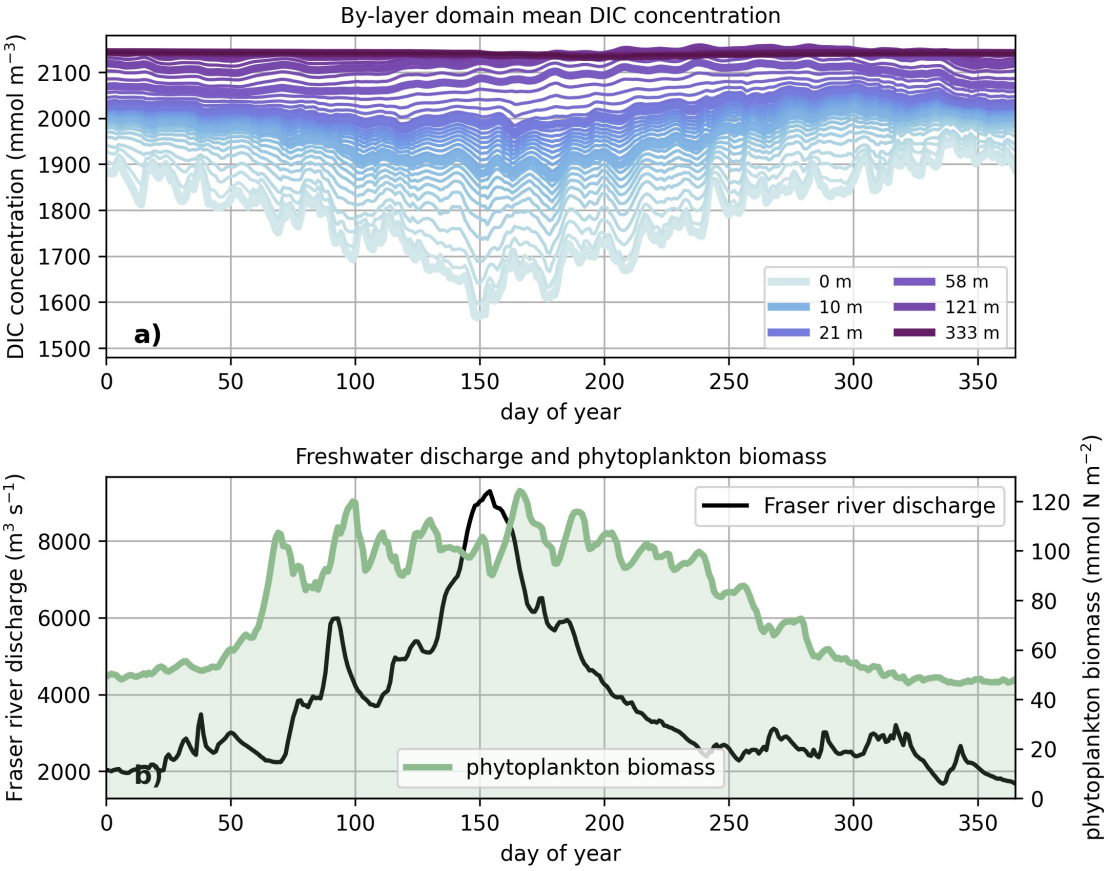

Figure B.12: Companion to Fig. 3.3. Panel (a) shows the changing concentration of layer-averaged DIC in the domain over the course of a year, while panel (b) shows Fraser river discharge and mean model phytoplankton biomass.

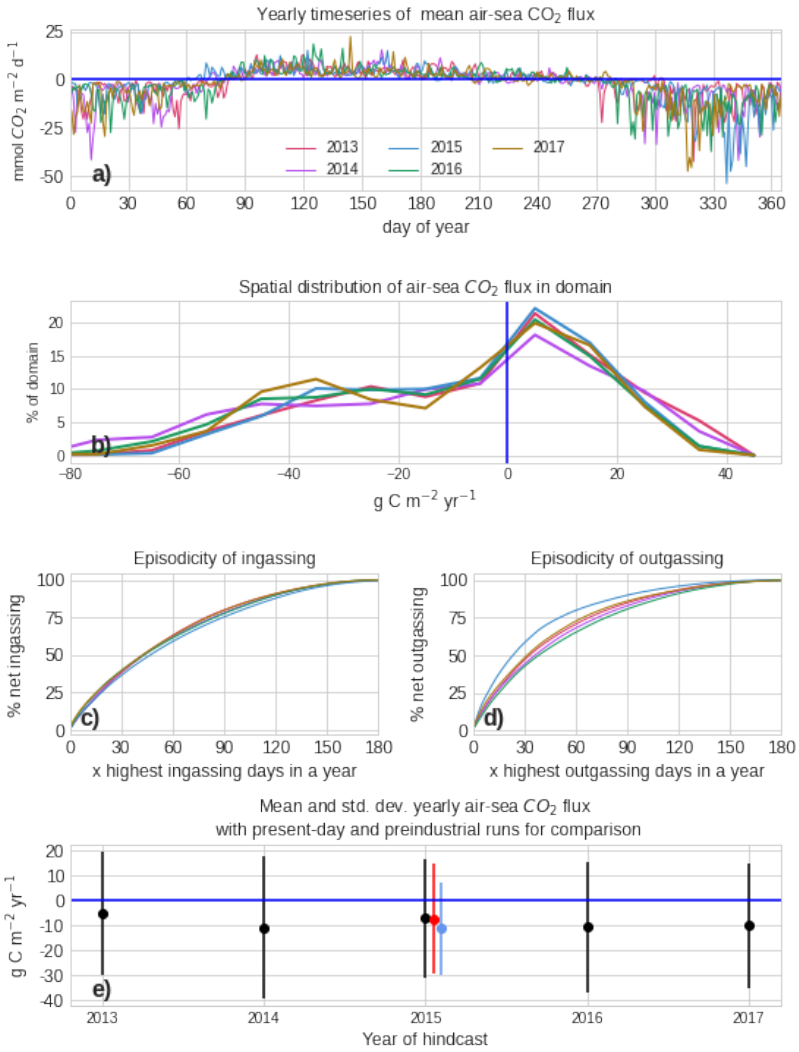

Figure B.13: Spatial and temporal distribution of air-sea CO_2 flux in five years of a contemporary model run. Panel a): daily averaged spatial mean over the domain for 5 years. Panel b): Histogam of yearly-averaged air-sea CO_2 flux by grid cell. Panel c) and d): Number of days contributing a given percent of ingassing and outgassing respectively, averaged over the domain. Panel e): The spatial and temporal mean and spatial standard deviation of five years of model hindcast (black), as well as the spatial and temporal mean and spatial standard deviation of the two model scenarios, which have physical forcing from year 2015 (present-day in red, pre-industrial in blue).

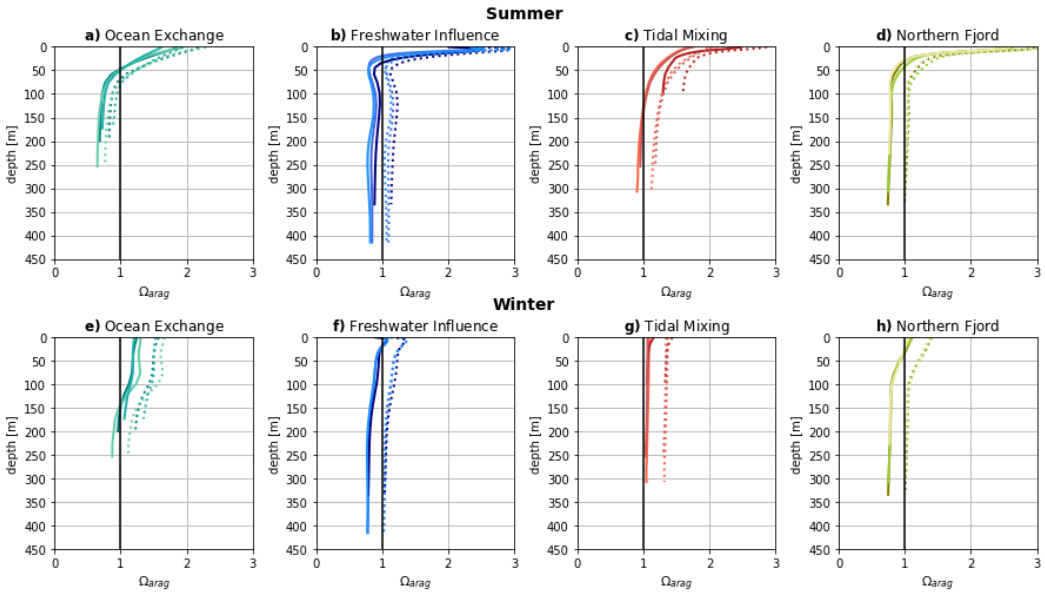

Figure B.14: Companion figure to Fig. 3.6. Depth profiles of Ω_{arag} for the present-day (solid lines) and pre-industrial (dotted lines) model runs in summer (upper panels) and winter (bottom panels) in each of the main dynamical regions of the domain. Colours correspond to each station in Fig. 3.1.

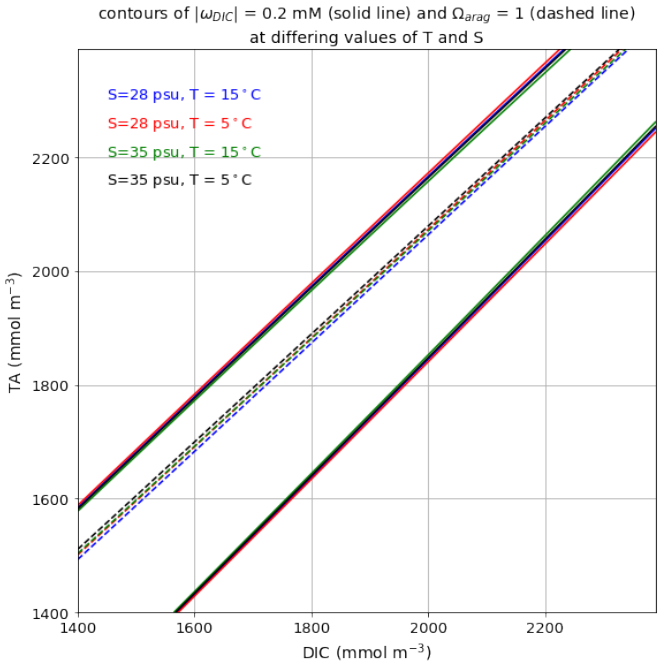

Figure B.15: Contours of $\Omega_{arag} = 1$ and $|\omega_{DIC}| = 0.2$ mM at differing temperatures and salinities. These quantities vary only modestly with temperature and salinity and are instead mostly controlled by the relative concentrations of DIC compared to TA.

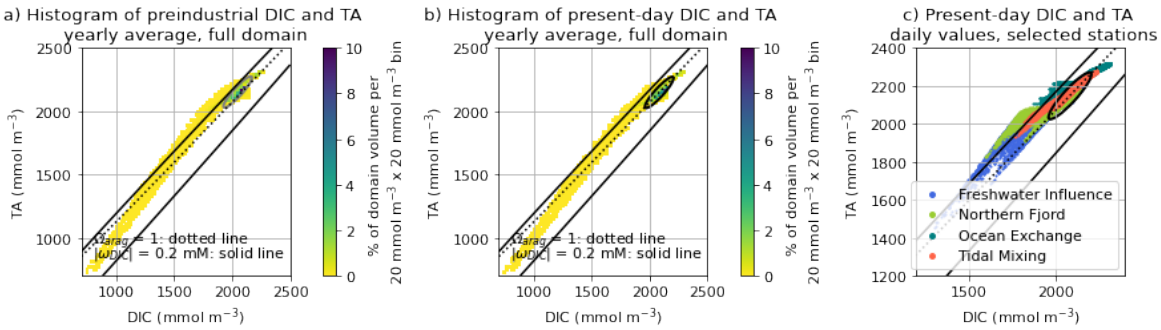

Figure B.16: Two-dimensional histograms of pre-industrial (panel a) and present-day (panel b) annual mean domain-wide Salish Sea DIC and TA data, shown with their summary ellipses, as in Fig. 3.7c. The ellipses that summarize the data are centered on the means of DIC and TA of each regional distribution and show the standard deviation of [TA+DIC] (major axis) and [TA-DIC] (minor axis). In both the present-day and pre-industrial case, approximately 83% of the model domain by volume has DIC and TA values within the summary ellipses. Model salinity ranges from 0 g/kg to 34 g/kg. Note that the global distributions (Fig. S19) do not include fresh water with salinity $<$ 20 psu. Daily values for each of the profile stations in Fig. 3.6 (present-day distribution) are shown in panel c, with one dot shown per model cell.

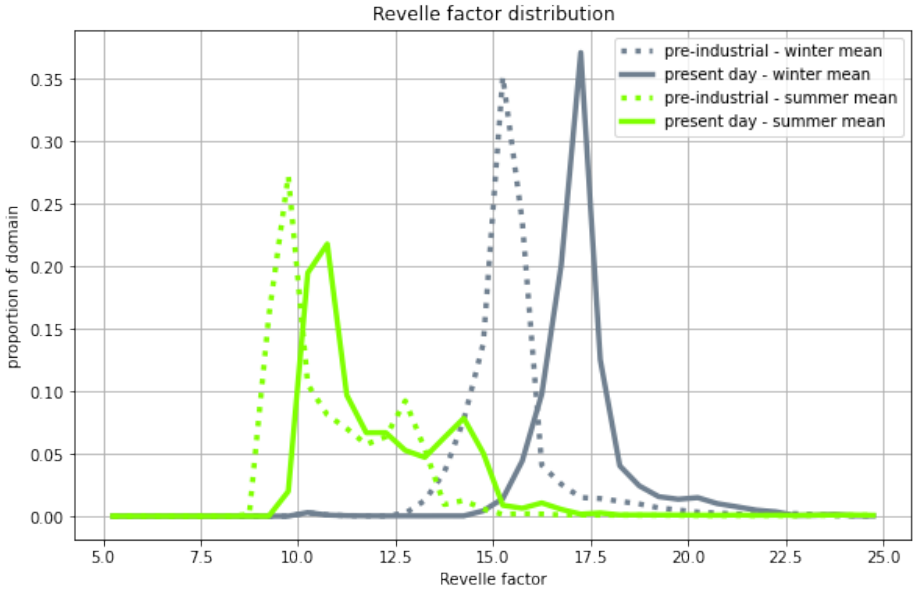

Figure B.17: The present-day and historical Revelle factor for the surface waters of the domain for the summer (Jun-Aug) and winter (Dec-Feb) seasons. The mean surface Revelle factor of the Salish Sea is 12.1 in summer and 17.2 in winter. These values represent an increase of $\sim$1.2-1.7 units from pre-industrial values (on average 10.9 in summer and 15.5 in winter), similar to the Revelle factor increases (0.5-1.6) reported by Feely et al. (2010).

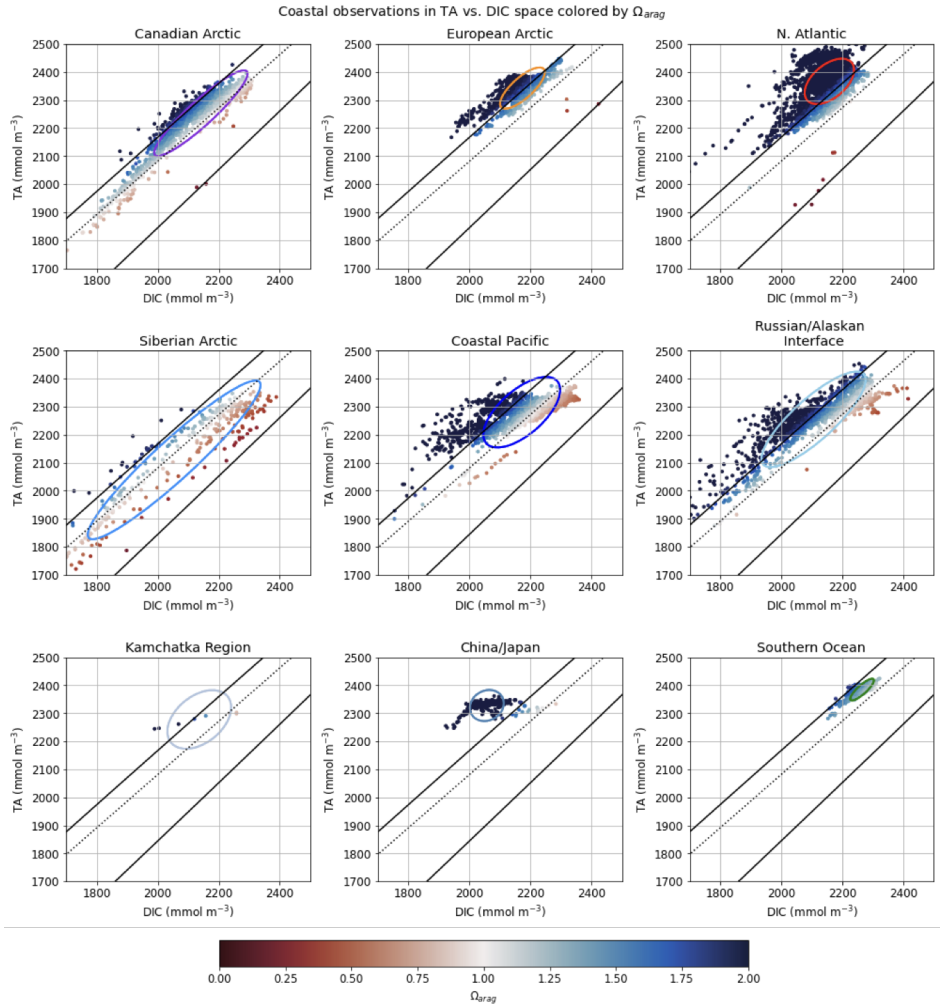

Figure B.18: Available coastal observations in each of the regions discussed in section 3.3.6, coloured by Ω_{arag}, shown with their summary ellipses, shown in Fig. 3.8b. The ellipses that summarize the data are centered on the means of DIC and TA of each regional distribution and show the standard deviation of [TA+DIC] (major axis) and [TA-DIC] (minor axis). Contours at Ω_{arag} = 1 (dotted) and $|\omega_{DIC}|$ = 0.2 mM (solid) are included to guide the viewer.

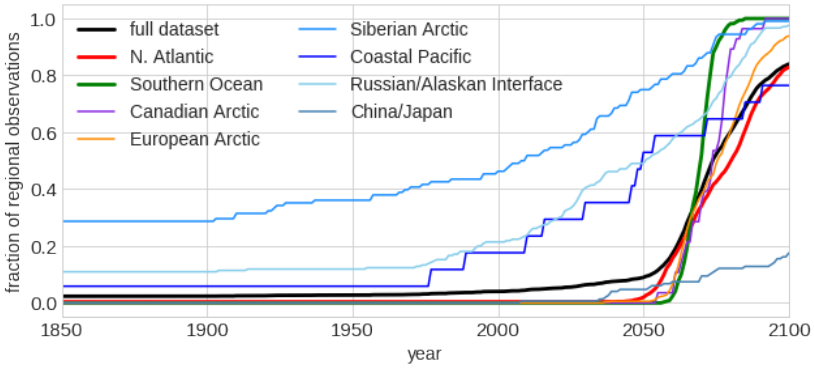

Figure B.19: A cumulative distribution function showing the year of emergence of the
[TA-DIC] <50 mmol m^{-3} signal as a proportion of observations, by ocean region. Regions of younger waters with many observations (the Southern Ocean and the North Atlantic) are highlighted; in addition, the dataset as a whole is shown in black. The North Atlantic and Southern Ocean have later times of emergence of the signal than waters in the Pacific Ocean. Approximately 97% of all Southern Ocean observations, 50% of North Atlantic observations, and 60% of the total dataset cross the [TA-DIC] $<$ 50 mmol m^{-3} threshold by 2080.

Appendix C

Appendix to Chapter 4

C.1 Supplementary figures

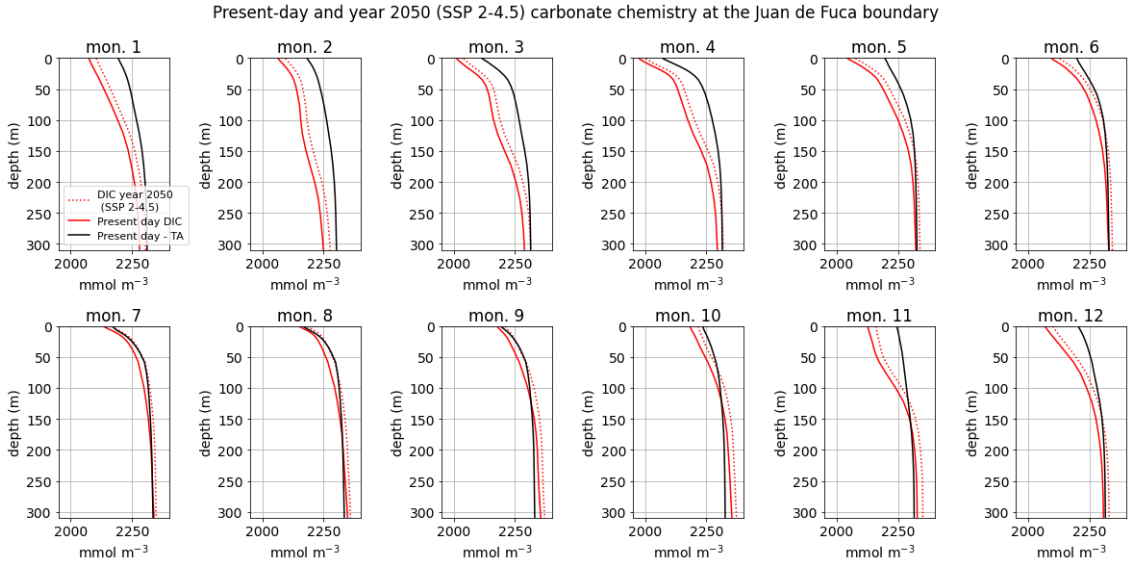

Figure C.1: Average depth profiles of present-day and year 2050 DIC and TA conditions at the Juan de Fuca boundary. DIC is shown in red (solid line = year 2017, dotted line = year 2050), while TA is shown in black.

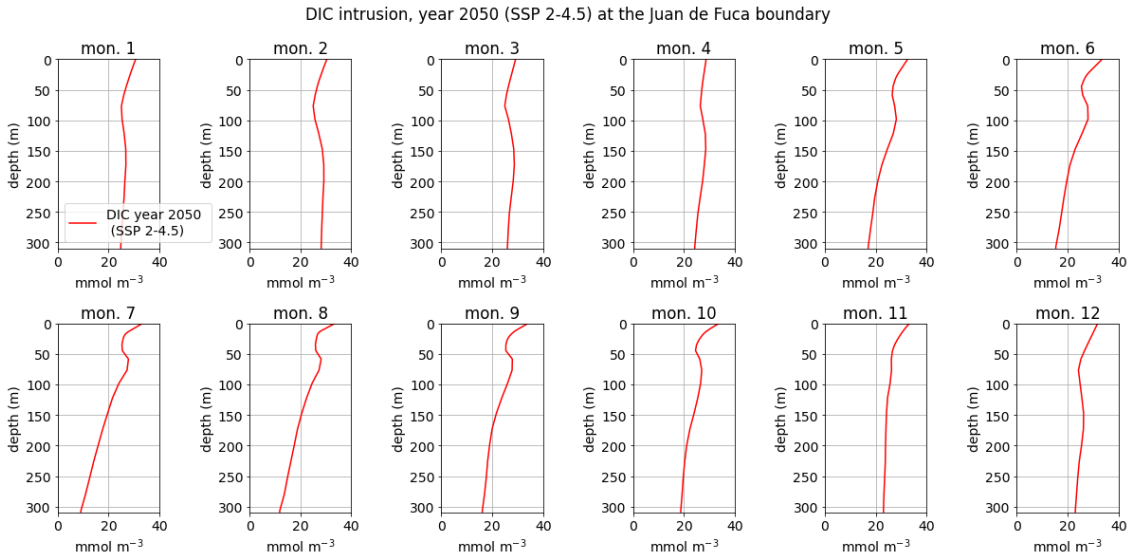

Figure C.2: The anthropogenic DIC increase at the Juan de Fuca boundary. The increase ranges from 8.6 – 34.1 mmol m^{-3}, with the mean increase at 100 m depth approximately 26.0 mmol m^{-3}.

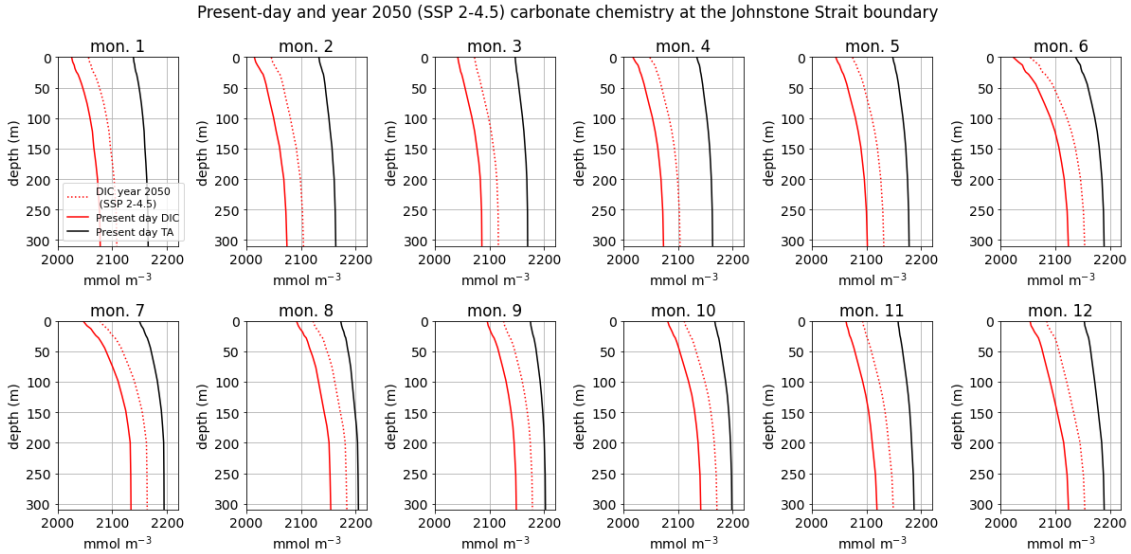

Figure C.3: Average depth profiles of present-day and year 2050 DIC and TA conditions at the Johnstone Strait boundary. DIC is shown in red (solid line = year 2017, dotted line = year 2050), while TA is shown in black. The anthropogenic DIC increase ranges from 29-31 mmol m^{-3}.

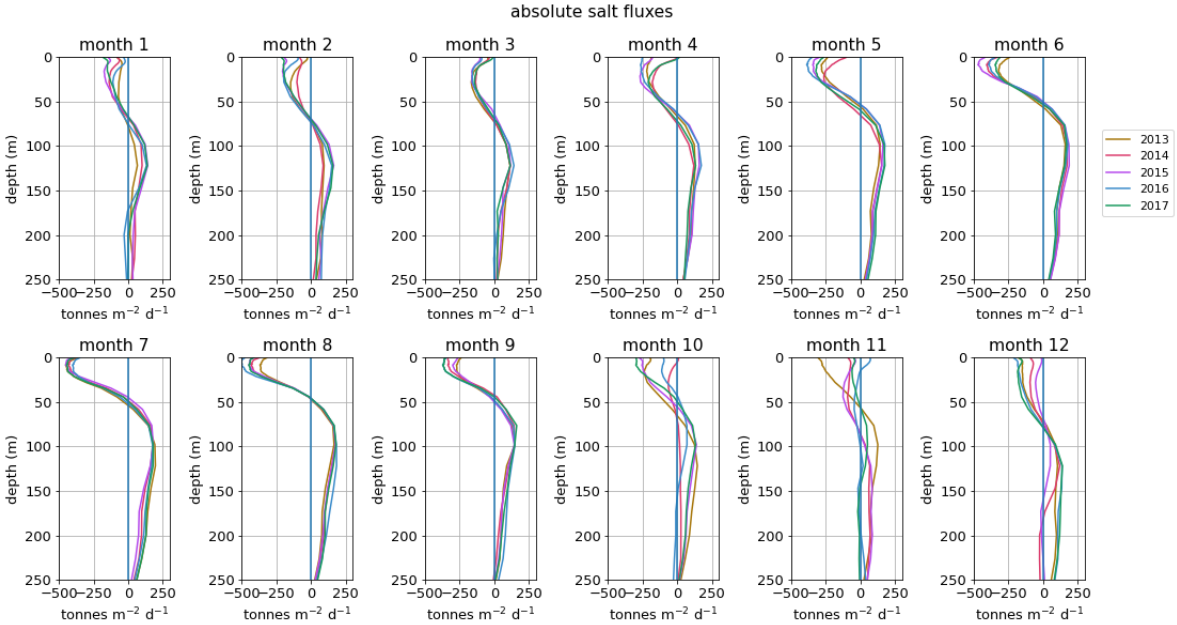

Figure C.4: Mean monthly salt flux profiles (tonnes m^{-2} d^{-1}) for years 2013-2017 at the Juan de Fuca boundary (∼5 km from the domain edge). Depth profiles show the mean for the full cross-section at the boundary at a given depth. Summers are marked by interannually consistent inflow of saltier water at depth and a prominent outflow of fresher water at the surface, while winters have weaker, more variable inflow and outflow patterns, likely influenced by episodic events (see section 4.3.3).

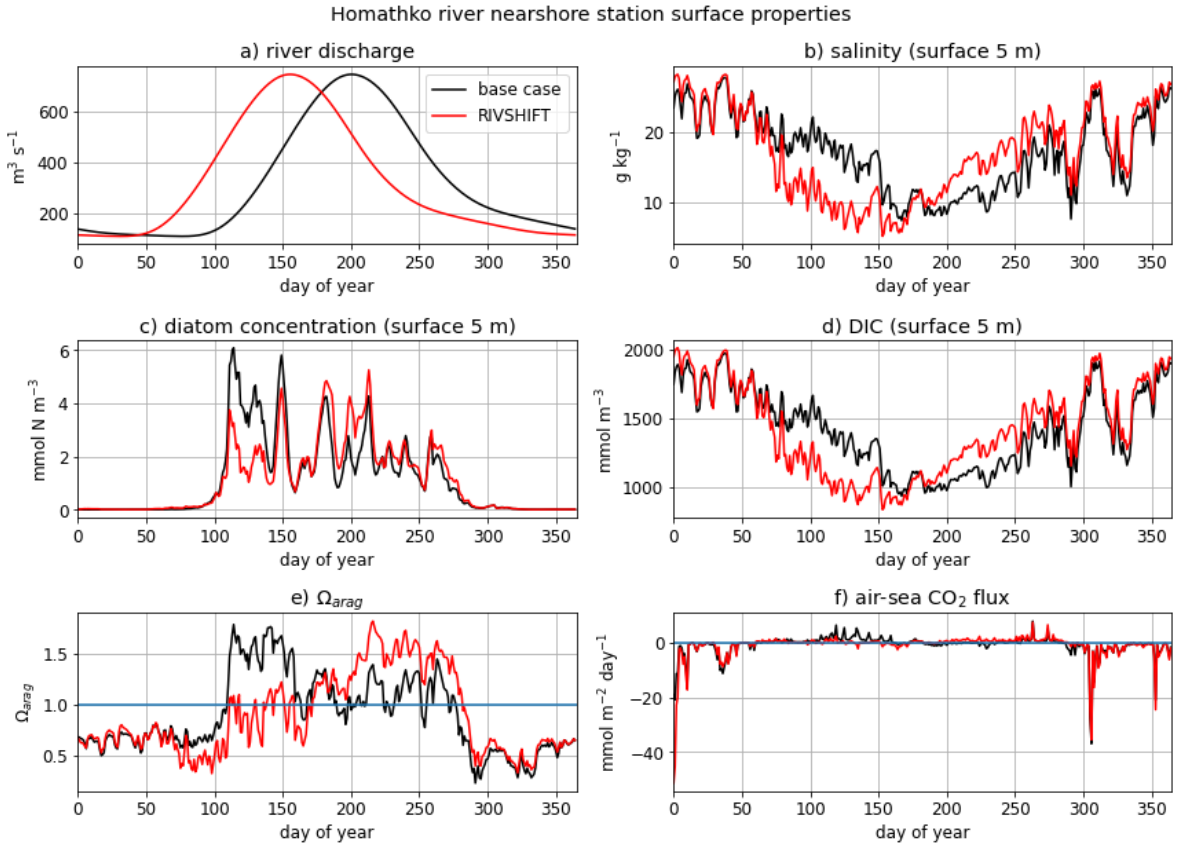

Figure C.5: Nearshore water properties of the vicinity of the Homathko rivermouth in the base and RIVSHIFT scenarios. Panel a) shows the base case (black) and shifted (red) hydgrographs. Panels b)-e) show surface 5m mean salinity, diatom concentration, DIC, and Ω_{arag}, respectively, while panel f) shows air-sea CO_2 flux.

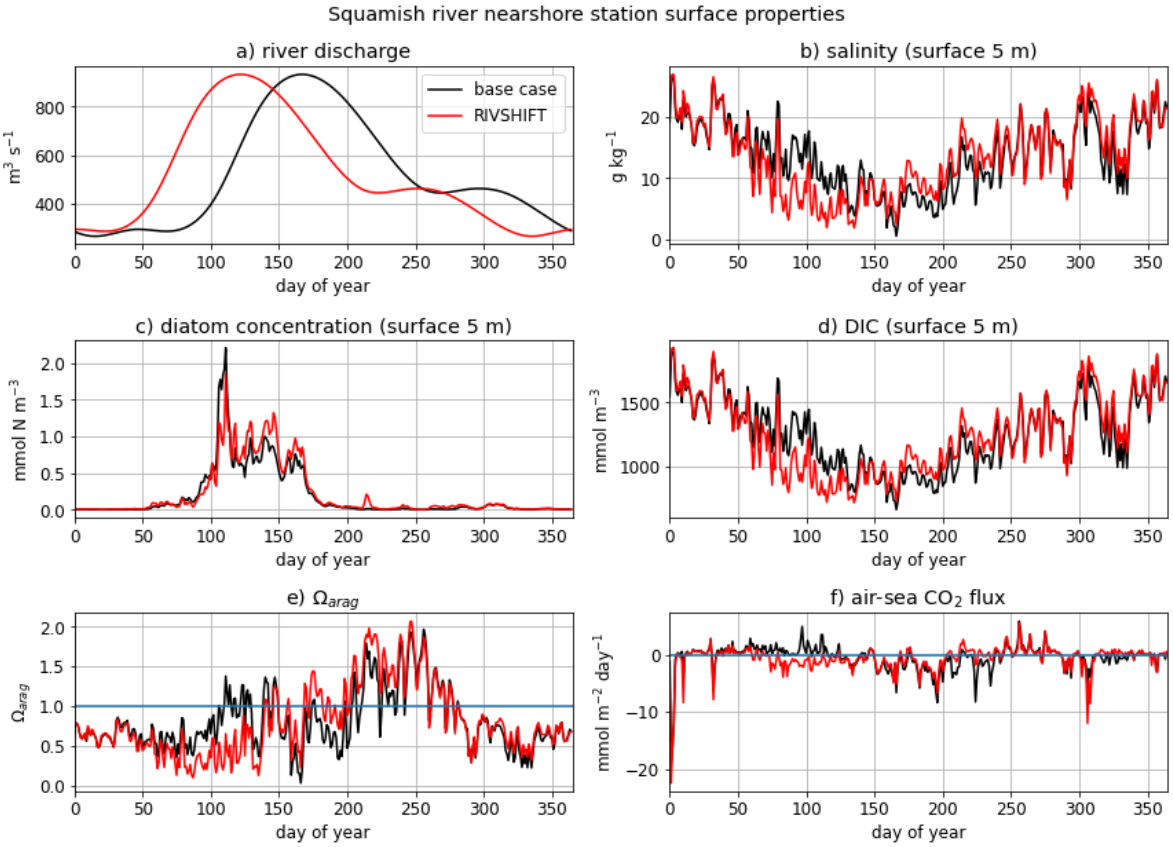

Figure C.6: Nearshore water properties of the vicinity of the Squamish rivermouth in the base and RIVSHIFT scenarios. Panel a) shows the base case (black) and shifted (red) hydgrographs. Panels b)-e) show surface 5m mean salinity, diatom concentration, DIC, and Ω_{arag}, respectively, while panel f) shows air-sea CO_2 flux.